UCLouvain
Institute of Mechanics,
Materials and Civil Engineering

Septembre 2024

Non-linear deformation in fibre-reinforced epoxies: micromechanical characterisation and modelling

Thesis submitted by,

Nathan Klavzer, Ingénieur,

in partial fulfillment of the requirements for the degree of docteur en Sciences de l'Ingénieur

Composition of the Jury

Pr. Eric Deleersnijder (Jury President)	Université catholique de Louvain, Belgium
Pr. Erik van der Giessen	University of Groningen, The Netherlands
Pr. Carlos González	Universidad Politécnica de Madrid, Spain
Pr. Hadrien Rattez	Université catholique de Louvain, Belgium
Pr. Pedro Camanho	Universidade do Porto, Portugal
Dr. Jérémy Chevalier	Syensqo, Belgium
Pr. Thomas Pardoen (Supervisor)	Université catholique de Louvain, Belgium

Abstract

Fibre-reinforced polymer (FRP) composites are ubiquitous in structural applications requiring high stiffness or strength and low weight. While the fibres are responsible for the superior stiffness and strength, the matrix material, typically made from highly cross-linked epoxies, often plays a crucial role in the damage and failure mechanisms dictating the overall strength of the composite. Hence, over the past two decades, bottom-up multiscale approaches have been at the heart of the research on composite materials. The understanding of the mechanisms defining the deformation and failure of the constituents at the microscale is of prime importance. This thesis provides experimental characterisation and modelling of an epoxy matrix at this scale.

Before entering into the micromechanical aspects, the macroscale properties of several highly cross-linked epoxies are compared and rationalised via the glass transition temperature. The aim is to determine if master trends exist in epoxies. (Non)-linear relationships between several mechanical properties, such as the yield stress, and the glass transition temperature are found, valid at different temperatures and strain rates.

Then, the microscale mechanical response of the matrix in confined volumes between fibres in a unidirectional FRP is studied. To that end, a novel nano digital image correlation (DIC) method has been developed, relying on the deposition of a fine, dense and homogeneous speckle pattern with nanoscale particles. Nano DIC allows quantification of strain fields at the submicron level and identification of regions of strain concentrations. Using the nano DIC results, a strain gradient plasticity model has been added to the constitutive model for the matrix material. This model delivered accurate predictions of the matrix strains at the microscale and of the macroscale stress-strain response of the composite.

Finally, nanoindentation was used to assess size effects within epoxies, namely the indentation size effect and the increase in the hardness of the matrix when in-between fibres of a composite. The influence of physical ageing and of the low strain rate response were carefully studied.

Résumé

Les composites à base de polymères renforcés de fibres (PRF) sont omniprésents dans les applications structurelles nécessitant une rigidité ou une résistance élevée et un faible poids. Alors que lLes fibres sont responsables de la rigidité et de la résistance supérieures., la matrice, généralement constituée d'époxy hautement réticulé, joue souvent un rôle crucial dans les mécanismes d'endommagement et de rupture qui déterminent la résistance globale du composite. C'est pourquoi, au cours des deux dernières décennies, les approches multi-échelles bottom-up ont été au coeur de la recherche sur les matériaux composites. La compréhension des mécanismes à l'origine de la déformation et de la rupture des constituants à l'échelle microscopique est d'un intérêt majeur. Cette thèse fournit une caractérisation expérimentale et une modélisation d'une matrice époxy à cette échelle.

Avant d'aborder les aspects micromécaniques, les propriétés à l'échelle macroscopique de plusieurs époxys hautement réticulés sont comparées et rationalisées à travers la température de transition vitreuse. L'objectif est de déterminer s'il existe des tendances maîtresses dans les époxys. Des relations (non)-linéaires entre plusieurs propriétés mécaniques, telles que la limite d'élasticité, et la température de transition vitreuse ont été trouvées, valables à différentes températures et vitesses de déformation.

Ensuite, la réponse micro-mécanique de la matrice dans les volumes confinés entre les fibres d'un PRF unidirectionnel est étudiée. À cette fin, une nouvelle méthode de corrélation d'images numériques (DIC) a été mise au point, reposant sur le dépôt d'un mouchetis fin, dense et homogène avec des particules de taille nanométrique. La nano DIC permet de quantifier les champs de déformation microscopique et d'identifier les régions de concentration de déformation. En utilisant les résultats de la nano DIC, un modèle de plasticité à gradient a été ajouté au modèle constitutif de la matrice. Ce modèle a permis de prédire avec précision les déformations de la matrice à l'échelle microscopique et la courbe contrainte-déformation à l'échelle macroscopique du composite.

Enfin, la nanoindentation a été utilisée pour évaluer les effets de taille dans les époxys, à savoir l'effet de taille au faible profondeur d'indentation et

l'augmentation de la dureté de la matrice lorsqu'elle se trouve entre les fibres d'un composite. L'influence du vieillissement physique et de la réponse à faible vitesse de déformation ont été soigneusement étudiés.

Zusammenfassung

Faserverstärkte Kunststoffe (FVK) sind in strukturellen Anwendungen, die eine hohe Steifigkeit oder Festigkeit bei geringem Gewicht erfordern, allgegenwärtig. Während die Fasern für die hohe Steifigkeit und Festigkeit verantwortlich sind, spielt das Matrixmaterial, das in der Regel aus hochvernetzten Epoxiden besteht, oft eine entscheidende Rolle bei den Schädigungs- und Versagensmechanismen, die die Gesamtfestigkeit des Verbundstoffs bestimmen. Daher standen in den letzten zwei Jahrzehnten Bottom-up-Multiskalenansätze im Mittelpunkt der Forschung an Verbundwerkstoffen. Das Verständnis der Mechanismen, die die Verformung und das Versagen der Bestandteile auf der Mikroskala bestimmen, ist von zentralem Interesse. Ziel dieser Arbeit ist die experimentelle Charakterisierung und Modellierung einer Epoxidmatrix auf dieser Skala.

Bevor wir auf die mikromechanischen Aspekte eingehen werden die makroskaligen Eigenschaften mehrerer hochvernetzter Epoxidharze verglichen und über die Glasübergangstemperatur rationalisiert. Ziel ist es, festzustellen, ob master Trends in Epoxiden existieren. Es werden (nicht)-lineare Beziehungen zwischen mehreren mechanischen Eigenschaften, wie der Fließspannung, und der Glasübergangstemperatur gefunden, die bei unterschiedlichen Temperaturen und Dehnungsgeschwindigkeiten gelten.

Zweitens wird die mikroskalige mechanische Reaktion der Matrix in eingeschränkten Volumen zwischen den Fasern in einem unidirektionalen FVK untersucht. Zu diesem Zweck wurde eine neuartige digitale Bildkorrelationsmethode (DIC) entwickelt, die auf der Aufbringung eines feinen, dichten und homogenen Speckle-Musters mit nanoskaligen Partikeln beruht. Nano-DIC ermöglicht die Quantifizierung von Dehnungsfeldern auf Submikron-Ebene und die Identifizierung von Regionen mit Dehnungskonzentrationen. Anhand der Nano-DIC-Ergebnisse wurde das konstitutive Modell für das Matrixmaterial um ein Modell der Dehnungsgradientenplastizität ergänzt. Dieses Modell führte zu genauen Vorhersagen der Matrixdehnungen auf der Mikroskala und des Spannungs-Dehnungs-Verhaltens der Verbundwerkstoffe auf der Makroskala.

Schließlich wurde die Nanoindentation eingesetzt, um die Größeneffekte in Epoxiden zu untersuchen, d. h. den Effekt der Eindruckgröße und die Zunahme der Härte der Matrix, wenn sie sich zwischen den Fasern eines Verbundstoffs befindet. Der Einfluss der Alterung und die Reaktion auf niedrige Dehnungsraten wurden sorgfältig untersucht.

Resumo

Os compósitos de polímeros reforçados com fibras (FRP) são omnipresentes em aplicações estruturais que exigem elevada rigidez ou resistência e baixo peso. Enquanto as fibras são responsáveis pela rigidez e resistência superiores, o material da matriz, normalmente feito de epóxis altamente reticulados, desempenha frequentemente um papel crucial nos mecanismos de dano e falha que ditam a resistência global do compósito. Assim, nas últimas duas décadas, as abordagens multiescala ascendentes têm estado no centro da investigação sobre materiais compósitos. A compreensão dos mecanismos que definem a deformação e a rotura dos constituintes à microescala é de primordial importância. Esta tese tem como objetivo fornecer a caraterização experimental e a modelação de uma matriz epoxídica a esta escala.

Antes de entrar nos aspectos micromecânicos, as propriedades à macroescala de vários epóxis altamente reticulados são comparadas e racionalizadas através da temperatura de transição vítrea. O objetivo é determinar se existem tendências principais nos epóxis. São encontradas relações (não)-lineares entre várias propriedades mecânicas, como a tensão de cedência, e a temperatura de transição vítrea, válidas a diferentes temperaturas e taxas de deformação.

Depois, é estudada a resposta mecânica à microescala da matriz em volumes confinados entre fibras num PRFV unidirecional. Para tal, foi desenvolvido um novo método de correlação de imagens nano-digitais (DIC), baseado na deposição de um padrão de manchas fino, denso e homogéneo com partículas à escala nanométrica. A nano DIC permite quantificar os campos de deformação ao nível submicrónico e identificar regiões de concentração de deformação. Utilizando os resultados do nano DIC, foi adicionado um modelo de plasticidade de gradiente de deformação ao modelo constitutivo do material da matriz. Este modelo resultou em previsões precisas das deformações da matriz à microescala e da resposta de tensão-deformação à macroescala dos compósitos.

Finalmente, a nanoindentação foi utilizada para avaliar os efeitos de tamanho estudados nos epóxis, nomeadamente o efeito do tamanho da indentação e o aumento da dureza da matriz entre as fibras de um compósito. A influência do envelhecimento físico e da resposta a baixas taxas de deformação foi cuidadosamente estudada.

Acknowledgements

Voilà que j'arrive enfin à cette dernière étape: le moment de remercier toutes les personnes qui ont contribué à la réalisation de cette thèse. Avant tout, je voudrais remercier mes chers collègues IMAP/Lacami qui font que ce labo offre une qualité scientifique incroyable tout en s'amusant beaucoup. Ca a souvent été dit, mais l'ambiance en IMAP est unique et a rendu ces années de thèse mémorables.

Ensuite, Thomas, merci de m'avoir offert cette possibilité ! J'ai vraiment pu profiter de ta passion pour la recherche, depuis mon mémoire déjà et le workshop à Porto. Tu as souvent mentionné que tu recherchais des doctorants avec des yeux qui pétillent pour la recherche. Je ne sais pas si j'avais ou si j'ai pu garder ce scintillement durant la thèse, mais sache que ton enthousiasme et ta curiosité m'ont toujours poussé à faire de mon mieux. Hélas, l'histoire des glassy polymers n'est pas encore finie, mais elle est entre bonnes mains.

I wish to extend my gratitude to all jury members who have kindly accepted to be part of this PhD. You have carefully read this manuscript and I really enjoyed and learned a lot from the discussion and comments of the private defense. I also want to thank Jérémy and Pedro for accepting to be part of the steering committee and for our various discussions over the years.

A big thanks to all the people from various institutions I had the opportunity to collaborate with: Fred, Yentl, Christian, Samuel, Mohamed, Xavier. I really appreciated all of our discussions and it was a pleasure to learn from all of you.

Je n'oublie pas évidemment les personnes qui ont été présentes au quotidien: Sarah (600 lb), Sophie (FFF), Charline, Maïté, Sanjay, Marion, Bruno, Alban, Jon. Merci pour tous ces bons moments passés ensembles, entre discussions douteuses à 8h du mat et aventures en conférences. Et le trio incroyable qui m'entoure littéralement - Marc, Catherine et Rania - nos débats à voix haute chacun sur sa chaise me manqueront beaucoup.

Ich möchte mich auch bei meiner Familie herzlich bedanken für ihre Unterstützung. Paulo, obrigado pelo apoio durante estes últimos quatro anos. E

certo que eu não estaria aqui hoje sem ti. Eu sei que nem sempre foi fàcil gerir o stress. Obrigado. Agora, a aventura està à nossa espera.

Contents

List of Figures xi

List of Tables xix

1 Introduction 1

2 Literature review 7

2.1 Viscoelastic-viscoplastic behaviour of thermoset resins 7

2.1.1 Deformation behaviour of epoxies 7

2.1.2 Physics-based modelling 12

2.1.3 Failure micromechanisms in epoxies 18

2.2 Deformation and failure in fibre-reinforced composites 24

2.2.1 Micromechanics of UD FRPs 24

2.2.2 Factors influencing the strength of UD plies 30

2.3 Nanomechanical characterisation techniques 31

2.3.1 Nanoindentation 31

2.3.2 Digital image correlation 42

2.4 Micromorphic approach 44

3 Mechanical behaviour of epoxies 47

3.1 Introduction 48

3.2 Experimental database on highly cross-linked thermosets 50

3.3 Results and discussion 52

3.3.1 Viscoelasticity 53

3.3.2 Onset of plastic yielding 55

3.3.3 Strain softening 62

3.3.4 Strain re-hardening 64

3.3.5 Failure 65

3.4 Final discussion and conclusion 66
3.5 Appendix 70
3.5.1 Curing cycles 70
3.5.2 Stress-strain curves 72
3.5.3 Compressive modulus determination 74

4 Nanoscale digital image correlation **75**
4.1 Introduction 76
4.2 Materials and experimental methods 79
4.2.1 Manufacturing of composite specimens 79
4.2.2 Speckle pattern deposition 81
4.2.3 SEM imaging and in-situ compression testing 81
4.2.4 DIC data processing 83
4.2.5 Atomic force microscopy 84
4.2.6 Finite element modelling 85
4.3 Results and discussion 86
4.3.1 Optimisation and validation of the DIC method 86
4.3.2 DIC results 91
4.3.3 Comparison to FE simulations 101
4.4 Conclusion 104
4.5 Appendix 106

5 Size-dependent plasticity **109**
5.1 Introduction 110
5.2 Experimental and numerical methods 112
5.2.1 Composite manufacturing and testing 112
5.2.2 Model formulations 113
5.2.3 FE implementation and calibration of the micromorphic model 117
5.3 Results and discussion 119
5.3.1 Assessment of the model sensitivity 119
5.3.2 DIC results and model calibration 122
5.3.3 Transverse compression of macro UD specimens 130
5.4 Conclusion 133
5.5 Appendix 135
5.5.1 Case of isotropic fibres 135
5.5.2 Influence of the fibre diameter 135

6 Nanoindentation of epoxy **139**
6.1 Introduction . . . 140
6.2 Theory . . . 141
6.2.1 Classical nanoindentation . . . 141
6.2.2 Constant contact stiffness relaxation . . . 142
6.3 Materials and methods . . . 143
6.3.1 Nanoindentation tests . . . 143
6.4 Results and discussion . . . 144
6.4.1 Indentation size effect . . . 144
6.4.2 In-situ indentation response inside composites . . . 156
6.5 Conclusion . . . 164

7 Conclusion **167**
7.1 What about the main scientific questions? . . . 168
7.2 Prospectives and future work . . . 170

A Appendix - Review on the nanomechanics of FRPs **173**
A.1 Introduction . . . 173
A.2 Nanoindentation . . . 176
A.3 Atomic force microscopy . . . 179
A.4 In situ mechanical testing in SEM coupled to DIC . . . 182
A.5 Fibre push-out . . . 185
A.6 Mesoscale modelling via shear transformation zone (STZ) dynamics 188
A.7 Conclusion and perspectives . . . 191

List of publications **193**

Bibliography **195**

List of Figures

1.1 Experimental and virtual test pyramids currently under use for the validation of FRP structures. From [2]. 2
1.2 Illustration of the bottom-up multiscale approach. Appropriate homogenisation schemes are required at each scale transition. . 3

2.1 Characteristic quantities of interest describing the overall elasto-viscoplastic stress-strain response of an epoxy up to failure. . . 8
2.2 Impact of physical ageing and rejuvenation on the stress-strain response of glassy polymers. 10
2.3 Example of polarized light microscopy images of shear band formation under plane strain compression for (a) PMMA and (b) PET. Adapted from [9]. 11
2.4 Example of stress-strain responses with full unloading and strain recovery for RTM6 epoxy at different levels of applied compressive strain. Adapted from [7]. 13
2.5 Schematic illustration of the modelling of a kink-pair by a pair of wedge dislocations in an elastic surrounding. Adapted from [44]. 14
2.6 Schematic illustration of the formation of cavities due to excessive stresses created during kink-pair creation. Adapted from [44] . 15
2.7 Stress-strain response in compression of a DGEBA/33DDS epoxy resin at 300 K. Comparison between the responses predicted by molecular dynamics simulation at 10^8 s^{-1} (circles), by rescaling the MD response to quasi-static conditions using Argon's double kink theory (squares) and measured experimentally (triangles). Adapted from [54]. 16
2.8 Schematic illustration of the activation of an STZ. A shear eigen-strain γ_0 causes a local change in the molecular configuration of a material volume Ω by overcoming an energy barrier ΔF. . . . 18
2.9 Schematic illustration of the typical features observed on the fracture surface of highly cross-linked epoxies (adapted from [35]) and corresponding fracture surface in tension of RTM6 (from [74]). The arrow in the bottom SEM image corresponds to the crack propagation direction. The letters correspond to specific features found at different locations on real fracture surfaces and shown in the schematic. 19

2.10 Schematic illustration of the general failure mechanism for highly cross-linked epoxies proposed by Chevalier et al. [76]. 20
2.11 Example of microscopic observation of a crack arrest during unstable propagation (adapted from [66]). 21
2.12 (a) Schematic illustration of the failure mechanism in the presence of a sharp crack proposed by Chevalier et al. [76] and (b) corresponding SEM micrograph of a crack blunting zone at the tip of sharp crack in a CT test. 23
2.13 Typical damage phenomena occurring in UD plies: (a) matrix plasticity favouring subsequent shear banding, (b) fibre/matrix decohesion, (c) fibre breaking and (d) fibre kinking. 25
2.14 Micrograph showing the failure under transverse compression due to matrix shear plastic deformation and fibre/matrix decohesion leading to a final failure plane oriented at 53° for a UD RTM6/carbon fibre composite. 27
2.15 Maps of cumulative plastic strain p numerically predicted for: (a) transverse compression, (b) transverse tension and (c) transverse shear. The white regions depict fibre/matrix decohesion. Adapted from [90]. 28
2.16 Schematic overview of the nanomechanical characterisation techniques used for the study of the constituents of FRPs. 32
2.17 Schematic representation of (a) the load-displacement during a nanoindentation test and (b) the sink-in phenomenon. 33
2.18 Comparison between the moduli measured from nanoindentation and classical macroscale tests for several glassy polymers studied in the literature: PS, PC, PET and iPP from [154], Epoxy 6376 [156], RTM6 [157], PMMA [153], EPON828 [158]. 34
2.19 Typical (a) modulus E and (b) hardness H dependence on the indentation depth h for different polymers in the literature: RTM6 [157], EPON828 [158] and PC and epoxy [167]. An indentation size effect (ISE) is found at low indentation depths for all systems. 36
2.20 Representation of the strain gradient $\bar{\chi}$ for (a) a sharp tip and (b) a spherical tip. 38
2.21 Schematic representation of three typical nanomechanical characterisation techniques similar to nanoindentation to assess in-situ properties of composite matrices: (a) atomic force microscopy (e.g. interphase characterisation), (b) micropillar compression (e.g. microscale stress-strain curve) and (c) fibre push-out (e.g. interfacial shear strength). 41
2.22 Schematic illustration of the concept of digital image correlation. 43

3.1 True stress-true strain responses of the different epoxies at room temperature and $\dot{\varepsilon} = 0.01\ \mathrm{s}^{-1}$. 52

3.2 Variation of the compressive Young's modulus E_C as a function of T/T_g. Each marker corresponds to a different resin. The effect of imposed strain rate is shown by the colour of the markers. The shaded area shows the ±10% bounds. The R^2 value of the linear regression including all data points is equal to 0.98. . . 54
3.3 Master curve of E_C/T as a function of $\log(\dot{\varepsilon})$ for all resins using a shift factor based on T_g given in Eq. 3.4 ($R^2 = 0.8$). The different colours for each resin represent the different test temperatures. 55
3.4 Variation of the compressive upper yield stress σ_y as a function of T/T_g. $R^2 = 0.79$. 56
3.5 (a) Strain rate sensitivity variation of the upper yield stress σ_y with T/T_g and (b) variation of the activation volume calculated in the context of an Eyring model as a function of T/T_g. 58
3.6 Variation of the identified ΔH_β with respect to T_g 59
3.7 (a) Variation of σ_y/T as a function of $\log(\dot{\varepsilon})$ at different temperatures and strain rates comparing the experimental values (markers) and the yield stress predicted by the enhanced Eyring's model of Eq. 3.5 and (b) relative error with respect to the experimental results. 60
3.8 Variation of the compressive upper yield strain ε_y as a function of T/T_g. $R^2 = 0.83$. 61
3.9 Variation of (a) the compressive lower yield stress σ_l ($R^2 = 0.85$) and (b) the normalised stress drop $\Delta\sigma$ as a function of T/T_g. . 63
3.10 Variation of the re-hardening modulus G_h as a function of T/T_g. $R^2 = 0.31$. 65
3.11 Variation of (a) the failure stress σ_f ($R^2 = 0.3$) and (b) the ratio σ_f/σ_y as a function of T/T_g. 67
3.12 Variation of (a) the failure strain ε_f ($R^2 = 0.68$) and (b) the ratio $\varepsilon_f/\varepsilon_y$ as a function of T/T_g. 68
3.13 Upper yield stress σ_y as a function of failure strain ε_f for all epoxies at different strain rates and temperatures. 70
3.14 Curing cycles of all the epoxy resins, which may differ from the manufacturer's protocols. Refer to references in section 3.2 for more details. 71
3.15 Stress-strain curves for RTM6. 72
3.16 Stress-strain curves for 8552. 72
3.17 Stress-strain curves for SR8500-1. 73
3.18 Stress-strain curves for SR8500-2. 73
3.19 Stress-strain curves for DGEBA at 25°C. 73
3.20 Stress-strain curves for TGDDM at 25°C. 74
3.21 Methodology to remove initial curve toe, as per ASTM D695. . 74

4.1 Unidirectional composite specimens for in-situ transverse compression testing: (a) glass fibre-reinforced TP and (b) carbon fibre-reinforced TS. Fibre orientation is parallel to the z-axis and compression is performed in the x-direction. All dimensions are in mm. 80
4.2 Thermoplastic composite specimen mounted on microtest compression stage. 82
4.3 Optimisation of the speckle pattern for DIC measurements: SEM images of a (a) 2 nm, (b) 5 nm, (c) 10 nm, (d) 20 nm and (e) 50 nm-thick indium speckle deposited by e-beam evaporation onto Si wafers. 88
4.4 Particle size distribution of indium speckle patterns with target thicknesses of (a) 2 to 50 nm and (b) 2 and 5 nm. 89
4.5 Comparison of particle size distributions obtained for a 5 nm-thick indium speckle pattern deposited onto two different substrates: Si wafer vs. carbon fibre-reinforced TS composite. 89
4.6 Region of interest for the quantification of the spatial and drift distortion amplitudes. 90
4.7 Horizontal displacement field measured by DIC: (a) without any correction, (b) after spatial correction and (c) after spatial and drift corrections. 91
4.8 Macroscopic load-displacement curves obtained from the in-situ compression testing and SEM micrographs of the corresponding ROIs used for DIC analysis of: (a) and (b) an RTM6/carbon fibre specimen and (c) and (d) an Elium/glass fibre specimen. Coloured arrows indicate the location of failure events observed within or close to the ROIs during testing, and the same colour code is used to show force-displacement values at these moments. 92
4.9 Strain maps and evolution of strain profiles across the carbon fibre-RTM6 matrix interface (white dashed line) obtained by DIC: (a) along the x and (b) xy directions. 94
4.10 Strain maps obtained by DIC in the Elium/glass fibre specimen along the x direction, (a) before first failure event and (c) before second failure event, and along the xy directions (b) before 1st failure event and (d) before 2nd failure event, alongside with corresponding strain profiles across the fibre/matrix interface (white dashed line) in the (e) x and (f) xy directions. The terms 'first and second cracks' refer to the failure events identified in Fig. 4.8. 95
4.11 RTM6 – Post-mortem observations of the failed material surface: (a) general overview, (b) main crack, (c) fibre/matrix level interface failure, (d) zoom of the interface failure in (c). 96

4.12 Elium – Post-mortem observations of the failed material surface: (a) general overview, (b) main cracks, (c) fibre/matrix level diffuse cracks and shear bands, (d) zoom of the cracks in (c). 97
4.13 Comparison between initial and final (post-failure) images for two ROIs: RTM6 system (a) in initial state versus (b) after failure, and Elium system (c) in initial state versus (d) after failure. Note that the failure regions are highlighted by white ellipses, while the white arrows represent sources of imperfection for the DIC analysis. 98
4.14 RTM6 - Horizontal ε_{xx} strain map at four different stages during the in-situ compression test until the last moment before failure: (a) at 600 N, (b) at 850 N, (c) at 1000 N and (d) at 1150 N. . . 99
4.15 Elium - Horizontal ε_{xx} strain map at four different stages during the in-situ compression test until the last moment before failure: (a) at 500 N, (b) at 700 N, (c) at 1000 N and (d) at 1300 N. . . 100
4.16 Evolution of the horizontal ε_{xx} strain along the three numbered profiles shown in Fig. 4.14 and 4.15 at different stages during the in-situ compression test: (a) and (b) profiles 1 and 2 on RTM6, respectively; (c) profile 3 on Elium. An interphase of around 300 nm marked by the shaded area is visible for both systems. 101
4.17 Atomic force microscopy measurements obtained by PeakForce Tapping on (a), (b) the RTM6/carbon fibre composite, and (c), (d) the Elium/glass fibre composite. DMT modulus maps are presented in (a) and (c), while (b) and (d) show the evolution of the DMT modulus along two profiles extracted from each map. 102
4.18 RTM6 – Horizontal ε_{xx} strain field (a) measured by DIC versus (b) predicted by FEA using a continuum model, and (c) comparison of strain evolution along the white dashed profile for both DIC and FEA. (d), (e) and (f) show the equivalent in terms of shear strains ε_{xy}. 103
4.19 Elium, before second failure event – Horizontal ε_{xx} strain field (a) measured by DIC versus (b) predicted by FEA using a continuum model, and (c) comparison of strain evolution along the white dashed profile for both DIC and FEA. (d), (e) and (f) show the equivalent in terms of shear strains ε_{xy}. 105
4.20 Horizontal ε_{xx} strain field measured by DIC: (a) without any correction, (b) after spatial correction and (c) after spatial and drift correction. 107
4.21 Maximum shear γ_{max} strain fields obtained by DIC (a) in the RTM6/carbon fibre system and (b), (c) in the Elium/glass fibre system before first failure event and before second failure event, respectively. 108

5.1 SEM images of the two regions of interest (ROIs) used for the DIC analysis before deformation. 114
5.2 Comparison of the experimental and model equivalent stress-equivalent plastic strain response in compression for RTM6 at $\dot{\varepsilon} = 10^{-3}\text{s}^{-1}$. 115
5.3 Geometry and mesh used in the FE models: (a) one of the studied ROIs in the nano-DIC analysis and (b) one of the RVEs related to the macroscopic transverse compression study. 119
5.4 Impact of the micromorphic parameter A on the stress-strain response in compression for the single fibre problem in (a) for (b) $V_f = 0.1$, (c) $V_f = 0.2$ and (d) $V_f = 0.4$. The reference curve of pure RTM6 under homogeneous compression is given in blue. 120
5.5 Variation of the normalized yield stress σ_y/σ_0 as a function of the ratio of the unit cell length over the approximate characteristic length l_c (assuming H = -100 MPa) for different V_f. 121
5.6 Maps of the cumulative plastic strain p in compression for $V_f = 0.2$ at a macroscopic load equivalent to $\bar{\varepsilon}_{xx} = 0.1$ [-] for (a) $A = 0$ N (classical model), (b) $A = 10^{-5}$ N, (c) $A = 10^{-4}$ N and (d) $A = 10^{-3}$ N. 122
5.7 Maps of the cumulative plastic strain p for $V_f = 0.2$ and $A = 10^{-4}$ N at a macroscopic load equivalent to $\bar{\varepsilon}_{xx} = 0.1$ [-]: (a) coarse (4,032 elements), (b) normal (9,720 elements) and (c) fine (25,200 elements) meshes. 123
5.8 ROIs after local failure in the DIC analysis: (a) ROI 1 and (b) ROI 2. The white dotted lines represent paths used to evaluate the strain profiles. 124
5.9 DIC results for the two ROIs of interest. (a), (c) ROI 1 ε_{xx} and ε_{yy} strain fields and (b), (d) ROI 2 ε_{xx} and ε_{yy} strain fields. . . 125
5.10 Maps of ROI 1 showing the vertical strain ε_{yy} just before failure for (a) the classical model, (b) $A = 10^{-3}$ N, (c) $A = 10^{-4}$ N, (d) $A = 10^{-5}$ N. 126
5.11 Evolution of strain profiles (a) for ε_{yy} along path (1) and (b) for ε_{xx} along path (2). 127
5.12 Maps of ROI 2 showing the maximum shear strain γ^{max} just before failure for (a) the DIC results, (b) the classical model, (c) $A = 10^{-3}$ N, (d) $A = 10^{-4}$ N, (e) $A = 10^{-5}$ N. 128
5.13 Evolution of strain profiles (a), (b) for ε_{xx} and for ε_{yy} along path (3) and (c) γ^{max} for path (4). 129
5.14 Stress-strain responses from the transverse compression of UD composites. Comparison between experimental results (blue triangles), the prediction of the classical model (dotted grey line) and the predictions of the micromorphic model for different values of A. 130

5.15 Maps of the cumulative plastic strain p at a macroscopic load equivalent to $\bar{\varepsilon}_{yy} = 0.045$ [-] for (a) $A = 0$ N (classical model), (b) $A = 1.6\ 10^{-3}$ N and (c) $A = 8\ 10^{-4}$ N. 132
5.16 Stress-strain responses from the transverse compression of UD composites for purely *isotropic* fibres. Comparison between experimental results (blue triangles), the prediction of the classical model (dotted grey line) and the predictions of the micromorphic model for different values of A. 136
5.17 Maps of the cumulative plastic strain p at a macroscopic load equivalent to $\bar{\varepsilon}_{yy} = 0.035$ [-] for (a) and (c) orthotropic and (b) and (d) isotropic fibres. (a) – (b) $A = 0$ N (classical model) and (c) – (d) $A = 2.5\ 10^{-4}$ N. 137
5.18 Stress-strain responses from the transverse compression of UD composites with a fibre diameter of 7 µm. Comparison between experimental results (blue triangles), the prediction of the classical model (dotted grey line) and the predictions of the micromorphic model for different values of A. Dotted line = orthotropic fibres, full line = isotropic fibres. 138

6.1 Indentation hardness H and modulus E with respect to the indentation depth h for bulk RTM6 at a rate $\dot{\varepsilon} = \dot{F}/F = 0.05$ s^{-1}. Both the hardness and modulus curve present an indentation size effect at low indentation depths (<500 nm). The shaded area shows the experimental error. 146
6.2 Impact of thermal rejuvenation on the indentation (a) hardness H and (b) modulus E with respect to the indentation depth h for bulk RTM6 at a rate $\dot{\varepsilon} = \dot{F}/F = 0.05\ s^{-1}$. 148
6.3 Variation of the loading rate $\dot{F}/F$ measured experimentally with the indentation depth h. The imposed indentation loading rates are given in the figure. The lower the imposed rate, the higher the stabilisation depth. 149
6.4 Variation of the (a) indentation hardness H with respect to the indentation depth h for bulk RTM6 at different strain rates and (b) of the hardness normalised by the value at the plateau H/H_0 illustrating the magnitude of the ISE as a function of the imposed rate. The amplitude of the ISE reaches less than 5% of the plateau value at $h \sim 200$nm. 151
6.5 Variation of the (a) indentation modulus E with respect to the indentation depth h for bulk RTM6 at different strain rates and (b) of the modulus normalised by the value at the plateau E/E_0 illustrating the magnitude of the ISE as a function of the imposed rate. The amplitude of the ISE reaches less than 5% of the plateau value at $h \sim 200$nm. 152

6.6 Comparison between the experimental hardness and the calculated rate-dependent hardness (based on the plateau values) associated to the stabilisation of the strain rate during indentation The colour code is the same as in the previous figures. 153
6.7 Variation of the hardness H, as measured by constant contact stiffness relaxation, as a function of the strain rate under the indenter $\dot{\varepsilon}_r$ at different indentation depths. 154
6.8 Relaxation tests: (a) activation volume V and (b) rate sensitivity m as a function of $\dot{\varepsilon}_r$ at different indentation depths. 155
6.9 Variation of the indentation hardness H and modulus E with respect to the indentation depth h comparing the bulk and UD pockets of RTM6 at a strain rate $\dot{\varepsilon} = \dot{F}/F = 0.05\ \mathrm{s}^{-1}$. 158
6.10 Variation of the UDRTM6 modulus normalised by the bulk RTM6 modulus as a function of the fibre constraint factor FCF=d_{fib}/h. A stable region exists for FCF in [30-60] where the response is unbiased by the presence of the fibres. 159
6.11 Variation of the indentation hardness H as a function of the indentation depth h for bulk RTM6 and UDRTM6 comparing the responses after thermal rejuvenation at 235°C for 15 minutes (colour) and as-cured (grey). 160
6.12 Relaxation tests at a depth of 500 nm: variation of (a) the hardness H and (b) the representative stress σ_r as a function of $\dot{\varepsilon}_r$ for the rejuvenated (colour) and as-cured (grey) bulk and UD specimens. 162
6.13 Relaxation tests at a depth of 500 nm: (a) activation volume V and (b) rate sensitivity m as a function of $\dot{\varepsilon}_r$ for the rejuvenated (colour) and as-cured (grey) bulk and UD specimens. 163

A.1 Description of some nanomechanics-based methods to quantitatively investigate the response of the matrix-fibre elementary volume, involving the confined matrix, the interphase layer, the interface with fibre and the fibre. 176
A.2 Application of nanoindentation to extract stiffness and hardness of polymer matrix in near-fibre confined volumes; (a) principle of nanoindentation; (b) example of hardness and elastic stiffness data in highly cross-linked RTM6 epoxy measured by nanoindentation, comparing bulk and confined values – the fibre constraint factor is the distance to fibre normalized by indentation depth; (c) finite element simulation of nanoindentation to account for and deconvolute the fibre constraint effect. 178
A.3 Characterisation of polymer-based composites by AFM: (a) instrumentation and length scales, (b) applications and (c) current limitations. 180

A.4 Digital image correlation applied to polymer-based composites; (a) length scales at play; (b) example of a carbon fibre-reinforced RTM6 composite [157]; (c) challenge related to speckle quality [225]. 184
A.5 Push out test applied to polymer-based composites: (a) micrograph of a typical nanoindenter flat tip, schematic representation of the single fibre push-out test and micrograph of a debonded fibre at the end of a test; (b) micrograph showing indented fibres with different surrounding configurations, load-displacement curves resulting from fibre push-out tests and time-displacement curves showing the displacement jump characteristic of final crack propagation; (c) 3D finite element simulation of a push-out test (equivalent plastic strain in the matrix), typical bi-linear stress-displacement law for cohesive zones, load-displacement curves from FEA with and without damage at the interface. 186
A.6 STZ approach applied to polymers. (a) Finite element mesh of the polymer matrix domain and illustration of the STZ assignment scheme: each element forms an STZ together with its node-sharing elements. (b) Illustration of the simplified energy landscape for deformation of an STZ in pure shear (via an eigenstrain of magnitude γ_0). (c) Predicted contours of constant maximum principle strain ε_I on a unidirectional fibre-matrix RVE in displacement-controlled transverse compression; the applied displacements on the RVE boundaries give an homogenised strain state equal to the homogenised strain state on a region of a SEM image (d) taken during transverse compression of a unidirectional carbon fibre-epoxy ply. 189

List of Tables

3.1 Epoxy systems of interest with corresponding glass transition temperatures and reference studies. The results for 8552 have not yet been published. 51
3.2 Coefficients of the linear relationships describing each property of interest with respect to T/T_g. 66

4.1 Elastic properties of the fibre and the matrix materials used of the FE modelling of the TP and TS composite systems. 86

4.2 Strain deviation analysis results obtained for various sets of DIC parameters. 87

5.1 Elastic properties of the fibres and matrix. 118

1

Introduction

Over the past few decades, the design of structures with optimisation of the mass towards higher performance applications has been synonymous to using fibre reinforced polymer-based (FRPs) composites. If one attempts to solve a material selection problem for a stiffness or strength dominated problem within the elegant framework proposed by Ashby [1], the answer is almost exclusively to select FRPs. The presence of FRPs is thus ubiquitous in high performance applications. For instance, wind turbine blades are huge structures, reaching over one hundred meters, while still rotating at high speed. In such instances, glass-fibre based composites constitute the only possible solution. Within the aeronautic and space sectors, mass saving is simply equal to cost and fuel savings, rendering composites irreplaceable. A similar situation occurs in the naval industry, high-performance sports, and the energy sector at large.

Despite the abundant use, FRPs are complex materials made up of a multi-scale and highly anisotropic layup. This structural complexity of the material inherently implies that its deformation and failure mechanisms are equally as complex. In fact, the choice of matrix (thermoplastic or thermoset) and fibre (carbon, glass, etc.) as well as the stacking sequence and relative orientation of the plies are all factors influencing the mechanical response of FRPs. This makes the failure of composites hard to predict.

Uncertainty associated to the failure of composite structures has been a limiting factor in the digitalisation of the testing procedures across different scales. Fig. 1.1 shows the current test pyramids for validation, as proposed by Arteiro et al. [2], from the experimental and numerical perspective. The increase in computational capacity and the progress in numerical modelling has allowed encompassing numerical validations within the overall test pyramid. Nonetheless, the sector is still far from being able to create accurate digital twins. Still, the use of digital twins is a major driving force for reducing both the financial and environmental costs of sectors such as the aeronautic one. To

that end, the ongoing trend in the research community is to rely on bottom-up multiscale approaches [3, 4] and, recently, in joint combination with machine learning designs [5].

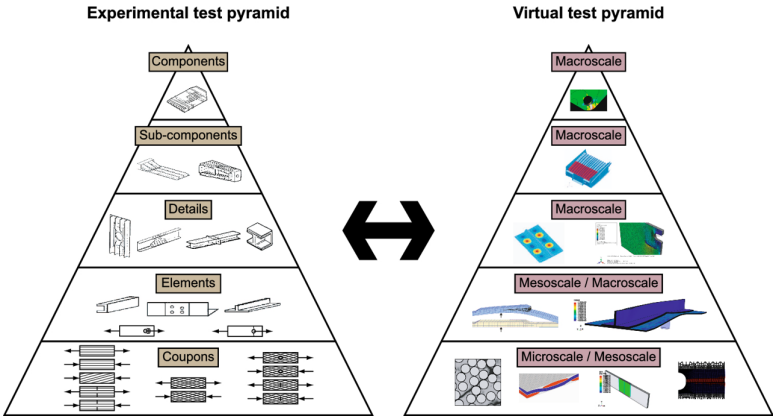


Fig. 1.1: Experimental and virtual test pyramids currently under use for the validation of FRP structures. From [2].

Fig. 1.2 illustrates the typical multiscale modelling approach for FRPs. At each level (i.e. constituents, ply, laminate, structure), the homogenised mechanical response and its influencing factors are assessed and transferred to the next level. The starting block of such approaches is the fundamental understanding of the deformation and failure response of the individual constituents and their combined responses within a unidirectional ply. At this microscale level, it is also possible to optimise the design of FRPs.

Currently, the aeronautic industry faces the challenge of the climate crisis and needs to significantly reduce its environmental impact. According to the most recent report of the International Transport Forum [6], the main drivers for reducing the CO_2 footprint of this industry are: increasing the fuel efficiency of aircrafts and replacing kerosene with alternative fuels (based on biomass or hydrogen). While both of these approaches are essential, they are still in the early stages of development and will, naturally, create new material challenges. Hence, the FRP sector reduces its environmental footprint by moving away from thermoset epoxy matrices, in favour of recyclable thermoplastic ones, in the hope of cutting environmental costs related to the manufacturing. This transition is naturally accompanied by new challenges related to the increased complexity of the microstructure of thermoplastic matrices. Hence, in order to make an efficient transition, it is crucial to fully understand the mechanical behaviour of current epoxy-based composites and incorporate this information within the multiscale modelling and design methodologies. This will facilitate

the knowledge transfer between thermoplastics and thermosets.

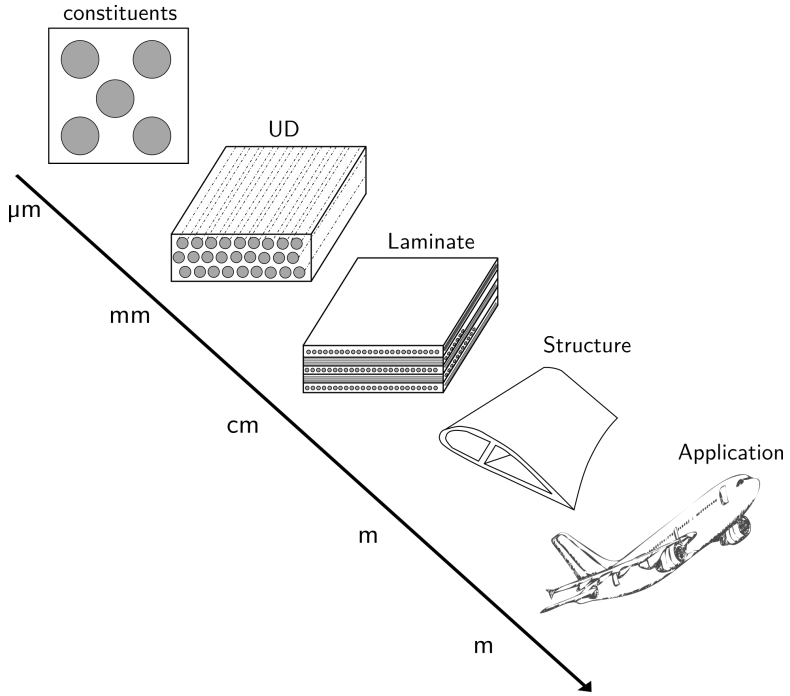


Fig. 1.2: Illustration of the bottom-up multiscale approach. Appropriate homogenisation schemes are required at each scale transition.

Objectives

This PhD thesis places itself at the microscale level of the multiscale paradigm described before. The goal of this work is to push the state of the art in the characterisation and modelling of the microscale mechanical response of an unidirectional (UD) carbon fibre-reinforced epoxy composite, with a specific focus on the behaviour of the matrix in micron-sized confined volumes between fibres. By providing accurate data at the nano- and microscale regarding the deformation and failure of the matrix, the vision is to help improve the predictive capability of computational micromechanics models, which often still rely on properties determined at the macroscale. The origin of this scientific hypothesis lies within recent studies, which showed that the local properties in FRPs may strongly differ from macroscale properties. The scientific questions guiding the PhD are:

1. Considering the reported differences between bulk and in-situ properties of epoxy matrices, what is the physical origin of the differences in properties

and what are the controlling factors?

2. May the change in behaviour be attributed to a difference in physico-chemical structure of the polymer and/or is this difference in deformation response the result of a confinement/size effect when the polymer is constrained in such a small volume?

3. Is there an influence of the heterogeneous nature of the deformation process of polymers on the local mechanical properties and what is the physical failure mechanism of the matrix at that scale?

4. What is the mechanical behaviour of the interphase that forms around the fibres and how does it affect the local matrix response and the load transfer to the fibres?

5. Is it possible to improve constitutive modelling frameworks to account for size effects present in glassy polymers? How do such size effects affect the UD response?

The objective of this thesis is to tackle these questions by a combined experimental and numerical approach. Aside from the purely fundamental interest of unravelling the detailed mechanisms of deformation and failure at the length scale of the matrix/fibre elementary volume, this work aims to model the macroscopic response of UD composites using some insights from the constituent properties. Some of these questions will be addressed with more intensity than others.

Outline

This first chapter serves as a general introduction to the scientific and technological context setting the motivation of this research.

Chapter 2 provides a literature review about the current state of knowledge within the glassy polymer and FRP communities. More specifically, the mechanical response of glassy polymers and epoxies, the micromechanical characterisation and modelling of FRPs and the main nano-/micromechanical techniques available to study such systems are described. At times, the reader will be referred to the introductions of subsequent chapters for more specific literature coverage.

Chapter 3 starts at the macroscale. In this chapter, the mechanical responses in compression of several epoxy resins used as matrices in high performance

FRPs are studied and compared. The objective is to determine universal characteristics within their stress-strain response and to correlate the resulting mechanical properties with the molecular structure of these resins and the fundamental deformation mechanisms. Knowledge of such universalities can aid with the design of future composite systems.

Chapter 4 addresses a major nanomechanical characterisation challenge in the community. Computational micromechanics currently requires experimental validation for strain fields at the fibre/matrix level. This chapter proposes a new nano digital image correlation (DIC) approach combined with in-situ mechanical testing in order to provide accurate strain field measurements going as small as submicron size bands between fibres.

Chapter 5 proposes a novel modelling approach based on strain gradient plasticity in order to account for size effects and solve regularisation issues within computational micromechanics approaches. In this chapter, the nano DIC results of chapter 4 serve as a basis for validation of the model. The model is then used to predict the stress-strain response of a UD composite, in comparison to experimental results.

Chapter 6 looks at the in-situ properties of the matrix. To that end, nanoindentation will be used. Bulk and in-situ properties will be critically compared, particularly in terms of external influencing factors and physical ageing. The low strain rate response is tackled using constant stiffness relaxation tests.

The work will end with a brief conclusion, which will summarise the main outcomes of this work and provide some future prospectives.

2

Literature review

2.1 Viscoelastic-viscoplastic behaviour of thermoset resins

"Glassy polymers" is the term that encompasses both thermoplastic and thermoset polymers used in applications below their glass transition temperature T_g. Thermoplastic polymers consist of entangled macromolecular chains whereas thermosets are based on chemically cross-linked networks of such chains. This section presents the fundamentals of this thesis, which is an overview of the mechanical response of glassy polymers, with a specific focus on thermosetting epoxy resins. It sets the basis for all the discussions, particularly in chapter 3. The section starts by describing the macroscale deformation response of epoxies. Then, some molecular models used to investigate the origin of the deformation in glassy polymers are briefly described. The section ends by studying the failure in highly cross-linked epoxies and how thermoplastics and thermosets differ in this aspect.

2.1.1 Deformation behaviour of epoxies

Fig. 2.1 shows a typical true stress-strain response of an epoxy loaded under uniaxial compression, highlighting the parameters defining the mechanical response. These parameters are explained in the next paragraphs.

Upon loading, glassy polymers exhibit an elastic response with a Young's modulus E generally between 1 and 4 GPa. This initial resistance to deformation comes from secondary intermolecular interactions, mainly Van der Waals and hydrogen bonds. At larger strains, the response becomes non-linear, mainly caused by local stress relaxation due to heterogeneous molecular movements. This behaviour is temperature and strain rate dependent. Highly cross-linked epoxies with high T_g do not exhibit significant viscoelasticity, particularly at

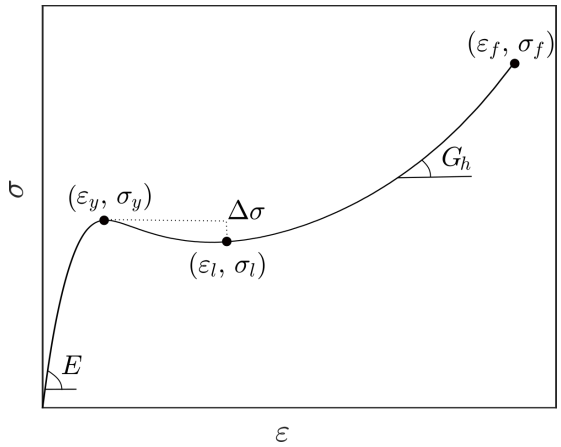


Fig. 2.1: Characteristic quantities of interest describing the overall elasto-viscoplastic stress-strain response of an epoxy up to failure.

ambient temperature, as they have a relatively low loss modulus, see [7], for instance, for RTM6 epoxy resin. Hence, viscoelasticity is not extensively addressed hereafter.

The yield point $(\varepsilon_y, \sigma_y)$ of glassy polymers has received most of the attention in the literature. This upper yield marks the transition from reversible to irreversible conformational changes in the polymer chains and is most often defined as the local maximum of the stress-strain curve. Ample experimental studies have shown that it is strongly affected by temperature, strain rate, hydrostatic pressure, thermomechanical history (i.e. ageing), relative humidity (i.e. water content of the network) and initial chain alignment [8–11]. Some polymer glasses also present a difference in yielding in compression and tension [12, 13]. Ageing, whether natural or induced by the thermomechanical history of the material, leads to an increase in the yield point [14–17]. Finally, some authors suggest that the upper yield point does not necessarily coincide with the true onset of irreversible plastic strain, which may occur well beyond this point (again, depending on the prior thermomechanical history) [18]. This also suggests that the pre-yield non-linearity may be due to a combination of elasticity and uncorrelated microplasticity events.

The strain softening regime leads to a decrease of the resistance characterised by the lower yield $(\varepsilon_l, \sigma_l)$ corresponding to the local stress minimum. The formation of localisation bands within the polymer drives this softening. These bands can be triggered by extrinsic factors, such as the geometry of the specimen or loading conditions. The origin of intrinsic softening has yet to be fully clarified, but the consensus in the community is that it lies within the

activation of microshear domains that create local stress concentrations and promote further activation within an avalanche mechanism. Argon (2013) [8] suggested using the concept of shear transformation zones (STZ), akin to the aforementioned microshear domains, to represent the fundamental mechanism driving the accumulation of permanent deformation. According to the STZ theory, the deformation within the polymer arises from overcoming a local energy barrier of an STZ and the subsequent accumulation of such activated STZs. Similarly to the upper yield point, the lower yield point is affected by temperature, strain rate and hydrostatic pressure. Since it also marks the transition towards the strain-hardening regime, it can exhibit some dependence on the network structure. Yet, some studies have shown that the lower yield is relatively unaffected by ageing/rejuvenation [16, 19, 20], as illustrated in Fig. 2.2.

The stress drop $\Delta\sigma$, defined as the difference between the upper σ_y and lower σ_l yield stresses, depends on temperature and strain rate within a specific range [21], and on the degree of ageing versus rejuvenation [16, 22].

Large strain re-hardening follows after softening and the stress increases again due to the network response and chain alignment. Strain-hardening is typically not observed for epoxies in tension due to their early brittle failure. A re-hardening modulus G_h is defined to quantify the re-hardening capacity. The re-hardening modulus has been shown to decrease [7, 23–26] or remain unchanged [7, 27] with temperature and/or strain rate. It is also strongly affected by the network structure and the cross-linking density [23, 27]. The amount of re-hardening of polymer glasses plays an important role in dictating the failure process. Large G_h tends to stabilise the localisation phenomena initiated by softening, leading to a more stable failure [28–30]. Defining G_h is not always straightforward as some systems may present continuously changing slopes in their post-softening stress-strain response. Hence, in this work, G_h is defined based on the assumption that a neo-Hookean representation is a convenient way to quantify the re-hardening response for comparative purposes despite being physically wrong [8, 31, 32]. This implies that the strength is proportional to $g(\lambda) = \lambda^2 - 1/\lambda$, where λ is the longitudinal stretch. Representing the stress in terms of $g(\lambda)$ means that the re-hardening part becomes linear. Hence, G_h is defined as the slope of the re-hardening part of the curve, expressed as a function of $g(\lambda)$. Note that although a large strain elasticity-based model is used to represent this part of the response, it does represent a strain hardening mechanism.

Shear yielding

Plastic deformation in polymer glasses is highly heterogeneous in nature and presents itself in the form of shear yielding, leading to permanent deformation.

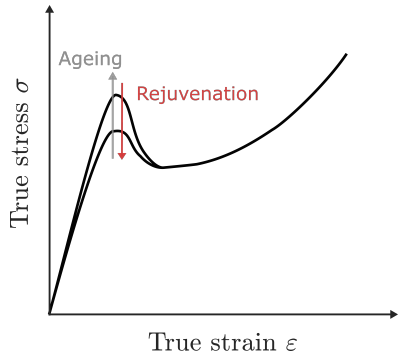


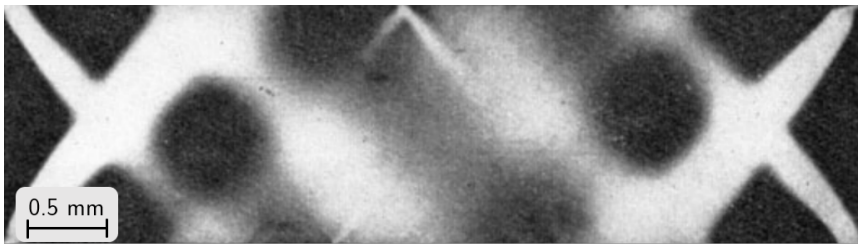
Fig. 2.2: Impact of physical ageing and rejuvenation on the stress-strain response of glassy polymers.

Shear yielding causes the formation of so-called shear bands, which have directly been observed for several glassy polymers [9, 33]. Fig. 2.3 illustrates some optical microscopy images of two types of shear yielding in PMMA and PET. Shear bands can either be rather large and diffuse or small and intense (or even a mixture of both). The type of shear band formation inherently depends on the structure of the polymer network and on the factors influencing it (e.g. temperature, strain rate, etc.) [9, 33, 34]. It also depends on the loading conditions, for instance with the formation of a neck in tension and shear band patterns in plane strain compression. Note that fine localised shear bands present significantly more plastic deformation compared to broad bands. Within the shear bands, the polymer chains are more strongly elongated due to orientation. In epoxies, the formation of micro and macro shear bands has also been observed [7, 35].

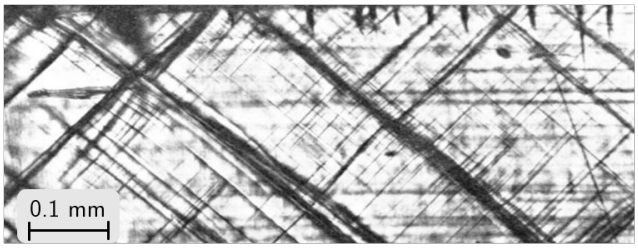
Bowden [9] demonstrated that shear band formation is dictated by both the stress drop $\Delta\sigma$ and the rate sensitivity of the material. Wu and Van der Giessen [36] showed that softening is indeed the driving force for shear band formation, whereas large strain re-hardening has a stabilisation effect on the shear band propagation. Van der Giessen [37] also pointed out that, depending on the polymer system, the formation of large shear bands is the consequence of the accumulation of a number of fine small-scale shear bands. Using Argon's [8] interpretation of plastic flow in terms of localised microshear events, shear yielding in the form of fine bands can be seen as the accumulation of such microshear domains. Subsequently, these bands may agglomerate to form large diffuse bands.

Influence of physical ageing

Physical ageing in glassy polymers is a fundamental yet crucially important aspect to consider. Ageing has been shown to affect the entire polymer's



(a)



(b)

Fig. 2.3: Example of polarized light microscopy images of shear band formation under plane strain compression for (a) PMMA and (b) PET. Adapted from [9].

behaviour, including viscoelastic, viscoplastic, thermal and physico-chemical properties. The specific use of epoxies in high performing FRPs has reinforced the need for investigating the origin of physical ageing. This can be seen by looking at the number of publications (see after) dedicated to the study of physical ageing on glassy polymers and their composites, in combination with studies focusing on hygrothermal ageing and its plastifying effects and even chemical ageing. Hence, a detailed analysis of ageing, and in particular physical ageing, largely extends the frame of this thesis. Thus, a brief overview of the concept and understanding of physical ageing and its impact on the mechanical response of epoxies will be given. Further discussions on ageing can also be found in chapter 3.

Physical ageing[1] is a consequence of the non-equilibrium state in which glassy polymers are. The process of physical ageing can be seen as the evolution of the system into low energy configurations. Physical ageing induces a change in the network structure, often accompanied by a slight increase in the glass transition temperature as well as an increase in the yield stress [8, 9, 14, 15, 17,

[1]Note that in subsequent chapters, the term ageing may appear instead of the more appropriate physical ageing term. This is done for simplification of the discussions.

22, 38, 39]. Two main physical mechanisms are associated to physical ageing. First, the frozen-in state of glassy polymers has been shown to entrap so-called free volume within the structure. Alternatively, one can look at excess energy to avoid the concept of free volume still under debate. Ageing is believed to be related to a decrease in free volume as the system reaches its equilibrium. Second, relaxation mechanisms involving long term configurational changes without volume change have also been identified and related to ageing. In the end, physical ageing reduces the mobility of the molecular chains in the system. However, the effects of physical ageing are fully reversible using rejuvenation either by heating the system up or by applying a mechanical load [14, 16, 17, 30]. Thermal rejuvenation involves an exposure to a temperature often above T_g, although sub-T_g rejuvenation has also been reported. Mechanical rejuvenation provides additional molecular mobility and allows "erasing" the effects of ageing as well. Ultimately, these physical origins of the ageing/rejuvenation processes are still under discussion in the community, hence the vastness of this topic in the literature.

Unloading response and strain recovery

The unloading response of glassy polymers is highly non-linear and presents a Bauschinger effect [7, 17, 40, 41]. Fig. 2.4 shows the stress-strain curves for a RTM6 epoxy under uniaxial compression at different levels of strain and the subsequent strain recovery. Morelle et al. [7] showed that the kinematic hardening was not affected by the test conditions and appeared to be intrinsically related to the epoxy of interest. The presence of accumulated back-stresses has been identified to cause the observed non-linearity in the unloading curve, thus favouring reversed deformation. Once unloaded, the amount of absolute recovered strain increases with increasing initial compression strain, however the recovery kinetics drastically slows down [7]. Still, recovery can be accelerated by heating the system up.

2.1.2 Physics-based modelling

The search for a physical origin for the plastic flow has been a key interest point since the early days of glassy polymer studies. The four most popular interpretations of the yield based on molecular changes in the polymer chains have been summarised in the following. Then, an overview of the STZ concept is given, followed by some molecular dynamics simulation results.

Molecular theories

Eyring [42] proposed a theory based on the transition of states to describe the plastic flow in polymers (it is not a molecular theory per se). Eyring suggests that deformation is a kinetic thermomechanically activated event, which needs to overcome an energy barrier in order to be triggered. This energy barrier

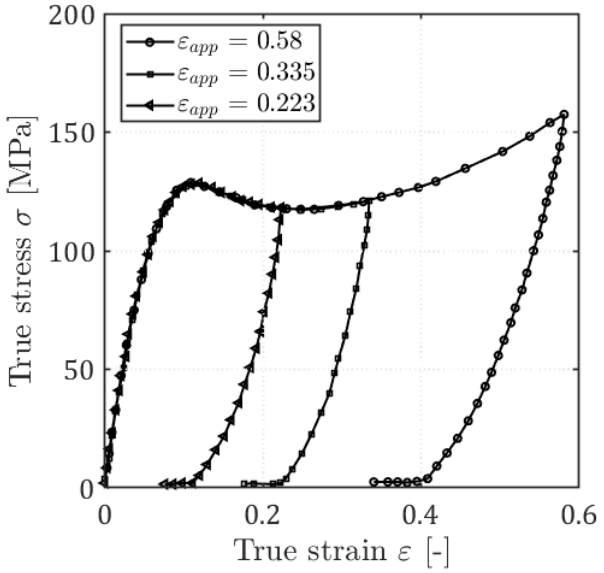


Fig. 2.4: Example of stress-strain responses with full unloading and strain recovery for RTM6 epoxy at different levels of applied compressive strain. Adapted from [7].

is lowered under forward acting stresses (i.e. in the direction of the change) and increased in the reverse case. The assumed underlying mechanism is the motion of polymer chains through holes in the network. Based on this theory, the macroscopic shear strain rate can be expressed as:

$$\dot{\gamma} = \dot{\Gamma} \exp\left(\frac{-\Delta G}{k_B T}\right) \sinh\left(\frac{\nu_0 \tau}{2 k_B T}\right), \tag{2.1}$$

where $\dot{\Gamma}$ is a constant, ΔG is the activation energy barrier, τ the applied stress and ν_0 the apparent activation volume. Eyring's representation of plastic flow has often been used in the literature to characterise the rate and temperature dependency of plastic flow in polymer glasses.

In an attempt to provide an actual molecular mechanism to the flow in polymer glasses, Robertson proposed the idea that shear stresses act on the polymer backbone and induce a change in local conformation [43]. This change in conformation is associated to the transition from bonds in their preferred state (called *trans*) to a rotated and flexed state (called *cis*). Robertson assumes that each bond can be treated independently of its neighbours. Note that as this model acts on conformational changes in the polymer chain, it presumes that plastic flow is dominated by the intramolecular energy rather than the intermolecular one (see for instance Argon's model). Plastic flow is the consequence

of an increasing number of *cis* bonds creating sufficient chain mobility. The model adequately captures the plastic yield properties for different temperatures and strain rates.

Argon proposed a model for yielding resulting from intermolecular interactions [44]. The assumption is that, in order for a polymer chain to deform and align with the direction of the applied load, a pair of kinks needs to occur in the molecular chain. The main resistance to the formation of such kinks is the elastic interaction from neighbouring molecules. As kink-pair formation results from elastic interactions, it is reversible in nature, solely requiring backward activation. Irreversible changes in the local chain structure only occur once chains in the vicinity of the kinks undergo the same process. The principle behind the intermolecular energy change associated with the kink-pair formation is illustrated in Fig. 2.5. The model considers the effect of temperature and strain rate in a similar fashion as proposed by Eyring. Pressure-dependence is accounted for by assuming that the local stresses around the kinks exceed the cohesive energy of the polymer, leading to the formation of cavities, as illustrated in Fig. 2.6. The model successfully predicts the ratio of yield stress over shear modulus for a relatively wide range of temperatures and strain rates. No post-yield phenomena is accounted for in the model but it is suggested that softening is the consequence of favourable yield conditions in the vicinity of the initial irreversibly deformed chains.

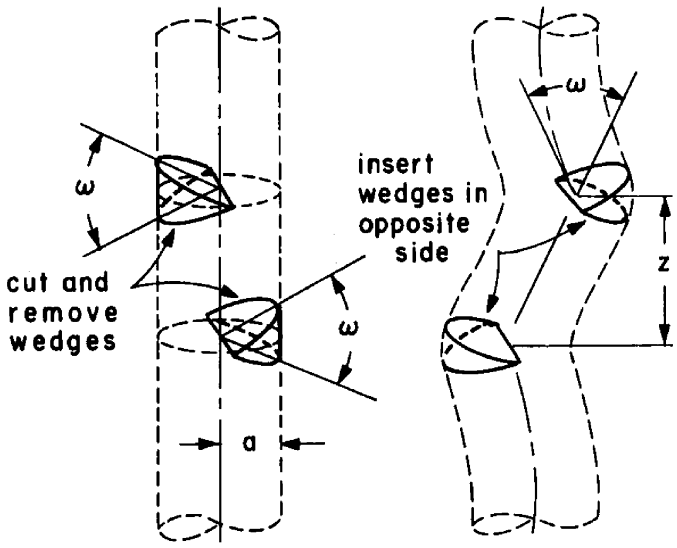


Fig. 2.5: Schematic illustration of the modelling of a kink-pair by a pair of wedge dislocations in an elastic surrounding. Adapted from [44].

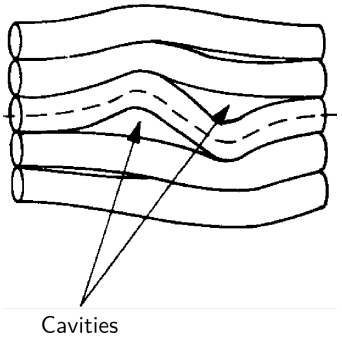


Fig. 2.6: Schematic illustration of the formation of cavities due to excessive stresses created during kink-pair creation. Adapted from [44]

To conclude, while different molecular origins of the permanent deformation have been proposed over the years, no consensus currently exists. Still, as mentioned above, the concept of shear transformation zones has become a popular choice to provide closed-form models for polymer glasses, as it overlooks the specificities of the exact molecular mechanism while still providing a physically sound representation of the deformation mechanisms.

Molecular dynamics simulations

With the increase in computational power, different approaches to molecular dynamics (MD) simulations have been used in an attempt to provide physical insights into the molecular mechanisms dictating not only plastic flow, but also aspects such as post-yield deformation and fracture. Few studies have dealt with the case of highly cross-linked epoxy resins. The reason lies within the complexity of generating a fully cross-linked network, requiring a large number of simulated atoms and potential interactions between all these atoms. Nonetheless, in recent years, some studies have been able to model the curing process of epoxies using MD simulations and to study the generated network in terms of deformation and failure [46, 47]. For instance, elastic properties as well as glass transition temperatures can now confidently be derived from MD simulations [48–51]. An accurate prediction of the yield and failure stresses and strains remains challenging. These values are often significantly overestimated [46, 51]. Nonetheless, the molecular mechanisms used in these MD models perfectly relate to the theories of, for instance, Robertson [52] or Argon [53]. For example, Vu-Bac et al. [54] performed nanoscale simulations of epoxies (at 82% cross-linking density) based on chain double kinking at 0 K and combined the predicted properties with the model of Argon to determine the macroscale properties at different temperatures under quasi-static loadings. Using this multiscale approach, they managed to provide a decent fit with experimental results for the stress-strain curve in tension and compression, as illustrated in

Fig. 2.7 for the case of compression. More recently, Konrad et al. [47] used MD simulations to study bond reorganisation of epoxies, starting out with the cure and up to final failure. They managed to recreate a network of 98% cross-linking density. Plastic deformation was accompanied by unwinding or sliding of chain loops and dissociation of nearby links followed by binding with near fertile sites (hence, not reducing the cross-linking density). Fracture resulted from the nucleation and coalescence of voids caused by bond dissociation. Interestingly, despite the high strain rates used in their MD models, they managed to get a close prediction of the yield strain and failure stress at ambient temperature.

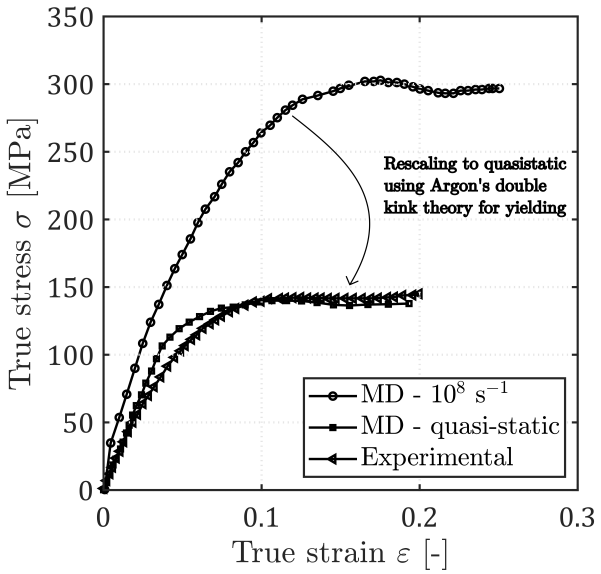


Fig. 2.7: Stress-strain response in compression of a DGEBA/33DDS epoxy resin at 300 K. Comparison between the responses predicted by molecular dynamics simulation at 10^8 s^{-1} (circles), by rescaling the MD response to quasi-static conditions using Argon's double kink theory (squares) and measured experimentally (triangles). Adapted from [54].

Shear transformation zones

The concept of shear transformation zones has originally been proposed by Argon to model the deformation of metallic glasses [55]. Since then, the idea has been adapted to represent the viscoplastic flow in polymer glasses as well [8]. The STZ theory states that viscoplastic flow results from the local thermal and stress induced activation of a small volume of material, leading to a permanent

inelastic shear deformation, as illustrated in Fig. 2.8. Hence, any of the aforementioned molecular mechanisms could be at the origin of an STZ. To activate an STZ, an energy barrier needs to be overcome, which is the combined effect of the transformation energy of the STZ and its elastic interaction with its surrounding. Thus, the change in Helmholtz free energy can be written as:

$$\Delta F = \Delta F_1 + \Delta F_2 + \Delta F_3 \tag{2.2}$$

where ΔF_1 is the shear strain energy associated to the transformation of an STZ, ΔF_2 is the matrix strain energy resulting form the temporary dilation required for STZ activation and ΔF_3 is the intermolecular energy required to shear an unconstrained STZ. ΔF_1 and ΔF_2 can be calculated based on Eshelby's solution for an isolated inclusion [56] whereas ΔF_3 can be evaluated based on the intrinsic intermolecular shear resistance $\hat{\tau}$:

$$\Delta F_1 = G\ \gamma_0\ \nu_0\ \frac{7-5\nu}{30(1-\nu)}, \tag{2.3}$$

$$\Delta F_2 = G\gamma_0\ \nu_0\ \beta^2\ \frac{2(1+\nu)}{9(1-\nu)}, \tag{2.4}$$

$$\Delta F_3 = \frac{\nu_0\ \hat{\tau}}{2}. \tag{2.5}$$

In these equations, G is the shear modulus, ν is the poisson coefficient, β is factor accounting for the ratio of unconstrained dilation over shear, γ_0 is the shear eigenstrain applied to an STZ, ν_0 is the apparent activation volume, as previously defined. Note that ν_0 results from a real material volume Ω subjected to an elementary shear strain γ_0: $\nu_0 = \Omega\gamma_0$. The attempt rate for STZ activation follows a transition state theory (i.e. Eyring's theory) whose activation energy barrier is the difference between ΔF and the mechanical work driving the transformation. Note that the change in local energy landscape following STZ activation favours subsequent activation in the vicinity.

Both analytical and finite element implementations of STZ frameworks have been developed over the years to model polymer glasses, based on similar implementations for metallic glasses [57]. STZ frameworks for polymer glasses have been used to study the intrinsic size of STZs [8], the yield, large strain and unloading response of epoxies [58, 59] and the indentation size effect [60–62], hence providing new insights into the fundamental deformation mechanisms in polymer glasses. Note that the numerical implementation of an STZ model of Chevalier et al. [58] seems to be the first numerical attempt for polymer glasses. These authors managed to model the sessile formation of thin micro-shear bands, in agreement with previous experimental and numerical results (see shear yielding section). A key difference in the application of the STZ framework to polymers [58, 59] with the original formulation of Homer and Schuh [57] is a different treatment of the time stepping compared to a Monte-Carlo procedure

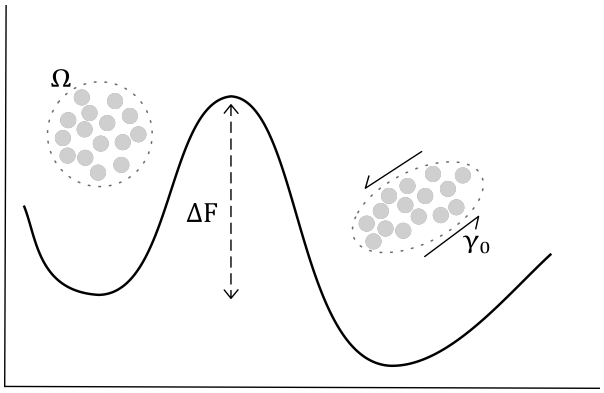


Fig. 2.8: Schematic illustration of the activation of an STZ. A shear eigenstrain γ_0 causes a local change in the molecular configuration of a material volume Ω by overcoming an energy barrier ΔF.

and the assumption that the activation angle of the STZ follows the direction of maximum shear.

2.1.3 Failure micromechanisms in epoxies

This section will focus on the failure in thermosets, particularly highly cross-linked epoxies. Failure in epoxies may differ from that in thermoplastics, which present a competition between crazing and shear yielding, depending on the entanglement density [63]. Highly cross-linked epoxies often fail in a brittle manner. Still, crazing, the main damage mechanism in thermoplastics leading to brittle failure, is never observed. Indeed, craze formation is inhibited by the high cross-linking density (highly entangled thermoplastics behave similarly). Instead, shear yielding will lead to failure in epoxies. Many authors have studied the failure mechanisms taking place at the crack tip in epoxies and found no evidence of craze formation [64–70].

Bulk failure

In uniaxial tension, epoxies (and many other glassy polymers) exhibit four typical features on their fracture surface, as illustrated in Fig. 2.9 [35, 71–73]. First, a defect, which may not be visible, causes crack initiation. The crack then propagates rapidly, forming a so-called mirror-like plateau. It receives its name from the lack of remarkable features. The mirror plateau is followed by a parabola-type pattern, which results from the interactions of the main crack with secondary cracks ahead of the crack tip. This pattern progressively roughens until complete failure due to branching of the main crack and the

increased influence of the aforementioned secondary cracks.

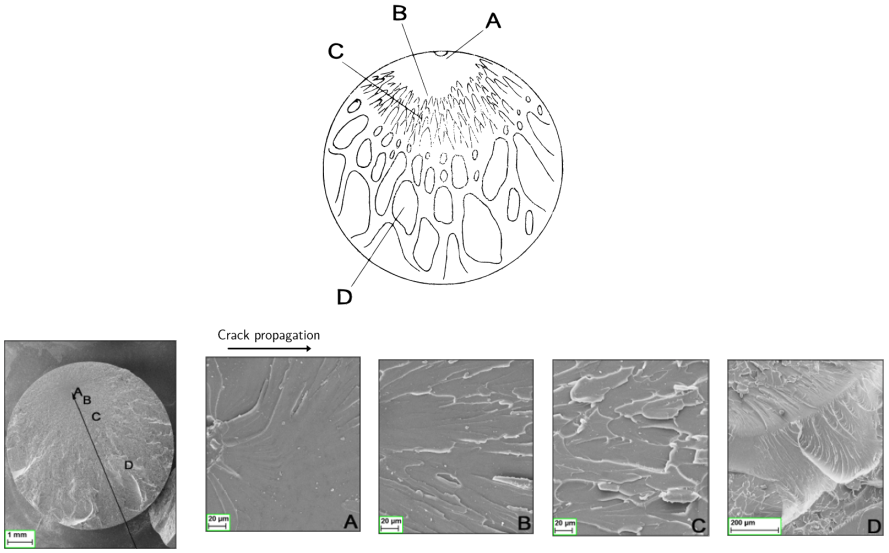


Fig. 2.9: Schematic illustration of the typical features observed on the fracture surface of highly cross-linked epoxies (adapted from [35]) and corresponding fracture surface in tension of RTM6 (from [74]). The arrow in the bottom SEM image corresponds to the crack propagation direction. The letters correspond to specific features found at different locations on real fracture surfaces and shown in the schematic.

The works of Chevalier et al. [74, 75] will serve as a basis for the discussion about failure in epoxies. These authors extensively studied the failure of RTM6 under quasi-static tests (e.g. compression, tension, notched tension and torsion), pre-cracked tests (i.e. compact tension) and fatigue tests. First, they performed a combined numerical and experimental analysis to define an appropriate failure criterion, irrespective of the loading condition. Following the knowledge that failure initiates at an intrinsic defect within the material, they proposed a criterion based on the idea of reaching a critical principal stress σ_c at the tip of a critical spheroidal defect of aspect ratio A_r:

$$\sigma^{local}_{princ}(A_r, \sigma^{RVE}_{ij}, E, \nu, \sigma_y(\bar{\varepsilon}^p)) = \sigma_c, \tag{2.6}$$

where σ^{RVE}_{ij} is the stress state at the local level representative of the macroscopic load, E and ν the elastic constants and $\sigma_y(\bar{\varepsilon}^p)$ the hardening law. A value of 0.27 for A_r and a critical maximum principal stress σ^{max}_{princ} equal to 300 MPa were identified for RTM6. The proposed failure criterion successfully predicts the macroscopic failure strain for different stress triaxiality, going from -1/3 (i.e. uniaxial compression) to almost 1 (i.e. notched tension) and has been shown to be independent of temperature. Note that in the case of shear yielding (e.g. in

compression), plastic deformation caused by the yielding process is necessary to, locally, reach a sufficiently high level of hardening to trigger the failure initiation at the defect. The criterion is likely valid for other highly cross-linked epoxies, provided A_r and σ_c are reidentified.

The combination of the failure criterion and the typical fracture surface features in epoxies led Chevalier et al. [75] to propose the failure mechanism illustrated in Fig. 2.10. Accordingly, failure in bulk epoxies happens in four stages. First, a critical principal stress is reached at the tip of a defect leading to initial crack propagation. This first crack propagation comes to a stop after a certain distance, describing a mirror-like region. Finally, crack blunting occurs accompanied by strong plastic deformation causing final crack propagation through the material.

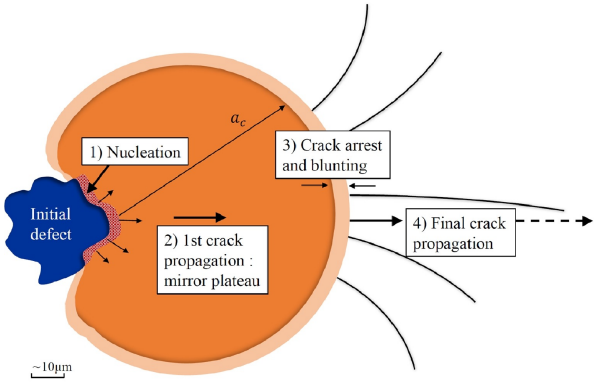


Fig. 2.10: Schematic illustration of the general failure mechanism for highly cross-linked epoxies proposed by Chevalier et al. [76].

The exact nature of the critical defect is still unclear, although fracture surface analyses clearly indicate a certain variability in the size of such defects. Nonetheless, this does not seem to significantly impact the subsequent failure mechanism, as no large variations in the failure strains can be observed, for instance, for RTM6.

The mirror-like zone reported by many authors can also be seen in the transition from stable to unstable crack growth in epoxies. Stable propagation implies that no crack arrest occurs during crack propagation. Many authors have addressed the topic of stable and unstable crack propagation in epoxies [64, 77, 78]. A key feature of unstable crack propagation is the presence of a severely deformed transition zone, as illustrated in Fig. 2.11. This zone is related to crack blunting and leads to a significant amount of plastic deformation. Hence, the factors affecting the plastic response of an epoxy (i.e. yield stress

and post-yield behaviour) have been shown to affect its failure response. For instance, the influence of hardener content and type were studied in [64, 77–79]. They found that the use of hardeners leading to high yield stress systems (e.g. primary amine hardeners) promotes stable crack propagation. Similarly, high temperature or low strain rate have been shown to trigger unstable crack propagation, whereas stable propagation occurred at low temperature or high strain rate [64, 77–79]. Recalling the discussion in section 2.1.1, shows that unstable crack propagation conditions align with ductile deformation conditions in glassy polymers, reinforcing the notion that plastic deformation takes place at the crack tip during unstable cracking. Hence, the ability of an epoxy to develop and accommodate plasticity will dictate its failure response. Gledhill and Kinloch [65] noted that unstable crack growth is caused by the accumulation of excessive deformation energy during crack blunting, which is then suddenly released in the form of kinetic energy, causing the next unstable propagation step until a new crack arrest occurs. Considering that the mirror plateau is initiated at a defect and bounded by a crack arrest zone, an unstable crack growth scenario can be related to it. Indeed, significant deformation is necessary at the defect tip in order to reach the critical stress. Once the failure criterion is met, the crack rapidly propagates over a certain distance, creating the mirror plateau.

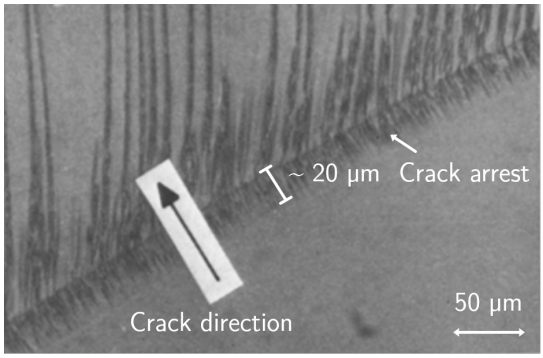


Fig. 2.11: Example of microscopic observation of a crack arrest during unstable propagation (adapted from [66]).

Presence of a pre-crack

In the presence of a pre-crack, the failure scenario skips the initiation step as the sharp crack (such as induced by razor blade tapping) is sufficient to act as an initiating defect. This is schematically illustrated in Fig. 2.12 (a), as proposed by Chevalier et al. [75]. Note that a crack blunting zone is required before final crack propagation, as observed on the fracture surface of a CT test

shown in Fig. 2.12 (b). The presence of a plastic zone implies that the failure criterion of Eq. 2.6 does not immediately apply as the critical stress should be reached at the crack tip. This suggests the need for an internal length, which dictates the development of plasticity. As mentioned before, plasticity has been shown to develop at the crack tip. Furthermore, Yamini and Young [66] used a stress-based failure criterion reached at a distance from the crack tip to accurately capture the critical stress intensity factor. Numerical investigations by Lai and Van Der Giessen [80] showed that shear yielding occurs at the tip of a sharp crack and that the shear bands join together after a certain distance. Hence, for failure to initiate on sharp cracks, the polymer chains need to be able to undergo large conformational changes to accommodate the stress and strain concentrations near the crack. The size of the plastic zone systematically observed for RTM6 is around 2-10 μm. Recently, Mishra et al. [81] also studied the failure mechanism of epoxies at the tip of cracks. They noted that, at the crack tip, within the plastic zone, crazing occurs and causes the final failure. They based their assumption on microscopic observations of leftover riverlines within the plastic zone. Additionally, they showed that the crazing process is dependent on the test rate. This novelty will require further investigation, as crazes are not typically expected.

Size effects on fracture strength

The fact that failure in epoxies originates due to the presence of internal defects has raised questions about the idea of an intrinsic strength of epoxies in the absence of defects. Few studies have attempted to determine the microscale strength of epoxies. Odom and Adams [82] were the first to find a size effect in epoxies, showing an increase in ultimate tensile strength as the the cross-sectional area of their specimens was reduced. Similar results were found by Fiedler et al. [72]. Following, these initial findings, two main approaches to study the intrinsic strength have been followed in the literature.

The first strategy relies on the work of Hobbiebrunken et al. [83], who produced micron-sized epoxy fibres, resulting in diameters as small as 22 microns. They reported a significant increase in the failure stress. Similar strategies were then pursued by Misumi et al. [84] and Sui et al. [85]. Misumi et al. tested five different epoxies and also studied the size effect on the yield stress. Both the yield and failure stress increased with decreasing size. Sui et al. use different shapes of tensile specimen but reached similar conclusions. They also reported the potential for the development of a stable necking process in smaller specimens and found, by X-ray scattering, that polymer chains presented preferred orientation in the necked region. Recently, Verschatse et al. [86] also investigated the stress-strain response of micron-sized polymer fibres. They only found an increase in the failure strength and strain as the fibre diameter decreased. They also showed the ability of the fibres to develop a necking

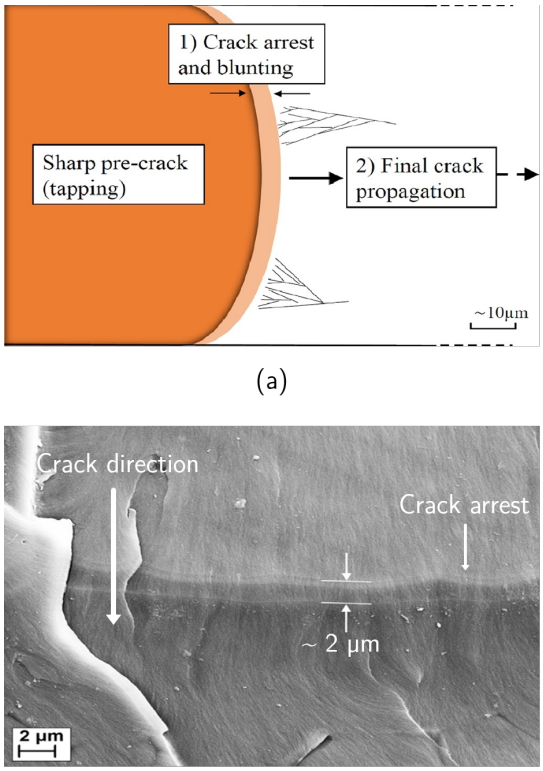


Fig. 2.12: (a) Schematic illustration of the failure mechanism in the presence of a sharp crack proposed by Chevalier et al. [76] and (b) corresponding SEM micrograph of a crack blunting zone at the tip of sharp crack in a CT test.

region, despite the absence of any significant difference in yield or necking stress with respect to the bulk material. Polarized light microscopy showed that the necking regions have chain alignment, in agreement with Sui et al. Hence, it is clear that the failure mechanisms differ at the microscale.

The second strategy is more indirect. Zike at al. [87] combined digital image correlation and double edge bending tests to determine the microscale fracture strength of epoxies. Using the strain fields measured at the crack tip, they were able to determine the J-integral around the notch and found that the failure stress should be around 220-300 MPa. Recently, Qiao et al. [88] performed single edge notched beam tests to formulate a two-scale cohesive zone model to describe the failure of epoxies. Using their experimental results, they estimated a submicron cohesive strength value of around 300 MPa, in agreement with the

measurement of Zike et al.

Considering the reported increase of the local failure stress and strain for material volumes of a few microns is crucial for the broader field of FRPs. Indeed, the typical matrix pocket size in FRPs is on the order of a few micrometers. Hence, a remaining question and motivation is to determine to what extent a failure criterion developed at the macroscale can readily be transferred to the study of the failure of FRPs.

2.2 Deformation and failure in fibre-reinforced composites

Fibre-reinforced composites are hierarchical structures, which are highly heterogeneous in nature and therefore present a complex multiscale combination of deformation, damage and failure. Predicting the failure of composite structures is a complex task, as failure may initiate at the microscale (i.e. ply level) by fibre/matrix decohesion or matrix cracking, and then propagate at the macroscale by means of inter-ply delamination. The specific damage and failure progression in the composite inherently depends on its stacking sequence and on the loading conditions. In tension, the damage occurs either by fibre breaking (if the load is parallel to the fibres) or by matrix cracking caused by fibre/matrix decohesion. In compression, fibre kinking usually affects the failure sequence. Fibre kinking is a result of local instabilities and is promoted by strong plastic shear deformation of the matrix. Hence, in order to accurately predict the deformation and failure response of the composite, it is crucial to determine the micromechanical behaviour of each ply.

The quest for an accurate description of the micromechanical origin of deformation and failure within FRPs has driven the development of micromechanical characterisation tools (both experimental and numerical), within the context of bottom-up frameworks. Hence, a significant amount of studies have been dedicated to the study of UD plies and the factors influencing the damage occurrence with respect to the applied load, in order to build towards accurate virtual tests [89]. This section aims at providing some fundamental insight into the micromechanics-based study of composites.

2.2.1 Micromechanics of UD FRPs

Experimental observations

The initiation of failure in FRPs presents some typical mechanisms, depending on the loading conditions, as illustrated in Fig. 2.13. Failure in FRPs can be categorized into two main fields: fibre dominated failure or interface and

matrix dominated failure. In longitudinal tension (i.e. parallel to the fibres), the strength of the composite is dictated by the (brittle) failure of the fibres. In longitudinal compression, fibre buckling or kinking trigger damage and failure. In transverse tension, fibre/matrix decohesion leading to matrix cracking perpendicular to the fibres is the main damage mechanism. In transverse compression and shear, it is the matrix plasticity that dominates the strength, particularly through the formation of shear bands (typically caused by the softening of the matrix in its stress-strain response). Additionally, shear-driven fibre/matrix decohesion also affects the strength in transverse shear [4, 90]. Over the years, a number of studies have investigated the damage initiation processes at the microscale for both categories.

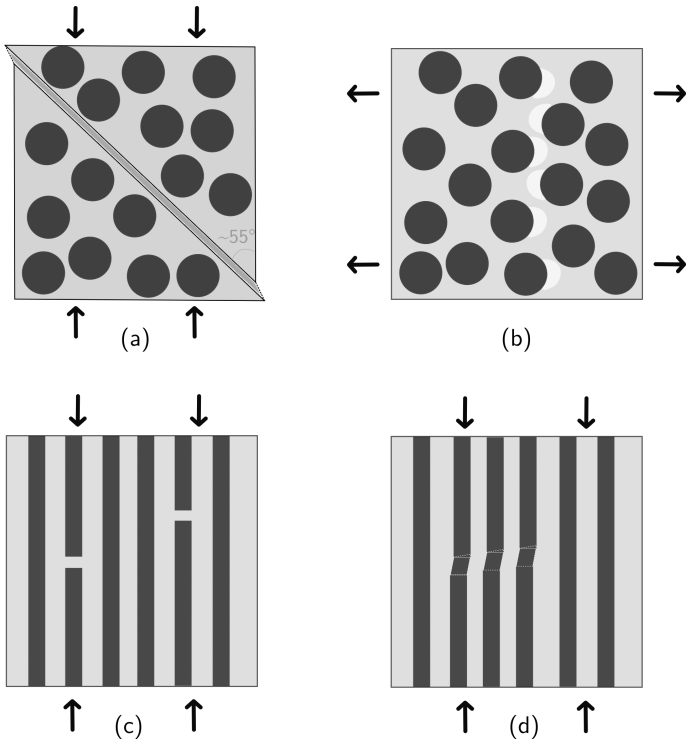


Fig. 2.13: Typical damage phenomena occurring in UD plies: (a) matrix plasticity favouring subsequent shear banding, (b) fibre/matrix decohesion, (c) fibre breaking and (d) fibre kinking.

For instance, in recent years, fibre breaking in longitudinal tensile loads has been extensively studied using X-ray tomography [91, 92]. In particular, these studies showed how the accumulation of broken fibres into clusters leads to the final failure of the composite. Breite [93] also pointed out the importance of

accounting for the intrinsic non-linear stress-strain response of the matrix to study time-dependent loadings. In longitudinal compression, it has been shown, also using synchrotron computational tomography, that kink bands form due to significant shear deformation of the matrix [94]. The increase of the shear strain leads to a stronger resistance of the matrix to deformation, causing the fibres to lock-up and bend, thus initiating the kink band [94, 95]. Furthermore, fibre/matrix decohesion may occur simultaneously, increasing the complexity in the failure sequence [96].

Fibre/matrix decohesion has also been extensively studied, particularly for transverse loads [96]. In transverse tension, Gamstedt and Sjorgen [97] first showed that the formation of transverse cracks results from the coalescence of several fibre/matrix decohesions. Subsequently, Parìs et al. [98] extensively studied the fibre/matrix decohesion process. They found that decohesion occurs in three stages. First, a small fibre/matrix interface arc is debonded. It then extends around the fibre until a critical size is reached. At this stage, the fibre/matrix crack kinks towards the matrix until a matrix crack perpendicular to the tensile load appears. A subsequent study by Correa et al. [99] showed that the final crack deviation may occur at different angles and is not necessarily perfectly perpendicular to the applied tensile load. The experimental results of these aforementioned studies are in agreement with previous attempts at damage observations in FRPs [97, 100, 101]. Furthermore, Hobbiebrunken et al. [100] also demonstrated that the matrix failure properties play an important role in the type of interfacial failure: brittle matrices lead to cohesive failure whereas more ductile matrices give rise to adhesive failure.

In a different study, Zumaquero et al. [102, 103] provided crucial microscopic observations about the failure sequence under transverse compression. The fibre/matrix decohesion follows a similar sequence as in tension, although the characteristic angles for the initial debonding and its extension differ due to the change in loading. Additionally, they showed that the interfacial crack deviation into the matrix predominantly occurred at angles in the 52-60° range. This is in agreement with theoretical predictions (e.g. [104]), similar experimental evidence [76, 105] and numerical predictions [105, 106]. Correa et al. [102] also noticed the frequent occurrence of small cracks in the matrix without prior fibre/matrix decohesion, assumed to be secondary damage. Fig. 2.14 is an example of these damage observation for the case of transverse compression of a thick UD RTM6/carbon fibre composite. The final fracture plane orientation agrees with the results of the aforementioned studies. As mentioned, prior to failure, significant plastic deformation occurs in the matrix under transverse compression [76, 105, 107, 108].

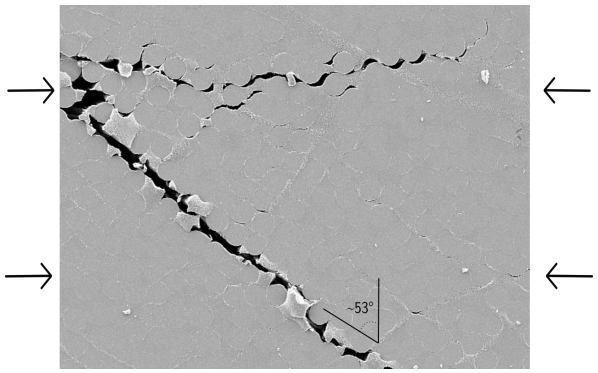


Fig. 2.14: Micrograph showing the failure under transverse compression due to matrix shear plastic deformation and fibre/matrix decohesion leading to a final failure plane oriented at 53° for a UD RTM6/carbon fibre composite.

FE modelling

While experimental observations of the deformation, damage or failure at the microscale remain somewhat limited in the literature (but seeing an increase in recent publications), the numerical study of the failure of FRPs has grown significantly over the last three decades. These studies range from 2D to 3D and cover most possible loadings and, especially in recent years, incorporate effects of curing conditions, presence of defects, fibre misalignment, etc. Gonzàlez and Llorca [105] were among the first to perform computational micromechanics studies using representative volume elements (RVEs) for the case of transverse compression. Here, failure is either the consequence of widespread shear banding in the matrix along planes aligned with the expected 50-60° range (for a Mohr-Coulomb criterion) or caused by interfacial decohesion (if the interface strength is lower than the matrix strength) and subsequent coalescence along matrix shear bands. Following numerical investigations found similar results [109–114]. Melro et al. [90] performed numerical simulations of RVEs under different types of loadings and managed to reproduce the expected damage and failure sequences mentioned above for each load case. Fig. 2.15 illustrates maps of cumulative plastic strain in three transverse loadings. Evidently, plastic deformation occurs in all instances to some extent.

The aforementioned experimental observations and numerical studies made it clear that matrix plasticity and interfacial debonding compete for many loading cases [115]. Hence, recent investigations have addressed the competition between these two mechanisms. Guo et al [116] performed a parametric study for transverse tension conditions to determine the relative influence of interface and matrix strength. A comparison with experimental results showed that damage initiation and subsequent crack propagation are strongly dependent

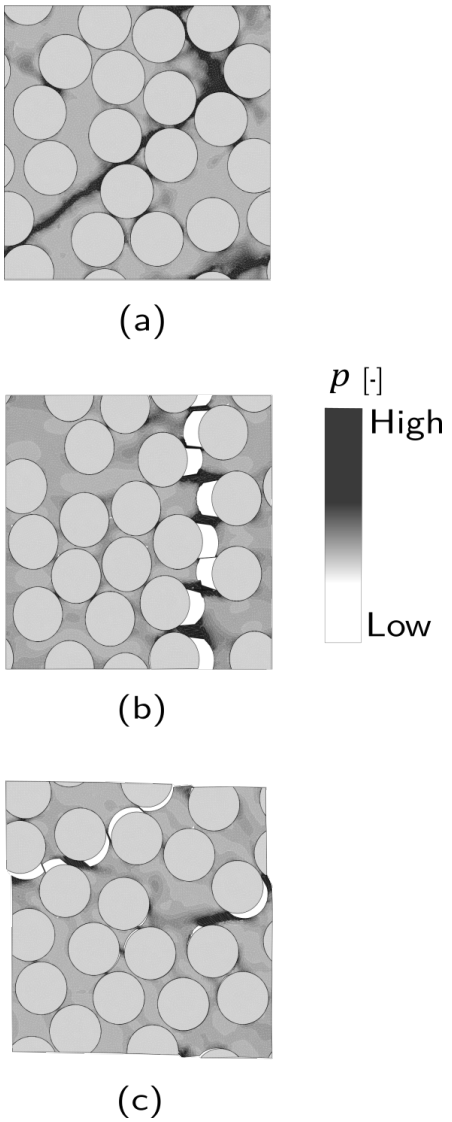


Fig. 2.15: Maps of cumulative plastic strain p numerically predicted for: (a) transverse compression, (b) transverse tension and (c) transverse shear. The white regions depict fibre/matrix decohesion. Adapted from [90].

on the strength of each constituent. Alternatively, Rueda-Ruiz et al. [117] studied the influence of the strain rate (up to very high rates) on the transverse compression response, both experimentally and numerically. Their numerical approach was based on a micromechanical characterisation of the constituent

properties. They showed that the damage mechanism shifted from interfacial debonding and matrix plasticity at low rates to purely matrix plasticity at higher rates, hence pointing out a rate-dependency of the interfacial strength. Interestingly, the angle of final failure plane seemed unaffected by the strain rate. May et al. [118] also experimentally addressed the influence of high strain rates and suggested that the angle of final failure shifts to slightly higher values at high strain rates, namely around 65°.

In the end, the challenging task in computational micromechanics is to accurately provide the constituent properties. Indeed, particularly in transverse and shear loadings, the predicted predominant failure process inherently depends on the relative strength of the interface and the matrix. Hence, recently, micromechanical numerical analyses are increasingly based on constituent properties measured at the microscale, see for instance recent publications from the group of Gonzàlez et al. [119] or the work of Sharma et al. [120]. Section 2.3 will provide a description of the necessary methodologies to extract the local constituent properties. In particular, the interphase region around fibres has received more attention recently. Sun et al. [121, 122] performed RVE simulations by explicitly accounting for the presence of an interphase around 200 nm wide with distinct properties. The interphase properties were modelled using an exponential gradient informed by molecular dynamics simulations. They demonstrated the potential for improved failure predictions under different loadings, when accounting for the interphase. Similarly, Riaño [123] also modelled an interphase region and accounted for the impact of ageing on the interphase properties. They stated the importance of considering the interphase in the numerical lifetime assessment of composites structures. Chowdhury et al. [124] used MD simulations to determine a strain rate dependent bilinear traction law to represent the interphase around glass fibres.

To complement the discussion, in recent years, phase-field modelling strategies have become increasingly popular to study not only the failure of FRP structures but also to provide insights into the microscopic failure mechanisms [125]. Phase-field models describe sharp cracks (e.g. interface cracks) as diffuse regions controlled by the phase-field variables. The literature on the subject has become vast and far exceeds the present work. Nonetheless, it is important to mention computational micromechanics efforts incorporating phase-field models [126, 127]. For instance, recently, Tan et al. [127] proposed a virtual design tool to assess microscopic fracture in FRPs, highlighting the influence of matrix and interface properties as well as accounting for the presence of voids. They demonstrated the potential to design FRPs with improved fracture toughness by strategically introducing some voids to promote crack blunting.

In conclusion, most FE studies, while accurate with respect to experimental observations, rarely provide direct experimental validation for the specific

model of interest (with either actual UD stress-strain responses or microscopic observations). Hence, even though numerical studies of RVEs have aided tremendously in the understanding of damage and failure in FRPs, a comparison with submicron experimental results is still required, for instance, to consider the effect of the interphase. This is particularly important in the current trend towards thermoplastic matrices, which present a more complex microstructure (e.g. presence of a transcrystalline layer, size of spherulitic crystals, etc.) [128, 129].

2.2.2 Factors influencing the strength of UD plies

Thermal residual stresses

The effect of residual stresses originating from thermal mismatch during processing has been of active interest since the early days of computational micromechanics. The earliest studies pointed out a detrimental effect of tensile residual stresses for low fibre volume fractions, but showed a shift to compressive stresses as the fibre volume fraction increased [130, 131]. Since then, many RVE numerical studies have come to a similar conclusion. Overall all, thermal residual stresses tend to prevent early failure in transverse tension, whereas they promote pre-emptive fibre/matrix debonding in transverse compression [105, 132, 133]. Recent studies tend to model the curing process to evaluate the relative causes for the creation of residual stresses, such as matrix shrinkage or a mismatch in the coefficients of thermal expansion between the matrix and fibres. They also reveal the favoured loci for residual stress concentrations. Danzi et al. [134] suggested that curing creates large hydrostatic stresses within resin pockets, potentially leading to more widespread damage compared to ideal cases (i.e. matrix unaffected by curing process). Gonçalves at al. [135] showed that curing induces stress concentrations in thin matrix ligaments between fibres, creating favourable zones for damage initiation.

Effect of resin-rich zones

The influence of resin-rich zones in the FRP microstructure has recently been the focus of several works. Given the imperfections in manufacturing processes, resin-rich regions can emerge inside the fibre tows or in-between tows. Ghayoora et al. [136] pointed out a detrimental impact of such zones on the stiffness and failure strain of the FRP. Similarly, Ahmadian et al. [137] found a negative effect for the strength and toughness. Pang et al. [138, 139] performed an extensive numerical study and showed that resin-rich zones can affect the damage initiation and preferred crack paths in FRPs.

Effect of defects

The presence of voids, mainly caused by air entrapment during manufacturing, has been shown, experimentally, to reduce the mechanical properties of FRPs, particularly in transverse loadings [140–142]. Vallmajó et al. [143] recently performed an extensive numerical study to assess the impact of microvoids on the elastic properties. As expected, the presence of voids reduces the transverse and shear moduli. Interestingly, these authors showed that voids located in resin pockets are significantly more detrimental that inter-fibre voids. Yet, smaller voids also proved to be more detrimental on the elastic properties. Similar results were found by Vajari et al. [144] and Chu et al. [145].

2.3 Nanomechanical characterisation techniques

This section aims at providing a thorough overview of the methods and relevant results available in the broad micromechanical characterisation of bulk glassy polymers and as part of matrices in FRPs. A previous review paper [146] broadly dealing with this subject and its necessity in the study of FRPs, entitled "*Nanomechanics serving polymer-based composite research*", can be found in appendix A. Fig. 2.16 schematically illustrates the four main groups of characterisation techniques that can be used to assess the microscale behaviour of the FRP constituents. First, contact methods based on nanoindentation allow determining the local mechanical properties. Second, atomic force microscopy permits refined characterisation of the interphase size. Then, fibre push-out/in methods manage to assess the interfacial strength of FRPs. Finally, digital image correlation combined with in-situ testing in scanning electron microscopes enables measurement of the local strain fields, providing crucial validation opportunities for FE studies. In this section, a more detailed description of the characterisation techniques will be given, with a specific focus on results linked to the core of this thesis: size effects, microscopic observation of strain localisation phenomena, strain gradient plasticity, etc.

2.3.1 Nanoindentation

Principle

Nanoindentation relying on a Berkovich indenter, with tip bluntness below 100 nm, is widely used today to determine the local hardness H and Young's modulus E of a material. The test follows three main steps, as illustrated in Fig. 2.17: a loading sequence to reach the necessary indentation depth h_{max}, a brief hold segment to minimise viscoelastic effects and an unloading. Both F_{max} and h_{max} are recorded and allow to determine the hardness H via:

$$H = \frac{F_{max}}{A_c}. \tag{2.7}$$

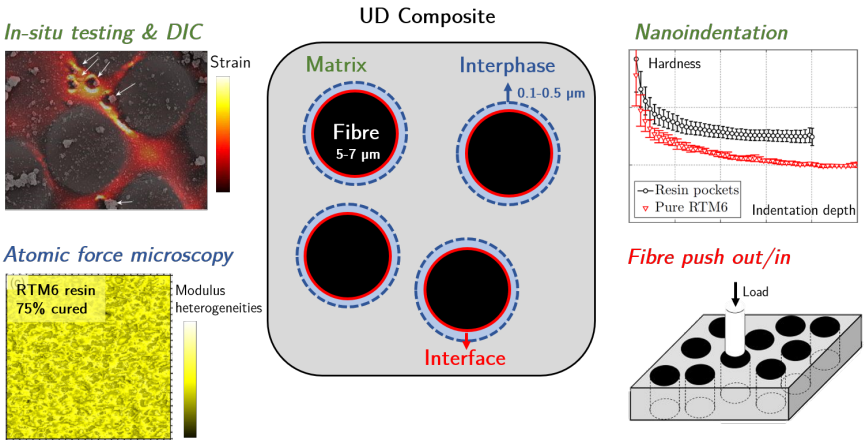


Fig. 2.16: Schematic overview of the nanomechanical characterisation techniques used for the study of the constituents of FRPs.

The determination of A_c is based on the actual contact depth h_c, which may differ from h_{max} due to pile-up or sink-in and leads to either an under- or overestimation of A_c, respectively. Fig. 2.17 (b) gives a schematic for the definition of h_c. The common practice to determine h_c relies on the work of Oliver and Pharr [147], which assumes sink-in under the indenter tip. In polymer glasses, in particular in highly cross-linked epoxies, this assumption is valid (but should always be verified). Hence, h_c is defined as:

$$h_c = h - \varepsilon \frac{F_{max}}{S}, \tag{2.8}$$

leading to

$$A_c = 24.5 h_c^2. \tag{2.9}$$

In these equations, ε is a tip-dependent geometrical constant and S is the contact stiffness, which is defined as the initial slope of the unloading curve dF/dh. Sneddon [148] and Oliver and Pharr [147] showed that the unloading curve can be fitted with a power law relationship:

$$F = B(h - h_p)^m, \tag{2.10}$$

where B, h_p and m are constants to be fitted, with typically $1 \leq m \leq 2$.
The contact stiffness can be related to the modulus of the material (assuming a depth-independent modulus) using:

$$S = 2E^* \sqrt{\frac{A_c}{\pi}}. \tag{2.11}$$

where E^* is the reduced modulus. The modulus E can then be derived from E^* following:

$$\frac{1}{E^*} = \frac{1-\nu^2}{E} + \frac{1-\nu_i^2}{E_i}. \tag{2.12}$$

with ν_i and E_i, respectively the Poisson ratio and Young's modulus of the indenter.

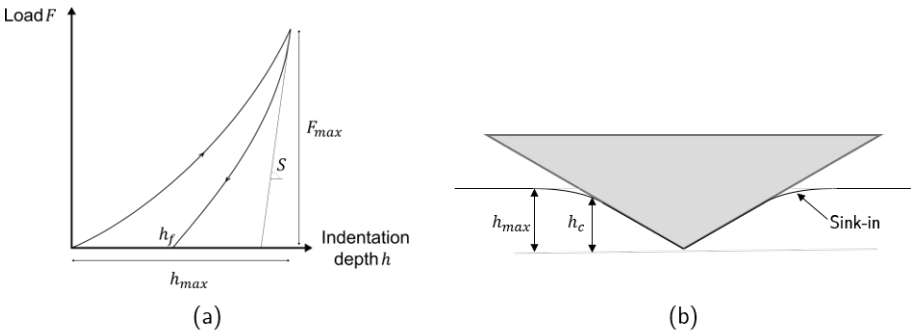


Fig. 2.17: Schematic representation of (a) the load-displacement during a nanoindentation test and (b) the sink-in phenomenon.

Micromechanical modulus and hardness

Over the years, nanoindentation has been extensively applied to the study of the (visco)elastic properties of glassy polymers. However, the data interpretation has been and remains to this day somewhat debated in the community. The main point of attention, as mentioned by Kranenburg [149], is the quasi-systematic overestimation of the measured indentation modulus of the polymer compared to the modulus derived from macroscale tensile or compression tests. Typically, indentation moduli are 20-60 % higher than their macroscale equivalent [150–155]. Fig. 2.18 shows some moduli measurements for different polymers studied in the literature compared to the expected macroscopic moduli. This overestimation may arise from the assumption and inaccuracies of the Oliver and Pharr approach itself, as it is based on elasticity while it is used to characterise viscoelastic materials. This argument is motivated by the inability of equation 2.10 to properly fit the unloading curve for some systems [154, 155].

The effects of the potential material pile-up or of the large hydrostatic (pressure) stresses under the indenter may also be the reason for such an increase in measured modulus. Pile-up has been shown to occur on some systems, particularly in composite systems where the matrix pockets are being probed, but only when the indenter gets close to the fibres. Still, the occurrence of pile-up is insufficient to fully explain the difference in moduli [156, 159]. The presence of compressive hydrostatic stresses under the indenter has been shown by a number of authors [160, 161] and Hardiman et al. [156] proposed the following correction for the modulus:

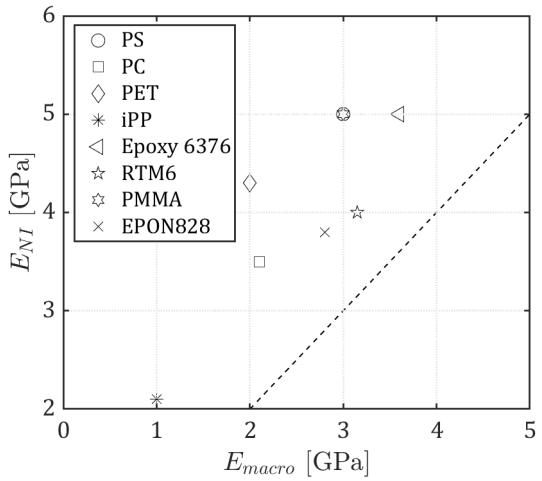


Fig. 2.18: Comparison between the moduli measured from nanoindentation and classical macroscale tests for several glassy polymers studied in the literature: PS, PC, PET and iPP from [154], Epoxy 6376 [156], RTM6 [157], PMMA [153], EPON828 [158].

$$E_{corrected} = E - 2\left(H - \frac{H}{C}\right)(5 - 4\nu)(1 - \nu). \tag{2.13}$$

In this equation, C corresponds to the constraint factor, first proposed by Atkins and Tabor [162] and revisited by Rodriguez et al. [163] to relate a material yield stress and the indentation hardness. Accounting for pile-up, viscoelastic effects and pressure effects allow correcting nanoindentation moduli to within roughly 5% of the macroscopic value [156]. While such corrections can be done, they are not systematically applied. Hence, the use of nanoindentation modulus values from the literature, for instance for micromechanical modelling purposes, should always be treated carefully.

In an attempt to confront experimental results, many numerical studies of indentation problems have been performed. The most common modelling approach consists in axisymmetric models using cone-equivalent indenter geometries (e.g. substituting the complex shape of a Berkovich indenter with a cone of equivalent tip surface to indentation depth, giving a semi apex angle equal to 70.3°). While this numerically cost-effective method has been proven successful in many instances [163, 164], some authors pointed out the difference in stress fields under the indenter in 2D axisymmetric versus 3D simulations [151]. This is particularly important in composite systems as the stress field interaction with the reinforcement may lead to erroneous predictions of the

material properties [165] (further details below). These studies have shown that the nanoindentation hardness can accurately be predicted using frameworks based on continuum models. In particular, Rodriguez et al. [163] proposed a framework to identify an amorphous material's yield stress based the nanoindentation hardness. The method relies on the concept of a characteristic stress under the indenter, which is related to the hardness using the apparent indentation hardness (without correcting for pile-up or sink-in) and the ratio of the elastic and plastic work done during indentation. They performed an extensive numerical and experimental study for different material classes to validate their method. Nonetheless, the predicted modulus from FE studies is often lower than the nanoindentation modulus (and equal to its macroscale value used in the model formulation). This, once more, suggests that the nanoindentation modulus value is indeed affected by the experimental factors mentioned above and/or inherent material behaviour characteristics, which are not captured by classical continuum models (e.g. strain gradient elasticity).

Indentation size effect

Modern nanoindentation methods employ a continuous stiffness measurement mode (CSM), which allows continuous monitoring of both the hardness and modulus of the material with increasing indentation depth. Fig. 2.19 gives examples of hardness and modulus evolutions as a function of the indentation depth obtained for different polymers in the literature. The reported nanoindentation E and H values always correspond to the so-called plateau values at large indentation depth. The reason is that some polymers present a indentation size effect (ISE) translating into an increase in both E and H for decreasing h. Lam and Chong [166, 167] were the first to report a size effect in epoxy (as shown in Fig. 2.19), and many other polymers, such as PS, PC, PMMA, PA66, have presented a similar response [153, 157, 168, 169]. Contrary to metals, where the modulus is not affected by the ISE, glassy polymers seem to present a coupled elasto-plastic ISE. The literature often reports a size effect of H, such as in [166, 170]. Still, some studies also present the increase in E at shallow depth, for instance in [152, 153, 171, 172]. Several explanations for the length-scale dependent behaviour in nanoindentation have been given over the years, such as higher order displacement gradients, surface irregularities and detection issues, tip bluntness, molecular structure and material inhomogeneity. Lastly, given the viscous nature of glassy polymers, the temperature and strain rate, as well as the thermomechanical history may affect the measured ISE.

To ensure a realistic estimation of the ISE, it is imperative to minimise external factors on the measured response. First, the material surface roughness (e.g. due to poor polishing) or the use of a blunted indenter tip lead to an artificial increase in the ISE as they lead to an inaccurate estimation of the actual contact depth h_c and thus a wrong contact area A_c [173]. Similarly,

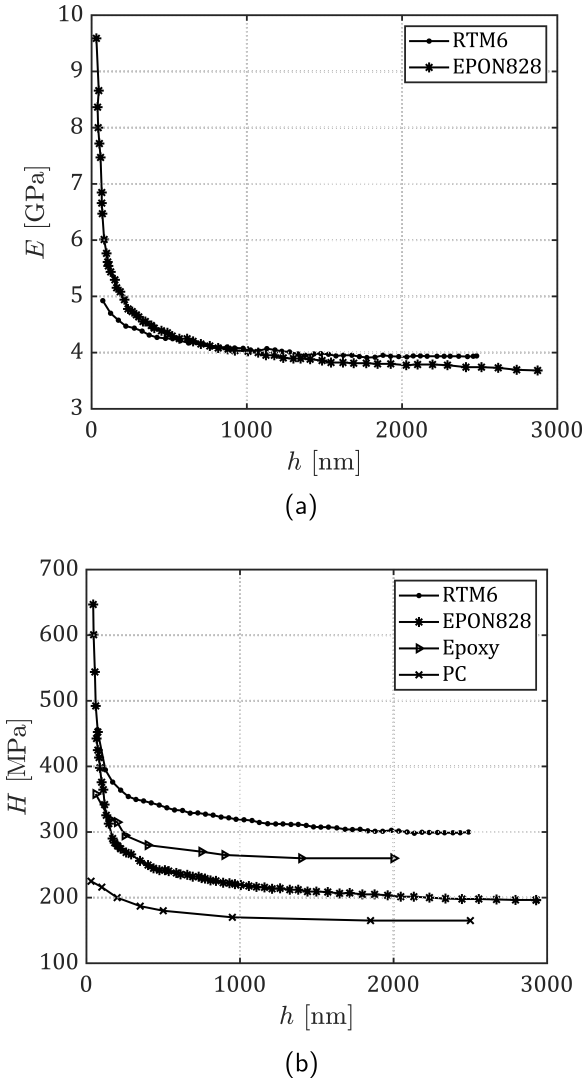


Fig. 2.19: Typical (a) modulus E and (b) hardness H dependence on the indentation depth h for different polymers in the literature: RTM6 [157], EPON828 [158] and PC and epoxy [167]. An indentation size effect (ISE) is found at low indentation depths for all systems.

the nanoindentation test protocol may affect the ISE depending on the accuracy of the surface detection method. Fulco et al. [174] reported an error as high as 15% on the ISE due to wrongful surface detection. Nonetheless, the use of a properly calibrated CSM method provides a highly accurate measure

of the surface detection, thus minimising this error [175]. At this stage, it is important to mention that a size effect in polymer glasses has also been reported in microbending experiments [176–178]. An increase of the bending stiffness was found with decreasing beam thickness. Hence, while the aforementioned extrinsic factors affect the amplitude of the ISE (emphasising the need for a careful test execution), its origin certainly relies in local surface material changes and in the presence of large strain gradients under the indenter tip.

Regarding the molecular structure of the polymer, several studies have shown that the ISE is inherently linked to the bending stiffness of the polymer chains [179]. As such, molecular chains comprised of aromatic groups tend to systematically show an ISE, whereas systems made of simple linear chains do not (or less). Similarly, the higher the molecular weight of the chain, the stronger the measured ISE [180]. Furthermore, the cross-linking density (in thermosets) also significantly affects the amplitude of the ISE: fully cured systems show a larger ISE [169, 181]. Lastly, the induced hydrostatic stress under the indenter has been shown to increase the apparent T_g of polymers at shallow indentation depths [172, 175]. The increase in T_g results from the inability of the polymer chains to properly relax under large hydrostatic stresses. This shift in T_g was related to a larger stiffness, hence promoting a size effect.

Many higher order displacement gradient theories have been developed over the years to predict the ISE. As classical elasto-viscoplasticity theories do not account for large strain gradients due to the lack of an internal length scale parameter, they are incapable of reproducing the depth dependent behaviour. Lam and Chong [166, 167] were among the first to propose a model based on the strain gradient plasticity theory of metals. Inspired by the Nix and Gao model [182] and working under the assumption that yielding is caused by the formation of molecular kinks, as proposed by Argon [44], they suggested that the change of hardness at low indentation depth is caused by the necessity of additional kink-pair formation under large strain gradients. This is akin to the idea of geometrically necessary dislocations in metals [183, 184]. They established a relationship between the hardness H and the indentation depth h:

$$\frac{H}{H_0} = \sqrt{\frac{h_0}{h}} + 1, \tag{2.14}$$

where H_0 is the classical hardness and h_0 is a constant containing material and temperature dependencies.

Shortly after, Han and Nikolov [185] proposed a different model based on the impact of rotational gradients on the polymer chain movements. Crucially, their modelling approach suggests that the ISE on the hardness is inherently connected to the elastic response (and not just to the plasticity mechanisms), which is different to metals. Their model relates H and h as:

$$\frac{H}{H_0} = \left(\frac{c_l}{h}\right)^{\gamma} + 1, \tag{2.15}$$

where c_l is a characteristic intrinsic length, and γ a fitting parameter in the range $0 < \gamma < 2$ and suggested to be equal to 1. An argument in favour of models based on rotational gradients is their ability to distinguish between the depth dependence of spherical and sharp tip indentations. For a spherical tip, see Fig. 2.20, the rotation gradient $\bar{\chi}$ is essentially independent of h and is only proportional to the tip radius R : $\bar{\chi} = 1/R$. By contrast, for a sharp tip, $\bar{\chi}$ is inversely proportional to h: $\bar{\chi} \propto 1/h$. This has also been experimentally validated [158, 186] on epoxies where no ISE is detected for a spherical indenter.

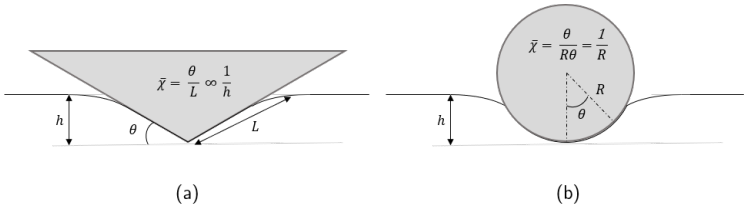


Fig. 2.20: Representation of the strain gradient $\bar{\chi}$ for (a) a sharp tip and (b) a spherical tip.

More recently, Voyiadjis et al. [61] incorporated a depth dependency in a shear transformation zone-type framework. The logic resides in the fact that at shallow indentation depths, the stressed volume under the indenter is too small to accommodate STZ activation. Hence, the whole region is directly deforming plastically. This is translated into a total shear stress acting on an STZ as the sum of a typical shear activation stress and a depth-dependent local stress for highly loaded regions. Their approach successfully reproduced the ISE on the hardness for PMMA at different strain rates. This approach has been extended by Lin et al [187] by implementing pressure sensitivity and Peng et al. [62] by proposing a coupled elasto-plastic depth dependent hardness.

While a number of theoretical models have been developed to study the ISE, the literature dealing with the implementation into a finite element framework is scarce in the context of polymers. Swaddiwudhipong et al. [188] incorporated the notion of geometrically necessary kinks proposed by Lam and Chong [166, 167] into the constitutive model of Govaert et al. [30] and provided a FE implementation. They accurately predicted the force-indentation curves of several nanoindentation tests. Later, Garg et al. [189, 190] developed an axisymmetric coupled stress elasticity model based on rotational gradients and implemented it into a FE software. Their numerical predictions matched the experimental hardness and modulus variations in PDMS.

Case of confined matrix volumes in FRPs

Nanoindentation has also been used to characterise the so-called in-situ properties of the polymer matrix in FRPs [191, 192]. The underlying motivation is to provide accurate local properties of the polymer for multiscale numerical frameworks. Gregory and Spearing [164] were the first to perform nanoindentation on bulk specimens and in matrix pockets of composites. The objective was to compare the measured load-displacement curves and to determine the properties of the matrix unaffected by the presence of the fibres. FE analyses showed that, in order for the measured in-situ properties to be unbiased by the interaction with the stiff fibres, the matrix pocket should be at least 50 times larger than the maximum indentation depth. Using this criterion, these authors demonstrated that the in-situ properties were 30% larger than the bulk ones. They postulated that such a drastic difference in material properties should be taken into account in micromechanical studies aiming at predicting the strength of composite plies. Later on, Hardiman et al. [165, 193] performed an extensive experimental and numerical study comparing the bulk and in-situ properties of an epoxy. They defined a fibre constraint factor (FCF) relating the size of the matrix pocket and the indentation depth. They determined that a FCF between 20 and 50 is necessary to avoid fibre interaction effects on the in-situ properties. Accounting for this, they reported a 20% increase in modulus compared to bulk values. Lastly, Chevalier et al. [157] followed a similar approach for RTM6 and also found a 20% increase for both the modulus and the hardness. Additionally, they showed that the fibre effect is mainly perceived on the modulus. The hardness is independent of fibre proximity, as the increase in hardness caused by the fibre is entirely compensated by a decrease of the amplitude of the sink-in phenomenon (but not leading to pile-up). Nonetheless, FE analyses using an advanced continuum model for the matrix failed to predict the increase in local properties.

The conclusion from these studies is that nanoindentation can be used to extract the in-situ properties in confined volumes between fibres, which tend to be larger than the bulk values. Thus, this raises doubts about the validity of using bulk properties in multiscale frameworks. The origin of this increase has been speculated to either be the result of different ageing levels between the bulk and the matrix pockets or an intrinsic difference in material structure (e.g. change in local cross-linking degree). The case of ageing has recently been addressed by Gayot at al. [142] for a PMMA-based thermoplastic matrix with glass fibres. They showed that, upon thermal rejuvenation of both the bulk and composite samples, no noticeable difference in properties could be detected. After ageing, the increase in property was more pronounced in the small matrix pockets, hinting towards the possibility of accelerated ageing in confined volumes in the presence of fibres.

Other nanomechanical test methods

Atomic force microscopy (AFM) has often been used in FRPs to study the interphase region between the fibres and the matrix, as illustrated in Fig. 2.21 (a). As mentioned before, the presence of fibres can affect the measurements. Hence, nanoindentation is inadequate to assess the presence and properties of the interphase due to its insufficient resolution below 100 nm. While AFM offers a higher spatial resolution, it is not immune to the fibre mechanical interactions. Nonetheless, studies have shown that there is no significant interaction with the fibre at distances beyond 10 nm from the fibre [194, 195]. Over the years, reported values for the interphase range from 20-500 nm for carbon fibre composites [196, 197] to 500-10,000 nm for glass fibre composites [198, 199]. The mechanical response of the interphase has been found to be stiffer or more compliant than the matrix, depending on the system [196, 199, 200].

Recently, micropillar compression tests, shown in Fig. 2.21 (b), have been applied to polymers and to composites [119, 201–203]. The principle relies on carving a pillar at the microscale using focused ion beam (FIB) and performing uniaxial compression tests with the help of a flat punch indenter. The advantage is that the test provides the full stress-strain curve at the microscale, allowing easy identification of the material properties. Nonetheless, the geometry of the carved beam and the stiffening effect of the external polymer layer affected by the FIB need to be accounted for to extract accurate properties [119]. Wang et al. [201] identified a size effect on the yield stress with decreasing pillar diameter for a DGEBA-based epoxy. Herraez et al. [119] reported a size effect on both modulus and yield stress for a 8552 epoxy when the pillar diameter is less than 5 μm. Additionally, they evaluated the in-situ properties of a 8552-based FRP and found no significant difference between the bulk and in-situ properties, in contrast to typical nanoindentation results. More recently, Rueda-Ruiz et al. [202] developed a test protocol for high strain rate tests on micropillars. Their results correlated well with similar rate tests at the macroscale, demonstrating the usefulness and accuracy of the method.

Lastly, it is important to mention characterisation efforts to determine the response of the fibre/matrix interface. In FRPs, a crucial part ensuing structural stability is the quality of the interface. Fibre/matrix decohesion is a predominant cause of the initiation of damage (e.g. fibre kinking or transverse cracking) leading to failure in FRPs [204–206]. Hence, within micromechanical studies of FRPs in the context of multiscale frameworks, an accurate representation of the interfaces is key to improve numerical predictions. Hence, in recent years, several interface characterisation techniques have been developed, as summarized in the thorough review by AhmadvashAghbash et al. [207]. A first category of tests involves the use of specific material samples, which isolate a single fibre. These tests include single fibre fragmentation [206, 208], micro droplet [209, 210] or fibre pull-out [211, 212] tests. The drawback of these methods is that they do

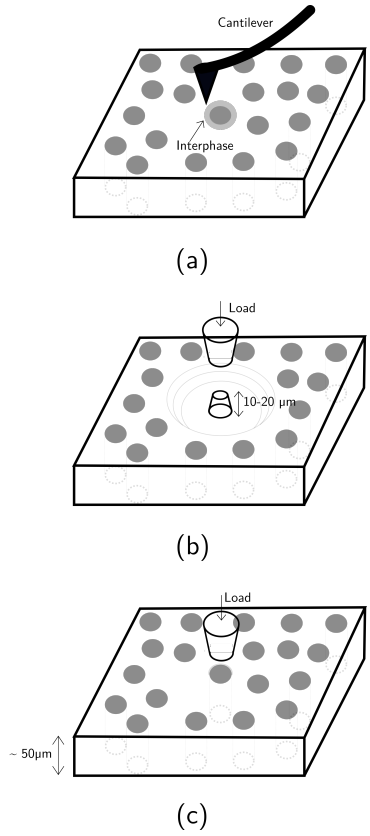


Fig. 2.21: Schematic representation of three typical nanomechanical characterisation techniques similar to nanoindentation to assess in-situ properties of composite matrices: (a) atomic force microscopy (e.g. interphase characterisation), (b) micropillar compression (e.g. microscale stress-strain curve) and (c) fibre push-out (e.g. interfacial shear strength).

not consider the fibre in its actual composite configuration, which may affect the interfacial properties due to fibre/matrix interactions (e.g. cross-links, curing degree, thermal stress, etc.). Therefore, the currently preferred test method relies on fibre push-in or push-out tests [4], as illustrated in Fig. 2.21 (c). Both of these methods have proven to be useful in determining the actual interfacial properties. However, the data interpretation of such tests is challenging and translating interfacial properties into traction-separation laws for cohesive zone models is not straightforward [213–219]. Note that Vu at al. [220] recently applied the fibre push-out method to evaluate process-induced residual stresses in FRPs.

2.3.2 Digital image correlation

Principle

Digital image correlation (DIC) is a non-contact technique developed to measure relative displacements on the surface of a material. A schematic illustration of the working principle is given in Fig. 2.22. To perform a DIC analysis, features on the material surface are tracked during the test. These features can be inherent to the material (e.g. prominent microstructural features) or artificially deposited, resulting in a so-called speckle pattern. During the DIC analysis, the region of interest (ROI) is divided into subsets of a given size (Fig. 2.22 (a)), which are then tracked during the deformation of the material surface (Fig. 2.22 (b)). The DIC software recognizes the grey level balance from the surface features to track the subsets during the deformation. Within each subset, the displacement is assumed to be homogenous. Hence, a displacement vector $\underline{u}$ can be measured between the centres of each subset. The combination of the displacement vectors $\underline{u_i}$ allows constructing the displacement field over the ROI (Fig. 2.22 (c)). Hence, a smaller subset and a smaller space between adjacent subsets improve the resolution of the DIC analysis. Still, an increase in resolution is systematically accompanied by an increase in noise in the displacement field. Excessive noise is problematic as the subsequent strain fields are calculated based on the derivatives of the displacements, amplifying any underlying disturbance. A multitude of commercial DIC softwares exist on the market, however a popular choice in recent years has been the open-source MatLab plugin called Ncorr [221]. Ncorr has been proven extremely useful and accurate when compared to commercial softwares [222], making it a suitable choice for DIC studies.

Ncorr uses contiguous round subsets positioned on integer pixels to calculate the displacements. Strains are calculated based on the Green-Lagrange expression using four displacement gradients:

$$E_{xx} = \frac{1}{2}\left(2\frac{\partial u_x}{\partial x} + \left(\frac{\partial u_x}{\partial x}\right)^2 + \left(\frac{\partial u_y}{\partial x}\right)^2\right), \tag{2.16}$$

$$E_{yy} = \frac{1}{2}\left(2\frac{\partial u_y}{\partial y} + \left(\frac{\partial u_x}{\partial y}\right)^2 + \left(\frac{\partial u_y}{\partial y}\right)^2\right), \tag{2.17}$$

$$E_{xy} = \frac{1}{2}\left(\frac{\partial u_x}{\partial y} + \frac{\partial u_y}{\partial x} + \frac{\partial u_x \partial u_x}{\partial x \partial y} + \frac{\partial u_y \partial u_y}{\partial x \partial y}\right). \tag{2.18}$$

Ncorr allows specifying independent strain subsets on which a least square plane fit is performed to minimise noise. The size of the strain subset can be adjusted separately from the initial displacement subset size. As before, a smaller strain subset improves resolution at the cost of an increase in noise.

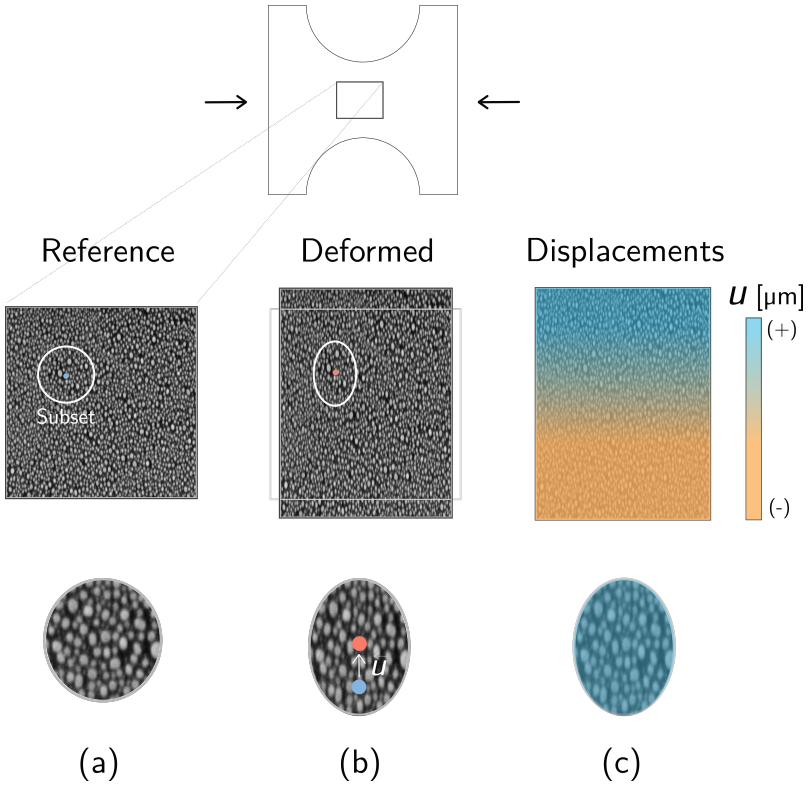


Fig. 2.22: Schematic illustration of the concept of digital image correlation.

Hence, the main challenge to get accurate DIC data, regardless of the scale at which the measurements are taken, is high-quality surface features to ease subset tracking and reduce noise.

While material surface features can be used for the study of FRPs, the most common approach is to deposit a speckle pattern. The speckle pattern guarantees the uniqueness of each subset. Therefore, a robust speckle pattern is dense, homogenous, non-repetitive and presents a high contrast. Such a pattern can easily be produced at the macro- or mesoscale using, for instance, paint spraying techniques. Patterns suited for microscale observations are more challenging to create but can rely on physical vapour deposition or the sedimentation of suspended particles.

DIC across scales in FRPs

DIC (as well as digital volume correlation, DVC) has often been used at the macro- and mesoscale to study the deformation and failure of FRPs, including environmental effects. Holmes et al. [223] recently published an extensive review of the application of DIC and DVC and their future prospects. Some key takeaways on the use of DIC are: imaging and quantification of damage initiation and propagation processes, determination of the influence of defects such as voids, in-situ monitoring of manufacturing processes, study non-standard geometries or structures, etc.

The use of DIC in FRPs at the microscale is still relatively recent. Canal et al. [224] were the first to apply DIC to composites to quantify strain fields in-between the fibres. Since then, only a few studies have attempted a similar approach [76, 225–227]. A comprehensive overview of these studies is given in the introduction of chapter 4. The main challenge limiting the widespread use of micro DIC is the complexity of generating a fine enough speckle pattern without affecting the underlying material. In the past few years, significant progress has been made in terms of patterning techniques. As a consequence, some micro DIC papers studying the micromechanics of polymer samples have started to emerge. Crack propagation by means of notched specimens has been studied by Zike et al. [87]. These authors proposed a method to extract the microscale failure strain and stress of an epoxy at the microscale, showing that the microscale strength is significantly higher than the macroscale one. Verschatse et al. [228] developed a fine patterning technique and showed its potential by quantifying necking strains on epoxy microfibres and crack tip strains in single-edge notched beam tests. An improved DIC approach for the case of FRPs is the core of chapter 4.

2.4 Micromorphic approach

Two phenomena affecting the mechanical behaviour of materials have pushed the development of so-called strain gradient plasticity (SGP) theories: "the smaller is stronger effect" and plastic localisation phenomena such as in the form of shear bands. On the one hand, the "smaller is stronger effect" or "size effect" has often been observed in metals when the size of the material specimen is reduced. This causes an increase of the hardness, which is caused by the presence of geometrically necessary dislocations needed to accommodate the deformation of the crystal lattice under the large strain gradient present in small specimens. Size effects have been reported for polymers as well, as described in section 2.1. On the other hand, strain localisation in the form of shear bands is problematic in finite element analyses of some rate independent material models as these lead to ill-posed problems. This, in turn, reflects into inaccurate simulations or mesh-dependent responses.

Hence, strain gradient plasticity theories have emerged in order to introduce an intrinsic length by taking into account the gradient of strain. Many different approaches exist nowadays, such as, for instance, the Aifantis theory [229], the Fleck and Hutchinson theory [230], the Voyiadjis theory [231] or the micromorphic approach [232]. Some approaches embed the intrinsic length based on the physical mechanisms dictating the deformation at the microscale (e.g. dislocations), such as the Nix and Gao model [182]. While it is not the focus of this work to dive into the complex world of SGP theories, a conceptual overview of the micromorphic approach is given below. An extensive mathematical description of such approaches can be found in [231] and references therein.

An example of a thermodynamically consistent approach is the micromorphic theory. In classical continuum theories, a body of material is defined by a reference set of degrees of freedom (DOF) and state variables:

$$DOF_0 = \{\underline{u}\}, \tag{2.19}$$

$$STATE_0 = \{F_{ij}, T, \alpha\}, \tag{2.20}$$

where $\underline{u}$ is the displacement vector, F_{ij} is the deformation gradient, T is the absolute temperature and α represents the post-yield behaviour of the material (i.e. hardening or softening). The micromorphic approach proposed by Forest et al. for small [232] and finite strains [233] is based on the introduction of an additional degree of freedom called the micromorphic variable χ. The micromorphic variable is associated to a variable from the set of internal state variables and has the same physical and tensorial dimensions (e.g. the cumulative plastic strain). Hence, the new DOF and state of the material can be written as:

$$DOF = \{\underline{u}, \chi\}, \tag{2.21}$$

$$STATE = \{F_{ij}, T, \alpha, \chi, \nabla\chi\}. \tag{2.22}$$

The micromorphic approach can be seen as a systematic framework to build strain gradient models. Indeed, Forest [232] showed that many gradient theories in the literature can be constructed following the micromorphic approach. The potential challenge of this method may lie within the physical interpretation of the size-dependent response of the modelled material.

3

Master trends in the elasto -viscoplastic behaviour of highly cross-linked epoxy resins

Abstract

Highly cross-linked epoxy resins are ubiquitous in high-performance applications, particularly when used as matrices for fibre-reinforced composites. The optimisation of composites requires a quantitative and predictive description of the mechanical behaviour of the epoxy matrix. To explore master trends in the mechanical response as well as to guide first-order modelling, the complete stress-strain response of six epoxies is characterised under uniaxial compression up to large strain and fracture. A number of characteristic properties are analysed and rationalised mainly through establishing relationships with the ratio T/T_g of test over glass transition temperature. Among others, an enhanced Eyring-type model is identified for the yield stress and found valid for a wide range of temperatures and strain rates below T_g. The yield stress of all six epoxies is related to T_g within 10% error without any other adjustment of parameters. A similar relationship for the modulus with T/T_g also accounts for strain rate. Lastly, the failure stress and strain are found to also correlate to T/T_g in subgroups of resins with similar molecular structure, while the re-hardening modulus does not.

This chapter is based on the submitted paper, the main difference being the removal of section 2 of the paper (which has been presented in the section 2.1.1).

3.1 Introduction

In the last few decades, the study of the elasto-viscoplastic behaviour of glassy polymers has received significant attention as a result of their omnipresence in engineering applications. Highly cross-linked thermosetting (TS) polymers, heavily used in the aeronautic and naval industries, partly suffer from a lack of in-depth investigation of their mechanical behaviour. This is based on the agreement that the general macroscale mechanical response is, to a large extent, inherently similar to that of thermoplastic polymers (TPs), except for a lower ductility on average [234–237]. The underlying assumption is that the plastic flow and the large strain behaviour in TP and TS glasses stem from a similar origin [67, 238]. Failure, however, appears to be inherently different, where TPs show progressive damage by crazing and TSs fail in a brittle manner due to micro-cavitation around defects [236, 237, 239–241]. Most of the literature addressing the mechanical response of epoxies focuses on lowly or moderately cross-linked resins, typically based on DGEBA prepolymers and often in the context of adhesives.

A number of recent studies have addressed the mechanical behaviour of epoxies, both from an experimental and from a modelling perspective, to push towards a deeper understanding of the link between the molecular structure and properties [242, 243]. The mechanical behaviour of highly cross-linked epoxies is impacted by the cross-linking density and by the nature of the polymer chains, on top of the test temperature, strain rate and hydrostatic pressure dependence [27, 238, 244–246]. In particular, the strain rate and temperature dependency of the stress-strain response is of crucial interest, to understand the influence on the modulus and yield stress, but also on the re-hardening capacity. Furthermore, a strong correlation with the glass transition temperature T_g is observed and some authors have found clear relationships between the yield strength of TS resins and the T_g [247–250]. Physical and/or hygrothermal ageing can significantly impact the mechanical response of epoxies, particularly the yield stress [14, 15]. Hence, first-order correlations with T_g can be biased by such effects, complicating the analysis of the stress-strain response. To the authors' knowledge, most studies dealing with finding closed-form relationships between the mechanical properties of epoxies and their molecular structure or physical properties limit themselves to the analysis of the elastic modulus and yield point (in the case of compressive loads) (e.g. [247, 251]).

In parallel to the disproportion in experimental studies between TPs and TSs, the modelling of the constitutive response of TSs displays a similar imbalance. While the most advanced models devoted to TPs include some strong physical grounds, models for TSs often stay at a more phenomenological level. Many studies linking the elasto-viscoplastic response of TPs with the molecular structure have indeed guided and optimised the development of constitutive

computational models [252, 253]. The recent literature dealing with the modelling of glassy polymers, mostly on TPs, includes validation performed on only one or two systems [254–260]. One of the common characteristics of these models is a high sophistication and a large number of physical parameters. The positive outcome is a good level of predictivity but at the expense of a difficulty to separate the first and second order effects and to understand the dominant physical influences and master trends. In recent years, modelling based on molecular dynamics simulations aims at linking the mechanical properties to the fundamental molecular interactions, though many fundamental questions still remain about the nature of the nanoscopic plastic deformation mechanisms (a deeper description of these mechanisms is given in section 2.1.1) [47, 50, 54, 261].

Lastly, the extensive use of epoxies as matrices for polymer matrix composites (PMCs) triggered the development of multiscale characterisation strategies focused on improving the understanding of the deformation and failure of these TSs [76, 217, 262]. The primary motivation guiding these studies is the recognition that an accurate description of the microscale deformation of epoxies is necessary to adequately predict the failure of composite structures, even for simple thermoset unidirectional (UD) fibre-reinforced composites [76, 146, 151]. In many loading conditions, plastic flow within the matrix is non-negligible, such as under shear, transverse compression or creep, re-emphasising the need to accurately describe the viscoplastic response beyond the onset of yielding.

Hence, there is a clear interest for the community to have access to a wider range of experimental data below T_g to serve as a basis to identify and validate advanced modelling attempts. The premises of this work were to gather a vast range of elasto-viscoplastic properties resulting from compression tests on different highly cross-linked epoxy systems. The advantage of compression tests is to allow investigating the large strain behaviour without premature failure as found for epoxies deformed in tension. Experimental data at different temperatures and strain rates are extracted and rationalised with respect to the magnitude of the T_g. Care was taken to consider resins presenting a similar physical state with respect to physical ageing. The three main objectives are the following:

- To offer a rich database about the mechanical response of epoxies with a range of T_g varying over almost 200°C to the interested community;

- To establish general master trends regarding the entire stress-strain response, including elasticity, yielding, softening and re-hardening, serving as a basis for first order modelling the mechanical behaviour of epoxy systems (bulk or as used in composites);

- To rationalise regularities within the stress-strain response with respect

to physico-chemical or molecular structure factors based on the current literature and to primarily link it to the T_g to provide simple robust phenomenological relationships.

In particular, the relationships are established to predict the modulus and yield stress of epoxies at any temperature (below T_g) and strain rate (in the low rate regime). Additionally, the re-hardening and the failure of the epoxies is related to T_g.

3.2 Experimental database on highly cross-linked thermosets

Uniaxial compression tests were chosen as they allow testing the large strain response of epoxies, which often fail before yielding in tension. The specimen geometry was a cylinder of aspect ratio 1:1. This geometry was identified by Morelle [7] to minimise buckling and friction of the specimen. As epoxies are pressure sensitive, PTFE films were used to lubricate the contact between test apparatus and the specimens to minimise friction and prevent buckling. Tests were performed using a constant true strain rate on a screw-driven Zwick-Roell universal testing machine with a 250 kN external load cell equipped with a Wyoming Test Fixture subpress.

In total, six epoxy-amine systems were analysed to determine the master trends in the mechanical response of this class of polymers, based on uniaxial compression tests. All resins were tested under perfectly lubricated conditions, avoiding barrelling at large strains. The stress-strain responses for the epoxies at all tested temperatures and strain rates can be found in appendix 3.5.2. Table 3.1 presents their name, glass transition temperature and corresponding original studies. The T_g were systematically measured by differential scanning colorimetry (DSC) using similar heating rates. A precise physico-chemical description of these resins was difficult to obtain, as they are commercial products. The difference between systems SR8500-1 and 2 comes from the change in hardener (both amine-based). The curing cycles of each resin, which may slightly differ from the manufacturer's protocols, can be found in appendix 3.5.1. The T_g of the systems investigated in this work varies from 100°C to 287°C, namely in a range of almost 200°C, providing a relatively wide spectrum of data.

The glass transition temperature T_g will be used as the main physico-chemical parameter to establish relationships valid throughout the entire database between the mechanical properties and a single characteristic of the epoxies affecting the molecular structure and deformation micromechanisms. The T_g of polymer glasses is mainly defined by three physico-chemical factors: the functionality of the cross-links, the cross-linking density (i.e. molecular weight between cross-links) and the stiffness of the backbone of the polymer chains.

	T_g [°C]	Manufacturer	Ref.
8552	226	HexCel [263]	–
DGEBA/DDS	100	Westlake Epoxy [264]	[265]
SR 8500-1	105	Sicomin [266]	[93]
SR 8500-2	113	Sicomin [266]	[93]
RTM6	220	HexCel [267]	[7]
TGDDM/DDS	287	Huntsmann [268]	[269, 270]

Table 3.1: Epoxy systems of interest with corresponding glass transition temperatures and reference studies. The results for 8552 have not yet been published.

It therefore represents the stiffness of the polymer network. In general, highly cross-linked epoxy systems based on high functionality precursors and amine hardeners lead to a densely interconnected network made of stiff aromatic-based chains, resulting in high values of T_g. In this work, all epoxy systems are amine-cured. RTM6 and TGDDM (Tetraglycidy1-4,40-diaminodiphenylmethane) are based on tetra-functional precursors, whereas SR8500-1 and 2, and DGEBA (bisphenol A diglycidyl ether) are based on di-functional precursors. TGDDM and DGEBA were cured using 4,4'-diaminodiphenyl sulfone (DDS). We will use the principle of corresponding states T/T_g to correlate the mechanical properties to T_g, instead of using the relative molecular mobility $T - T_g$. Nevertheless, both options have been shown to be equally efficient in the case of yielding [247, 250]. The key question at the core of the analysis to come is to determine if T_g alone is sufficient to rationalise, below T_g, the entire mechanical response up to failure of highly cross-linked epoxies or if another material/structure parameter plays a primary role on top of T_g.

Several characteristics of the mechanical response of glassy polymers (e.g. elastic modulus and yield stress) can be rationalised by time-temperature superposition principles [242, 243, 271–274]. A typical starting point is the Eyring-type approach, accounting for the temperature and strain rate, e.g. [8, 275, 276]. The yield stress is related to the strain rate as (also see section 2.1.2):

$$\sigma_y \;=\; \frac{\Delta G}{\nu_0} \;+\; \frac{k_b T}{\nu_0}\, log\, \left(\frac{\dot{\varepsilon}}{\varepsilon_0} \right), \tag{3.1}$$

where ΔG is the activation energy and ν_0 the activation volume. The time-temperature superposition can be constructed by plotting σ_y/T as a function of $\log(\dot{\varepsilon})$ and by defining horizontal (Eq. 3.2) and vertical (Eq. 3.3) shift factors to generate a master curve for a specific polymer. These shift factors are defined as:

$$\Delta \log(\dot{\varepsilon}) = \log(\dot{\varepsilon}_{T_{ref}}) - \log(\dot{\varepsilon}_T), \tag{3.2}$$

$$\Delta \frac{\sigma_y}{T} = \frac{\sigma_y(T_{ref})}{T_{ref}} - \frac{\sigma_y(T)}{T}. \tag{3.3}$$

An extended form of the Eyring-based formalism will be used to analyse some of the experimental data addressed in this paper.

Lastly, it is important to note that the reported values of σ_y correspond to naturally aged systems (i.e. with an arbitrary time between manufacturing and testing) kept at the same level of relative humidity and at constant room temperature. The yield stress can be significantly reduced if rejuvenation is imposed by thermomechanical treatment. Ageing is also known to induce a slight increase in T_g [14]. Nevertheless, a first study on RTM6 highly cross-linked epoxy network (and thus high T_g) has shown that the variation of σ_y is marginal despite strong accelerated ageing treatment or rejuvenation [7]. Therefore, in contrast with TPs, we suspect that in the case of highly cross-linked epoxy networks (such as the ones studied here), these effects of ageing and rejuvenation on σ_y might be hampered by the dense and rigid network. Hence, future works should also consider the comparison between rejuvenated and aged systems and its impact on the hereafter established linear relationship.

3.3 Results and discussion

Fig. 3.1 shows the true stress-true strain curves at room temperature and at a true strain rate equal to 0.01 s^{-1} of all the systems addressed in this study. Evidently, the post-yield response strongly depends on the type of epoxy. In the subsequent sections, linear correlations will be established between the mechanical properties and the ratio T/T_g. The corresponding R^2 values of the regressions are systematically given.

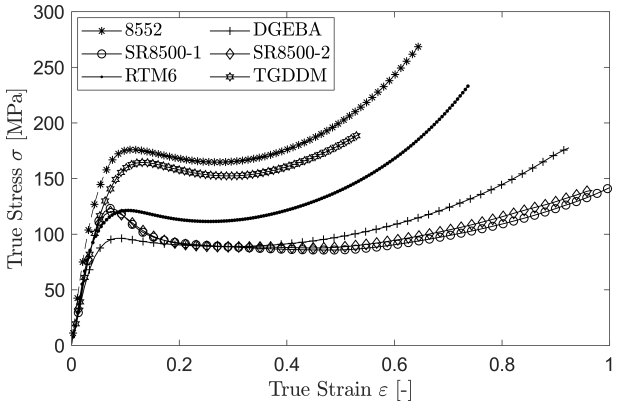


Fig. 3.1: True stress-true strain responses of the different epoxies at room temperature and $\dot{\varepsilon} = 0.01$ s^{-1}.

3.3.1 Viscoelasticity

Fig. 3.2 shows the variation of the compressive Young's modulus E_C as a function of the normalised temperature T/T_g (a brief description of the method used to determine the modulus in compression is given in appendix 3.5.3). The vertical spread within a set of data points corresponds to the effect of different imposed strain rates. The shaded area represents the $\pm 10\%$ bounds with respect to a linear regression. As expected, a decrease in temperature or an increase in strain rate leads to an increase in modulus [13, 21, 236, 277–280]. Evidently, regardless of the strain rate, E_C linearly scales with T/T_g. The linear relationship with T/T_g is indeed expected as all systems are highly cross-linked networks based on aromatic chains; in other words their polymer backbone nature and stiffness are rather similar. Hence, despite their differences in T_g, as a result of chemistry and cross-linking density, it is mainly the test temperature that appear to affect the modulus. This is very clear for T/T_g around 0.75-0.8 where three systems present similar moduli for similar T/T_g. Now, the differences in molecular configuration and cross-linking density lead to variations typically less than 10% from system to system.

Nevertheless, two exceptions are worth discussing. For T/T_g higher than 0.95, the correlation fails and E_C drops significantly. This can be explained by the proximity to T_g. The glass transition is a continuous process over a specific temperature range, here defined via its mid-point T_g. Hence, for T/T_g above 0.95, the polymer systems are already partially in their transition phase, leading to a drop in the modulus to reach the value of the rubbery plateau modulus. Conversely, for TGDDM, a drop shows up at lower temperatures, yet the behaviour of this polymer does not follow the master curve of the others. Comparing the different values for different T/T_g and strain rates show that it has an overall remarkably stable E_C as the data at different strain rates overlap. The reason for this could be found in the higher functionality of the TGDDM molecules and the inclusion of the strong sulfone dipoles, favouring the formation of hydrogen bonds. Still, this does not explain the relatively low value of the modulus.

In order to account for the temperature and strain rate simultaneously, we use the formalism described by Eq. 3.2-3.3 in section 3.2. While originally justified for the yield stress, its application to the modulus has been shown effective as well [281]. However, to also address the impact of T_g, the vertical shift factor of Eq. 3.3 is redefined as follows:

$$\Delta \frac{E_C}{T} = \frac{E_C(T_g)}{T_g} - \frac{E_C(T)}{T} \tag{3.4}$$

where $E_C\,(T_g)$ is the modulus estimated for each resin based on the linear relationship shown in Fig. 3.2. The reference strain rate used for the horizontal shift is $\dot{\varepsilon} = 0.01\ \mathrm{s}^{-1}$. Fig. 3.3 gives the new relationship between E_C/T and

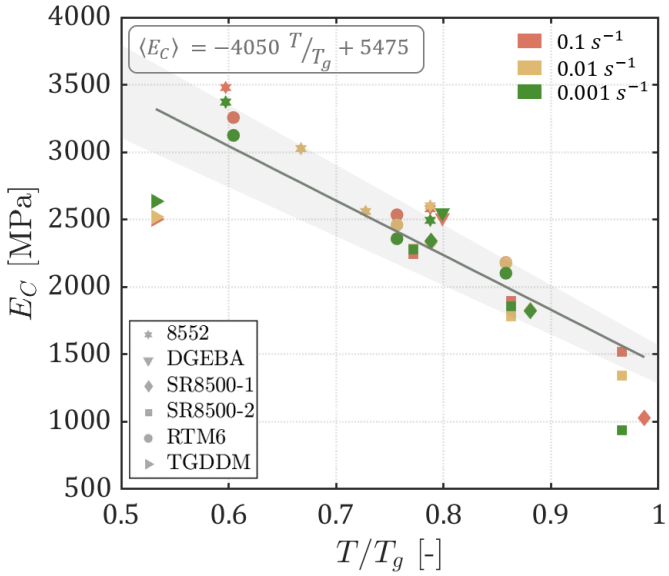


Fig. 3.2: Variation of the compressive Young's modulus E_C as a function of T/T_g. Each marker corresponds to a different resin. The effect of imposed strain rate is shown by the colour of the markers. The shaded area shows the ±10% bounds. The R^2 value of the linear regression including all data points is equal to 0.98.

$\log(\dot{\varepsilon})$. A decent fit is found, with the exception of one data point for SR8500-2. This data point was already ruled out as an outlier in the E_C versus T/T_g graph, as the test temperature is too close to the T_g of the resin. The results of Fig. 3.3 show that it is possible to predict the modulus within ±10% at different temperatures and strain rates through the knowledge of T_g only.

Literature dealing with the elastic modulus of epoxies suggests that increasing the degree of cure (as defined by the molecular weight between cross-links) for a specific epoxy system leads to a decrease in the measured modulus [67, 237, 246]. The suggested reason is the additional spacing between chains created by the cross-links, leading to reduced inter-chain interactions. As the degree of cure is directly proportional to the T_g of the system, the modulus does in fact decrease with increasing T_g, for a specific system. For instance, Moosburger-Will [244] et al. have shown that, for RTM6, a higher degree of curing yields a higher T_g and a lower modulus. Morelle [7] found similar results for RTM6 using uniaxial compression tests. However, for the same specimens, a measure for the Derjaguin, Muller, and Toporov (DMT) modulus by atomic force microscopy showed an increase of the modulus with increased cross-linking density. Still, in the present case, all systems are fully cured, hence the deviation

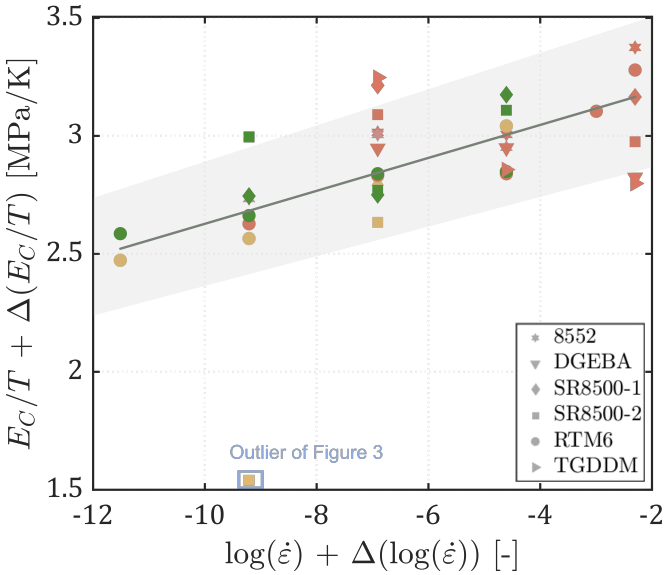


Fig. 3.3: Master curve of E_C/T as a function of $\log(\dot{\varepsilon})$ for all resins using a shift factor based on T_g given in Eq. 3.4 ($R^2 = 0.8$). The different colours for each resin represent the different test temperatures.

of TGDDM cannot be explained in this way. Some studies have also found a marginal increase in the modulus with the ageing time of the system [14]. Note that plastifying effects due to water (or other solvents) adsorption may also significantly impact modulus measurement [282]. Ultimately, despite the challenges of accurately assessing the link between T_g and E_C, this work shows that, for highly cross-linked and fully cured systems, a first-order correlation with T/T_g exists.

3.3.2 Onset of plastic yielding

Fig. 3.4 presents the variation of the upper yield stress σ_y with T/T_g. The temperature and strain rate dependencies of the resins are as expected, namely an increase of σ_y as the temperature decreases or as the strain rate increases. Furthermore, a linear relationship between σ_y and T/T_g is found. Note that the strain rate does not significantly impact the established relationship. The comparison with Fig. 3.5 (a), showing the strain rate sensitivity of the upper yield stress, confirms that all systems present a similar dependence on strain rate with respect to T/T_g. The T_g of an epoxy directly dictates its strength as it defines its molecular mobility, whether it is a mobility associated to reversible changes of configuration (i.e. elasticity in Fig. 3.2) or irreversible changes. From a micromechanical point of view, the origin of plastic flow is assumed to

be the consequence of the nucleation of local shear events whose collaborative percolation leads to increased chain mobility, allowing for large conformational changes to occur [8, 9, 33, 235], also associated with softening, see section 3.3.3. Hence, in general, high T_g systems require the overcoming of a larger energy barrier to initiate this chain of events. The thermomechanical plastic yielding process can be rationalised by relying on an Eyring-type formalism (see Eq. 3.1). The variation of the activation volume ν_0 with T/T_g is given in Fig. 3.5 (b). It shows that ν_0 increases with T/T_g, with the exception of the SR8500-1/2 resins. The comparison with Fig. 3.4 shows that, for each T/T_g, a higher yield stress system involves a lower activation volumes. In general, the activation volume has been found to increase with temperature [245, 283] and entanglement density [284]. The exception of the SR8500-1/2 resins may be due to a slightly lower cross-linking density.

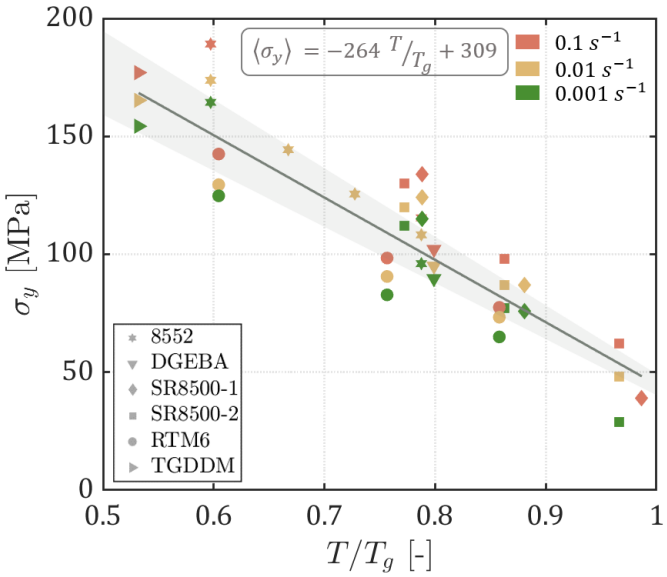


Fig. 3.4: Variation of the compressive upper yield stress σ_y as a function of T/T_g. $R^2 = 0.79$.

Richeton et al. [276] extended the Eyring formalism presented in section 3.2 into the so-called cooperative model. An expression was established for relating the yield stress to the temperature and strain rate of TPs, in the form:

$$\sigma_y = \sigma_i\,(0) - mT + \frac{2k_bT}{\nu_0}\sinh^{-1}\left(\frac{\dot{\varepsilon}}{\dot{\varepsilon}_0\,\exp\left(\frac{\Delta\ H_\beta}{k_bT}\right)}\right)^{1/n}, \qquad (3.5)$$

where $\dot{\varepsilon}_0$ is a constant pre-exponential factor, $\Delta\ H_\beta$ is the activation energy of the β relaxation, $\sigma_i\,(0)$ is the athermal internal yield stress, ν_0 the activation volume in Eq. 3.1 and m a material parameter and n a fitting parameter.

Although Richeton et al. [276] identified the specific material parameters of Eq. 3.5 for each TP under investigation, the goal is here to determine if one can find a single set of parameters either identical for all thermosets or dependent only on T_g. From the established linear relationship between σ_y and T/T_g from Fig. 3.4 (σ_y = -264 T/T_g+ 309), one can readily identify m = $264/T_g$ MPa/K and $\sigma_i\,(0)$ = 309 MPa. A curve fitting algorithm was applied to all resins and the best values are given by $n = 6$, $\dot{\varepsilon}_0 = 10^{15}$ s^{-1}. The activation volumes are readily available from Fig. 3.5 (b), depending on T/T_g. Finally, a different parameter ΔH_β has been identified for each resin and a dependence on T_g has been explored. Fig. 3.6 shows that the identified values for ΔH_β depend linearly on T_g. Fig. 3.7 (a) shows the σ_y/T versus $\log(\dot{\varepsilon})$ plots at different temperatures and strain rates. It compares the experimental data for σ_y with the calculated values for the yield stress based on Eq. 3.5. The model reproduces the experimental data very well. This is confirmed by looking at Fig. 3.7 (b), which plots the relative error for each data point as function of $\log(\dot{\varepsilon})$. The error is systematically below 10%. This means that the model expressed by Eq. 3.5 with the identified parameters (which only depend on T_g) can predict the yield stress for many different epoxies within 10% in the range of strain rates and temperatures covered in the analysis. The final form of the enhanced Eyring model of Eq. 3.5 that can be used to estimate the yield stress of highly cross-linked thermosets (below T_g and at a strain rate below 1 s^{-1}) writes as:

$$\sigma_y = 309 - 264\ T + \frac{2k_bT}{\nu_0\,(T_g)}\sinh^{-1}\left(\frac{\dot{\varepsilon}}{10^{15}\ \exp\left(\frac{0.078\ T_g+14}{k_bT}\right)}\right)^{1/6} \tag{3.6}$$

The fact that ΔH_β increases with increasing T_g as ΔH_β = 0.078 T_g+14 can be simply understood as ΔH_βrepresenting the energy barrier for secondary relaxation mechanisms that act as precursors to the main chain motion [275].

As mentioned in the introduction, the yielding of epoxies has been the main focus of many mechanical studies. Lemay et al. [250] synthesised DGEBA resins, using 4,4'-diaminodiphenyl sulfone as curing agent, with varying molecular weight between cross-links M_c (and so in cross-linking density) and found that M_c scaled with the initial molar mass of the monomers, meaning that monomers with larger molar masses also involved higher M_c. Naturally, resins that present a lower M_c also have a higher T_g. When looking at the mechanical properties, they found that the yield stress σ_y linearly scales with $T - T_g$. Mayr et al. [237] also studied DGEBA systems cured with aliphatic and aromatic amine hardeners to determine the influence of the cross-linking density and the strain rate on the yield stress. The yield stress increased with the cross-linking

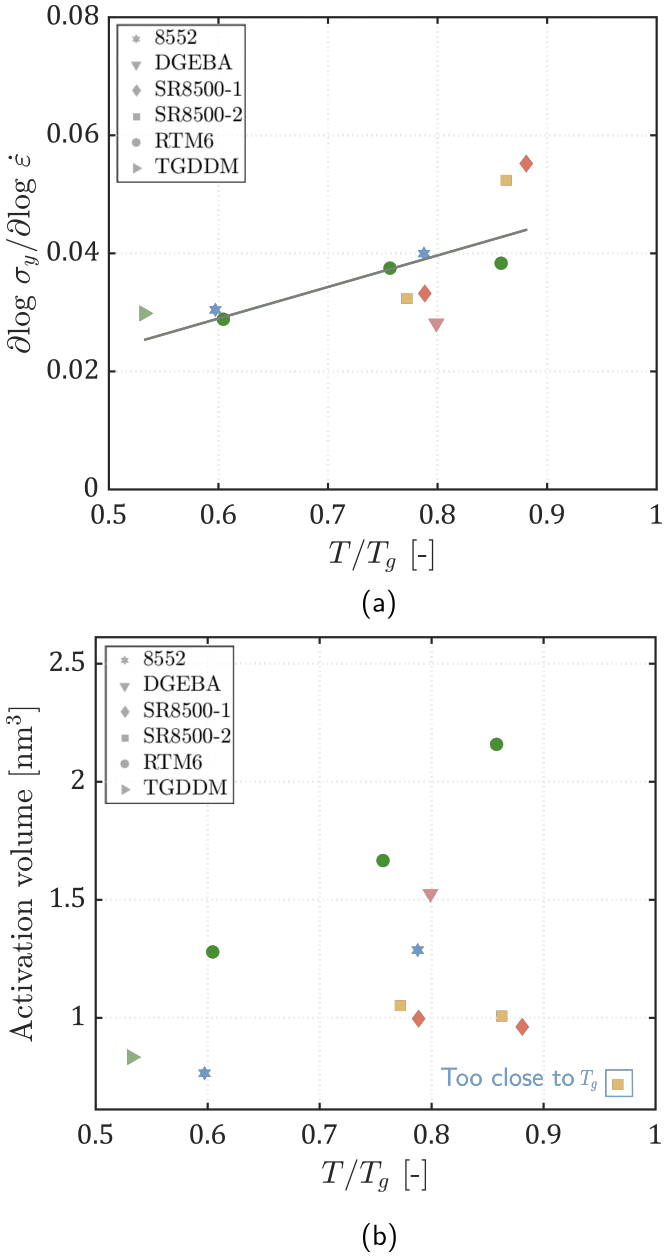


Fig. 3.5: (a) Strain rate sensitivity variation of the upper yield stress σ_y with T/T_g and (b) variation of the activation volume calculated in the context of an Eyring model as a function of T/T_g.

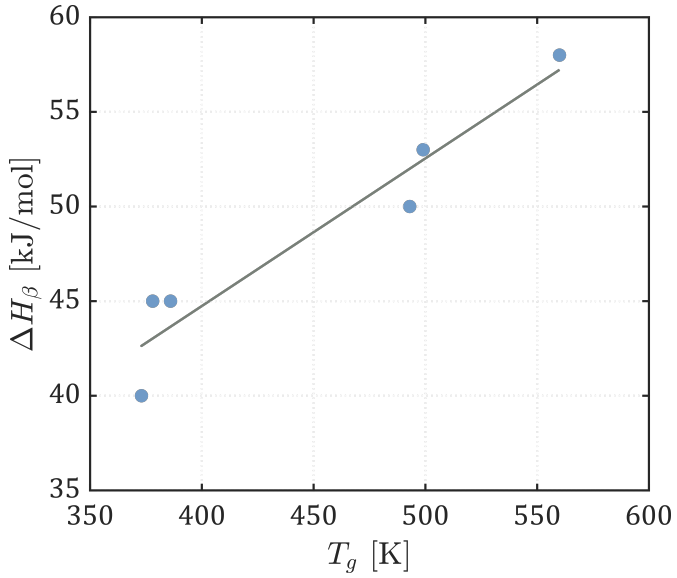


Fig. 3.6: Variation of the identified ΔH_β with respect to T_g

density, however, no general trend was deduced as the cross-linking density impacts the yield strength of epoxy resins but only indirectly via the associated T_g increase.

Still, the correlations found in the aforementioned studies fail to collapse all epoxies into a single line (taking strain rate effects aside), suggesting that solely considering T_g is insufficient to fully capture the yield phenomenon. Calzia et al. [247, 248] suggested the use of a second parameter for the influence of the physical properties, which is the cohesive energy density E_{coh}. E_{coh} is defined as an energy density parameter that reflects the cohesive strength of the network, namely the inter-molecular interactions. They established a correlation between the physical properties, described by T/T_g and E_{coh}, and σ_y for different epoxy networks. They studied DGEBA-based resins hardened with aliphatic, aromatic and phenolic compounds to create a variety of chemical architectures with varying cross-linking density. Thus, their work encompassed E_{coh} and two factors that influence T_g. The choice of using E_{coh} is based on the fact that it characterises the strength of the network and is thus complementary to T_g (i.e. stiffness) to determine the resistance of a material to internal distortions. Using their own resins and additional data from published papers, these authors fitted the results with a model that comprehends T/T_g and E_{coh}. Alternatively, the inability to establish a stronger linear regression could lie with the molecular relaxation mechanisms active at yielding (see section 3.3.3).

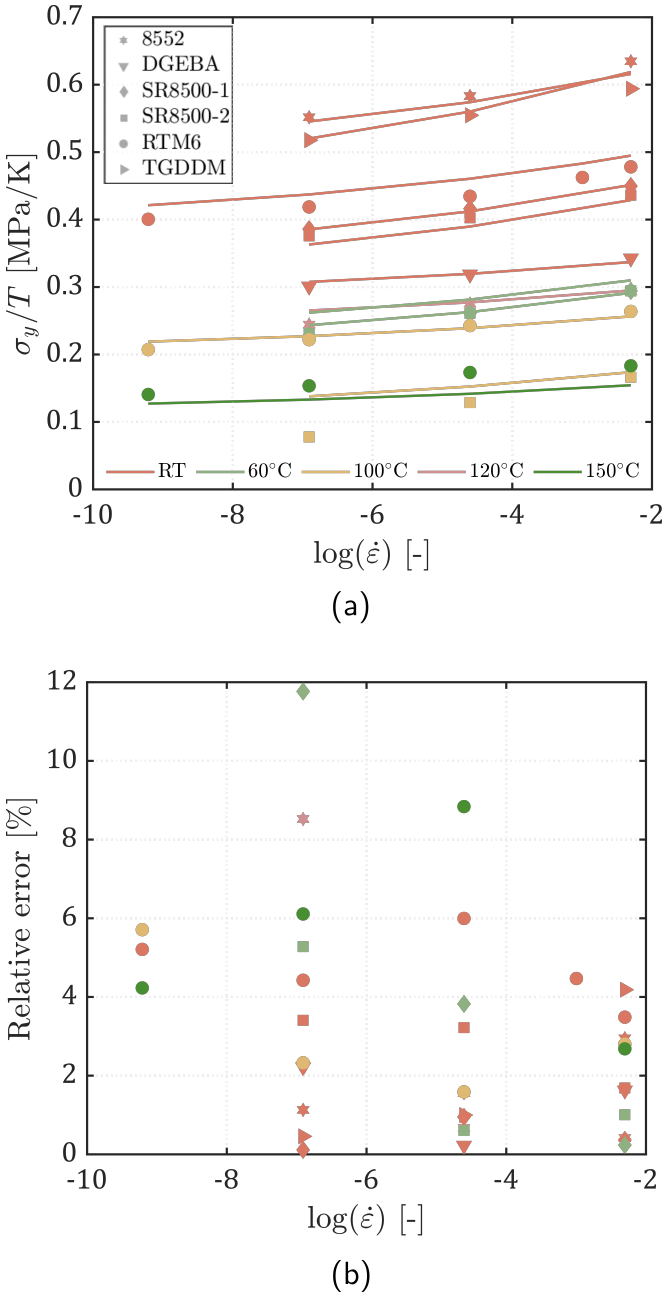


Fig. 3.7: (a) Variation of σ_y/T as a function of $\log(\dot{\varepsilon})$ at different temperatures and strain rates comparing the experimental values (markers) and the yield stress predicted by the enhanced Eyring's model of Eq. 3.5 and (b) relative error with respect to the experimental results.

The yield strain ε_y corresponding to the onset of plasticity has not received much attention in the literature. Fig. 3.8 shows the linear decreasing dependence of ε_y on T/T_g. Additionally, it is worth noting that higher strain rates lead to higher ε_y, without any significant variations with the rate sensitivity except for TGDDM. Marano et al. [18] studied the onset of yield in terms of the strain and found that the strain at peak yield does not necessarily coincide with the onset of plasticity. They found that, typically, the real onset of plasticity takes place beyond the peak yield. Earlier, Quinson et al. [33, 285] studied the strain component evolution for two thermoplastics, and divided the total strain as the sum of three contributions: elastic, anelastic (recoverable over longer periods) and plastic. Similar results were found by Hasan and Boyce [38]. The anelastic strain significantly increases from the beginning and peaks around the upper yield stress level. Conversely, the plastic strain was only initiated when the stress reached σ_y. Hence, a significant portion of ε_y must be dictated by its anelastic component ε_{an}. Quinson et al. also showed that ε_{an} decreases with increasing temperature, in accordance with Fig. 3.8. Lastly, as ε_{an} is at its highest when the stress reaches σ_y, the similarity in tendencies of Fig. 3.4 and Fig. 3.8 becomes clear.

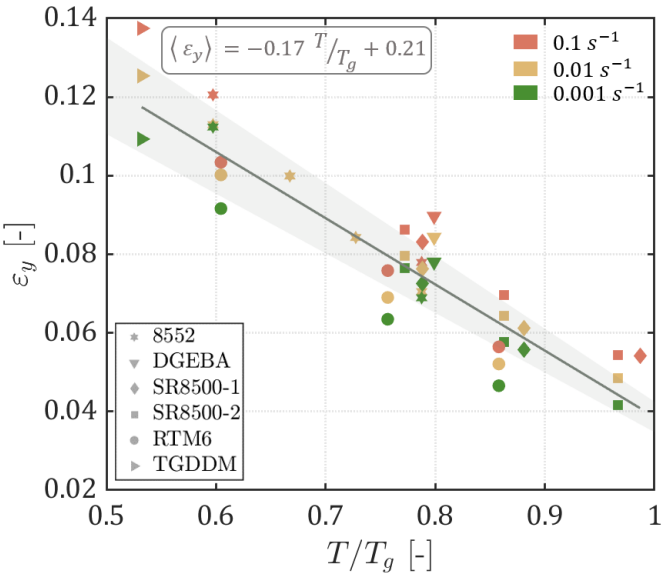


Fig. 3.8: Variation of the compressive upper yield strain ε_y as a function of T/T_g. $R^2 = 0.83$.

Reconsidering the phenomenology of yielding from an STZ physical point of view, the distinction between anelastic and yield strain becomes meaningless,

as the macroscopic strain is then simply the consequence of the accumulation of progressive local conformation changes that bring forth the pre-peak non-linearity and the yield point (and all subsequent changes) [59, 60, 157, 173]. Plastic deformation can then be interpreted as the successive percolating activation of STZs whose energy barrier to return to their initial configuration is too high to overcome without the help of external energy in the form of heat or mechanical loading.

3.3.3 Strain softening

Fig. 3.9 (a) illustrates how the lower yield stress σ_l scales with T/T_g. The correlation appears to be even better than for the upper yield, which could have been expected as the mechanical rejuvenation in the post-yield regime negates potential prior ageing-related effects. Naturally, both upper and lower yield stresses are closely linked and present the same dependencies on external factors. Hence, a similar dependency on T/T_g could have been expected. Van Breemen et al. [21] offer a potential argument justifying the stronger correlation. They investigated the evolution of both the upper and lower yield stresses with temperature and strain rate of thermoplastics to determine the impact of molecular relaxation mechanisms on softening. They demonstrated that three distinct phases can exist depending on the temperature and strain rate. At high temperatures or low strain rates, both upper and lower yield stresses are only affected by α-relaxations. Then, at intermediate temperature or strain rate, the upper yield stress is affected by both α and β relaxations while the lower yield stress remains only affected by α-relaxations. Finally, at low temperatures or high strain rates, both yield stresses are affected by α and β relaxations. Hence, they determined that the stress drop $\Delta\sigma$ is constant only if both the upper and lower yield stresses are affected by the same mechanisms. Fig. 3.9 (b) gives the evolution of $\Delta\sigma/\sigma_y$ for the studied epoxy systems. One can see that RTM6 is the only one presenting limited rate dependency as T/T_g increases, suggesting that its yield may only be affected by α relaxations only under these conditions. This implies that the aforementioned correlation for σ_y in Fig. 3.4 is impacted by a superposition of two relaxation mechanisms, whereas the correlation of σ_l in Fig. 3.9 (a) is only affected by one and therefore correlates better with T/T_g. In addition, Fig. 3.9 (b) highlights that DGEBA presents little softening and lies outside the linear relationship. Odegard [14], G'Sell [15] and co-authors have shown that ageing does not significantly affect the lower yield stress. Thus, DGEBA may be in a more rejuvenated state than the other systems, as full rejuvenation of glassy polymers has been shown to suppress softening completely by reducing the amplitude of the upper yield. Ultimately, the linear relationship for σ_l emphasises an important aspect: plasticity allows these systems to find configurations that tend to suppress any other effects than the ones affecting T_g.

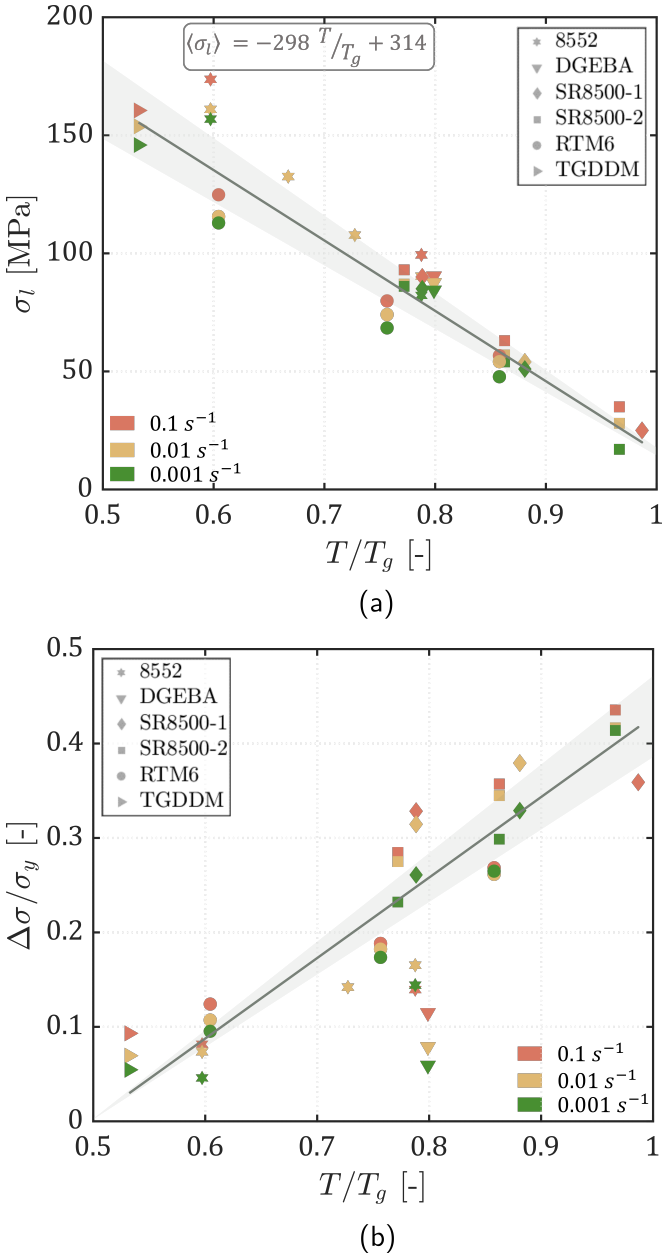


Fig. 3.9: Variation of (a) the compressive lower yield stress σ_l ($R^2 = 0.85$) and (b) the normalised stress drop $\Delta\sigma$ as a function of T/T_g.

3.3.4 Strain re-hardening

Fig. 3.10 illustrates the evolution of the re-hardening modulus G_h with T/T_g. While no global correlation with T/T_g can be made, three subgroups can be distinguished. Furthermore, G_h appears relatively independent of temperature for each subgroup, yet seems to be slightly impacted by the strain rate. Still, note that data for DGEBA and TGDDM correspond to one temperature only. The effect of temperature is less clear, with studies showing an increase [23, 24, 26] or independence on temperature [7, 27]. Additionally, the categorisation of epoxies with similar T_g into subgroups suggests that higher T_g resins also present a stronger re-hardening capacity. Indeed, the lowest group encompasses resins presenting a T_g close to 100°C, whereas the middle group corresponds to resins with T_g above 200°C. Van Melick [23] suggested that G_h increases with increasing network density. More recently, Tian et al. [27] experimentally characterised the re-hardening of a thermoset polymer over a wide range of temperatures (going from rubbery to glassy state), strain rate and cross-linking density. They showed that, in the glassy state, G_h is relatively unaffected by the temperature or strain rate. Furthermore, for highly cross-linked systems, G_h is independent of the network density and the more pronounced re-hardening that is observed for such systems comes from a lower stretch capacity of the polymer chains in between cross-links. Hence, future work will consist of characterising the molecular chains of these resins, to determine their relative stretch capacity and see if it relates to T_g. The case of 8552, which shows a huge G_h, can be explained by the thermoplastic toughening inclusions in the formulation, namely polyethersulfone (PES, T_g= ∼225°C). While the addition of PES only slightly increases the pre-softening properties [286], its impact on G_h is significant.

Several modelling studies have shown that entropic and viscous contributions to strain re-hardening are necessary to reproduce the experimental results [8, 24, 25, 31, 287]. Additionally, it appears that irreversible local conformation changes continue to occur during re-hardening. Hence, a fully neo-Hookean representation of the re-hardening capacity, albeit successful for certain polymer glasses [26], cannot justify all the experimental trends. In the end, the experimental and modelling studies have shown that no clear physical origin has yet been attributed to the large strain re-hardening of highly cross-linked epoxies, or glassy polymers in general. Using the idea of STZs, Voyiadjis et al. [60] suggested that re-hardening results from the increased difficulty of activating new STZs.

The re-hardening process is rightly denominated “hardening” as it implies that the yield stress increases for strain hardening or kinematic hardening reasons. Hence, if one unloads and reloads the system during that stage, the stress-strain curve resumes at the point of unloading. In other words, the connection to the neo-Hookean representation, although convenient and with some physical relevance regarding chain orientation, is not, strictly speaking,

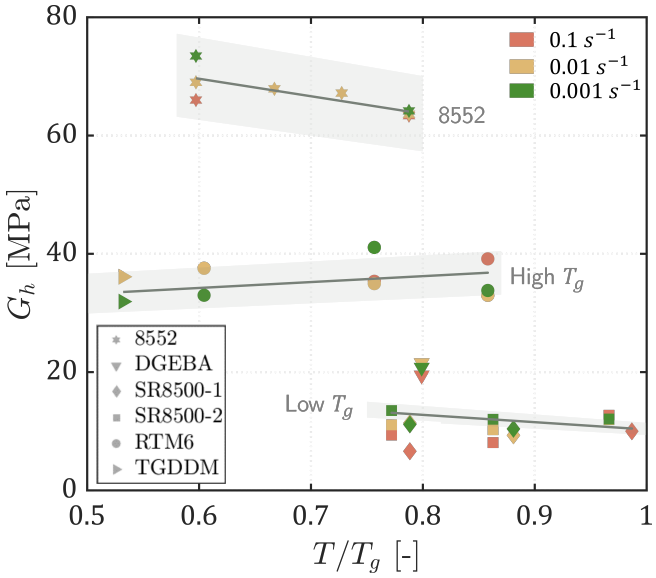


Fig. 3.10: Variation of the re-hardening modulus G_h as a function of T/T_g. $R^2 = 0.31$.

representing the correct physics of plasticity. If there is strong re-hardening, it seems that the process of plasticity is made more difficult, which means fewer options to activate STZs and to find regions available for configurational changes (i.e. due to the aligned elongated chain configurations).

3.3.5 Failure

Fig. 3.11 (a) and Fig. 3.12 (a) show the dependence of the failure stress σ_f and of the failure strain ε_f on T/T_g, respectively. In both cases, a linear relationship can be identified by separating the data into subgroups. For σ_f, the 8552 resin is an outlier. As mentioned in the previous section, 8552 contains tough PES inclusions increasing its re-hardening capacity and failure resistance. Still, for σ_f, setting aside 8552, the lower subgroup presents a clear correlation with T/T_g for all resins. In addition, the slope of the regression is almost equal to the one of 8552. This indeed suggests a dependency on T/T_g. However, the correlation of the subgroup is far from perfect (R^2 around 0.5). This may not be surprising, as failure is in principle dictated by pre-existing defects, whose presence should not affect T_g. Chevalier et al. [74, 75] extensively studied the failure of RTM6 and determined that the failure is triggered by the attainment of a local critical stress value σ_c in the vicinity of an internal defect, which can be a cluster of voids [288], both in tension and in compression (which is naturally larger than the overall σ_f value), explaining the pressure dependence of σ_f in epoxy resins.

Additionally, they found that $\sigma_c = 300$ MPa and is valid for all test temperatures. Regarding ε_f, the same two subgroups as for G_h can be identified, namely the separation between higher and lower T_g systems. Each group presents a linear correlation (R^2 around 0.7) with T/T_g with similar slopes. The lower T_g resins have a higher failure strain, which appears to be related to their low re-hardening capacity. The natural explanation is that lower stress levels build up and, assuming failure is stress driven in epoxies [74, 75], larger ε_f are attained.

To put this criterion into context within this analysis, Fig. 3.11 (b) and Fig. 3.12 (b) show the dependence of the ratio σ_f/σ_y and $\varepsilon_f/\varepsilon_y$ on T/T_g, respectively. The ratio $\varepsilon_f/\varepsilon_y$ for each resin presents an increasing slope with T/T_g, partly due to the decrease of ε_y with T/T_g and partly because of the necessity to reach sufficiently high stresses to cause failure. In addition, the ratio σ_f/σ_y for each resin presents a similar slope with T/T_g, but shifted upwards for the higher T_g systems Hence, the combination of lower initial yield stress at higher T/T_g and temperature independent re-hardening capacity lead to larger deformations required to locally reach the σ_c of the epoxy.

3.4 Final discussion and conclusion

Linear relationships have been established between several key characteristic parameters describing the mechanical response of six different epoxy resins, tested at different temperatures and strain rates, and the corresponding ratio T/T_g. The coefficients describing each property in the form of $\gamma = a\ T/T_g + b$ are summarised in Table 3.2 and are readily available for first-order modelling of the mechanical response of highly cross-linked epoxies solely based on the T_g and under the assumption of a limited influence of the strain rate. In addition, Eq. 3.4 for the modulus and Eq. 3.6 for the yield stress fully account for temperature and strain rate and predict the yield stress of a highly cross-linked thermoset solely based on the knowledge of the T_g.

Property γ	a	b
E_c [MPa]	-4050	5475
σ_y [MPa]	-364	309
ε_y [-]	-0.17	0.21
σ_l [MPa]	-298	314

Table 3.2: Coefficients of the linear relationships describing each property of interest with respect to T/T_g.

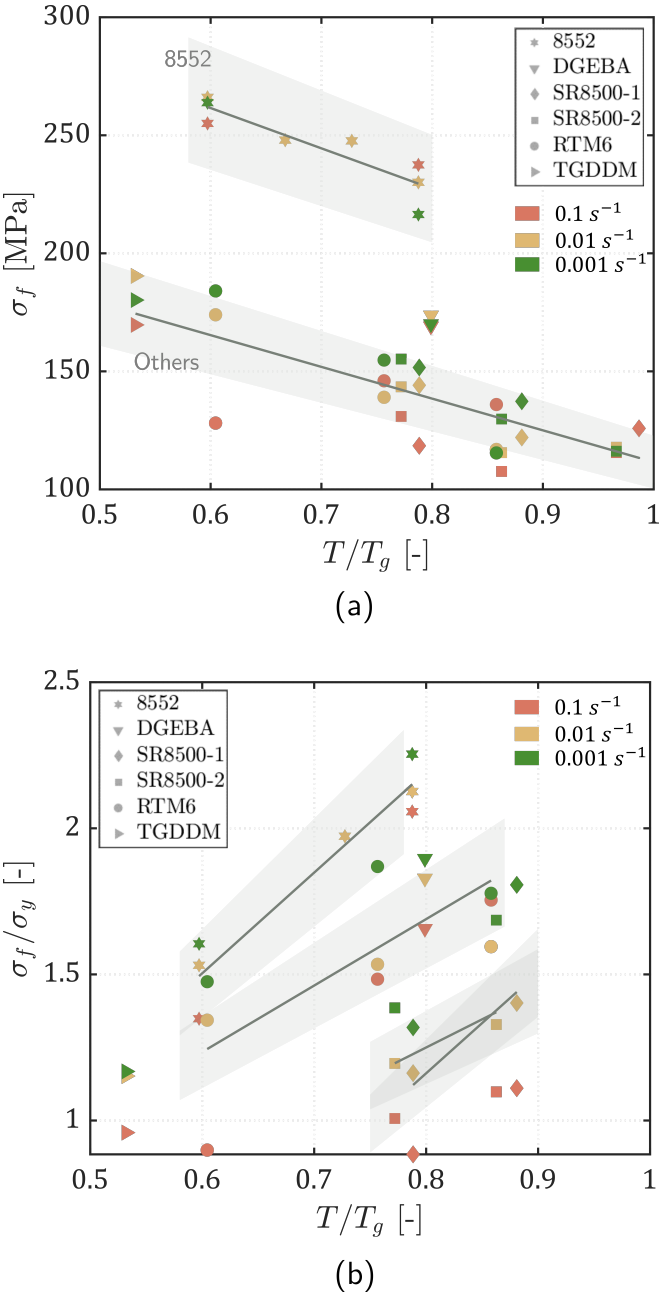


Fig. 3.11: Variation of (a) the failure stress σ_f ($R^2 = 0.3$) and (b) the ratio σ_f/σ_y as a function of T/T_g.

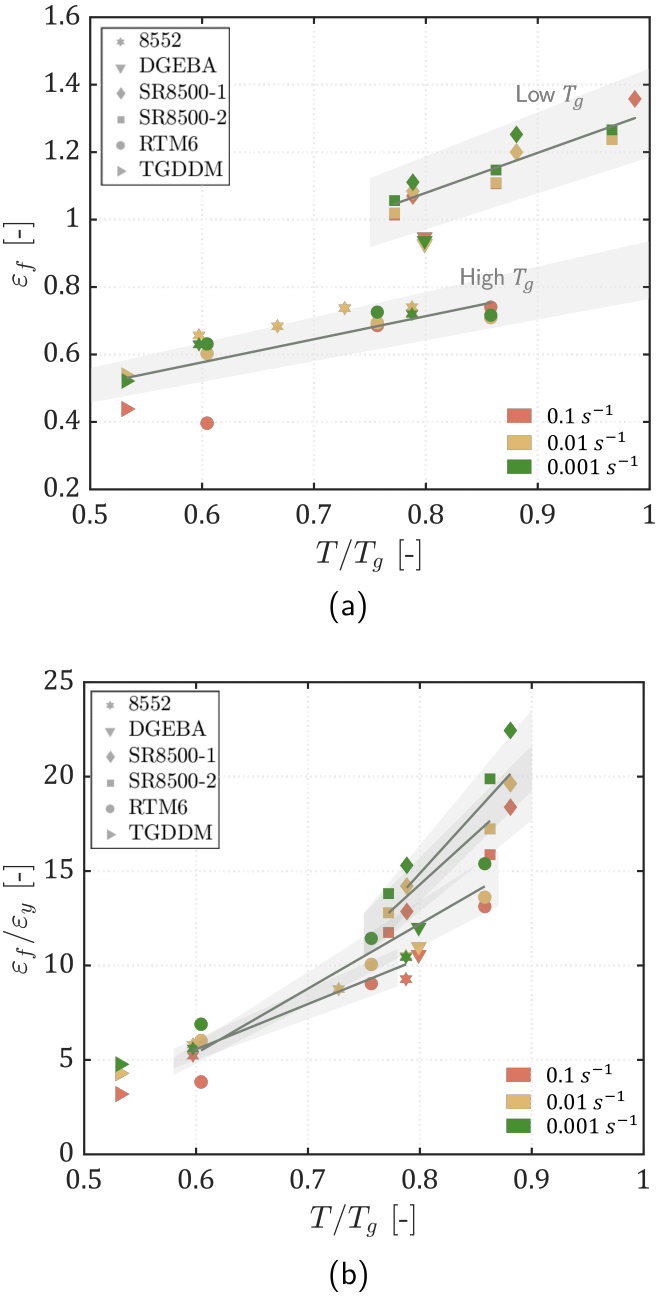


Fig. 3.12: Variation of (a) the failure strain ε_f ($R^2 = 0.68$) and (b) the ratio $\varepsilon_f/\varepsilon_y$ as a function of T/T_g.

The fact that the T_g is such a dominant marker that sets the magnitude of elastic modulus and strength is not a surprise and can be readily understood from a molecular description of the deformation mechanisms of polymers in the glassy state. What is more surprising is that such a first-order connection with T_g also remains true for the fracture strain (especially when normalised by yield strain). The fracture strain also follows a connection to T_g, but this connection seems to depend on the re-hardening modulus and on the factors influencing the re-hardening. The re-hardening modulus is the only parameter that cannot be rationalised with T_g. Nonetheless, the data collapse into two subgroups, based on the value of T_g suggesting a first order effect of a molecular parameter not directly influencing the magnitude of T_g. In other words, T_g is very much an aggregated signature of the resistance of chain segments towards distortion whether small and elastic or larger with some degree of irreversibility. About this last point, it is important to remember that even heavily deformed (50% or more) epoxy systems, if heated next to T_g, almost entirely recover the initial undeformed state, indicating that the "plastic" deformation is not totally irreversible like in a metal.

A question at this stage could then be to determine what is the best epoxy among all the systems that have been tested? There is no absolute answer to this question. As for almost all material classes, larger strength (and stiffness) is accompanied by lower fracture strain, as shown Fig. 3.13. The requirements associated to different specific applications will be decided based on the constraints: the load to be carried, the maximum allowable deflection, the temperature of operation, the maximum deformation, etc. Obviously, there are systems in Fig. 3.13 which are clearly dominated by others, meaning with both σ_f and ε_f larger at the same temperature. One could envisage, as a next step of the analysis, applying a rational materials selection procedure following Ashby's method [1], to the data as, for instance, recently pursued for adhesive systems (often thermosets with lower cross-linking density) [289]. However, it would then be highly relevant to pursue the present effort and extend it to the mapping of fracture toughness and fatigue resistance.

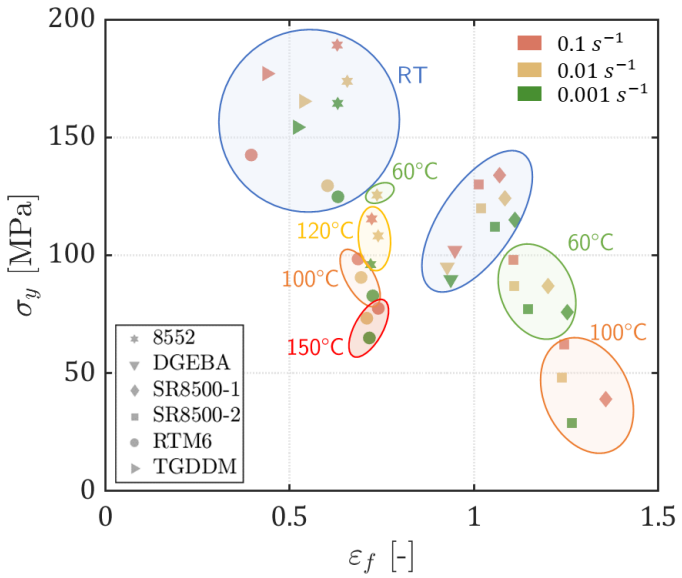


Fig. 3.13: Upper yield stress σ_y as a function of failure strain ε_f for all epoxies at different strain rates and temperatures.

When using epoxies as matrices for composites, many recent studies have revealed the need to get a better insight into the local mechanical response at the fibre/matrix scale [76, 126, 226, 290, 291]. Even if globally the strains often remain small (except for specific loading conditions, such as shear), locally the matrix can reach extremely large strains, especially within tiny shear bands, and characteristics such as the softening amplitude, the re-hardening modulus and the true fracture strain matter. There is still room for advanced modelling studies to understand better, using STZ models or MD simulations, the connection between molecular arrangement and configurations, the fracture strain or re-hardening modulus and the T_g. This could also guide the formulation of improved epoxy systems concerning the large strain behaviour.

3.5 Appendix

3.5.1 Curing cycles

The curing cycles for RTM6 and 8552 differ from the manufacturer's protocols. In this work, a third curing step was required. The reason was the desire to manufacture thick specimens. As the curing reaction is exothermic, the curing cycle was adapted to prevent an exotherm to occur during the preparation of thick specimens. Further details can be found in the work of Morelle [7].

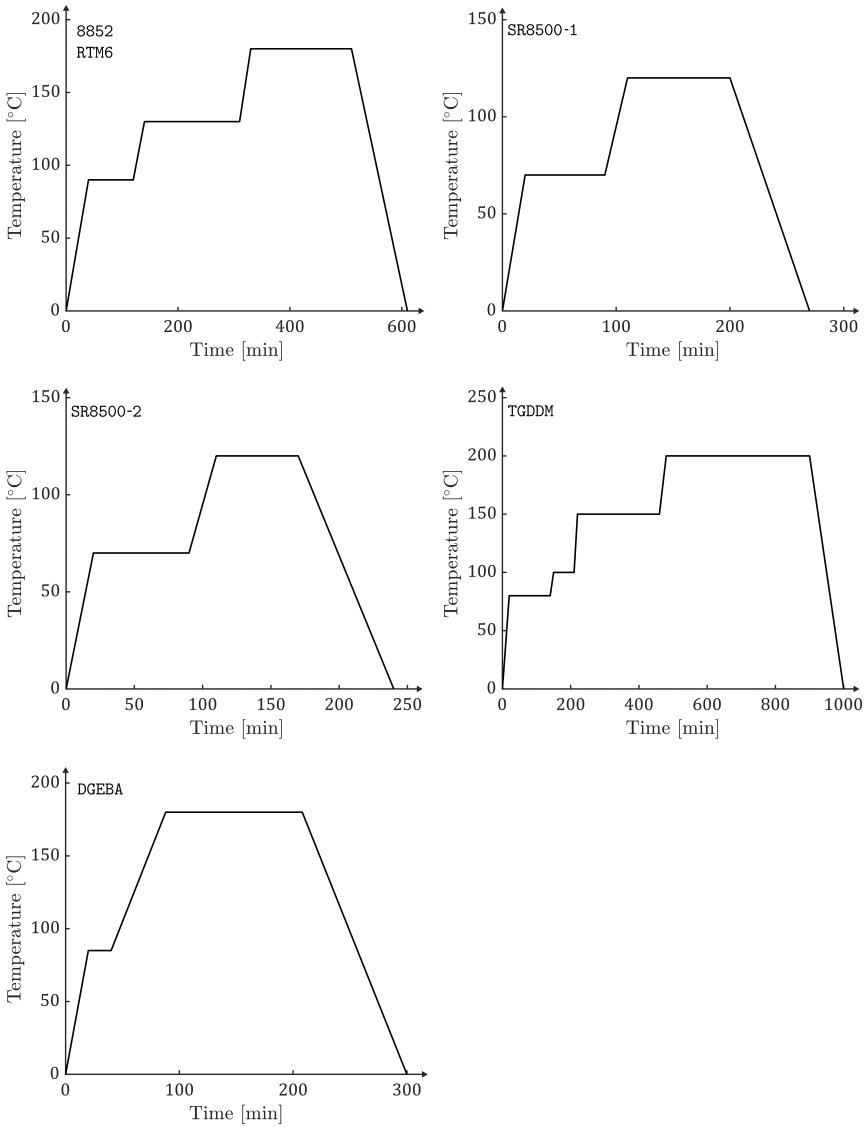


Fig. 3.14: Curing cycles of all the epoxy resins, which may differ from the manufacturer's protocols. Refer to references in section 3.2 for more details.

3.5.2 Stress-strain curves

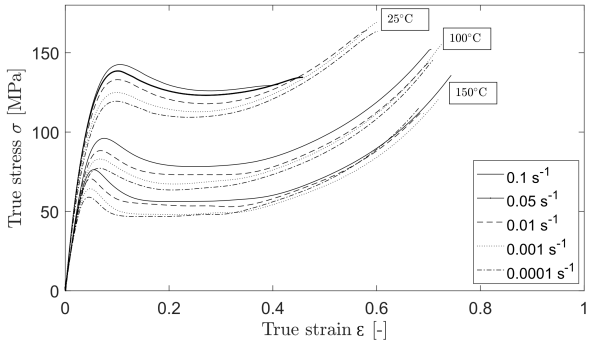


Fig. 3.15: Stress-strain curves for RTM6.

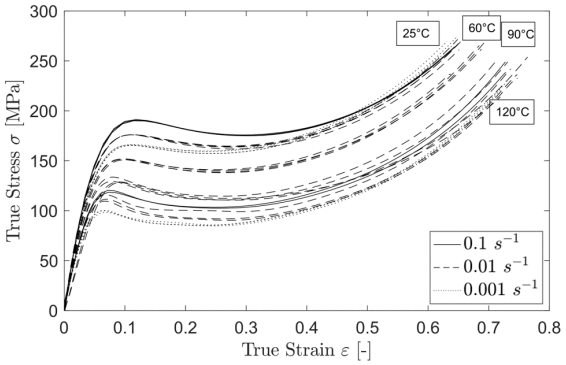


Fig. 3.16: Stress-strain curves for 8552.

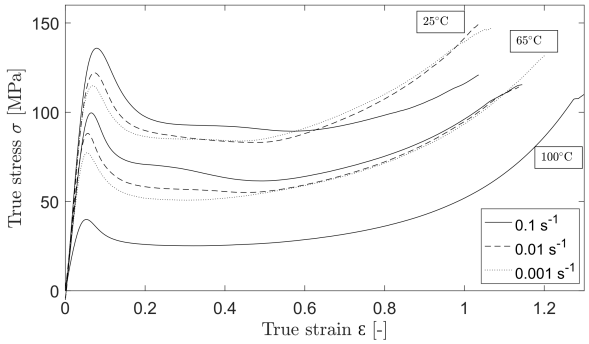


Fig. 3.17: Stress-strain curves for SR8500-1.

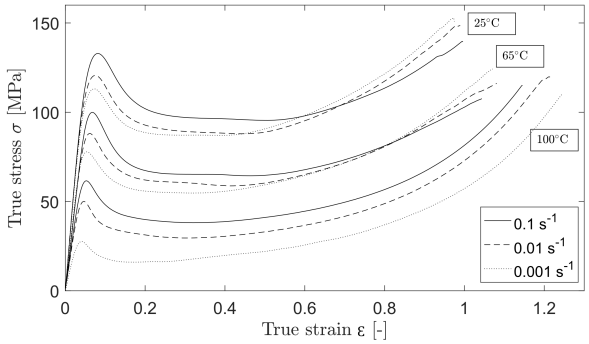


Fig. 3.18: Stress-strain curves for SR8500-2.

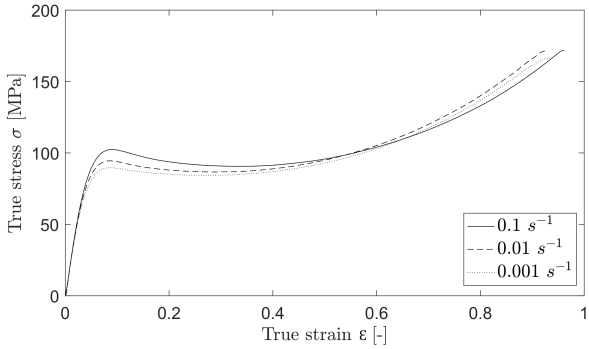


Fig. 3.19: Stress-strain curves for DGEBA at 25°C.

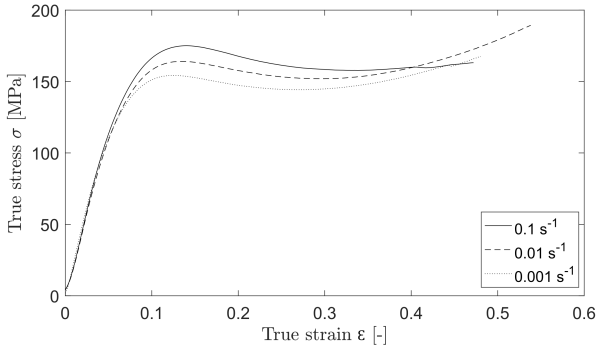


Fig. 3.20: Stress-strain curves for TGDDM at 25°C.

3.5.3 Compressive modulus determination

The compressive modulus has been determined following the ASTM D695 standard. A correction for the machine compliance has been systematically applied to the raw displacement data. Additionally, the initial curve toe has been corrected by applying the procedure detailed in ASTM D695, as illustrated in Fig. 3.21: a linear regression is made on the linear part of the stress-strain curve, which is then shifted such that the regression starts at the origin of the graph. This procedure minimises the error on the compressive modulus determination.

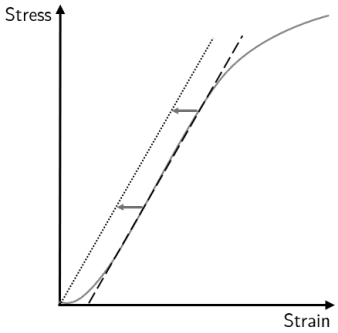


Fig. 3.21: Methodology to remove initial curve toe, as per ASTM D695.

4

Nanoscale digital image correlation at elementary fibre/matrix level in polymer–based composites

Abstract

Multiscale mechanical modelling aims at predicting the failure of composites from the fibre/matrix level up to the component scale. Existing frameworks are limited by the lack of reliable experimental data and by an incomplete understanding of the submicron deformation and failure mechanisms. A novel digital image correlation (DIC) method has been developed for the characterisation of the nanoscale mechanical response in composites, based on latest advances in surface patterning. Indium has been deposited on unidirectional composites leading to a dense, homogeneous speckle with particle diameter around 15 nm. The specimens were subjected to transverse compression in a scanning electron microscope, while minimising distortion effects. Strain concentration areas, like submicron shear bands and fibre/matrix interphases, were successfully captured for two systems: a carbon fibre-reinforced thermoset and a glass fibre-reinforced thermoplastic. DIC results were compared with alternative experimental data, obtained by atomic force microscopy, and with finite element simulations based on a conventional elastoplastic model.

Klavzer and Gayot et al. Composites Part A 168 (2023)

4.1 Introduction

Quantitative submicron scale experimental data about the deformation and failure of fibre-reinforced polymer (FRP) composites at the matrix/interface/fibre level is currently missing, preventing a full understanding of the local mechanics and impeding the development of enriched micromechanical models. Bottom-up multiscale mechanics approaches are indeed at the core of the advanced design strategy of fail-safe composite structures [262]. Available finite element (FE) numerical frameworks rely on experimental results for modelling the behaviour of FRPs at the micro- (ply level), meso- (laminate level) and macro- (part level) scales [90]. While macro- and mesoscale properties are relatively straightforward to extract using classical mechanical tests, the response at the microscale has yet to be fully explored especially in terms of quantitative mechanical behaviour data. Evidence shows that neglecting the local fibre/matrix behaviour, such as possible size effects, the presence of an interphase of different nature, local variations in polymer structure and/or constraint effects on local shear banding, significantly limits the accuracy of numerical predictions, particularly in loading conditions where the matrix is the main carrier of deformation (i.e. transverse compression or shear) [76]. In other words, one cannot 'simply' rely on the bulk polymer mechanical response and known fibre behaviour to model the microlevel.

A number of experimental approaches are available to address the local matrix, fibre/matrix interface and interphase characterisation, see recent review [146]. Nanoindentation has been widely used to characterise both bulk polymer glasses and 'confined' matrices within FRPs [111, 151, 153, 168, 217, 290, 292]. Although the interpretation of experimental load-penetration curves in small matrix pockets remains controversial, the properties determined by nanoindentation very often differ from those extracted from macroscale tests. The local strength in FRPs tends to be 15-20% higher compared to bulk samples, while stiffness is also often found to be larger within inter-fibre matrix regions. Nanoindentation data have been used to either determine the underlying deformation mechanisms or to feed FE models [163]. Atomic force microscopy (AFM) has been applied to FRPs to determine local heterogeneities and to map the size of the interphase region around the fibres. The local property landscape in polymer glasses is systematically heterogeneous and the size of the interphase is found to be ranging from a few tens of nanometres up to a few microns [197, 199, 200, 293]. However, nanoindentation and AFM do not provide information on the stress and strain fields during loading.

Recently, micro digital image correlation (DIC) has been adapted to the study of FRPs, aiming at characterising the local deformation processes [224, 225]. DIC is a non-contact method, which tracks the relative displacement of material points between two images. The strain field is then extracted from the displacement field [294, 295]. DIC can, in theory, be applied at any scale as

long as a suitable speckle pattern (used for the tracking) can be created or by using inherent material surface features. Although macro DIC is widely used by the composite community [296–298], the use of micro DIC remains scarce and nano DIC has, to the authors' knowledge, not been applied to FRPs yet.

Micro DIC on FRPs was first introduced by Canal et al. [224]. In-situ transverse compression tests were performed within a scanning electron microscope (SEM) on unidirectional (UD) composite samples to favour matrix plasticity. A fine alumina dispersion was used to track displacements. The potential of micro DIC was demonstrated by qualitatively mapping the strain fields over the region of interest (ROI), in accordance with FEA predictions. Inter-fibre strain localisation was also detected, however the overall strain measurements for each phase were inaccurate due to averaging by the correlation algorithm linked to speckle coarseness. Subsequent studies by Mehdikhani et al. [225, 226] showed that micro DIC is also capable of clearly identifying regions of strain concentration or even the presence of carbon nanotube clusters. Yet, the authors pointed out the importance of evaluating the error resulting from the speckle pattern quality, DIC analysis parameters and SEM-related effects (e.g. charging, spatial and drift distortion, etc.). Hence, the speckle pattern quality is the primary factor limiting the quantitative use of micro DIC at the fibre/matrix level. More recently, Chevalier et al. [76] performed an extensive experimental and numerical study on the transverse compression of UD specimens. The DIC maps did not match the FE predictions obtained with a classical continuum model in confined regions between fibres, where the FEA largely overestimates the strain amplitude. The key conclusions from these studies are, on the one hand, that the accuracy of micro DIC is mainly limited by the speckle pattern quality and SEM artefacts and, on the other hand, that macroscale continuum models are unable to quantitatively capture the microscale deformation behaviour in confined volumes.

In order to extract quantitative information from micro DIC, issues related to the speckle pattern and SEM have to be addressed. Improving the speckle pattern quality has been a point of interest for many material systems [295, 299, 300]. The goal is to obtain a high contrast and dense speckle pattern with a submicron speckle size, which significantly increases the spatial resolution of the DIC analysis. Hoefnagels et al. [301] recently proposed a novel approach allowing for a resolution of a few tens of nanometres, hence justifying the use of the "nano DIC" terminology. The method relies on the ability of some metals to create thin films from the nucleation, growth and coalescence of nanometric clusters or 'islands' (Volmer-Weber growth mode). This particular growth mode is observed when adatoms have a high diffusion length on the substrate surface, which may be achieved by depositing a metal (or alloy) with a low melting temperature, while providing high kinetic energy to the deposited atoms via low-pressure deposition methods, e.g. physical vapour deposition (PVD) [301,

302]. Hoefnagels et al. showed that the physical vapour deposition of certain indium-based solder alloys by magnetron sputtering yields the formation of speckle patterns with controlled morphologies (i.e. particle shape, size, and density) on metallic substrates, without requiring substrate heating. This method was successfully used to quantify strain localisation – and thus predict failure location - in polycrystalline iron foils [301].

Nevertheless, a high-resolution speckle is not sufficient to guarantee the overall spatial resolution of DIC measurements, which also depends on the accuracy of the imaging technique. In the case of in-situ mechanical tests performed in a SEM chamber, so-called image distortions (i.e. deviations with respect to the 'ideal' image positions [303]) can occur and eventually give rise to spurious displacements and thus invalid extraction of strains. SEM-related distortions may be separated into space- and time-dependent effects, as proposed by Sutton et al. [303, 304] and other subsequent studies [305–307]. Spatial distortions (e.g. due to lens aberrations) do not evolve over time, unlike temporal or 'drift' distortions. The latter may arise from the components making up the SEM or even charging of the imaged material. Positioning errors of the electron beam during scanning, referred to as 'scan line shifts' [295, 303, 306], may also fall under this category, but their impact on DIC measurements has not been extensively studied in the literature – probably because they give rise to highly recognisable line patterns on DIC strain maps.

Spatial distortions have been shown to remain relatively constant throughout a given experiment and to be more prevalent at low magnifications, meaning that the effect on micro or nano DIC should be limited [308]. Drift distortions, however, are more significant at high magnifications, and can induce large overestimations in the measured displacements. Several methods have been proposed to correct for drift distortions, but the simplest approach consists in taking pairs of images at each step during in-situ testing and evaluating the relative shift between them [308]. When the material presents strong stress relaxation, as in polymer glasses, accounting for the effect of stress relaxation on the drift is key and can lead to degraded DIC measurements if not properly dealt with [308]. An alternative approach is to improve the correlation algorithm to take into account such artefacts, as done in [305, 307].

In this study, we combine the latest advances in patterning techniques for micro and nano DIC with in-situ transverse compressions on UD FRPs in order to reveal, for the first time, fine details of the local deformation and failure of the constituents at the fibre/matrix level. This application of nano DIC on FRPs has been made possible by adapting the speckle deposition technique developed by Hoefnagels et al. [301]. Here, we simplify the approach by using electron beam (e-beam) evaporation of pure indium, where only the deposition time (and hence the particle size) can be controlled. The resulting dense and

homogeneous nanoscale pattern exhibits particle sizes ranging from 10 nm to a few hundred nm. This pattern is applied to two types of FRPs: a glass fibre-reinforced thermoplastic and a carbon fibre-reinforced thermoset. It allows overcoming the main challenge of low-scale DIC on FRPs, which is the accurate separation of the displacements and strains in each of the constituents. In particular, the size of the matrix-modified interphase region around the fibres can be measured, which was impossible so far due to the averaging within the DIC algorithm linked to an insufficiently fine speckle pattern. The methodology adopted to minimise the impact of SEM-related distortions is also presented in this paper. The results are first compared to AFM data and then to FE predictions made using a continuum model with pre-identified parameters for the matrix.

4.2 Materials and experimental methods

4.2.1 Manufacturing of composite specimens

Glass fibre-reinforced thermoplastic composites

UD glass fibre-reinforced thermoplastic (TP) composite samples were provided by Arkema (France). The thermoplastic matrix comprised a pultrusion-grade methyl methacrylate-based monomer formula, Elium 591 (Arkema), and 1 part per hundred ratio of the following peroxide thermal initiators: Perkadox 16 (Nouryon, the Netherlands), Trigonox 141 (Nouryon) and Luperox DEC (Arkema). 2400-tex SE 4740 glass rovings (3B-The Fiberglass Company, Belgium) were used as reinforcement. Continuous unidirectional composite profiles with a final thickness equal to 2 mm and fibre volume fraction (V_f) close to 65% were produced by pultrusion. Parallelepipedic specimens of dimensions 4×2×3 mm^3 were machined using a water-cooled disc milling cutter, as shown in Fig. 4.1 (a). The choice of specimen geometry and dimensions was driven by two factors: (1) the limitation associated to the 2 mm-thick UD composite samples manufactured industrially by Arkema and (2) the features of the compression stage and SEM chamber used for in-situ testing, see section 4.2.3. More precisely, the z-dimension was matched with the groove depth of compression jaws (i.e. 3 mm) to optimize electric contact with the metal and minimize working distance during SEM imaging. Additionally, the strength of the specimen had to remain below the load limit of the compression stage, i.e. 2 kN.

Carbon fibre-reinforced thermoset composites

A UD carbon fibre-reinforced thermoset (TS) composite plate was produced by resin transfer moulding according to the procedure described in [76], using the monocomponent HexFlow RTM6 resin from Hexcel (CT, USA) and HTS 12k carbon fibres (Saertex Gmbh, Germany). The final V_f value was close to 40%.

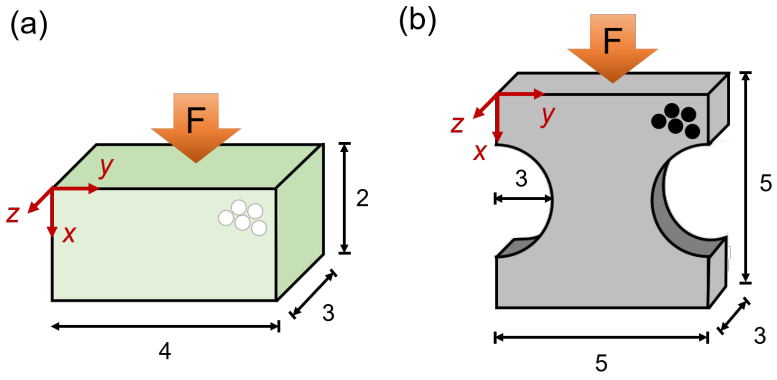


Fig. 4.1: Unidirectional composite specimens for in-situ transverse compression testing: (a) glass fibre-reinforced TP and (b) carbon fibre-reinforced TS. Fibre orientation is parallel to the z-axis and compression is performed in the x-direction. All dimensions are in mm.

Parallelepipeds of dimensions 5×5×3 mm^3 were machined using a water-cooled disc milling cutter, and two notches were drilled parallel to fibre orientation as shown in Fig. 4.1 (b). In this case, specimen geometry and dimensions had already been determined by Chevalier et al. [76] so as to remain within the limits of the compression stage load cell (see section 4.2.3) and induce stress concentration during testing. Note that different geometries and fibre volume fractions were used for the carbon fibre-reinforced TS and the glass fibre-reinforced TP transverse compression specimens, for the practical reasons mentioned above. However, this should not compromise the comparability of DIC measurements between the two systems, as the nature of nanoscale plastic deformation and failure phenomena occurring between fibres in a given system depends mostly on the local fibre arrangement within the ROI (i.e. inter-fibre distance, fibre diameter and orientation of the inter-fibre matrix strip with respect to the unidirectionally-applied load).

Polishing of composite surfaces

Both types of composite specimens were polished perpendicular to the fibre orientation (i.e. z-axis) on a semi-automatic MultiPrep Precision Polishing System (Allied High Tech Products, USA). Resin-bonded diamond discs with successive grit of 1200 and 4000 (MD-Piano from Struers Inc., OH, USA) were used for grinding, while finishing was performed with a 0.3 µm alumina suspension (AP-D Suspension 0.3 µm, Struers Inc.).

4.2.2 Speckle pattern deposition

The protocol developed by Hoefnagels et al. [301] for depositing nanometric DIC speckles onto metallic specimens by PVD was simplified and applied to polymer composite substrates as follows. Indium deposition was performed by e-beam evaporation, using indium pellets with a purity of 99.99%. The deposition rate was kept equal to 1 Å.s^{-1} and the operating pressure never exceeded 4×10^{-7} mbar. The influence of the deposition time on speckle pattern morphology was assessed using silicon wafers as the substrate material. More precisely, several deposition times were tested, in order to produce the following target coating thicknesses: 2 nm, 5 nm, 10 nm, 20 nm and 50 nm. The results of this preliminary study are presented in section 4.3.1. Note that indium was selected among the list of commonly evaporated materials for several reasons. First, pure indium has a low melting point under standard temperature and pressure conditions (around 157 °C [309]), which should favour the formation of metal 'islands' on the substrate material instead of a continuous film during PVD, as mentioned previously [301]. It is also chemically inert to air and water under ambient conditions, which guarantees the stability of the coating between the deposition and imaging steps. Metallic indium is easily available and relatively inexpensive compared to other metals used for e-beam evaporation [310]. Lastly, human toxicity of metallic indium is low under occupational conditions [311].

4.2.3 SEM imaging and in-situ compression testing

Imaging of Indium-coated Si-wafers

An Ultra 55 Field-Emission SEM (Zeiss, Germany) was used for imaging the indium speckle patterns deposited onto Si wafers, see section 4.3.1. The acquisition parameters were similar to those applied during the in-situ compression testing of composite specimens, see below.

Preparation of composite specimens for SEM imaging and mounting on compression stage

Unwanted charging effects arise when poor electric conductors, like polymer composites, are imaged by SEM. As detailed in section 4.2.4, charging may be detrimental to image quality (especially at high magnifications) and can ultimately lead to surface degradation, impacting in turn the accuracy of DIC measurements. Following indium deposition, polished composite surfaces were therefore subjected to carbon sputtering, and all other free surfaces were coated with a thin layer of silver lacquer. Composite specimens were mounted on a microtest compression stage equipped with a 2 kN load cell (Deben UK Ltd., UK) and further placed inside the chamber of an Ultra 55 Field-Emission SEM. Fig. 4.2 shows the experimental setup ready for insertion in the SEM.

Compression testing and acquisition of DIC data

For each specimen, one or two zones of interest were selected for DIC measurements and imaged with a 5.7×4.3 μm^2 and a 11.4×8.6 μm^2 field of view (i.e. at a magnification of 20,000 and 10,000 in our case), and a pixel size close to 6 and 12 nm, respectively. Acceleration voltage was kept in the 2-4 keV range to limit charging effects. When needed, contrast and brightness values were adapted during the test in order to counter the progressive darkening of SEM images induced by remaining charging effects and carbon contamination.

Each region of interest (ROI) was imaged before and during uniaxial compression along the x-axis. Loading was performed using 50 to 100 N increments, in between which the stage motor was stopped. SEM images were taken at each load increment after the specimen was left to relax until the load drop over a two-minute period (i.e. average time to take two successive SEM images) was less than 1 N (see section 4.2.4 for further details). Compression was continued until macroscopic fracture of the specimen.

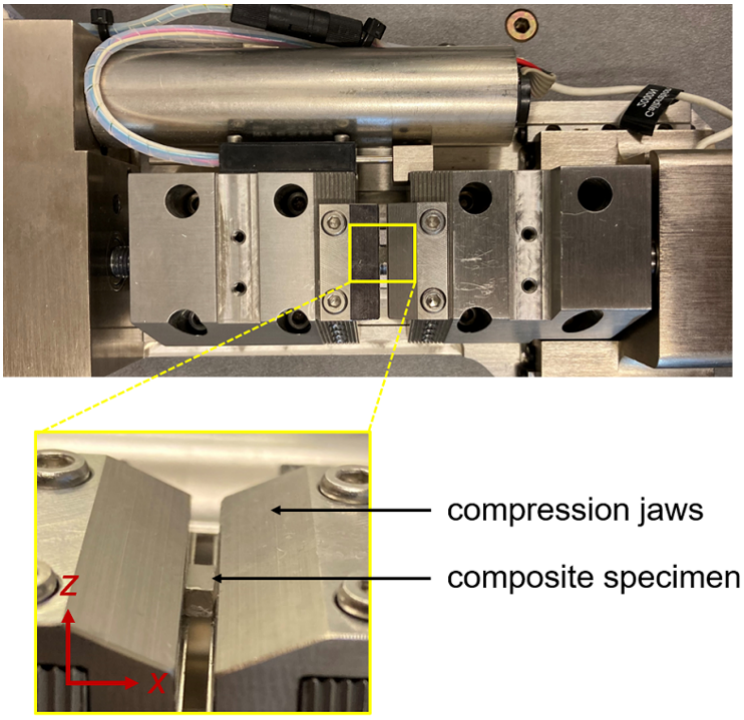


Fig. 4.2: Thermoplastic composite specimen mounted on microtest compression stage.

4.2.4 DIC data processing

Image analysis

The size distribution of indium particles deposited on silicon wafers and composite specimens was assessed using the open-source software ImageJ. SEM images were subjected to binary thresholding, and a watershed segmentation algorithm was applied to separate any spuriously connected particles. The built-in particle analysis tool of ImageJ was run, and the resulting data were processed with Matlab. A sample size of at least 1,000 particles was used for each case.

DIC measurements

The DIC analyses were carried out using the open-source software Ncorr [221], which relies on three input parameters: the subset size, step size and strain radius value. The 'subset' refers to a group of pixels in which strains are assumed to be homogeneous, while the 'step' denotes the spatial shift between two adjacent subsets. The value of the strain radius indicates the size of the smoothing filter applied when converting displacement fields into strain fields. Note that the choices of subset and step sizes condition the spatial resolution of calculated displacements, while that of strain radius impacts the level of numerical noise in the final strain maps. The systematic approach of Mehdikhani et al. [225] was followed in order to find a suitable combination of input parameters with respect to (1) the morphology of the speckle pattern and (2) the quality of the SEM images obtained in this work. More precisely, a well-speckled zone of an undeformed TP composite specimen was imaged by SEM at the magnification levels of interest for DIC, i.e. 10,000 and 20,000. The images, of respective dimensions 991×673 px^2 and 828×612 px^2, were then numerically stretched by 10 px in the x-direction using the lanczos3 tool of Matlab. The extracted uniaxial strains ε_{xx} were close to the expected values of 0.0101 and 0.0121, respectively. For both levels of magnification, DIC measurements were performed between the original and stretched SEM images, with different sets of subset size, step size and strain radius values. The values obtained by DIC for the mean strain (and corresponding standard deviation) were compared to the theoretical values of ε_{xx} mentioned above. The results of the strain deviation analysis are presented in section 4.3.1.

As mentioned in the introduction, SEM imaging induces spatial and drift (i.e. temporal) distortions. Kammers et al. [308] proposed a straightforward method for addressing both types of artefacts without modifying the DIC algorithm. First, to correct spatial distortions for each sample, a series of four overlapping images in the horizontal (u) and four images in the vertical (v) directions are taken over a defined distance. In addition, at each displacement increment, a pair of images is taken to correct for drift distortions (i.e. see below). The total applied displacement increment should be selected so that the total displacement

in each direction does not exceed 25% of the field of view of the DIC analyses. However, the smallest possible translation within this study was limited to 1 µm due to the SEM stage accuracy. Since the imposed displacement is known (from the rigid body motion principle), it can be subtracted from the calculated displacement fields, resulting in so-called 'spatial distortion maps'. A linear relationship relating the amplitude of the distortion in the u and v directions and the imposed translation is extracted from the results. This function may be used as a correction tool for spatial distortions, which takes, as input, the u and v displacements at each point of the DIC fields. Second, drift distortions can be measured by taking two consecutive images at each load increment. For each pair of SEM scans, the calculated DIC maps are subtracted from one another. The resulting difference in displacement amplitude over the ROI determines the error related to drift distortions. The horizontal and vertical displacement drift maps are then subtracted from the actual DIC displacement maps to get drift-free maps. Finally, the impact of stress relaxation was determined on the two consecutive images used for drift correction. The evolution of the load as a function of time was monitored during image acquisition. Hence, each pixel may be related to its acquisition time and the corresponding load value, resulting in so-called 'load maps'. In this study, the composite specimens were systematically left to relax in between load increments, so that the load drop never exceeded 1 N during the acquisition of two consecutive images. The corresponding error on DIC strain measurements was found to be negligible, as shown in Fig. 4.20 in the appendix of this chapter.

4.2.5 Atomic force microscopy

Micromechanical analysis of the Elium and RTM6 composite systems by AFM was performed on Dimension Icon and MultiMode 8 systems (both from Bruker Corp., USA), using PeakForce Tapping-QNM mode [40] and a factory-calibrated RTESPA-300-30 probe (Bruker). The cantilever spring constant and nominal tip radius values were respectively close to 50 $\mathrm{N.m^{-1}}$ and 30 nm. AFM scans of dimensions 6×6 $\mu\mathrm{m}^2$ were acquired with a resolution close to 47 $\mathrm{nm.px^{-1}}$. The PeakForce frequency and amplitude parameters were respectively set to 0.5 kHz and 30 nm for Elium, and 1 kHz and 25 nm for RTM6. In both composite systems, the PeakForce setpoint was selected in order to achieve a 2 to 3 nm indentation depth in the resin. In these conditions, the contact radius remained smaller than 10 nm. The selected PeakForce setpoint values were equal to 150 nN for Elium and 100 nN for RTM6. Modulus images were obtained from the built-in Derjaguin-Muller-Toporov calculation tool of NanoScope 9.4 (Bruker). More information on the acquisition method is presented in [142] for the Elium composite system.

4.2.6 Finite element modelling

Finite element analyses were carried out using the commercial software Abaqus [312]. The models were created using the exact same geometries as the experimental ROIs. The applied boundary conditions were determined from the displacement profiles measured by DIC on the edges of the respective ROIs. 2D plane stress elements (CPS3) were used for the meshing of the fibres and the matrix to compare with the 2D DIC results. Table 4.1 presents the material properties used for the mechanical modelling of both composite systems. The carbon or glass fibres were considered as linear elastic. The thermoset matrix was modelled as rate-dependent elastoplastic using the constitutive continuum model identified and validated by Morelle et al. for RTM6 [12]. In brief, the pressure-dependent yield criterion for the matrix, used to account for the dependence of the polymer to the hydrostatic stress, was defined by a linear Ducker-Prager model, which writes as

$$F = t + p\tan\beta - d = 0, \tag{4.1}$$

where t is the yield stress, $p = \sigma_{kk}/3$ the pressure (with σ_{kk} the trace of the Cauchy stress tensor), β the friction angle and d the cohesion term. β defines the slope of the yield surface in the $p - t$ plane while t is expressed as

$$t = \frac{\sigma_{eq}}{2}\left[1 + \frac{1}{r} - \left(1 - \frac{1}{r}\right)\left(\frac{I_3}{\sigma_{eq}}\right)\right] \tag{4.2}$$

where σ_{eq} is the von Mises equivalent stress, r the stress ratio between the yield stress under tension and compression and I_3 the third invariant of the deviatoric stress tensor. The associated flow rule writes as $G = \sigma_{eq} + \sigma_{kk}/3\tan\phi$, with G the flow potential and ϕ the dilation angle. The isotropic hardening law was defined as the sum of three contributions: a pre-peak yield non-linearity, a softening term and a re-hardening capacity (the full description can be found in [12]). The strain rate dependence is considered via the coefficients of the hardening law. Following identification over six decades of strain rate, $r = 1$ and thus $t = \sigma_{eq}$, $\beta = 7.86$ and $\phi = 0$ (assuming plastic incompressibility). A similar model, calibrated for Elium by Maes [313] on four decades of strain rate, was used for the thermoplastic matrix. In that case, $r = 1$ and thus $t = \sigma_{eq}$, $\beta = 26$ and $\phi = 0$. Simulations were performed using Abaqus explicit to overcome convergence issues related to the softening of the matrix, which are difficult to solve with Abaqus Standard (implicit). Perfect interfaces were considered between the fibre and matrix materials, i.e. no damage mechanisms were considered.

	Carbon fibres	Glass fibres	RTM6	Elium
E_{11} [GPa]	238	80	3	2.8
E_{22}, E_{33} [GPa]	28	–	–	–
ν_{12}	0.28	0.22	0.34	0.35
ν_{23}	0.33	–	–	–
ν_{31}	0.02	–	–	–
ρ [g.cm^{-3}]	1.8	2.54	1.14	1.17

Table 4.1: Elastic properties of the fibre and the matrix materials used of the FE modelling of the TP and TS composite systems.

4.3 Results and discussion

4.3.1 Optimisation and validation of the DIC method

Optimisation of speckle pattern

In addition to providing excellent contrast during imaging, the ideal speckle pattern for a given DIC experiment should meet a number of requirements. The particles should be small with respect to the length scale of the mechanical phenomena of interest, while remaining larger than the image pixel size. Additionally, the distribution of particle sizes should be narrow and speckle density should be high, in order to avoid the presence of 'featureless' subsets in DIC. SEM micrographs of the speckle patterns obtained by e-beam evaporation of indium onto Si wafers for different target coating thicknesses (2, 5, 10, 20 and 50 nm, see section 4.2.2) are presented in Fig. 4.3, while the associated distributions of particle radii R are displayed as boxplots in Fig. 4.4. Fig. 4.3 shows the increase of the average particle size as more metal gets deposited, though the film remains discontinuous. Moreover, for coating thicknesses larger than or equal to 10 nm, the particles segregate into two distinct populations: the 'large ones' (for which $R \sim 100$ nm), and the 'small ones' (for which $R \sim 10$ nm). Note that the average radius of the larger particles increases from ~ 50 to ~ 100 and finally ~ 300 nm as the target coating thickness is raised from 10 to 20 nm and then to 50 nm, respectively. Fig. 4.4 confirms these trends, while providing quantitative information on the evolution of the statistical distribution of particle radii as the coating thickness increases. The plots corresponding to the 2 and 5 nm-thick coatings are short and symmetric (see Fig. 4.4 (b)). This indicates a narrow normal distribution for R values in both cases, making both coatings potentially eligible for DIC measurements. In this work, only the 5 nm-thick coating was used as a DIC speckle pattern. The 2 nm-thick coating was excluded from the study as the mean particle radius (close to 5 nm) was too close to the smallest pixel size used for SEM imaging (6 nm.px^{-1}, see section 4.2.4). From coating thicknesses of 10 nm onwards, the

boxplots get longer and more skewed towards the high R values. As described previously, this indicates the emergence of a second, more scattered population of 'large particles' arising from the coalescence of smaller ones. Note that the lower half of the plots (i.e. lower whisker, first quartile and median R values) only evolves marginally with the coating thickness. This suggests that the size distribution of the 'small particles' remains relatively unchanged. Finally, the selected deposition method developed on Si wafers was applied to a TS composite sample (CFRP) to assess the reproducibility of the speckle pattern on the substrate of interest. Fig. 4.5 shows the corresponding particle size distributions obtained on both materials. The difference in particle size between both substrates remains within the margins of error, consolidating the use of this method on polymer composite specimens.

Choice of DIC input parameters

Table 4.2 shows the results of the strain deviation analysis described in section 4.2.4. In all cases, the mean strain value obtained by DIC matches that of the numerically applied strain, with a standard deviation value at least one order of magnitude smaller. Note that this result also confirms the quality of the speckle pattern after optimisation (see section 4.2.3). The optimum parameters selected for the DIC calculations at both magnification levels were the following: a 10-px subset size (smallest possible size in Ncorr), a 2-px step size and a 5-px strain radius. This combination offers the highest possible spatial resolution for the strain maps, while limiting the amount of noise.

Magnification	Subset [px]	Step [px]	Strain radius [px]	Mean strain [-]	Std. dev. [-]
10,000	30	2	5	0.0101	5.07E-5
10,000	20	2	5	0.0101	8.33E-5
10,000	10	2	5	0.0101	2.10E-4
10,000	10	2	3	0.0101	3.59E-4
10,000	10	2	1	0.0101	7.99E-4
10,000	10	1	5	0.0101	3.20E-4
10,000	20	1	5	0.0101	1.09E-4
10,000	10	1	3	0.0101	4.90E-4
10,000	10	1	1	0.0101	1.10E-3
20,000	30	2	5	0.0121	4.65E-5
20,000	20	2	5	0.0121	7.47E-5
20,000	10	2	5	0.0121	1.50E-4
20,000	10	2	3	0.0121	2.37E-4
20,000	10	2	1	0.0121	5.40E-4
20,000	10	1	5	0.0121	2.32E-4
20,000	20	1	5	0.0121	9.45E-5
20,000	10	1	3	0.0121	3.38E-4
20,000	10	1	1	0.0121	7.79E-4

Table 4.2: Strain deviation analysis results obtained for various sets of DIC parameters.

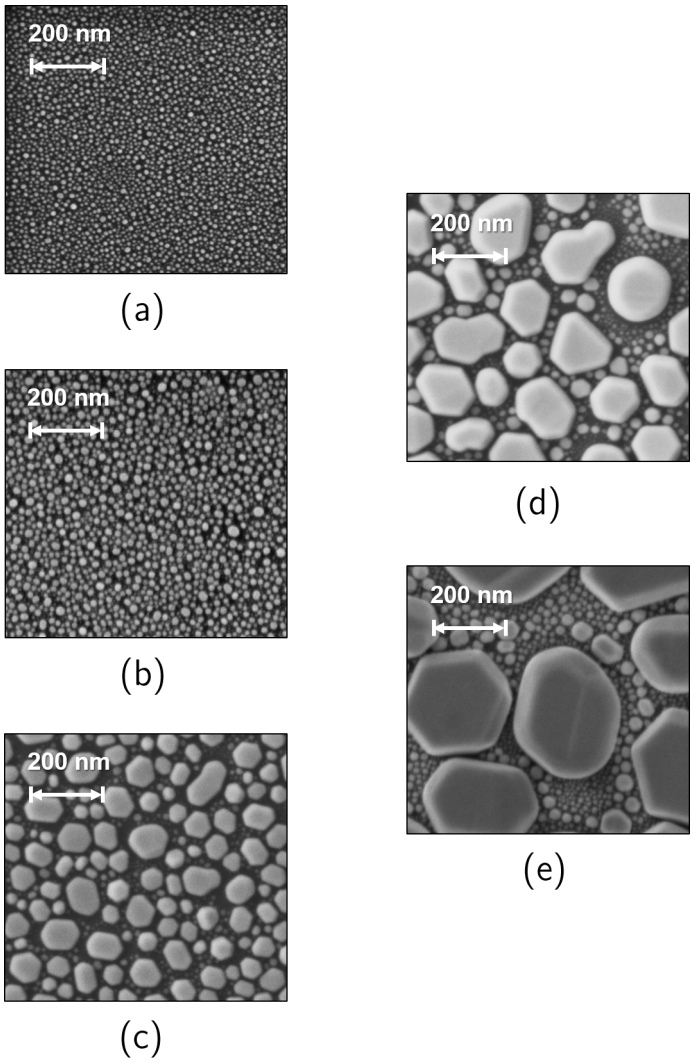


Fig. 4.3: Optimisation of the speckle pattern for DIC measurements: SEM images of a (a) 2 nm, (b) 5 nm, (c) 10 nm, (d) 20 nm and (e) 50 nm-thick indium speckle deposited by e-beam evaporation onto Si wafers.

Impact of SEM distortions

As mentioned in the introduction, drift and spatial distortions can cause significant errors in the displacements determined by DIC. Fig. 4.6 is a SEM micrograph showing a ROI that was subjected to a rigid body motion of -4 µm in the x-direction in order to quantify the amplitude of the distortions

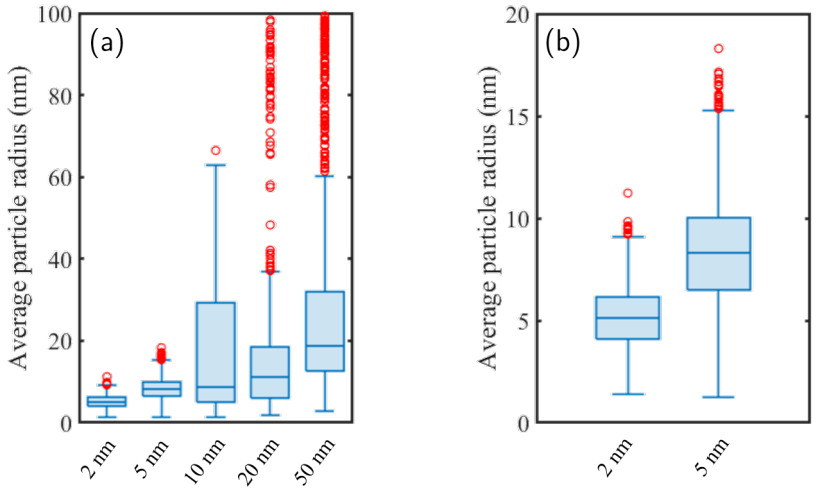


Fig. 4.4: Particle size distribution of indium speckle patterns with target thicknesses of (a) 2 to 50 nm and (b) 2 and 5 nm.

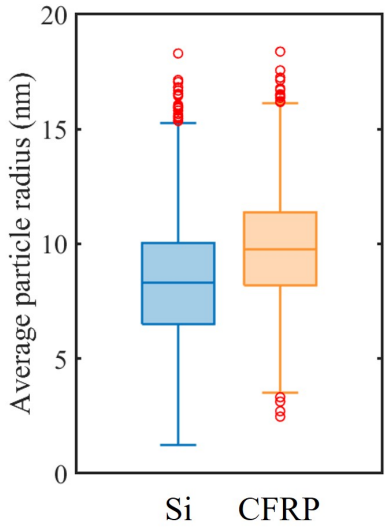


Fig. 4.5: Comparison of particle size distributions obtained for a 5 nm-thick indium speckle pattern deposited onto two different substrates: Si wafer vs. carbon fibre-reinforced TS composite.

described in section 4.2.4. The results of the DIC measurements and corrections are shown in Fig. 4.7. The initial DIC measurements shown in Fig. 4.7 (a) delivered a displacement of around -3.5 µm over the whole ROI. This represents a -0.5 µm discrepancy with respect to the imposed rigid body motion. First, spatial distortions coming from the SEM stage movements were corrected. The corrected displacement field shown in Fig. 4.7 (b) presents an average displacement over the ROI of -3.863 µm. The amplitude of spatial distortions is therefore close to -0.3 µm. Next, the drift distortion field between the initial and displaced states was determined and subtracted from the corrected field of Fig. 4.7 (b). The resulting distortion-free displacement field is shown in Fig. 4.7 (c). The average displacement over the ROI is now -3.9 µm. Comparing Fig. 4.7 (b) and (c) allows quantifying the amplitude of the drift distortion, which is around 0.04 µm. Typically, drift distortions are dominant at high magnification DIC applications. Yet, in the present case, drift distortions are relatively low. This can be related to an excellent grounding of the composite samples via the combination of the conductive carbon coating, evacuating the surface charges, and the silver paste covering the edges of the sample to guide the charges away via the test machine. Thus, proper sample preparation allows overcoming one of the key challenges of nano DIC linked to the excessive amount of drift.

Ultimately, neglecting corrections on DIC measurements for both spatial and drift distortions can induce, at most, an error of around 0.5 µm in the present study. In what follows, the presented DIC maps are systematically corrected for both spatial and drift distortions.

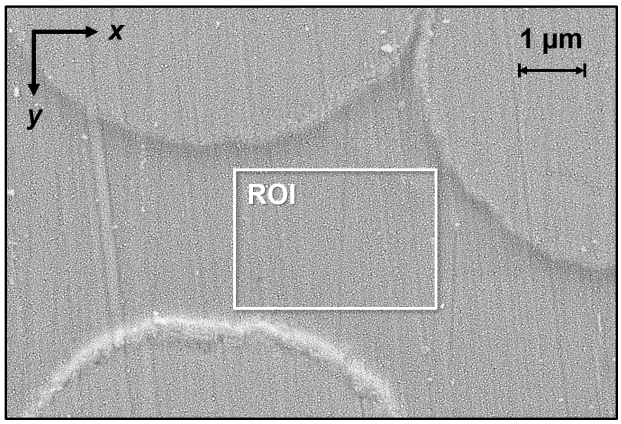


Fig. 4.6: Region of interest for the quantification of the spatial and drift distortion amplitudes.

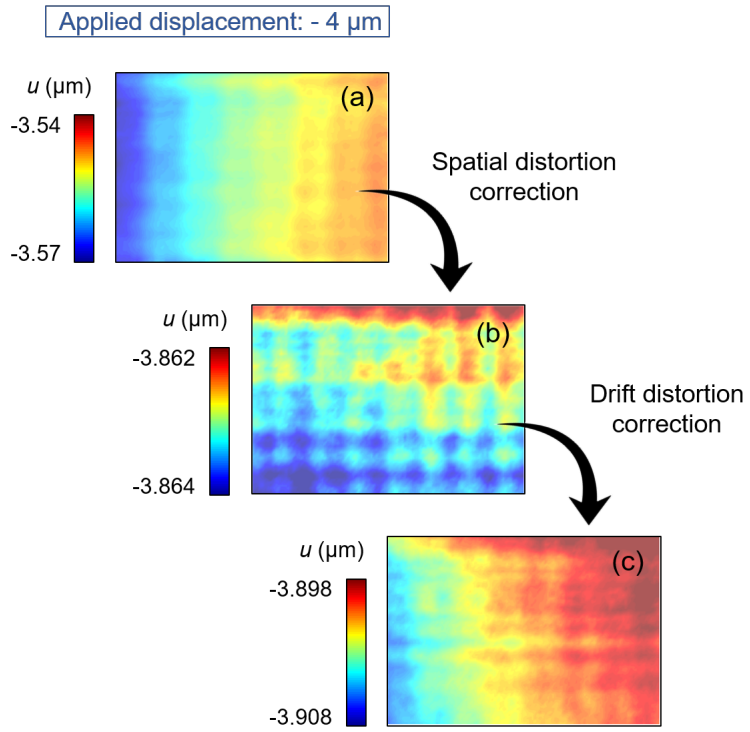


Fig. 4.7: Horizontal displacement field measured by DIC: (a) without any correction, (b) after spatial correction and (c) after spatial and drift corrections.

4.3.2 DIC results

Validation of nano DIC

In order to validate the proposed nano DIC approach, in-situ tests were carried out on the RTM6 and Elium fibre-reinforced systems at a magnification of 20,000. Fig. 4.8 (a) and (c) present the macroscopic load-displacement curves obtained during compression of a RTM6/carbon fibre and an Elium/glass fibre specimen, respectively. In both cases, the alternance of peaks and drops results from specimen relaxation following each load increment (see section 4.2.4), while the non-linear behaviour at very low displacements is caused by the compression of the soft layer of silver lacquer present on the lateral and lower surfaces of the specimens, i.e. the surfaces in contact with the compression jaws (see section 4.2.3). Fig. 4.8 (b) and (d) provide a zoomed-out view of the ROIs selected for DIC analysis in both systems. Note that the ROIs are shown *after* failure, whose loci are indicated with coloured arrows. The force value corresponding to each failure event is shown in Fig. 4.8 (a) and (c). For the RTM6 specimen,

failure occurs within the ROI via interface debonding, see Fig. 4.8 (b). For the Elium/glass fibre specimen, however, two subsequent failure events are reported. First, a crack opens in the matrix outside the ROI but close to its boundaries (green arrow), and interface debonding then occurs within the ROI (red arrow), see Fig. 4.8 (d). In this section, only the displacement and strain fields recorded just before each failure event are presented. The corresponding DIC strain maps are presented in Fig. 4.9 and 4.10, respectively.

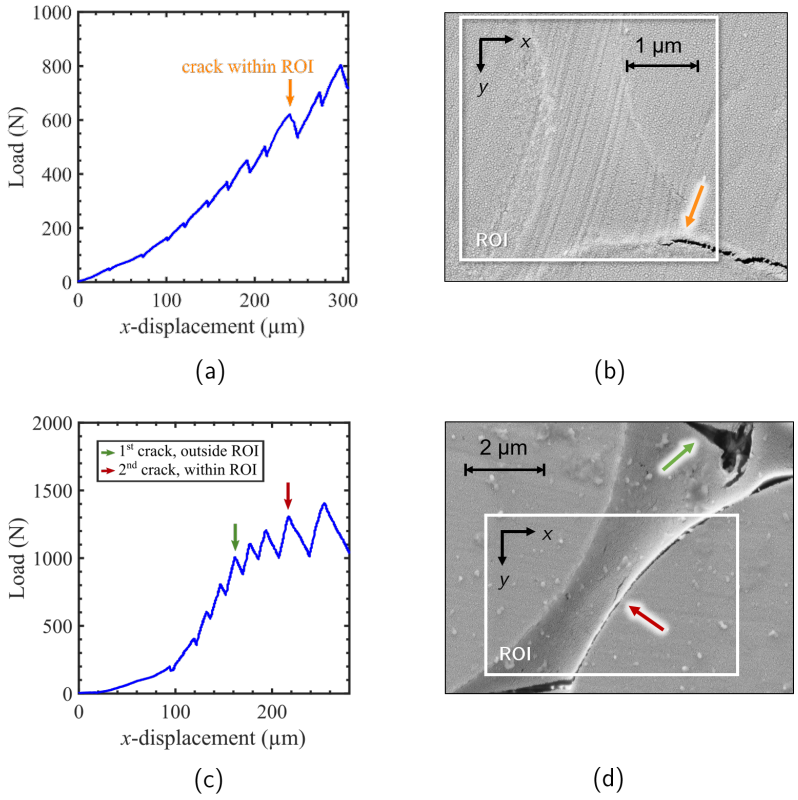


Fig. 4.8: Macroscopic load-displacement curves obtained from the in-situ compression testing and SEM micrographs of the corresponding ROIs used for DIC analysis of: (a) and (b) an RTM6/carbon fibre specimen and (c) and (d) an Elium/glass fibre specimen. Coloured arrows indicate the location of failure events observed within or close to the ROIs during testing, and the same colour code is used to show force-displacement values at these moments.

Fig. 4.9 (a) and (b) show the ε_{xx} and ε_{xy} strain fields for the RTM6 system. Nano DIC clearly distinguishes the fibre and matrix response. Indeed, being

much stiffer than the matrix, the average amplitudes of ε_{xx} and ε_{xy} are close to zero in the fibres. The fibre/matrix interface can also easily be distinguished, which suggests that the resolution of nano DIC is sufficient to avoid smoothing of the fibre and matrix strains. The ε_{xx} and ε_{xy} strain fields displayed in Fig. 4.10 (a), (c) and (b), (d), respectively, show the analogous results for the Elium system. Hence, the combination of a high-quality nanoscale speckle pattern and careful specimen preparation (i.e. grounding, etc.) allows overcoming the main restriction related to the use of micro DIC on FRPs in the literature. The proper phase separation in the DIC results opens the door to investigate the interphase behaviour of FRPs. To illustrate this, Fig. 4.9 (c) and (d), as well as Fig. 4.10 (e) and (f) show the strain distribution along different paths (depicted as white dashed lines) for both systems. A transition zone between the fibre and the matrix is systematically present. Within this region, a smooth transition from the quasi-zero strain level of the fibres to the matrix strains is observed. This transition zone spreads over 200 nm to 500 nm (assuming a peak-to-peak width). The literature reports that an interphase layer exists in FRPs that can spread from a few hundreds of nanometres to a few microns depending on the fibre sizing and curing conditions [197, 293, 314]. Hence, the observed transition zone can be related to the interphase of each system.

Localised areas of large strain amplitudes in between fibres are captured by DIC, as observed in Fig. 4.9 (b) and 10 (b) for the RTM6 and Elium systems, respectively. Note that high strain amplitudes are systematically found around fibres, highlighting the importance of getting accurate DIC measurements in both the fibre and matrix zones. In particular, shear strain localisation is visible at the bottom right of Fig. 4.9 (b) for RTM6 and near the right fibre/matrix interface in Fig. 4.10 (d) for Elium. Comparing these two regions with the loci of interface debonding depicted in Fig. 4.8 (b) and (d) for RTM6 and Elium, respectively, large shear strains accumulate exactly where failure ensues. In the case of Elium, DIC also captures the redistribution of strains following a matrix cracking event starting outside the ROI, indicated in Fig. 4.8 (c) and (d) by the green arrows. This is especially clear when comparing Fig. 4.10 (a) and (c), which show the ε_{xx} strain fields before and after the event. One can notice the homogenisation of the matrix strain field in Fig. 4.10 (c), with respect to Fig. 4.10 (a). The same trend is also observed, to a lesser extent, when comparing Fig. 4.10 (b) and (d) in terms of the shear strains ε_{xy}. Fig. 4.21 in the annex displays the maximum shear strain maps for RTM6 and Elium, which clearly indicate that the maxima of shear coincide with the loci of failure in both systems.

Surprisingly, shear bands propagating between two fibres are not observed in any of the two systems, contrary to what is expected in FRPs subjected to transverse compression [76]. Still, in Fig. 4.9 (b), strain concentrations can be found not only near the bottom of the right-hand fibre (i.e. in the region where

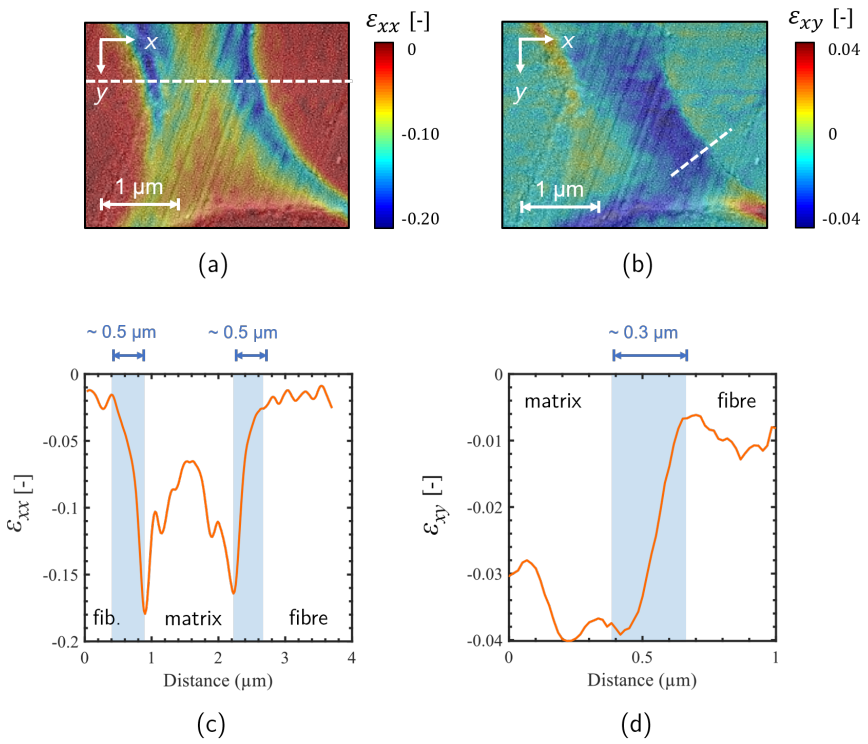


Fig. 4.9: Strain maps and evolution of strain profiles across the carbon fibre-RTM6 matrix interface (white dashed line) obtained by DIC: (a) along the x and (b) xy directions.

a crack follows), but also near the top of the left-hand fibre. This could suggest that a shear band started to develop in the RTM6 ROI, but could not propagate as the induced localisation led the fibre/matrix interface failure first. Hence, the lack of significant shear banding measured by DIC may simply be related to an unfortunate choice of region of interest for a given test. Or, as the observed ROIs are quite small in both systems, it is also possible that large-scale shear band formations are missed. Therefore, further investigation will require a screening of more regions of interest per specimen during each compression test, in order to identify and quantify the presence and amplitudes of micro shear bands.

In addition to the DIC measurements presented above, post-mortem SEM observations were carried out outside the ROIs to analyse the failure behaviour of both systems. The fracture surfaces are presented in Fig. 4.11 for RTM6 and Fig. 4.12 for Elium, for different length scales. The micrographs in Fig. 4.11 (a) and (b) suggest that failure initiates suddenly in the RTM6 composite. The crack

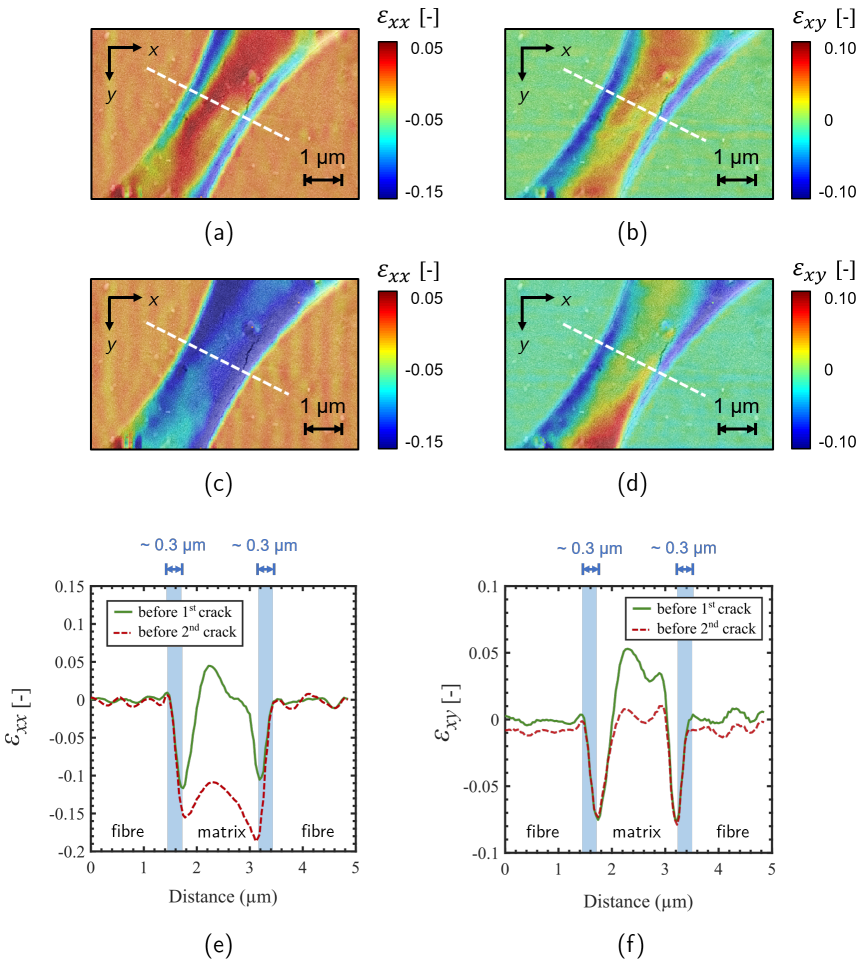


Fig. 4.10: Strain maps obtained by DIC in the Elium/glass fibre specimen along the x direction, (a) before first failure event and (c) before second failure event, and along the xy directions (b) before 1st failure event and (d) before 2nd failure event, alongside with corresponding strain profiles across the fibre/matrix interface (white dashed line) in the (e) x and (f) xy directions. The terms 'first and second cracks' refer to the failure events identified in Fig. 4.8.

path follows the fibre/matrix interface, though no sign of progressive damage from interface decohesion or matrix cracking was observed, as demonstrated in Fig. 4.11 (c) and (d). Still, Fig. 4.11 (c) shows that the conductive coating displays a significant amount of micro cracks, confirming that the RTM6 matrix below undergoes strong local plastic deformation via the creation of nano or micro shear bands. These observations are in line with the results of Chevalier

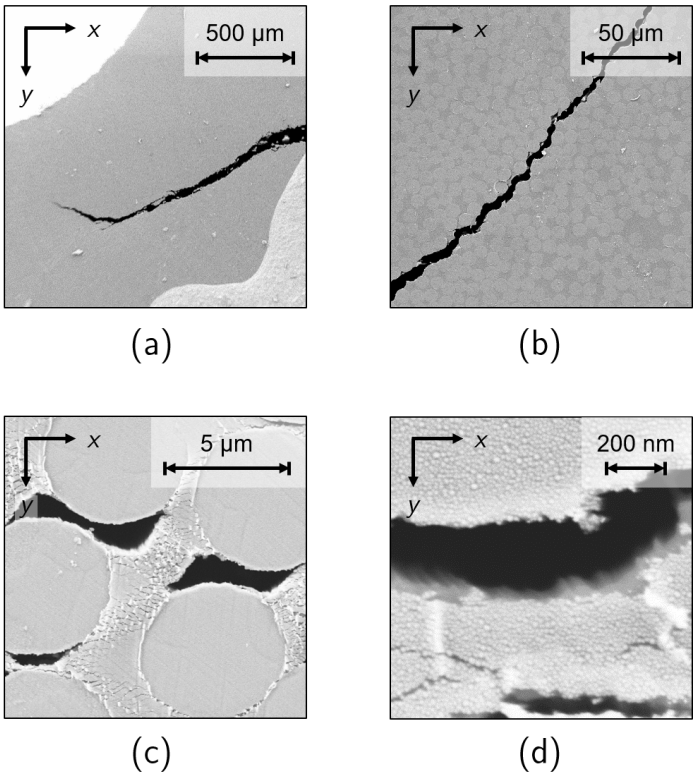


Fig. 4.11: RTM6 – Post-mortem observations of the failed material surface: (a) general overview, (b) main crack, (c) fibre/matrix level interface failure, (d) zoom of the interface failure in (c).

et al. [76]. Lastly, a close-up of the fibre/matrix interface in Fig. 4.11 (d) shows the absence of crazes, which reinforces the idea of the absence of damage at the interfaces. The case of the Elium system in Fig. 4.12 (a) and (b) is different, showing clear signs of damage accumulation all over the matrix. Note that this difference in behaviour between the two composite systems can also be inferred from the load-displacement curves presented in Fig. 4.8 (a) and (c), which respectively suggest that the RTM6 macroscopically fails in a brittle manner, whereas the Elium system only fails after entering global plasticity. However, these differences as well as those observed on the post-mortem SEM micrographs may partially be explained by the difference in specimen geometry, which leads to different levels of stress triaxiality associated to the barrelling effect. Still, Fig. 4.12 (c) clearly indicates strong plastic deformation in the Elium matrix via micro shear bands developing in between fibres. Finally, in Fig. 4.12 (d) crazes of around 20 nm in thickness can be observed, confirming that progressive damage accumulates within the Elium matrix during deformation. Ultimately,

the DIC analysis is thus able to identify the regions of stress concentration near the fibre/matrix interface that lead to failure for systems that involve progressive damage, such as the Elium/glass fibre composite, and for those that do not, like the RTM6/carbon fibre composite.

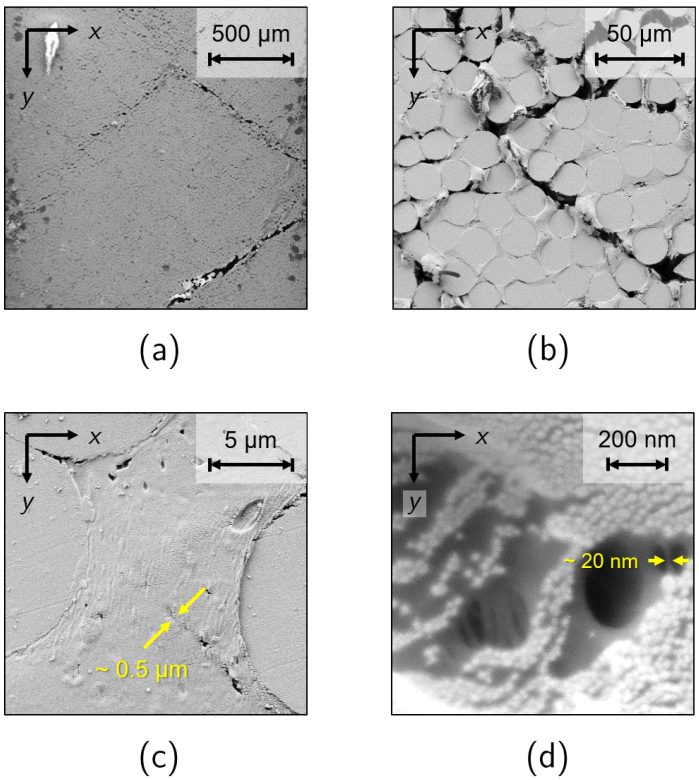


Fig. 4.12: Elium – Post-mortem observations of the failed material surface: (a) general overview, (b) main cracks, (c) fibre/matrix level diffuse cracks and shear bands, (d) zoom of the cracks in (c).

Although the above analysis demonstrates the potential of the nano DIC approach, DIC artefacts are still detected in Fig. 4.9 and 4.10. The potential sources for these artefacts are presented in Fig. 4.13, using SEM micrographs of both ROIs before and after failure. In particular, a clustering of indium particles indicated by arrow 1 in Fig. 4.13 (a) results in an unclear separation between the fibre and matrix strains in RTM6, see Fig. 4.9 (a) and (b). This particle clustering is most likely due to differential erosion between the fibre and the matrix that was created during the polishing phase ($\leq$ 50 nm difference). The presence of shallow leftover polishing scratches on the matrix is made

more visible by the indium deposition, as shown by arrow 2. This leads to spurious strain fluctuations in the DIC maps of RTM6, which are most visible in Fig. 4.9 (a). Finally, the combination of deformation around the fibres and repeated observation can lead to some charging of the interfaces, as shown by arrows 3 and 4 where the fibre/matrix interface is whitened. The charging effect decreases the contrast within these whitened zones, potentially leading to a loss of correlation in some cases. Hence, although the novel nano DIC approach allows reaching high resolution and achieving proper DIC characterisation of heterogeneous material systems such as FRPs, careful specimen preparation is crucial to avoid any artefacts.

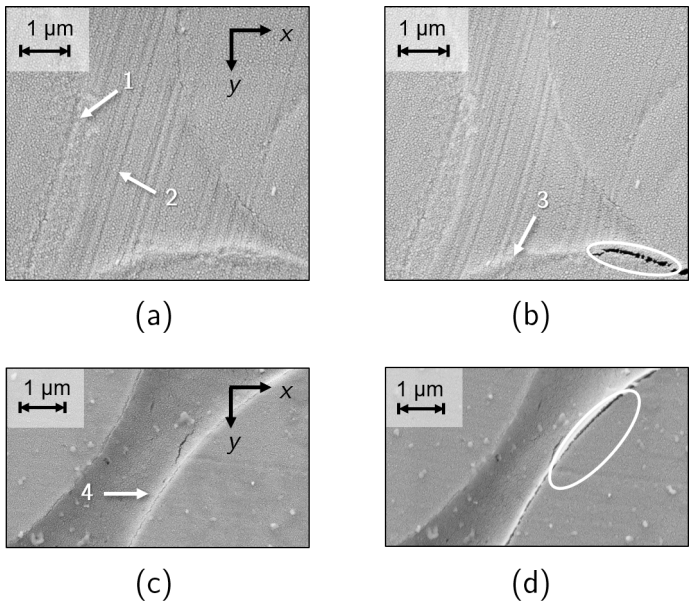


Fig. 4.13: Comparison between initial and final (post-failure) images for two ROIs: RTM6 system (a) in initial state versus (b) after failure, and Elium system (c) in initial state versus (d) after failure. Note that the failure regions are highlighted by white ellipses, while the white arrows represent sources of imperfection for the DIC analysis.

Investigating the interphase behaviour

The previous section showed that a transition region of a few hundreds of nanometres exists in the strain fields between the fibres and the matrix. It presumably corresponds to the fibre/matrix interphase. To confirm that nano DIC is a viable and relatively direct alternative to measure the interphase size of FRPs, DIC was performed on successive images during a single test. At

each load, the current image was compared to the reference image, to avoid propagation of artefacts. The aim was to study whether the transition zone size changes during the test, which would indicate that it does not correspond to the interphase. Fig. 4.14 shows the ε_{xx} field at different moments during the test for RTM6. Fig. 4.15 presents the same for Elium. For each system, the strains were evaluated along paths crossing at least two fibre/matrix interfaces. The results are given in Fig. 4.16. In both systems, for all three paths, the amplitude of the maximum strain attained in the transition zone increases during the test. The thickness of the zones grows marginally up until the last load before failure.

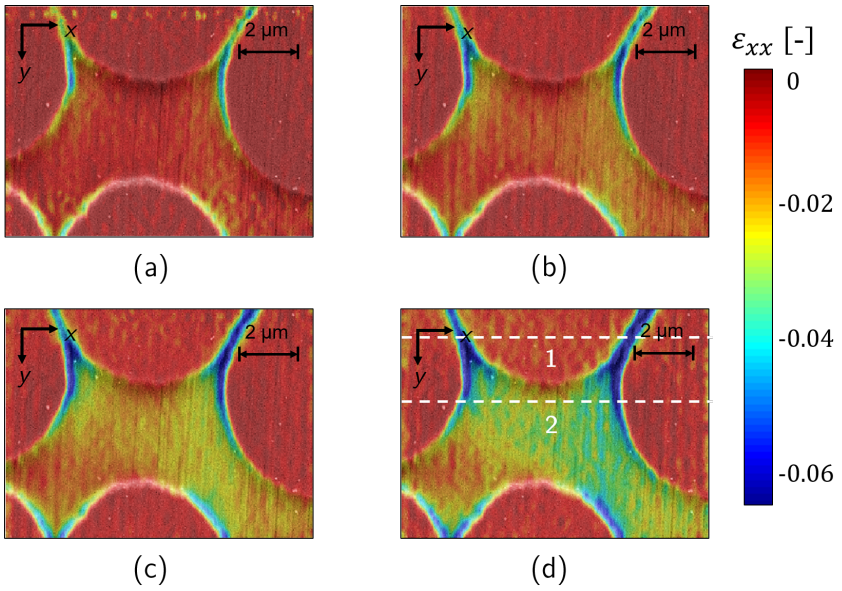


Fig. 4.14: RTM6 - Horizontal ε_{xx} strain map at four different stages during the in-situ compression test until the last moment before failure: (a) at 600 N, (b) at 850 N, (c) at 1000 N and (d) at 1150 N.

For RTM6, path 1 crosses through very thin matrix regions in between fibres whereas path 2 traverses a single large matrix pocket. Yet, the transition zone thickness in paths 1 and 2 is around 300-400 nm. This is in line with the aforementioned results of Fig. 4.9. Considering the thin matrix ligaments in path 1, it is questionable whether defining a distinct interphase is meaningful as the ligament size is roughly 300 nm as well. If the matrix is capable of developing an interphase in such a confined space, then it would imply that in such regions, the mechanical response is entirely dictated by the interphase layer properties (which differ from the bulk matrix). As failure systematically occurs by sudden debonding of the fibre/matrix interface, these findings highlight

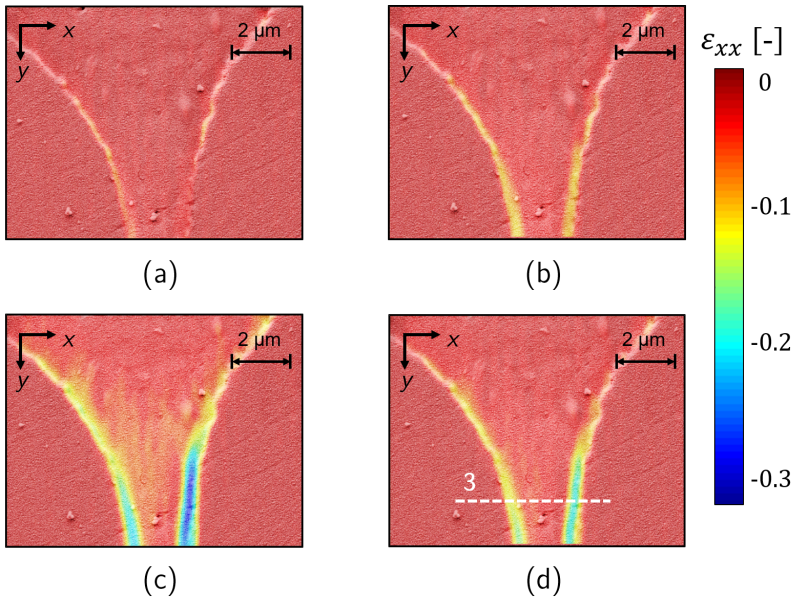


Fig. 4.15: Elium - Horizontal ε_{xx} strain map at four different stages during the in-situ compression test until the last moment before failure: (a) at 500 N, (b) at 700 N, (c) at 1000 N and (d) at 1300 N.

the importance of studying the interphase surrounding the fibres. For Elium, the transition zone along path 3 is about 400 nm as well. Again, this result correlates well with the results of Fig. 4.10.

To confirm the DIC results, AFM measurements were performed on both composite systems. The AFM modulus map of Fig. 4.17 (a) shows two profiles along a path from the carbon fibre to the RTM6 matrix. The evolution of the modulus along these profiles is given in Fig. 4.17 (b). An interphase layer of around 150 nm can be identified for this system. Similarly for Elium, the profiles shown in Fig. 4.17 (c) and (d) indicate the presence of a 200 nm interphase region between the glass fibre and the Elium matrix. For both systems, the interphase thickness measured by AFM is on the same order of magnitude as the width of the transition zone captured by DIC, i.e. a few hundreds of nanometres. Note that the interphase thickness varies within a given system, depending on (1) the amount of sizing present on each fibre, (2) the local fibre arrangement, and also on (3) the matrix pocket size [197, 199, 200, 293]. This reinforces the idea that nano DIC is capable of capturing interphases in FRPs relatively well.

Ultimately, nano DIC appears as a promising tool to detect the interphase

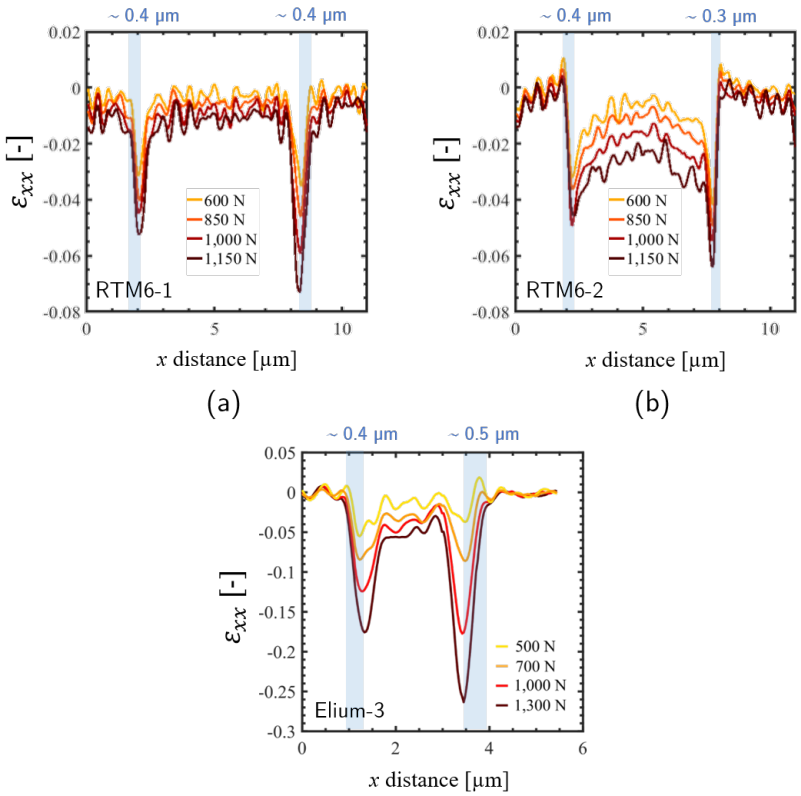


Fig. 4.16: Evolution of the horizontal ε_{xx} strain along the three numbered profiles shown in Fig. 4.14 and 4.15 at different stages during the in-situ compression test: (a) and (b) profiles 1 and 2 on RTM6, respectively; (c) profile 3 on Elium. An interphase of around 300 nm marked by the shaded area is visible for both systems.

of FRPs. As this technique is simpler to set up than AFM (less tedious sample preparation), it offers a convenient alternative. Furthermore, it provides quantitative data about the deformability while AFM remains semi-quantitative regarding the magnitude of the local stiffness. Now, extracting material properties from DIC requires inverse identification through modelling.

4.3.3 Comparison to FE simulations

In an attempt to evaluate the validity of using calibrated continuum models for micromechanical analyses, FE simulations were carried out on the ROIs presented in Fig. 4.8 (b) and 8 (d) for the RTM6 and Elium FRPs, respectively. The ε_{xx} and ε_{xy} fields measured by DIC and predicted by FEA are compared in Fig. 4.18 (RTM6) and 4.19 (Elium). For RTM6, the predicted strain

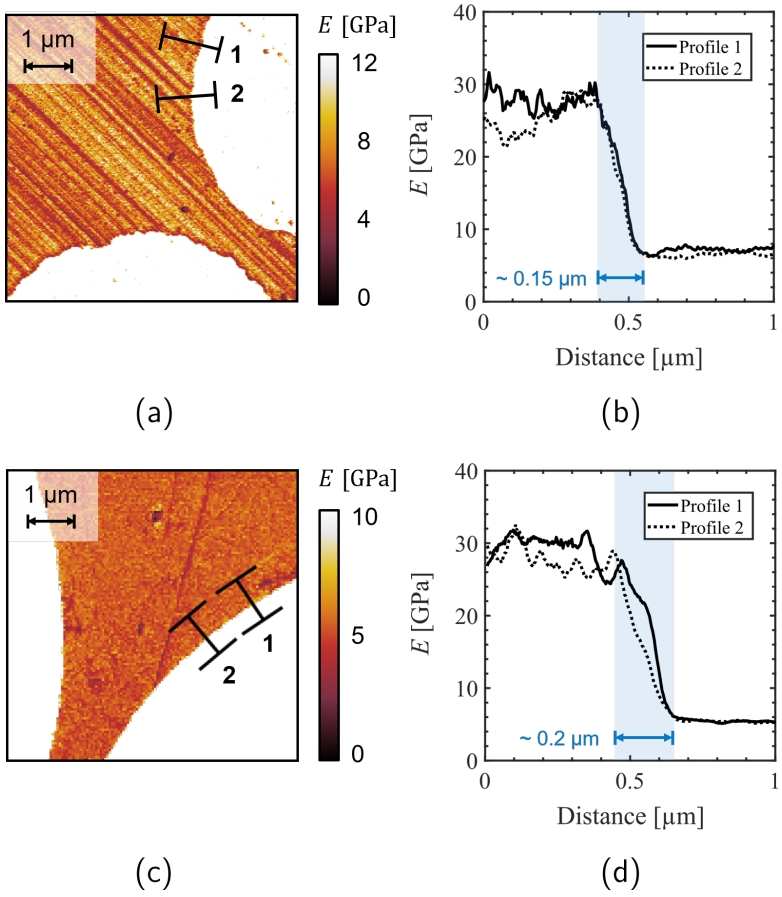


Fig. 4.17: Atomic force microscopy measurements obtained by PeakForce Tapping on (a), (b) the RTM6/carbon fibre composite, and (c), (d) the Elium/glass fibre composite. DMT modulus maps are presented in (a) and (c), while (b) and (d) show the evolution of the DMT modulus along two profiles extracted from each map.

distribution and amplitude within the large matrix pocket fit well with the DIC measurements, in particular for ε_{xx}, see Fig. 4.18 (a) and (b). However, in the thin matrix bands at the top, the model drastically overestimates the strains compared to DIC. Within the ε_{xy} map, the opposing diagonal shear pattern around the fibres is also captured by FEA, as shown in Fig. 4.18 (d) and (e). Yet, the strain amplitude of the shear accumulation around the fibres is, again, largely overestimated. This is further illustrated in Fig. 4.18 (c) and (f) along a path. Furthermore, no transition zone at the interface is predicted by the model. The comparison between FE and DIC analyses for Elium before the second failure event, which is displayed in Fig. 4.19, yields the same conclusions.

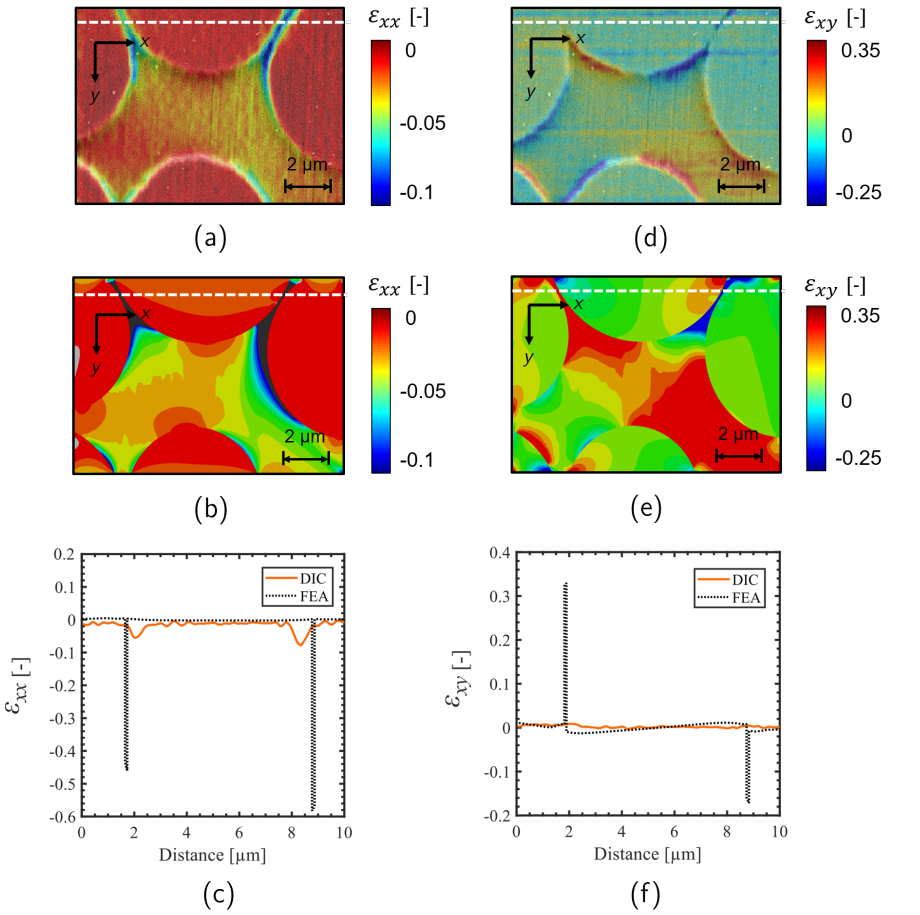


Fig. 4.18: RTM6 – Horizontal ε_{xx} strain field (a) measured by DIC versus (b) predicted by FEA using a continuum model, and (c) comparison of strain evolution along the white dashed profile for both DIC and FEA. (d), (e) and (f) show the equivalent in terms of shear strains ε_{xy}.

In Fig. 4.19 (b) and (e), the average ε_{xx} and ε_{xy} strain distributions within the matrix fit well with the DIC results in Fig. 4.19 (a) and (d), yet some discrepancies remain as, for example, the presence of a positive shear strain around the left-hand fibre in Fig. 4.19 (e) compared to Fig. 4.10 (d). Fig. 4.19 (c) and (f) show the strain variations along a path for both DIC and FEA. At the interfaces, a sharp transition with higher strain amplitudes is once more seen, indicating that no interphase is predicted by FEA for both systems. Furthermore, in Fig. 4.19 (e), the size of the positive strain band in the bottom right extends further, leading to an inversion to positive rather than negative strains along the path.

The validity of the use of the continuum of Morelle et al. [12] was already questioned by Chevalier et al [76]. They demonstrated that the model overestimates the strain amplitudes in matrix pockets, while the overall strain distribution remains close to DIC measurements. The present FE results are therefore not surprising. However, the comparison between FEA and DIC clearly shows that the interphase region around the fibres is crucial. As the presence of the interphase can be confidently confirmed by DIC, assuming a homogeneous matrix within the FE framework limits its ability to accurately model the load transfer at the interfaces. In addition, neglecting the presence of progressive damage is a reasonable assumption for RTM6 (and may be debated for Elium). This suggests that micromechanical modelling strategies should consider the presence of an interphase with intrinsic stiffness and hardness larger than the bulk matrix, as indicated by the AFM maps for the Young's modulus. Chevalier et al. pointed out two possibilities to overcome the discrepancy between the DIC and FEA. The first is related to intrinsically different local properties in the matrix, which may arise from difference in curing conditions due to the presence of fibres. The present study indeed suggests local variations in the properties of the matrix due the presence of an interphase around the fibres. The second possibility assumes true size-dependent plasticity [158, 167, 186, 315]. This last aspect requires further investigations to determine if this second effect plays an important role, in the addition to the interphase effect.

4.4 Conclusion

The development of predictive micromechanics-based multiscale models requires accurate data about the local fibre/matrix level deformation and failure, as well as a deep understanding of the mechanisms themselves in order to select the right ingredients in the constitutive model. In this study, the use of DIC on FRPs was extended to the nanoscale to determine the deformation behaviour of the matrix in the vicinity of fibres. To this end, a novel nanoscale speckle pattern deposition technique was simplified and used on UD fibre-reinforced thermoplastic and thermoset polymers. In order to assess the robustness of the experimental approach, the quality of the speckle pattern was carefully checked and SEM-induced distortions were quantified. The main challenges associated to the use of nanoscale DIC on FRPs are linked to charging effects in the SEM and related drift distortions. This assessment ensures that the proposed DIC analysis is quantitative. A comparison with FE predictions was performed to determine the differences with DIC. The main findings of this study are the following:

- Careful specimen preparation of FRPs allows minimising spatial and drift distortion-related errors.

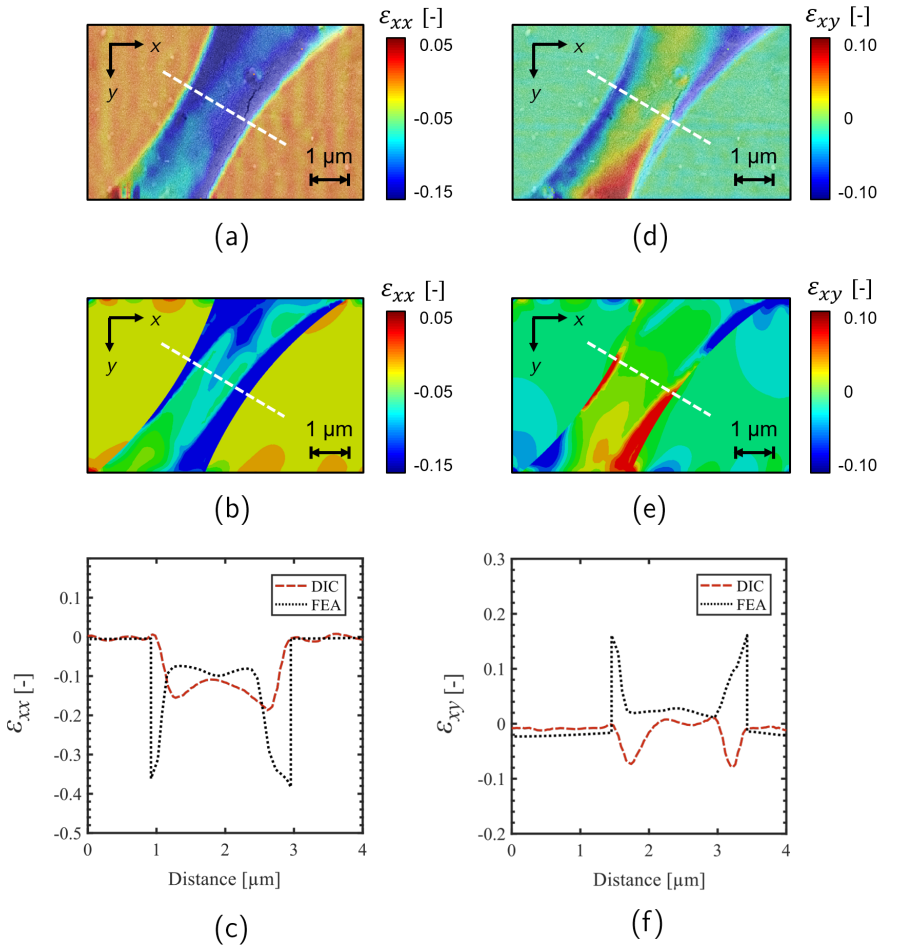


Fig. 4.19: Elium, before second failure event – Horizontal ε_{xx} strain field (a) measured by DIC versus (b) predicted by FEA using a continuum model, and (c) comparison of strain evolution along the white dashed profile for both DIC and FEA. (d), (e) and (f) show the equivalent in terms of shear strains ε_{xy}.

- The nano DIC approach accurately determines displacement and strain fields at the local fibre/matrix scale, despite the significant contrast in mechanical properties between the constituents. Hence, the main issue reported in the literature of submicron level DIC was overcome.
- The local micro shear band formation and interface failure are well captured in the DIC maps within highly confined material regions, even though the strain gradients are very steep.

- DIC data reveal the systematic presence of an interphase around the fibres for both material systems. The measured interphase width perfectly relates to the AFM measurements made on the same material system.
- The average strain amplitude predicted by FEA in large matrix pockets agrees with DIC. However, the strain distribution and localisation differ, especially in the near fibre region. In particular, the FEA largely overestimates the strain concentration within confined regions and/or at the fibre/matrix interface.

In the end, this study provides a robust method to acquire data about the mechanics of FRPs at submicron levels. The interphase of FRPs can be easily and reliably measured in comparison to other techniques. The importance of characterising the matrix at this scale is highlighted by the inability of FEA using continuum models to reproduce the experimental results in conditions where the matrix is the main carrier of the deformation. As failure occurs at the fibre/matrix interface, it may be necessary to include an interphase region around the fibres and maybe strain gradient plasticity effects to accurately model the load transfer occurring between the matrix and fibre. Still, this means that quantitative data in the interphase region need to be gathered. The physical reason behind the difference in response of the interphase remains unknown. It may be due to different local curing conditions and strain gradient effects.

4.5 Appendix

The distortion correction analysis presented in section 4.2.4 stated that the impact of the displacement distortion correction on the strain fields was negligible. Fig. 4.20 presents the strain maps obtained after each correction. The strain variations are one order of magnitude below the measured strain amplitudes in the main DIC analysis. Fig. 4.21 presents the maximum shear strain maps discussed briefly in section 4.3.2. The maps clearly show that failure coincides with the areas of strain concentration.

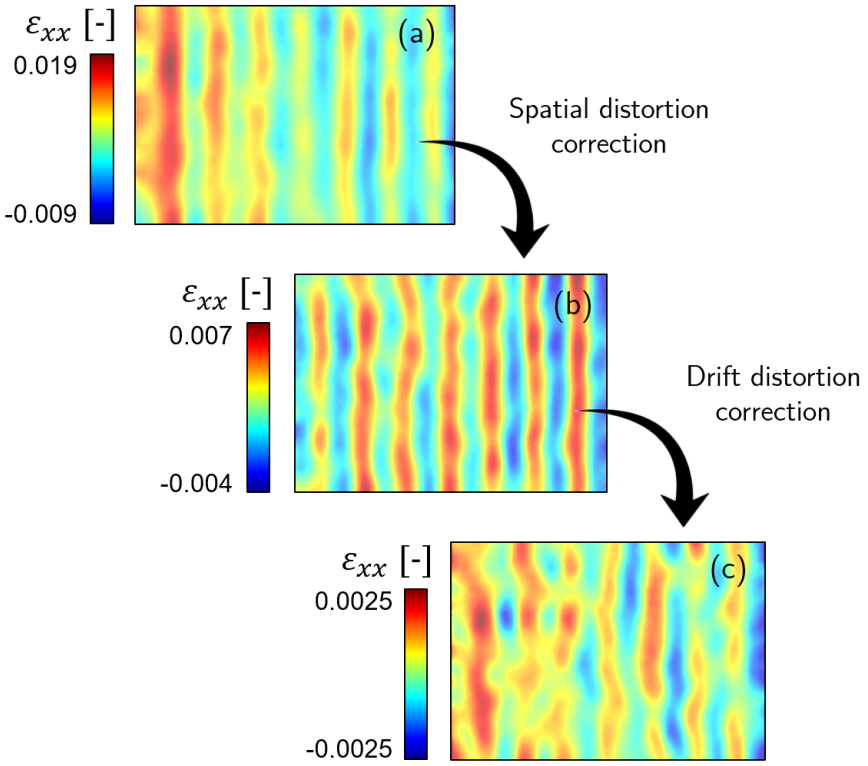


Fig. 4.20: Horizontal ε_{xx} strain field measured by DIC: (a) without any correction, (b) after spatial correction and (c) after spatial and drift correction.

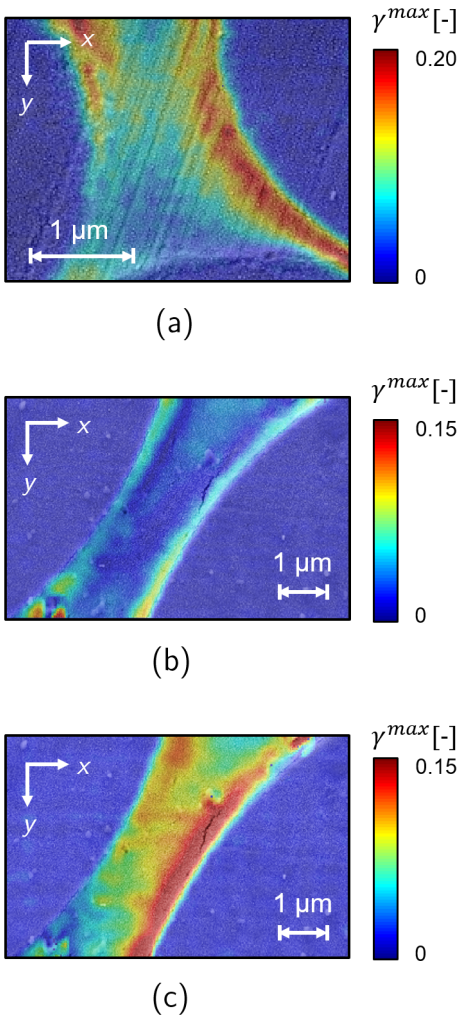


Fig. 4.21: Maximum shear γ_{max} strain fields obtained by DIC (a) in the RTM6/carbon fibre system and (b), (c) in the Elium/glass fibre system before first failure event and before second failure event, respectively.

5

Modelling of size-dependent plasticity in polymer-based composites based on nano- and macroscale experimental results

Abstract

A number of experimental evidences indicate that the local response of polymer matrices near fibres is inadequately represented by classical continuum models relying on the bulk polymer behaviour. This results from size-dependency associated to large plastic strain gradients, complex interphase behaviour and/or changes of polymer structure. Classical multiscale models require artificial tuning of the properties to provide realistic macroscale predictions. We demonstrate that an unprecedented modelling approach based on a micromorphic theory is able to capture such size effects in long-fibre composites. The model is identified via nano digital image correlation strain fields and validated by predicting the strengthening found in transverse compression of UD composites, not captured by classical models. Micro-shear bands are properly regularised by the model, thus correctly handling the size-dependent plasticity and softening effects. The improved prediction of the strain localisation pattern in the matrix opens avenues to more accurately model interfacial failure and damage processes.

Klavzer et al., Composites Part A 185 (2024)

5.1 Introduction

The field of computational micromechanics of fibre-reinforced composites (FRPs) lacks validation against micromechanical experimental data [203, 227]. Within the context of bottom-up multiscale approaches, the determination of the response at the ply level via representative volume elements (RVE) relies on proper modelling of the response of the fibres, matrix and interphase/interface [3, 316, 317]. While the fibres can generally be considered as linear elastic with properties readily available, it remains challenging to accurately predict the matrix response, particularly in loading scenarios leading to extensive plasticity within the matrix, such as under transverse compression or shear. Furthermore, micromechanics predictions generated using elastoplastic models are rarely compared to experimental microscale strain/stress fields.

The use of macroscale elastoplastic constitutive models for the prediction of the matrix response at the microscale and in confined volumes has already been questioned by the community [76, 106, 318]. Chevalier et al. [76] showed that a continuum macroscale model for a unidirectional (UD) simulation could not capture the overall experimental strength levels without artificially increasing the hardness of the matrix above the value measured on bulk specimens. It was pointed out that, considering the micron-sized pockets of matrix present in the composite, large strain gradients develop, thus raising doubts on the capacity of classical constitutive laws to properly capture the mechanisms occurring in such regions as these models are assessed on tests involving homogenous conditions. When considering the small matrix volumes present in the inter-fibre regions, it is reasonable to question this hypothesis. Micro digital image correlation (DIC) tests performed within a scanning electron microscope (SEM) on UD composites have provided microscale strain fields that allow direct comparison with numerical predictions [76, 224–226, 291]. Overall, while the predicted strain maps resemble the experimental measurements, the models are typically unable to accurately capture the strain fields near the fibre/matrix interface. In addition, abundant nanomechanical experimental results on FRPs suggest that the properties of the matrix at the fibre/matrix level clearly differ from those measured at the macroscale. Nanoindentation and atomic force microscopy (AFM) have often been used to extract the local properties. AFM has shown the existence of an interphase region between the fibre and the matrix extending over a few tens of nanometres up to a few microns [198–200]. In nanoindentation, at large indentation depths, the local hardness and stiffness can be up to 15-20% higher than at the macroscale, depending on the polymer system [150, 159, 163, 165]. Furthermore, a strong increase in both hardness and stiffness is found at low indentation depths [153, 166, 168, 186, 292, 319]. This effect has been identified in matrix pockets within FRPs but also in pure polymer samples. All these elements point towards the same conclusion: the polymer matrix elastoplastic behaviour exhibits some degree of size dependency that should

ideally be taken into account in the formulation of the constitutive models.

Size-dependent plasticity in polymer glasses has been the subject of several studies in the literature. Size effects have been identified for many polymers during nanoindentation, such as in PC, PMMA, epoxy, PA and PI [158, 167, 170, 186, 320]. These studies suggest that polymer chains containing aromatic rings tend to systematically exhibit a size effect, whereas simple chain structures may be less prone to it [179]. Furthermore, a size effect has also been found in micro-bending experiments, showing an increase in bending stiffness with a decrease of sample thickness [176–178, 321, 322]. Lastly, experiments performed to determine the true strength of epoxies using micron-sized fibres have shown that the fracture strength and fracture strain increase as the gauge volume decreases [83–85]. These results agree with microscale crack propagation studies on epoxies [87, 88].

Models used to represent the behaviour of the interphase in between the fibre and the matrix include molecular dynamics simulations of polymer chains around a spherical particle (e.g. in [323]) as well as micromechanical descriptions of the effective elastic behaviour, for instance by means of generalised self-consistent schemes (e.g. in [324]). As an alternative, a surface enhanced modelling of the particle has been proposed in [325]. To account for nonlinear effects, strain gradient elastoplasticity models have been developed, inspired by works in the metal community, for example in metal matrix composites [326]. Lam and Chong [166, 167] proposed a size-dependent plasticity model based on the formation of additional polymer kink pairs upon yielding, which accurately captured the size dependence of the hardness of an epoxy during indentation. Nano-indentation tests of glassy polymers were simulated by the finite element method using strain gradient plasticity in [188]. Han and Nikolov [185] suggested that size-dependent elasticity originates from rotational gradients, introducing an intrinsic length related to the polymer chain segments. Later, Voyiadjis et al. [327] introduced a strain gradient dependency into a viscoplastic constitutive law to model semicrystalline polymers. They concluded that the intrinsic length depends on the network structure and the applied deformation. Recently, Deng et al. [177, 178] developed a constitutive model to account for both size-dependent elasticity and plasticity using the effect of the rotational gradient. They successfully reproduced experimental micro-bending results and identified intrinsic elastic and plastic lengths of a few tens of microns. Nguyen et al. [328] studied the RTM6 epoxy and used a nonlocal implicit gradient formulation for the softening and failure within a large strain hyperelastic phenomenological model to account for size effects. They also applied to the case of the UD composite of Chevalier et al. [76] under transverse compression and demonstrated the potential of a nonlocal approach to improve numerical predictions of the stress-strain response [329].

A specific feature of the tensile (and compressive) behaviour of some polymer materials is the presence of a peak strength at the early deformation stage, followed by a true softening response and a subsequent re-hardening. The softening branch is associated with strain localisation and formation of a necking region, which then propagates along the gauge length. It is reminiscent of the Lüders phenomenon in metals like mild steels, with a similar stress peak and stress plateau corresponding to the propagation of the Lüders band. The modelling of the Lüders phenomenon requires a softening-hardening law and the introduction of a characteristic length accounting for the thickness of the band front. A micromorphic theory akin to strain gradient plasticity has been applied for that purpose in [330, 331]. In other words, two phenomena in polymers are not correctly handled by classical continuum models: the increase of the yield stress induced by the strain gradient and the softening response associated with a finite localisation band size. The micromorphic model is an efficient alternative to strain gradient plasticity [233, 332] and is able to capture both effects mentioned above. It can be applied to plasticity and ductile failure of metals and alloys, as recently demonstrated in [333]. It has also been used to combine finite plastic deformation and damage of polymers [334]. To the authors' knowledge, such an analysis, in the context of FRPs, has never been attempted.

The objective of the present study is, for the first time, to model the response of UD composites at the micro- and macrosale with a strain gradient plasticity approach and to demonstrate that it captures both the strengthening and the fine softening induced localisation bands. For this purpose, a micromorphic constitutive model is developed to better capture the post-yield response of the matrix under large strain gradients and in the context of softening and size-dependent effects. The model is identified and assessed through experimental results related to different length-scales. First, the sensitivity of the micromorphic enhancement is assessed via simulations on single fibre cells. Second, experimental nano DIC results on several fibre configurations are used to calibrate the modified strain gradient plasticity constitutive law of the matrix polymer material and to identify the associated characteristic length. Finally, the calibrated model is used to predict the homogenised stress-strain response of UD RVEs, and the results are compared to macroscale transverse compression tests from Chevalier et al. [76].

5.2 Experimental and numerical methods

5.2.1 Composite manufacturing and testing

UD carbon fibre-reinforced composite specimens were produced by resin transfer moulding using the HexFlow RTM6 thermoset resin (Hexcel) for the matrix and HTS 12k carbon fibres (Saertex Gmbh), following the procedure in [12],

resulting in a fibre volume fraction of around 40%. Notched specimens of dimensions 5x5x3 mm were machined by disc milling. In order to be used for in-situ DIC tests, the samples were polished to a mirror-like finish, while minimising differential erosion between the matrix and fibres. A speckle pattern made of indium nano particles was deposited on the samples for DIC analysis, according to the method described in [291]. Lastly, the samples were coated with a thin conductive layer of carbon. In-situ transverse compression tests were performed within a scanning electron microscope (Ultra 55, Zeiss) using a 2 kN microtest compression stage (Deben, UK). A complete description of the test and DIC analysis can be found in [291] (i.e chapter 4). Fig. 5.1 presents the two regions of interest (ROI) that will be analysed in detail in this work.

In a previous study [76], macroscopic transverse compression tests were performed on cubic UD specimens at different strain rates. Their results showed that the UD response was strongly strain rate dependent and exhibited a non-linear trend, emphasising that the deformation is mainly controlled by the matrix. In addition, macroscale localisation bands on the sample surfaces were reported, confirming the highly localised nature of the deformation. Brittle failure was always observed with final cracks initiating or deviating towards the maximum shear direction. Earlier test results combined with original data will serve as validation of the hereafter proposed numerical approach.

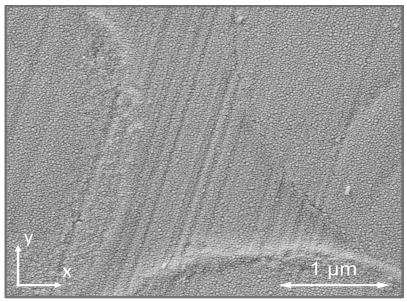
5.2.2 Model formulations

Finite element analyses of RVEs were carried out relying on two different types of constitutive models for the RTM6 matrix: a classical semi-phenomenological continuum model and an Aifantis-based micromorphic model to account for size effects.

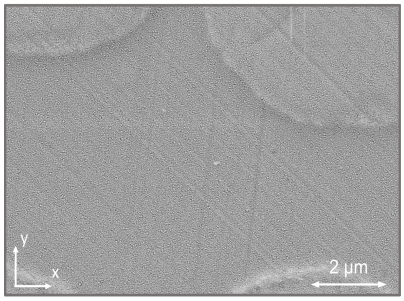
Classical model

A rate-dependent elastoplastic model was identified for the bulk RTM6 matrix by Morelle et al. [12]. It relies on a pressure-dependent Drucker-Prager yield criterion. For the sake of simplicity and to put the focus on the size-dependent effects, a rate-independent von Mises criterion is adopted for the model. The hardening law provided by Morelle et al. [12] is comprised of three contributions:

- A pre-peak non-linearity term resulting from the activation of segmental rotations: $\sigma_0 + \sigma_A \left(1 - e^{-r_{Ap}}\right)$ with σ_0 the initial yield stress and $\sigma_A > 0$,
- A softening term leading to a stress drop caused by intermolecular motions: $\sigma_B \left(1 - e^{-r_{Bp}}\right)$ with $\sigma_B < 0$,
- A re-hardening term expressing the network's contribution due to chain alignment (expressed based on the Arruda-Boyce eight-chain model [31] and assuming only an axial contribution): $\sigma_{C_{11}} > 0$.



(a)



(b)

Fig. 5.1: SEM images of the two regions of interest (ROIs) used for the DIC analysis before deformation.

The impact of the strain rate is considered via the parameters of the hardening law and calibrated to the case of $\dot{\varepsilon} = 10^{-3}\mathrm{s}^{-1}$ in the present work. At last, the full hardening law writes as:

$$\sigma_y(p) = \sigma_0 + \sigma_A(1 - e^{-r_A p}) + \sigma_B(1 - e^{-r_B p}) + \sigma_{C_{11}} \tag{5.1}$$

Fig. 5.2 shows a comparison between the experimental stress-strain response of the RTM6 matrix and the behaviour predicted by the classical (size-independent) model formulation in the case of uniaxial compression. The model based on Eq. (5.1) used to describe the hardening fits almost perfectly the experimental curve.

Micromorphic model

The micromorphic plasticity model proposed by Abatour et al. [332] involves an additional degree of freedom, called the micromorphic variable p_χ, which is associated to the cumulative plastic strain p (i.e. an internal variable). This model is based on the finite strains micromorphic approach proposed by Forest

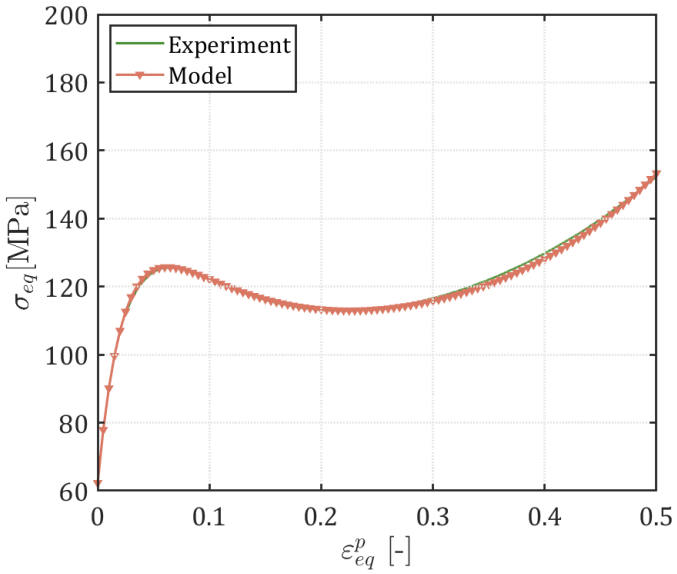


Fig. 5.2: Comparison of the experimental and model equivalent stress-equivalent plastic strain response in compression for RTM6 at $\dot{\varepsilon} = 10^{-3}\text{s}^{-1}$.

[233] The gradient of the micromorphic variable with respect to the Lagrangian coordinates is introduced in the constitutive theory, as mentioned in section 2.4. The theoretical framework is summarised hereafter. A multiplicative decomposition of the deformation gradient into elastic and plastic parts is assumed as:

$$\underline{\underline{F}} = \underline{\underline{F}}^e \underline{\underline{F}}^p. \tag{5.2}$$

The gradient of additional degrees of freedom related to the micromorphic enhancement is defined as:

$$\underline{K} = \frac{\partial p_\chi}{\partial \underline{X}} = \nabla \underline{p}_\chi. \tag{5.3}$$

where $\underline{X}$ is the material position points in the reference (Lagrange) configuration. The power density of internal forces in the Lagrangian coordinates is given by:

$$\mathcal{P}_0^{(i)} = \underline{\underline{P}} : \dot{\underline{\underline{F}}} + a_0 \dot{p}_\chi + \underline{b}_0 \cdot \dot{\underline{K}}, \qquad \forall \underline{X} \in \Omega_0, \tag{5.4}$$

where $\underline{\underline{P}}$ is the Boussinesq stress tensor and, Ω_0 the body in the reference configuration, a_0 and $\underline{b}_0$ are generalised stresses associated to the micromorphic variable. Applying the principle of virtual powers and neglecting volume forces

on the body Ω_0, the following balance laws are obtained:

$$\begin{cases} \mathrm{div}(\underline{\underline{P}}) &= \underline{0} \\ \mathrm{div}(\underline{b}_0) &= a_0 \end{cases} \forall \underline{X} \in \Omega_0, \quad \begin{cases} \underline{T} &= \underline{\underline{P}} \cdot \underline{n}_0 \\ a_0^c &= \underline{b}_0 \cdot \underline{n}_0 \end{cases} \forall \underline{X} \in \partial\Omega_0, \tag{5.5}$$

where $\underline{n}_0$ is the outward surface normal, $\underline{T}$ the surface traction vector and a_0^c the generalised surface traction. A quadratic form of the Helmholtz free energy potential is chosen and writes as:

$$\Psi_0(\underline{\underline{C}}^e, p, \underline{\underline{\alpha}}, p_\chi, \underline{K}) = \Psi^{ref}(\underline{\underline{C}}^e, p, \underline{\underline{\alpha}}) + \frac{1}{2\rho_0}\underline{K} \cdot \underline{\underline{A}} \cdot \underline{K} + \frac{H_\chi}{2\rho_0}(p - p_\chi)^2. \tag{5.6}$$

where Ψ^{ref} is the free energy potential related to the classical constitutive model. Applying the Clausius-Duhem dissipation inequality to Eq. 5.6 leads to the following expression of the generalised stresses:

$$a_0 = H_\chi(p - p_\chi), \qquad \underline{b}_0 = \underline{\underline{A}} \cdot \nabla \underline{p}_\chi. \tag{5.7}$$

Assuming an isotropic and homogeneous case $\underline{\underline{A}} = A\underline{\underline{1}}$, results in an enhancement of the von Mises yield function:

$$f(\sigma_{ij}, \sigma_y(p), p_\chi) = \sigma_{eq} - \sigma_y(p) + A\Delta p_\chi, \tag{5.8}$$

where σ_{eq} is the suited equivalent stress measure, here the von Mises invariant of the Mandel stress tensor within the framework of finite multiplicative plasticity [233, 332, 335], and σ_y is the yield stress defined in Eq. (5.1). The Laplace operator Δ, with respect to Lagrange coordinates, is applied to the micromorphic plastic variable p_χ. This gradient contribution is equal to the Aifantis strain gradient plasticity model [326] and results from the choice of micromorphic variable and energy potential. In addition, the micromorphic model involves a penalization modulus H_χ, which constrains the micromorphic variable p_χ to remain close to the value of the cumulative plastic strain p, following:

$$p = p_\chi - \frac{1}{H_\chi}\Delta p_\chi. \tag{5.9}$$

When the penalisation parameter is high enough, $p_\chi \equiv p$ and the Laplacian term in Eq. (5.8) can be replaced by Δp, so that the micromorphic model essentially coincides with the well-known Aifantis model, see [229] for the initial formulation and [326] for its application to metal matrix fibre composites. The yield function Eq. (5.8) involves the additional material parameter A, defined as a higher order modulus, whose physical dimension are in MPa.mm$^2 \equiv$ N. In the following simulations, the value of the penalization parameter is fixed to $H_\chi = 10^5$ MPa. This value is significantly larger than the modulus of the matrix. It has been pre-determined via a parametric study, establishing a strain gradient plasticity approach. The modulus A will be identified from the experimental

results.

The micromorphic plasticity model will be used for two purposes, already indicated in the introduction. In the case of a hardening material, a *smaller is stronger* size effect is predicted by the model [332]. Decreasing the size of the system or increasing the material parameter A lead to enhanced hardening in the presence of plastic strain gradients. In the case of softening behaviour, strain localisation bands will form with a finite width controlled by the micromorphic material parameters. This corresponds to the regularisation capabilities of the micromorphic model for the localisation phenomena. If H denotes the instantaneous hardening/softening modulus of the classical plasticity model (not to confuse with G_h the large strain re-hardening modulus), an intrinsic length emerges from the theory of the order of

$$\ell_c = \sqrt{\frac{A}{|H|}}, \tag{5.10}$$

for a wide range of boundary value problems explored in [332], like constrained shearing, bending and torsion. In this way, a physical length scale is introduced in the continuum model.

Since the constitutive behaviour of the polymer matrix exhibits softening and hardening behaviour, successively, both aspects of the micromorphic plasticity model will be involved in the analysis. In particular, localisation bands forming at the early stage will propagate like Lüders bands in the matrix [330].

5.2.3 FE implementation and calibration of the micromorphic model

The micromorphic polymer model has been implemented in the FE code Zset [336], within the same theoretical and computational framework as exposed in [332]. The new ingredient introduced in the FE model is the combined softening-hardening law of Eq. (5.1) (specific of the polymer matrix) instead of only softening or hardening. A monolithic resolution method is used whereby displacement and micromorphic degrees of freedom are attached to each node, with quadratic interpolation functions for the displacement and linear ones for the micromorphic variable. Fully implicit resolution schemes are adopted with a Newton solver at the global level, and a so-called Newton theta-method for implicit time integration of plasticity evolution equations, as described in [337]. In order to test and calibrate the micromorphic model, three types of analyses were carried out. First, to evaluate the impact of the micromorphic enhancement on the mechanical response of a composite, the simple case of a periodic fibre distribution with varying volume fraction V_f was studied. In that sense, a 2D plane strain periodic square cell of length $w = 20$ µm containing a fibre of radius r at its centre was compressed by applying an overall strain in

the horizontal direction. The selected V_f are equal to 0.1, 0.2 and 0.4 (implying that r = 3.568, 5 and 7.136 µm, respectively). C2D8R elements of size around 0.4 µm were used for meshing. Periodic boundary conditions are applied to both the displacement fluctuation, as usual in classical periodic computational homogenisation, and to the micromorphic variable. The elastic properties of the matrix (measured by Morelle et al. [12]) and of the fibres [54] are given in Table 5.1.

Second, micromechanical analyses of the ROIs studied with the nano DIC experiments were performed to identify the material parameter A related to the characteristic length of the micromorphic medium. The idea of identifying the characteristic length from field measurements in regions undergoing strong strain gradients goes back to [338, 339], where the technique was applied to short glass fibre-reinforced composites. It is extended here to UD composites. The geometries of the experimental ROIs were exactly reproduced by the FE meshes. The boundary conditions were interpolated based on the measured displacements on the edges of the ROIs. Two-dimensional plane strain elements were used for meshing to compare with the strain fields measured by DIC, without significant differences in this case of UD fibre composites. Fig. 5.3 (a) gives an illustration of one ROI. No damage law between the matrix and the fibre was introduced, assuming perfect interfaces.

	Carbon fibre	RTM6
E_{11} [GPa]	238	3
E_{22}, E_{33} [GPa]	28	–
ν_{12}	0.28	0.34
ν_{23}	0.33	–
ν_{31}	0.02	–

Table 5.1: Elastic properties of the fibres and matrix.

Third, RVEs with a random fibre distribution were analysed to predict the mechanical response of the UD composite. For such RVEs, three 2D plane strain squares of 100 µm were created with a random fibre distribution of radius equal tp 5 µm, as in [76], resulting in a fibre volume fraction $V_f = 0.4$. Fig. 5.3 (b) presents the corresponding mesh view. The plane strain assumption is justified by the large longitudinal stiffness of the fibres compared to the matrix in the out-of-plane direction. Periodic boundary conditions, defined as constraints on corresponding nodes on opposing edges, were applied to the RVEs. For that purpose, special periodic finite elements were used involving additional macroscopic deformation degrees of freedom to impose average strain or stress components to the unit cell, see [337] for the finite element framework and [340] for its extension to micromorphic media.

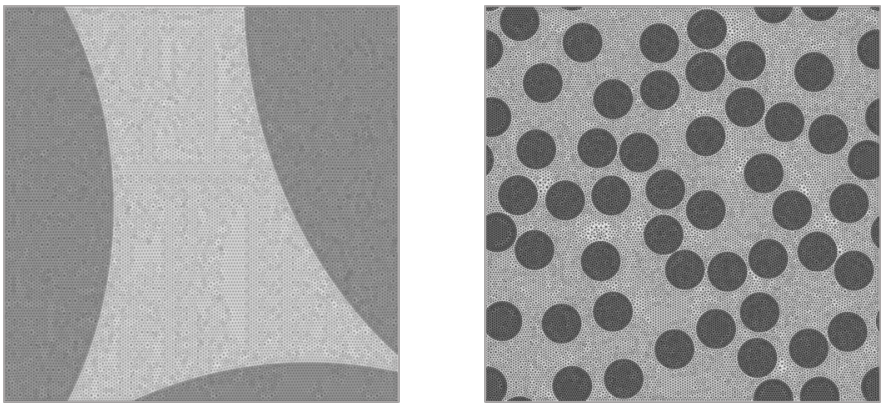


Fig. 5.3: Geometry and mesh used in the FE models: (a) one of the studied ROIs in the nano-DIC analysis and (b) one of the RVEs related to the macroscopic transverse compression study.

The micromorphic modelling approach also enforces special continuity conditions at the interface between the fibre and the matrix, namely continuity of the micromorphic variable p_χ and continuity of the generalized traction vector $A\nabla \underline{p}_\chi \cdot \underline{n}$, $\underline{n}$ being the normal vector to the interface. Since no plastic flow occurs in the fibre, the plastic strain p, and therefore the micromorphic variable, almost vanish close to the interface. This choice agrees with the reduced mobility of polymer chains at the interface. This enhanced interface condition induces a strong plastic strain gradient in the matrix region around the fibre. This effect reflects, to some extent, the specific behaviour of the interphase region, which exists next to the interface.

5.3 Results and discussion

5.3.1 Assessment of the model sensitivity

Unit cells of width w containing a single fibre were first simulated under compressive loading. In an attempt to evaluate the impact of the micromorphic enhancement on the stress-strain response of the composite, three values of the micromorphic parameter A were tested: 10^{-5}, 10^{-4} and 10^{-3} N. Fig. 5.4 illustrates the stress-strain responses (volume averaged over all elements) for three fibre volume fractions predicted by the micromorphic model for different values of A and for the classical description (i.e. $A = 0$). Both V_f and A play a first order effect on setting the magnitude of the yield stress. At low V_f, the response of the composite resembles that of the pure polymer, whereas at high

V_f (i.e. typical of commercially used composites), the composite presents little strain softening and a pronounced apparent hardening. For A equal to 10^{-5} and 10^{-4} N, no significant impact can be observed on the stress-strain responses for $V_f = 0.1$ and 0.2 compared to the classical model. Yet, for $V_f = 0.4$, the yield stress of the composite increases, even for low values of A. Additionally, the degree of softening is further reduced with increasing V_f but the hardening capacity remains relatively unchanged compared to lower V_f. With $A = 10^{-3}$ N, there is no apparent softening and a clear increase of the yield stress with V_f.

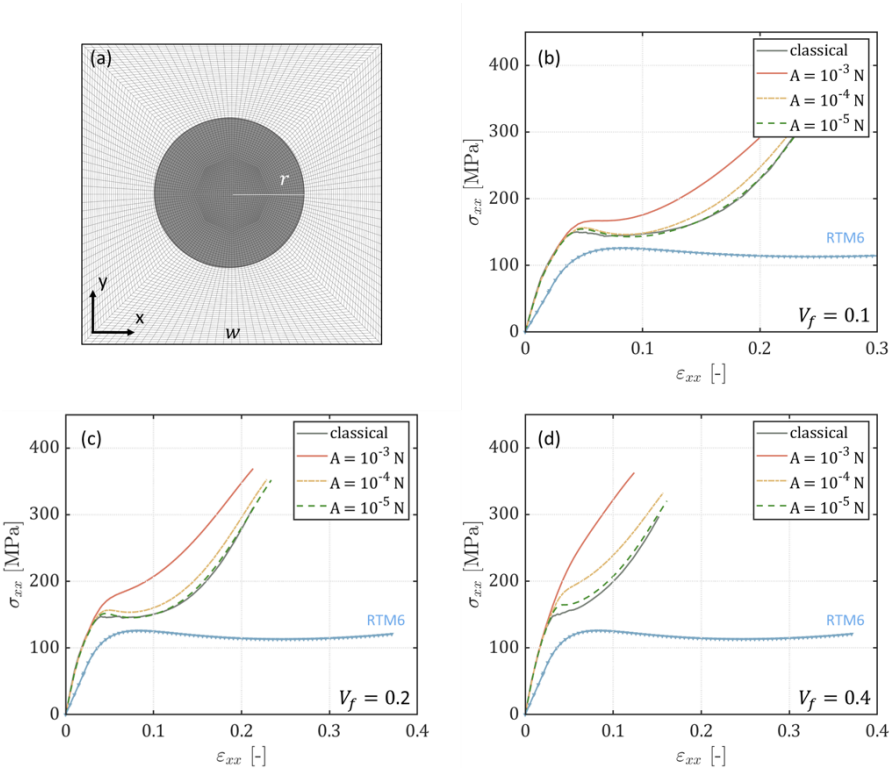


Fig. 5.4: Impact of the micromorphic parameter A on the stress-strain response in compression for the single fibre problem in (a) for (b) $V_f = 0.1$, (c) $V_f = 0.2$ and (d) $V_f = 0.4$. The reference curve of pure RTM6 under homogeneous compression is given in blue.

To assess the relative sensitivity of the model to V_f and A, Fig. 5.5 shows the variation of the normalized yield stress with the ratio w/l_c of the length of the unit cell w and the approximated characteristic length l_c (in the range 2-20 µm, assuming H = -100 MPa, i.e. slope between upper and lower yield

stresses) for the three V_f. As the ratio w/l_c decreases (i.e. increase in A), the strengthening of the material is more pronounced. However, this effect is amplified for larger V_f, suggesting that the strengthening is primarily related to the fibre volume fraction. This can be further explored by looking at maps of cumulative plastic strain p in Fig. 5.6 for the classical model and three values of A at $V_f = 0.2$. The classical model tends to intensely localise the plastic strain in narrow bands. For the micromorphic model, small values of A lead to thin initial bands, which then spread until no space is left in the matrix, leading to re-hardening. Conversely, for $A = 10^{-3}$ N, the size of the plastic band is already too wide with respect to the available matrix space left, leading to an absence of softening and a faster re-hardening. Hence, high V_f results in a plastic strain confined in narrow matrix strips and high A maximises the use of the remnant matrix space leading to a more pronounced size effect. Lastly, Fig. 5.7 demonstrates that the micromorphic model also eliminates any mesh dependency, as long as the intrinsic length (i.e. choice of A) is larger than the smallest element size of the mesh. The width of the localisation bands is equal for the three meshes. This is particularly advantageous in the study

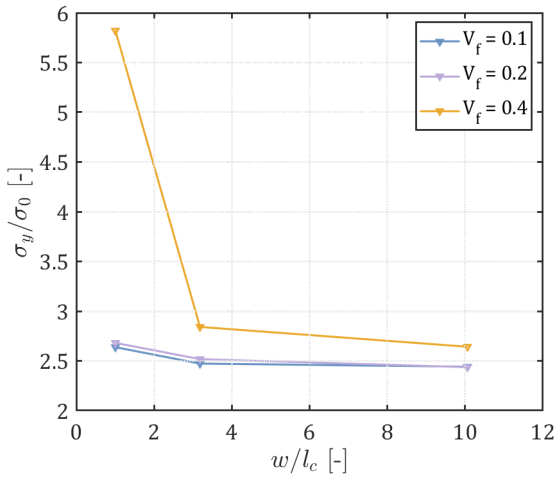


Fig. 5.5: Variation of the normalized yield stress σ_y/σ_0 as a function of the ratio of the unit cell length over the approximate characteristic length l_c (assuming H = -100 MPa) for different V_f.

of polymer glasses as they exhibit an initial strain softening behaviour, leading to shear-banding with a spurious mesh size dependence of the band front width in the absence of regularisation. Such a regularisation is ensured by the use of the micromorphic model, see [332].

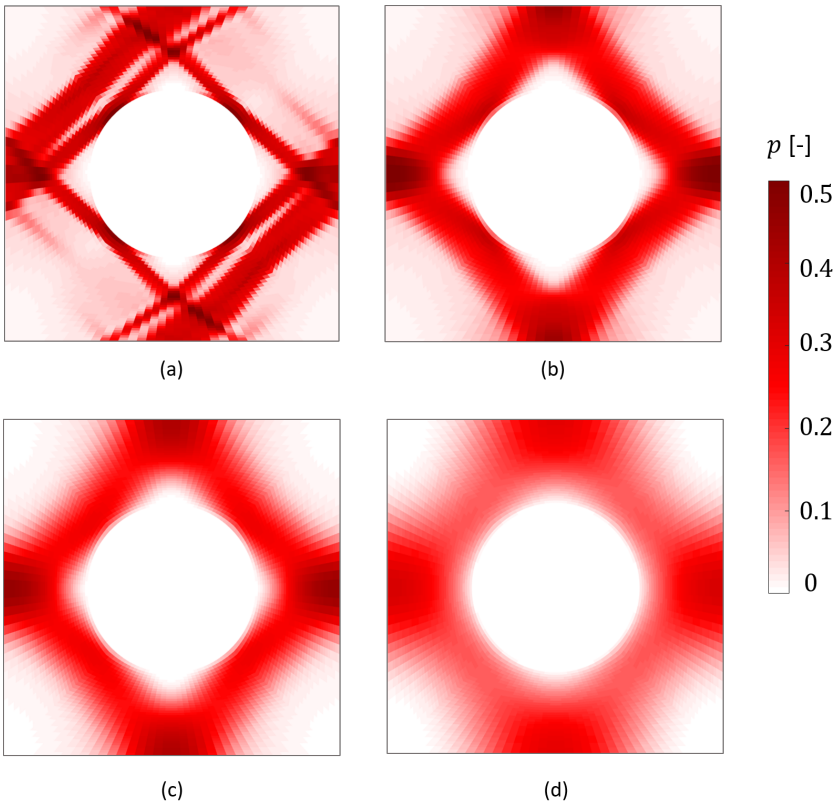


Fig. 5.6: Maps of the cumulative plastic strain p in compression for $V_f = 0.2$ at a macroscopic load equivalent to $\bar{\varepsilon}_{xx} = 0.1$ [-] for (a) $A = 0$ N (classical model), (b) $A = 10^{-5}$ N, (c) $A = 10^{-4}$ N and (d) $A = 10^{-3}$ N.

5.3.2 DIC results and model calibration

Fig. 5.8 shows the analysed experimental ROIs at the point of local failure. Note that cracks appear in the lower right corner of Fig. 5.8 (a) and on the left-hand fibres of Fig. 5.8 (b), corresponding to fibre decohesion. Fig. 5.9 (a) and (c) illustrate the ε_{xx} and ε_{yy} strain fields for ROI 1 whereas Fig. 5.9 (b) and (d) show the ε_{xx} and ε_{yy} strain fields for ROI 2. In all strain maps, the speckle pattern is fine enough for the DIC to detect the near-zero strain amplitude in the fibre and to properly distinguish between the fibre and matrix strains. This can be justified by the presence of strain amplitude gradients at the fibre/matrix interfaces. Additionally, strain concentrations systematically appear near the fibre/matrix interfaces. A previous study [291] demonstrated that an interphase layer of 200-500 nm is likely to be found around these fibres.

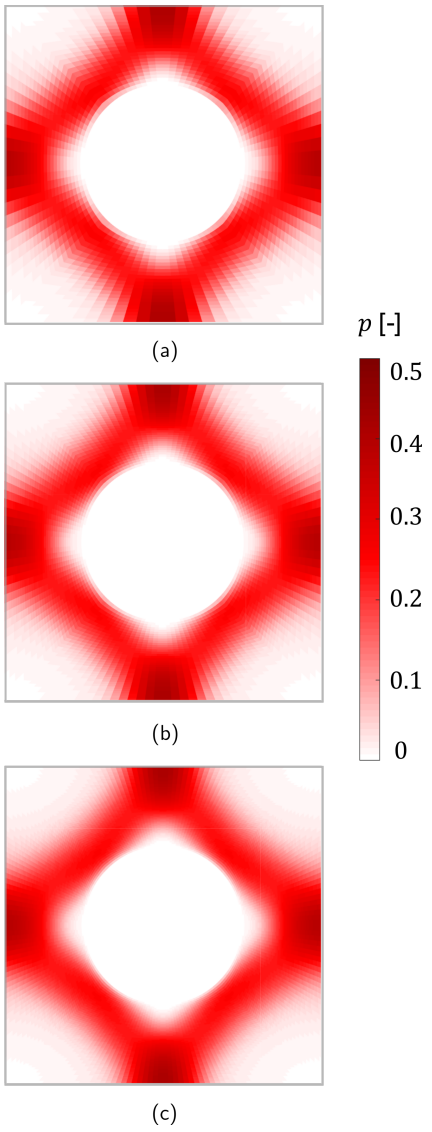


Fig. 5.7: Maps of the cumulative plastic strain p for $V_f = 0.2$ and $A = 10^{-4}$ N at a macroscopic load equivalent to $\bar{\varepsilon}_{xx} = 0.1$ [-]: (a) coarse (4,032 elements), (b) normal (9,720 elements) and (c) fine (25,200 elements) meshes.

Finally, strain concentrations can also be found at the loci of failure within the ROIs. Comparing Fig. 5.8 (a) and (b) with Fig. 5.9 (c) and (d), respectively, one can see that the concentration in the vertical strain ε_{yy} coincides with the locus of crack initiation in the ROIs. Still, as discussed in [291], the analysis

shows that crack initiation is driven by the maximum shear strain attained inside the localisation bands. Fig. 5.9 also highlights that the strain does not drop immediately next to the fibre, but a transition is needed to reach the lowest strain. This indicates that the polymer matrix, as long as it is firmly attached to the fibre, is constrained in its ability to deform.

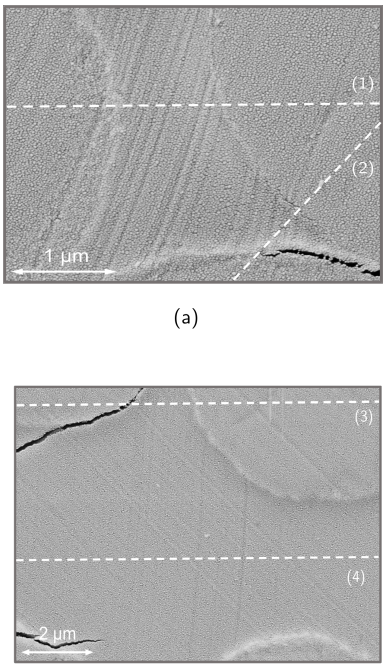


Fig. 5.8: ROIs after local failure in the DIC analysis: (a) ROI 1 and (b) ROI 2. The white dotted lines represent paths used to evaluate the strain profiles.

In an attempt to determine the appropriate value of the micromorphic parameter A for the composite system of interest (i.e. the intrinsic length needed for the micromorphic model), a microscale identification via the nano DIC results is proposed. Hence, the DIC results have been reproduced via finite element simulations. Klavzer and Gayot have shown that the use of a classical macroscale model for the matrix leads to overestimations of the strain amplitudes within the ROIs, which was a strong motivation for the present study [291]. Fig. 5.10 compares the ε_{yy} strain maps for ROI 1 measured by (a) the classical model and (b-d) the micromorphic one for different values of A, ranging from 10^{-5} to 10^{-3} N (directly comparable to Fig. 5.9 (c)). Fig. 5.12 presents maps of the maximum shear strain γ^{max} (defined as $(\varepsilon_I - \varepsilon_{II})/2$, where ε_I and ε_{II} are the principal strains) for ROI 2. In both cases, the classical

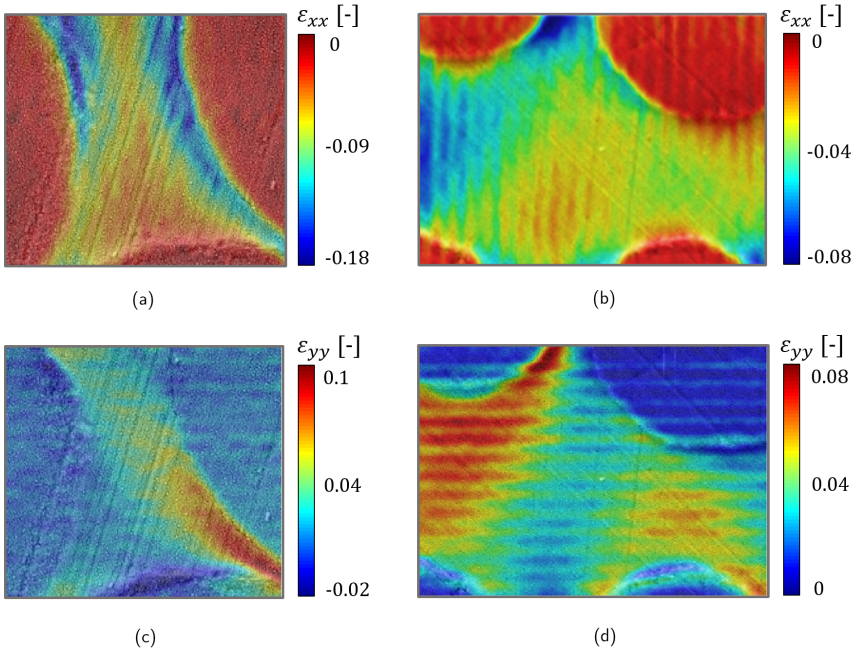


Fig. 5.9: DIC results for the two ROIs of interest. (a), (c) ROI 1 ε_{xx} and ε_{yy} strain fields and (b), (d) ROI 2 ε_{xx} and ε_{yy} strain fields.

model leads to strong strain localisation very close to the fibre/matrix interface and significantly overestimates their amplitudes with respect to the DIC results. As the value of A increases, the band in which the strain concentrates widens, hence reducing the strain amplitude. Fig. 5.11 (a) and (b) show the evolution of ε_{xx} and ε_{yy} across paths (1) and (2) of ROI 1 shown in Fig. 5.8 (a), respectively. Fig. 5.13 illustrates the evolution of ε_{xx} and ε_{yy} along path (3) and of γ^{max} along path (4) of ROI 2 shown in Fig. 5.8 (b). First, the strain amplitudes within the strain concentration regions (around fibres for ε_{xx} and in the failure locus for ε_{yy}) predicted by the micromorphic model match much better with the experimental results. Still, the agreement is not perfect. For ε_{yy} in Fig. 5.11 (b), the DIC results present a gradual strain increase from the fibre to the matrix (see region between 1.4-1.7 µm). This transition was attributed to the interphase between the fibre and the matrix [291]. The FE model only considers the pure matrix and fibre, with a perfect interface in-between them. Hence, the classical model and values of A equal to 10^{-4} and 10^{-5} N lead to sharp strain peaks at the fibre/matrix interface. However, for A equal to 10^{-5} N, a small gradual change in strain amplitude appears over roughly 100 nm, which shifts the strain peak away from the fibre and the curve fits more closely to the DIC results. A similar trend can be seen in Fig. 5.11 (b) for the right-hand fibre (no

gradual transition is observed for the left-hand fibre) and, to a lesser extent, in Fig. 5.13 (a) and (b).

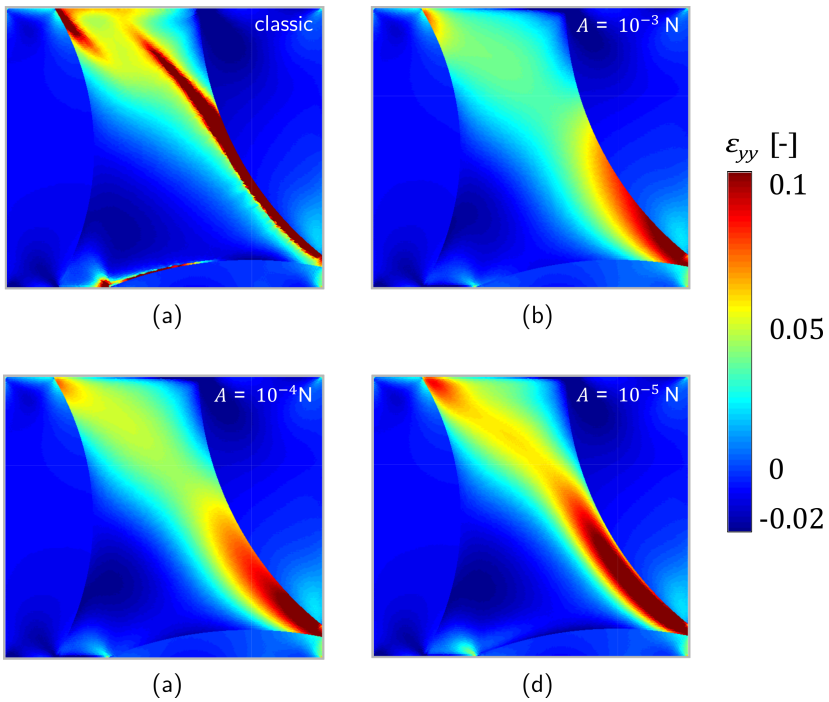


Fig. 5.10: Maps of ROI 1 showing the vertical strain ε_{yy} just before failure for (a) the classical model, (b) $A = 10^{-3}$ N, (c) $A = 10^{-4}$ N, (d) $A = 10^{-5}$ N.

As discussed in the previous section, lower values of A lead to plastic strain localisation in thinner ligaments. As the fibres are purely elastic, these thin strain bands may appear away from the fibre/matrix interface. Thus, the interphase effect is somehow captured in the micromorphic simulation by the interface condition of vanishing plastic strain. This higher order effect, caused by the associated characteristic length, can thus indeed be one of the reasons for the stronger interphase behaviour found in some systems, while one may not disregard effects such as a different chemistry due to the sizing and/or chain alignment for other systems. For ε_{xx} in Fig. 5.11 (a), the strain fluctuations between 1-2 µm along the path (i.e. within the larger matrix strip) are not predicted by the classical nor by the micromorphic model. The difference may partially result from some noise within the DIC results. Still, in this wider gap, it must be recognised that the classical model fits best to the average strain amplitude within the strip. By contrast, Fig. 5.13 (c) shows that in larger matrix pockets away from the fibres, the classical and micromorphic model tend to predict almost exactly the same response, all in agreement with the DIC

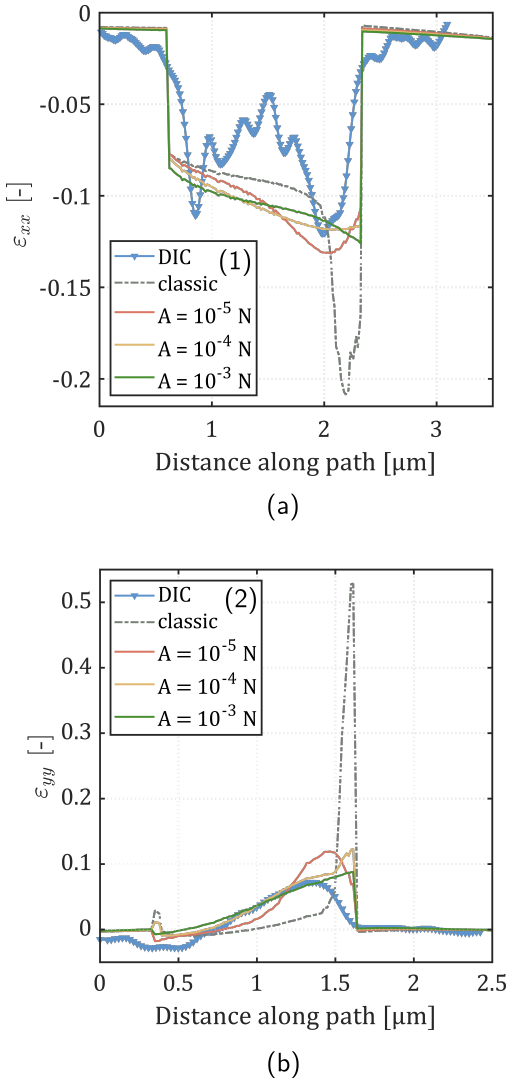


Fig. 5.11: Evolution of strain profiles (a) for ε_{yy} along path (1) and (b) for ε_{xx} along path (2).

results. The good fit of both FE models in large matrix pockets was expected considering the moderate strain levels that prevail and coincides with a previous study [157].

The values of A giving the best fit to the DIC results correspond to a range of characteristic lengths between roughly 2 and 20 µm. The available literature

on strain gradient elasticity and plasticity applied to pure glassy polymers provided estimates of internal lengths equal to 24-34 µm for PMMA [176, 177] and 4-34 µm for epoxy [321, 322], in good agreement with the identified value for A in this work.

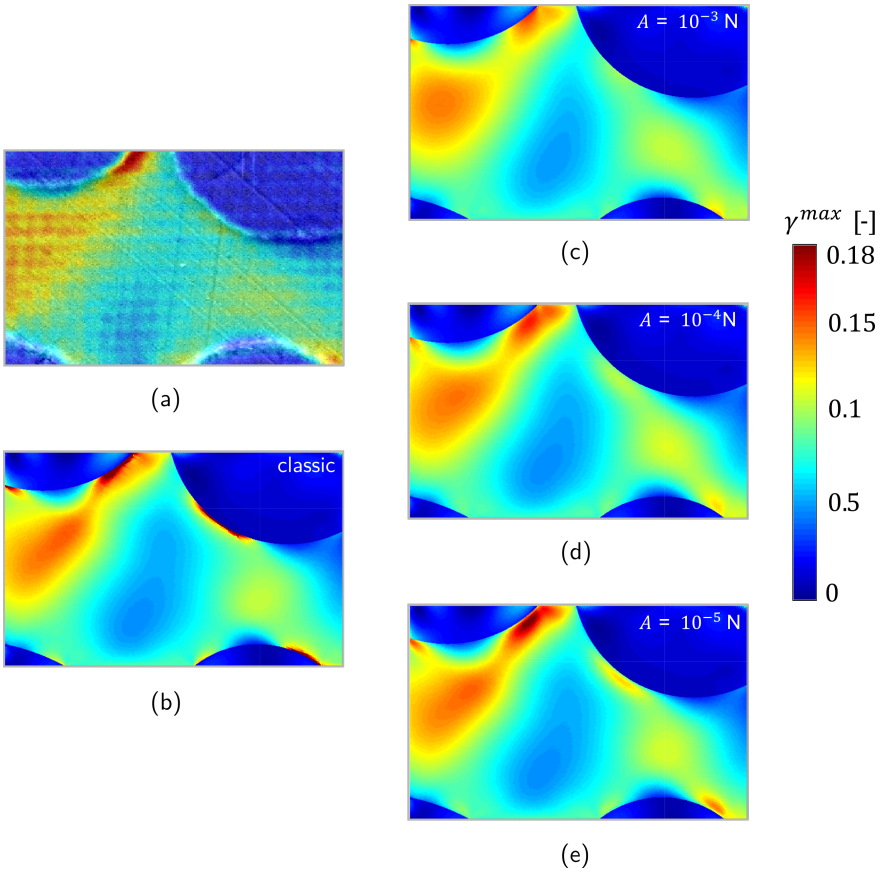
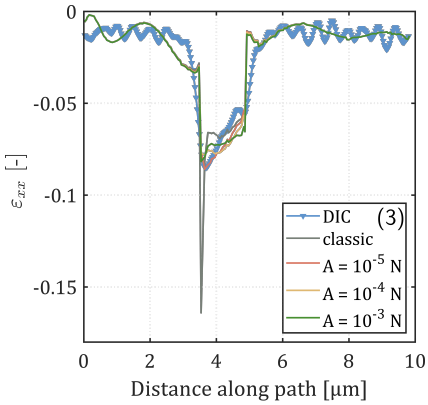
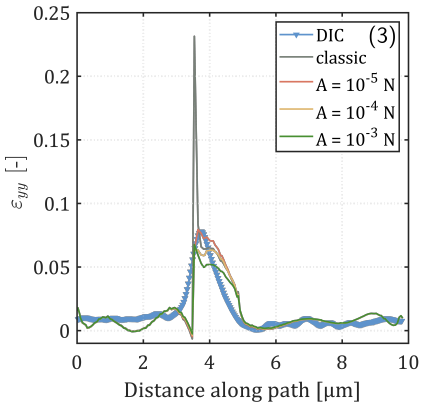


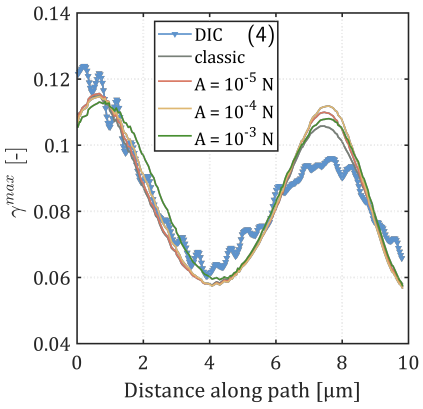
Fig. 5.12: Maps of ROI 2 showing the maximum shear strain γ^{max} just before failure for (a) the DIC results, (b) the classical model, (c) $A = 10^{-3}$ N, (d) $A = 10^{-4}$ N, (e) $A = 10^{-5}$ N.



(a)



(b)



(c)

Fig. 5.13: Evolution of strain profiles (a), (b) for ε_{xx} and for ε_{yy} along path (3) and (c) γ^{max} for path (4).

5.3.3 Transverse compression of macro UD specimens

The previous section showed that the micromorphic enhancement provides predictions that capture the microscale strain field with the capacity to also reproduce and regularise the plastic localisation bands. The question now is whether the model validated at the microscale is able to capture the macroscopic strengthening found in compression tests without any artificial increase of the matrix yield stress. To this end, the response of a UD composite deformed transversely was investigated. Fig. 5.14 illustrates the results of Chevalier et al. [8] mentioned in the introduction, namely the underestimation of the stress-strain curve predicted by a macroscale continuum model for a UD in a FE analysis, by comparing the experimental response (blue curve) and the predictions of the classical model (dotted grey curve).

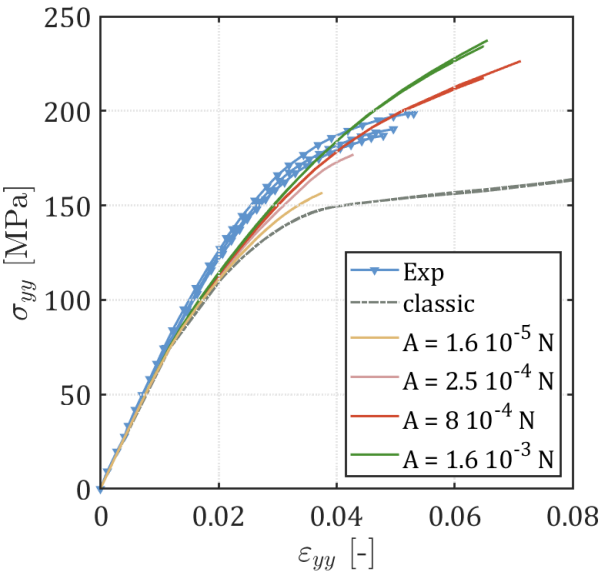


Fig. 5.14: Stress-strain responses from the transverse compression of UD composites. Comparison between experimental results (blue triangles), the prediction of the classical model (dotted grey line) and the predictions of the micromorphic model for different values of A.

To illustrate the impact of the micromorphic enhancement of the model, Fig. 5.14 presents the stress-strain curves obtained using different values of A (coloured curves) within the range identified in the previous section. Several realisations of the RVE are simulated with different arrangements of fibres. Higher values of A lead to a more pronounced strengthening effect, as expected. Notably, for A between 10^{-4} - 10^{-3} N, the predicted stress level before failure

reproduces much better the experimental results. Contour plots of the cumulative plastic strain p in Fig. 5.15 provide a basis for explaining the trends in Fig. 5.14. The plastic strain localises in bands aligned with the maximum shear direction for both model formulations, as expected for transverse loading conditions [76, 105, 112, 114]. For the classical model in Fig. 5.15 (a), the strain localises excessively in these bands, due to the strain softening behaviour of the matrix. Hence, once the first elements enter the softening regime, a localisation band is formed, which then propagates but does not widen. The onset of strong non-linearity in the stress-strain curve is a direct consequence of the propagation of such localisation bands. The contour plots for the micromorphic model in Fig. 5.15 (b)-(c) show that, although the strain localisation pattern is equivalent to the classical model, the width of the localisation bands and the strain amplitudes within the bands greatly differ. Similarly to the single fibre case of section 5.3.1, higher values of A lead to plastic localisation in wider bands. As a consequence, the strain amplitudes within broader bands are lower as larger material regions are involved in the softening. Hence, the micromorphic enhancement delays the initiation of the localisation bands and allows delocalising the plastic strain. The combination of these effects leads to an increased load-bearing capacity of the RVE, therefore increasing the stress level in the stress-strain curves.

Still, despite the increase in peak stress, the pre-peak non-linearity predicted by the micromorphic model does not completely match with the experimental results. This may point out some missing elements in the modelling strategy. For instance, the source of the experimental non-linearity could be caused by the impact of localisation bands formed in the inter-tow matrix regions, by the necessity to implement a damage model for the fibre/matrix interface or by a combination of both.

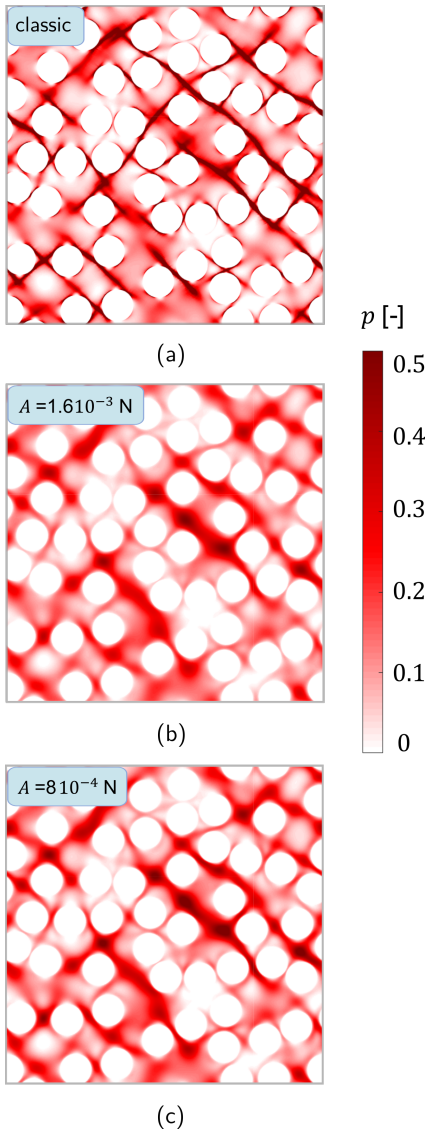


Fig. 5.15: Maps of the cumulative plastic strain p at a macroscopic load equivalent to $\bar{\varepsilon}_{yy} = 0.045$ [-] for (a) $A = 0$ N (classical model), (b) $A = 1.6\ 10^{-3}$ N and (c) $A = 8\ 10^{-4}$ N.

First, inter-tow shear band formation has been experimentally observed for the transverse compression of UD composites by Chevalier et al. [76]. Yet, the present RVE formulation solely focuses on the intra-tow representativeness of the composite. Hence, as inter-tow regions within the composite are filled

with larger matrix pockets prone to form localisation bands, it is possible that part of the observed non-linearity results from these mesoscale shear bands. The discrepancy of the non-linear part of the stress-strain curve between experiment and FEA may then simply be a consequence of inadequate choice of RVE. Second, incorporating damage in the model will affect the load-bearing capacity of the RVE. RTM6 UD composites have been shown to not develop progressive damage in the matrix under transverse compression [12, 76, 291], hence it most likely will not improve the numerical predictions. Although no significant amount of fibre/matrix decohesion has been observed prior to failure, implementing a fibre/matrix decohesion criterion (via cohesive elements for instance) can provide an additional source of non-linearity. As the DIC results of section 5.3.2 have shown, intense strain localisation systematically occurs at the fibre/matrix interface in regions of high maximum shear, leading to subsequent fibre/matrix cracks appearing shortly prior to global failure of the specimen.

Regardless of the underlying physical reason, traditional macroscale models are not able to capture the response of confined matrix regions in-between fibres, which must accommodate large strain gradients while enforcing the plastic strain to be zero on the interface. The micromorphic model delays and diffuses the strain in these microscale regions, limiting the intensity of the local strain gradients, hence allowing the material to more easily adapt to the loading. This is a consequence of the extra hardening associated to the accommodation of large strain gradients. Still, the question remains whether true size-dependent plasticity or inherently different properties of the matrix between fibres is the most realistic representation. The DIC results confirmed that a non-negligible interphase region exists around the fibre, yet the micromorphic model is able to mimic the effect of the interphase. In the case of the RVE predictions, stiffer fibres in the transverse direction provide a better match with experimental results (see appendix 5.5). Hence, explicitly considering a stiffer interphase around each fibre could partially lead to a similar effect. At this stage, it is not entirely feasible to deconvolute strain gradient plasticity effects and possible intrinsic change in properties in the interphase region. Additionally, the apparent higher matrix hardness and stiffness, as identified by nanoindentation, may also play a role in delaying the onset of plasticity in the matrix pockets. Nonetheless, this work clearly demonstrates that size-dependent plasticity plays a significant role in dictating the shear-band formation during loading. Further investigations using, for instance, nanoindentation tests and simulations will provide additional insights.

5.4 Conclusion

In the context of bottom-up multiscale approaches, computational micromechanics requires an accurate representation of the composite constituents to generate

trustworthy predictions [146]. In loading scenarios where the matrix develops significant plasticity, common phenomenological matrix constitutive models used in composite RVEs fail in numerous occasions to reproduce experimental results. In this work, a multiscale investigation and validation of a constitutive model enhanced by a micromorphic formulation is, for the first time, applied to polymer-based composites. Experimental validation at the microscale was established by transverse compression of notched specimens relying on advanced nano DIC with a resolution at the scale of the plastic heterogeneities. Macroscale validation was sourced from a previous study in which transverse compression tests were performed on cubic UD specimens. The main results from this work are:

- The micromorphic enhancement of the constitutive model using the cumulative plastic strain successfully predicts a strengthening effect in confined matrix volumes while simultaneously providing a regularisation which prevents excessive strain localisation in the form of shear bands.
- The use of the micromorphic model applied to the case of microscale DIC transverse compression tests provides significantly improved predictions for the local strain distribution in-between fibres. Particularly, regions of strain concentration at the fibre/matrix interface prior to cracking are accurately captured by the model.
- The calibration of the model with the experimental DIC results provides an estimate for the ideal intrinsic length needed for the material model, namely around 10-20 µm.
- The prediction for the macroscale transverse compression tests using the micromorphic model and the identified intrinsic length fit significantly better with the experimental results. The main remaining source of discrepancy lies within the pre-yield non-linearity.

The potential of a simple - at least in its formulation - micromorphic model to improve the predictive capabilities for composite systems in loading conditions leading to strong plastic deformation has been demonstrated. The combined impact of size effect strengthening via the introduction of an internal length scale to an existing constitutive model and the regularisation potential overcome the limitation caused by the strain softening behaviour of the matrix in such simulations. While this study did not include damage or failure neither in the matrix nor for the interfaces (which is left for further investigation), it provides significantly improved predictions of the plastic strain localisation pattern in-between the fibres. The knowledge of the loci of maximum shear strain should improve the prediction of failure in transverse compression. It further opens the door to study the case of nanoindentation in resin-rich pockets. Ultimately, this work demonstrates the necessity to provide experimental validation across different length scales for computational micromechanics.

5.5 Appendix

5.5.1 Case of isotropic fibres

The match between the predictions of the micromorphic model using orthotropic fibres and the experimental curves is not perfect, as mentioned above. Particularly, the onset and the magnitude of the non-linearity within the stress-strain curves significantly differ. Several reasons have been postulated to explain this discrepancy. In an attempt to provide additional insights, the RVE simulations were repeated using purely isotropic fibres with elastic constants equal to the fibre's properties in the axial direction. The corresponding stress-strain curves are shown in Fig. 5.16. Surprisingly, the match between FE predictions and experimental curves is perfect for $A = 2.5$ - $8\ 10^{-4}$ N. Fig. 5.17 compares the contour plots of p obtained using orthotropic and isotropic fibres for the classical case and A = $2.5\ 10^{-4}$ N. Evidently, as the isotropic fibres are much stiffer in the transverse direction, they deform less for a given macroscopic strain, resulting in higher strains within the matrix. Hence, in the case of isotropic fibres, the initiation of localisation bands, which still follows the maximum shear direction, is triggered earlier. This leads to an earlier onset of non-linearity within the stress-strain curve. Simultaneously, the micromorphic model spreads the plastic strain localisation, therefore allowing the matrix to carry the load for longer and thus providing an almost perfect match with the experimental results.

5.5.2 Influence of the fibre diameter

Lastly, the SEM images indicate that the actual fibre diameter is around 7 µm rather than the 5 µm used as reference in this work. Therefore, the RVE simulations were once more performed using this new fibre diameter while preserving the same volume fraction. Both the orthotropic and isotropic cases were considered. Fig. 5.18 plots the stress-strain responses of the UD for different values of A. Comparing with Fig. 5.14 for the orthotropic fibres (dotted curves in this case), the increase in fibre diameter promotes a bit more non-linearity, hence slightly improving the fit with experimental results. This suggests that the matrix pocket sizes in the RVE (dictated by the fibre size) also impact the non-linearity of the stress-strain response.

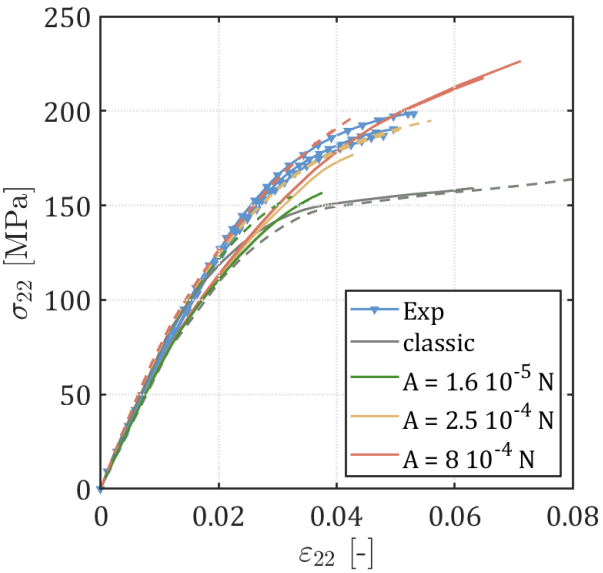


Fig. 5.16: Stress-strain responses from the transverse compression of UD composites for purely *isotropic* fibres. Comparison between experimental results (blue triangles), the prediction of the classical model (dotted grey line) and the predictions of the micromorphic model for different values of A.

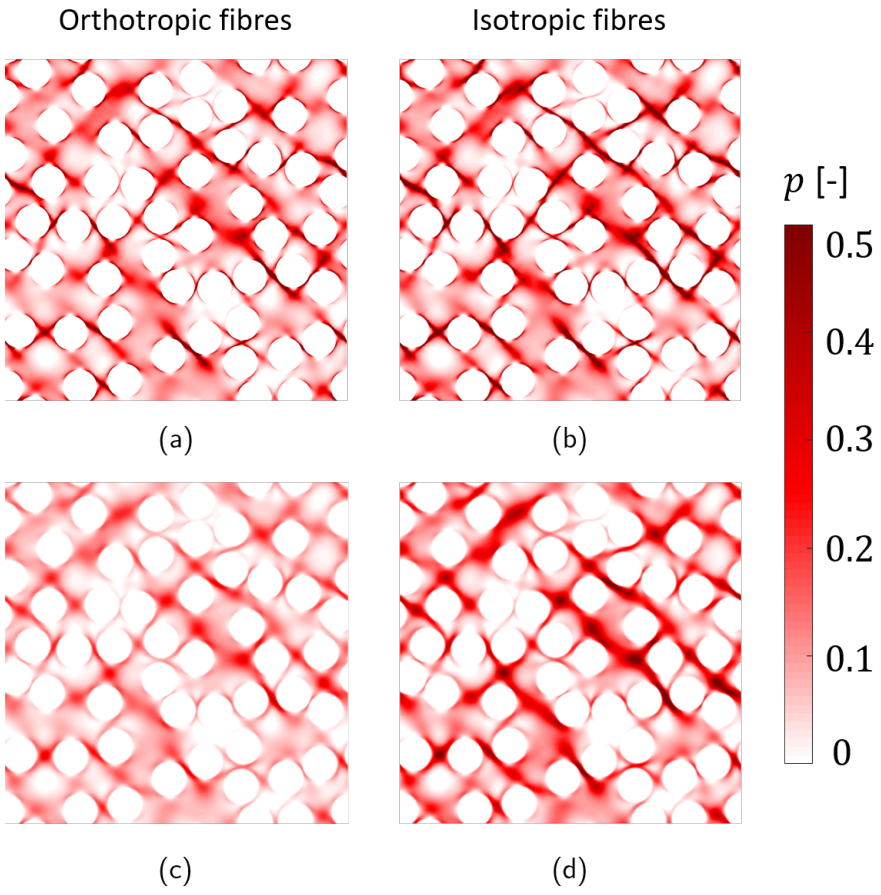


Fig. 5.17: Maps of the cumulative plastic strain p at a macroscopic load equivalent to $\bar{\varepsilon}_{yy} = 0.035$ [-] for (a) and (c) orthotropic and (b) and (d) isotropic fibres. (a) – (b) $A = 0$ N (classical model) and (c) – (d) $A = 2.5\ 10^{-4}$ N.

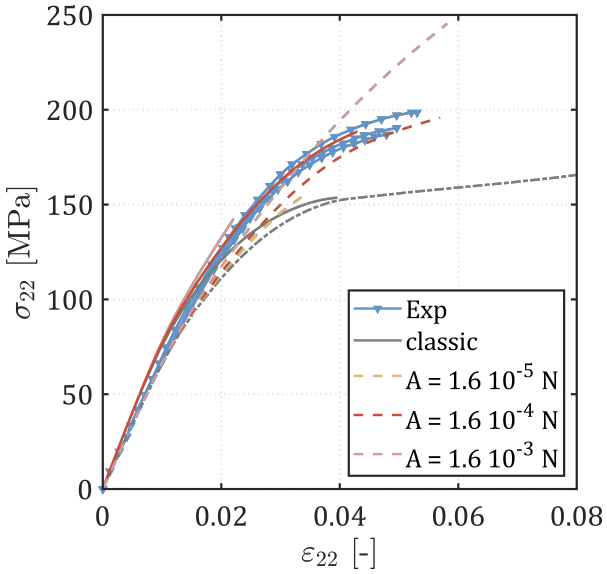


Fig. 5.18: Stress-strain responses from the transverse compression of UD composites with a fibre diameter of 7 µm. Comparison between experimental results (blue triangles), the prediction of the classical model (dotted grey line) and the predictions of the micromorphic model for different values of A. Dotted line = orthotropic fibres, full line = isotropic fibres.

6

Nanoindentation response of bulk epoxy and in confined volumes

Abstract

The local mechanical characterisation of the matrix of fibre-reinforced composites via nanoindentation provides the essential in-situ elastoplastic properties, needed for multiscale modelling purposes. However, two key features of the nanoindentation response of glassy polymers remain unsolved: the origin of the indentation size effect (ISE) at small indentation depth and the impact of confined volumes (i.e. in-between fibres) on the local polymer structure and/or properties. In particular, effects related to physical ageing or the test strain rate which may bias the amplitude of hardness for the ISE and the matrix pockets are not often addressed in the literature. In this chapter, the impact of physical ageing/rejuvenation and of the strain rate (in the low regime) on the ISE and the in-situ pockets have been studied for a highly cross-linked thermoset epoxy. Physical ageing is found to contribute to both the ISE and the in-situ properties, but it is not the underlying cause of the observed phenomena. The very low strain rate response assessed via indentation relaxation tests show a change in rate-dependency, hinting towards a reduction of the ISE at low strain rates. The aged in-situ properties indicate a different rate-dependency as well, compared to the rejuvenated case.

6.1 Introduction

The current trend in the field of micromechanics of fibre-reinforced composites is to determine the local properties of the constituents (i.e. fibres, matrix, interphase and interface) in the so-called *in-situ* configuration, namely as part of a composite structure. The objective is to provide the community with essential data regarding the deformation and failure mechanisms at the (sub-)micron level to aid advancing multiscale modelling as well as to improve the understanding of the mechanisms that can guide towards more efficient materials. Studies have shown that an inaccurate representation of one of the constituents may strongly affect the predictive capability of numerical models for composite applications [76, 217]

In recent years, the determination of the matrix in-situ properties has gained increased interest driven by the need to understand and predict the formation of shear bands in the matrix, which has been shown to cause large stress and strain concentrations leading to interfacial damage in transverse loadings by compression or shear. Consequently, many characterisation techniques have been developed to assess the in-situ properties. Section 2.3 and appendix A already provided an overview of the main progress within the field. Nanoindentation and its derivative techniques, such as micropillar compression and AFM, have become key tools in the arsenal of the micromechanics community. In particular, it allowed for the identification of size effects in glassy polymers [168], the presence of an interphase in FRPs [194], the influence of fibre proximity on the in-situ polymer properties [151], etc.

While significant progress has been made in the understanding of the deformation of glassy polymers in confined volumes or under large strain gradients (e.g. in between fibres), open questions remain regarding the origin of the indentation size effect (ISE) and of the cause for the higher in-situ properties.

Regarding the ISE, the literature dealing with the effect of rejuvenation and physical ageing on the amplitude of the ISE remains scarce and no systematic approach has been developed to further quantify the ISE on both the hardness and the modulus. Nikaeen et al. [290] showed that plastic deformation of bulk glassy thermoplastics leads to rejuvenation of the polymer. The hardness evolution shows evidence of a reduced size effect for the deformed polymer. The influence of the strain rate on the ISE, particularly at very high or low rates, has not been addressed in the literature. Voyiadjis et al. [153] showed that, for typical indentation rates, the rate-dependency of glassy thermoplastics could not fully account for the ISE. Still, Baral et al. [341] studied the extremely low strain rates (down to 10^{-8} s^{-1}) of PMMA and showed that a change in rate sensitivity occurs at low strain rates at large indentation depths. Such a phenomenon may also occur at lower depths. Finally, the use of finite element

models based on strain gradient plasticity or elasticity frameworks to study the ISE is also rarely applied to polymer glasses.

Regarding the in-situ properties, most studies report a difference in the properties between the bulk polymer and the matrix pockets, however an in-depth characterisation is still missing. Recently, Pecora et al. [192] tackled the case of viscoelasticity for an epoxy and reported a difference in modulus between in-situ measurements at the surface and in the core of the composite, hinting towards an impact of the thermomechanical history on the measured in-situ properties. Gayot et al. [142] addressed the effect of physical ageing on a PMMA-based thermoplastic and showed that ageing occurs faster in the matrix pockets compared to the bulk, leading to a difference in properties over time.

The purpose of this chapter is two-fold. First, the ISE in RTM6 epoxy is studied by carefully measuring the low indentation response and minimise tip-related bias. The effects of physical ageing and of the rate dependency of the epoxy are assessed in order to provide insights into the mechanisms at the origin of the ISE. Second, the in-situ properties of RTM6 composites at large indentation depths is addressed experimentally to carefully determine the difference in mechanical response between bulk and in-situ properties. In particular, the very low strain rate behaviour is studied by means of indentation relaxation tests allowing the extraction of rate sensitivity factors and activation volumes. The impact of physical ageing/rejuvenation is also addressed, as a difference in ageing has been speculated to cause the difference in in-situ properties. The chapter starts by briefly reminding the necessary nanoindentation theory. Then the ISE on pure RTM6 is tackled. The chapter finishes with the characterisation of the in-situ mechanical response.

6.2 Theory

In this section, the theory of nanoindentation is briefly recalled to aid with the derivation of the constant contact stiffness strain relaxation formalism developed by Baral et al. [341].

6.2.1 Classical nanoindentation

As described in section 2.3.1, the hardness is defined as:

$$H = \frac{F_{max}}{A(h_c)}, \tag{6.1}$$

where $A(h_c)$ is the actual contact area based on the Oliver and Pharr method [147]:

$$A(h_c) = 24.5h_c^2 = 24.5\left(h - \varepsilon\frac{F_{max}}{S}\right)^2. \tag{6.2}$$

Here, S is the harmonic contact stiffness and ε a geometry factor.

The modulus can be calculated based on:

$$\frac{1}{E^*} = \frac{1-\nu^2}{E} + \frac{1-\nu_i^2}{E_i}, \tag{6.3}$$

where

$$E^* = \frac{S}{2}\sqrt{\frac{\pi}{A(h_c)}}. \tag{6.4}$$

6.2.2 Constant contact stiffness relaxation

Nanoindentation relaxation tests offer the possibility to assess a material's rate-dependent behaviour over a large range of strain rates. In this work, constant contact stiffness relaxation tests have been performed based on the newly developed method of Baral et al. [341]. The advantage of the constant contact stiffness method compared to typical constant strain rate relaxation tests is its insensitivity to thermal drift issues, allowing to perform longer tests (i.e. covering a wider range of strain rates) [342, 343]. During the nanoindentation relaxation test, the load is progressively increased at a constant strain rate to reach a target contact stiffness value, where a hold segment is set for a given time, followed by a constant rate unloading given by $\dot{F}/F$, where F is the imposed force. The hardness can be determined by combining equations 6.1 and 6.4:

$$H = \frac{4F}{\pi}\left(\frac{E^*}{S}\right)^2, \tag{6.5}$$

where the value of E^* is taken at the end of the loading step.

As no displacement of the indenter tip occurs during the hold segment, the typical expression of the indentation rate as $\varepsilon = \dot{h}/h$ does not hold and it is necessary to redefine a representative strain rate. As detailed in Baral et al. [341], by imposing that the total strain rate $\dot{\varepsilon} = 0$ and assuming that $\dot{\varepsilon}$ is the sum of the elastic $\dot{\varepsilon}_{el}$ and viscoplastic $\dot{\varepsilon}_{vp}$ strain rates, one can express the representative strain rate under the indenter as:

$$\dot{\varepsilon}_r = \dot{\varepsilon}_{vp} = \frac{|\dot{\sigma}_r|}{E^*}, \tag{6.6}$$

where σ_r is the representative stress under the indenter. Rodriguez et al. [163] developed a methodology for amorphous cohesive frictional materials to

determine the representative stress under the indenter based on the work of Johnson [344]. Following this approach, it is possible to relate the measured hardness H during the hold segment to σ_r using:

$$\sigma_r = \frac{H}{C}, \tag{6.7}$$

where C is a constraint factor that can be identified by prior knowledge of the friction angle β of the material. For RTM6, $\beta = 7.86$ and the derived value for C is around 2.15.

Finally, a rate sensitivity m can be defined by relating the change in representative stress σ_r with the indentation rate $\dot{\varepsilon}_r$:

$$m = \frac{d\log \sigma_r}{d\log \dot{\varepsilon}_r}. \tag{6.8}$$

The related apparent activation volume can then be expressed as:

$$V = \sqrt{3}kT\frac{d\log \dot{\varepsilon}_r}{d\sigma_r}. \tag{6.9}$$

6.3 Materials and methods

6.3.1 Nanoindentation tests

Nanoindentation tests were carried out using a Nanoindenter G200 (KLA) with a Berkovich tip using a Dynamic Contact Module (DCM II) head allowing for high precision measurements. In all instances, the continuous stiffness measurement (CSM) mode was activated. The CSM mode allows continuous measurement of both the hardness and the contact stiffness by superimposing a small oscillatory load over the main loading segment. Two types of tests were performed: classical indentation and constant contact stiffness relaxation. Both types of tests were carried out on bulk epoxy and UD composite specimens.

Classical nanoindentation tests were carried out at different prescribed loading rates $\dot{F}/F$ ranging from 0.01 s^{-1} to 0.1 s^{-1}. The surface approach rate and the contact stiffness detection criterion were set to 5 nm/s and 25 N/m, respectively. On bulk samples, the maximum indentation depth reached up to 2500 nm whereas the maximum depth in the resin pockets of the UD was limited to 1000 nm. The chosen resin pockets were large enough to avoid significant fibre-bias effect below a depth of 1000 nm.

The relaxation tests were based on a DCM II tip combined with a CSM mode with a frequency of 75 Hz. The oscillation amplitude was set to 2 nm. A loading rate $\dot{F}/F$ of 0.05 s^{-1} is applied. The contact stiffness S for the hold

segment is mostly set to 12 kN.m^{-1} corresponding to an equivalent indentation depth of 500 nm. Some depth-dependent relaxation tests were also carried out and required adapting the hold contact stiffness. The hardness during the hold segment is calculated using Eq. 6.5. The control of the contact stiffness is made by a PID controller. A crucial step is to minimise the amplitude of the initial overshoot, as it gives unreliable results, hence care was taken to calibrate the PID controller for each pair of target contact stiffness and indentation depth.

To accurately evaluate the plastic strain rate under the indenter, the measured signal needs to be cleaned, as any noise in the signal will be amplified upon differentiation. Hence, the post-treatment included a re-sampling at a constant spacing of 0.02 on a log-time scale of each test curve, followed by averaging of all re-sampled test curves per sample, and finally re-processing using a moving average of 50 points. This procedure allows generating a smooth curve suited for differentiation without affecting the general trend of the H or σ_r curve, as explained by Baral et al. [341].

6.4 Results and discussion

6.4.1 Indentation size effect

Tip-related factors

Fig. 6.1 shows the hardness and modulus measured for bulk RTM6 as a function of the indentation depth. The hardness decreases with indentation depth for penetrations below 500 nm, as expected for an amine-based highly cross-linked epoxy [168]. Fig. 6.1 (a) also shows the fitting of the hardness curve with the previously defined depth-dependent hardness model of Lam and Chong [176] and Han and Nikolov [185] (assuming $\gamma = 0.45$). In the present case, the Lam and Chong model overestimates the amplitude of the ISE on the hardness, whereas the Han and Nikolov model provides a better fit. This is in contradiction with the results of Chevalier [157] for the same RTM6 material (the experimental curve is given in Fig. 2.19). The reported results of Chevalier [157] give a similar amplitude for the ISE on RTM6 but accompanied with an increase in depth range, leading to a more gradual decrease and hence giving a better fit with the Lam and Chong model. One may wonder what is the cause of this discrepancy?

These results point out a key challenge in the study of the ISE in polymers. The reported ISE may strongly differ depending on the test conditions, hence making modelling attempts to unravel an underlying physical reason beyond the ISE more challenging. Therefore, extrinsic factors affecting the nanoindentation test have to be considered. As mentioned in section 2.3.1, three main factors contribute to an inaccurate estimate of the material properties at low

indentation depths: the tip force-displacement resolution, the surface quality, and the tip bluntness.

The G200 nanoindenter used in this work (and in the work of Chevalier [157]) has two main loading heads: an XP head and a DCM II head [345]. The main difference between the two indentation heads is the increased resolution of the DCM head, allowing for accurate force-displacement measures at depths as low as 10 nm. As the determination of the contact area is based on the indentation depth, any error on the displacement below 100 nm may significantly impact the perceived indentation hardness, potentially leading to a false ISE. Coming back to the discrepancy of the RTM6 results, the apparent higher and more extending ISE of Chevalier [157] may originate from their use of the XP head compared to the DCM II head used in this work.

Tip bluntness or surface irregularities strongly influence the measured contact area using the Oliver and Pharr or Loubet methods [346–349]. For instance, Loubet et al. [350] showed that the tip bluntness should be accounted for in the contact area determination as it may otherwise induce artificial ISE in certain materials. Similarly, surface bumps or cavities can have a similar impact as tip bluntness on the apparent contact area [173]. Such features are typically less than 20 nm in size. Therefore, extreme care must be taken in the determination of the area function in order to avoid propagation of errors in the measured contact area, hardness or modulus.

A prime example in the literature of the difficulty to determine a true ISE is the study of PMMA. PMMA has been a model candidate to study the mechanical behaviour of glassy amorphous thermoplastics for decades. Regarding the ISE on the hardness, several studies either claim that an ISE exists [61, 153, 351–353] in PMMA or that it does not [142, 347, 349, 354]. In principle, PMMA should not exhibit an indentation size effect [179], given its simple molecular structure (assuming that simple molecular chain structures cannot indeed lead to any ISE). Thus, the case of PMMA illustrates that, depending on the study, an ISE may be found or not, making it difficult to distinguish true ISEs from experimentally biased ones (at least partially).

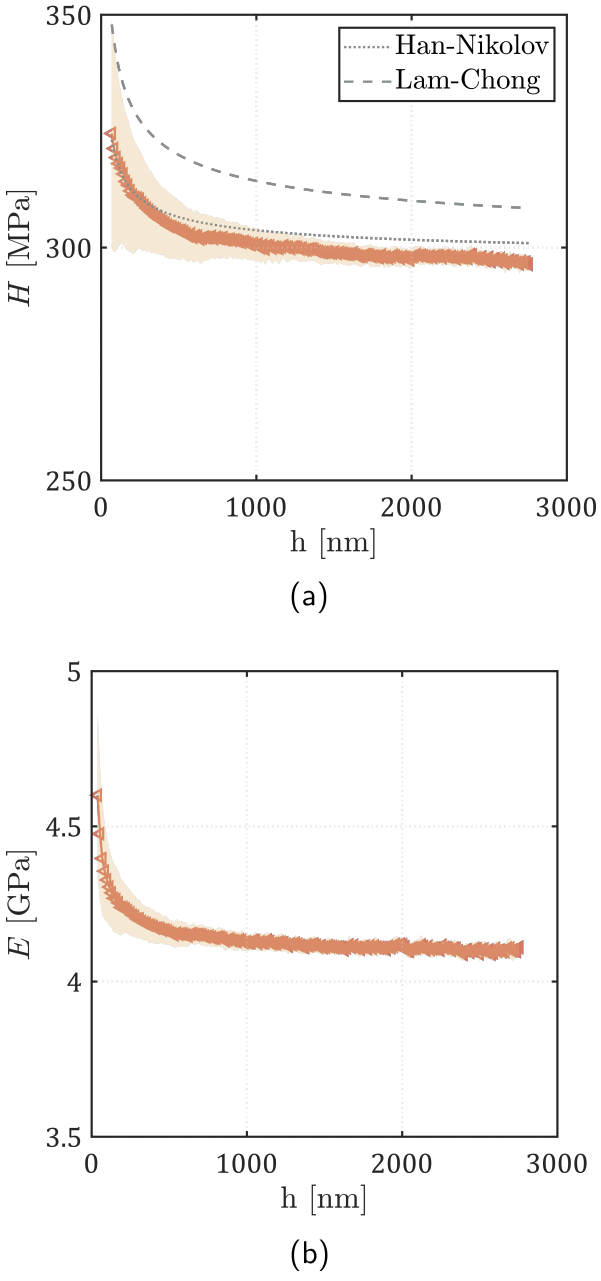


Fig. 6.1: Indentation hardness H and modulus E with respect to the indentation depth h for bulk RTM6 at a rate $\dot{\varepsilon} = \dot{F}/F = 0.05\ \mathrm{s}^{-1}$. Both the hardness and modulus curve present an indentation size effect at low indentation depths (<500 nm). The shaded area shows the experimental error.

Thus far, the discussion focused on the hardness. Nonetheless, an ISE also appears on the elastic modulus. Recent investigations have pointed out that the ISE in polymer glasses is highly elastic in nature [62, 355]. As such, an ISE on the modulus is almost always observed, whether the hardness exhibits an ISE or not. First, one should not forget that the measured modulus is still influenced by factors such as the hydrostatic stress. As mentioned in section 2.3.1, the high hydrostatic stress under the indenter in the beginning of indentation has been linked to a shift of the local T_g, inducing a stiffer response [172, 175]. Analytical models using the gradient of elastic strains (potentially coupled with plasticity) have proven useful for capturing the ISE on the modulus [62, 355]. For instance, these studies indeed suggest that PMMA should present a size effect, both on the modulus and the hardness.

To summarise, the present modulus and hardness curve clearly show an ISE for RTM6, considering that the aforementioned factors have been taking into account in the data treatment. The maximum amplitude of the ISE on both hardness and modulus is around 15% and extends over a depth of around 500 nm.

Effect of rejuvenation and ageing on ISE

The impact of physical ageing is considered in an attempt to provide additional insights into the physical mechanism at the origin of the ISE. A rejuvenation treatment consisting of 15 minutes at 235°C (i.e. above T_g) has been applied, following the work of Morelle [7]. The resulting H and E variations as a function of the indentation depth are given in Fig. 6.2. The as-cure and rejuvenated curves are very similar, not only in terms of ISE but also regarding the plateau value. This could have been expected as RTM6 does not show significant variations in stiffness and yield stress with physical ageing, as reported by Morelle [7]. Still, the rejuvenated sample shows a more severe decrease of H and E in the first 250 nm compared to the as-cured sample. This could be related to the increased mobility of the polymer chains in the rejuvenated stated. Ultimately, these results suggest that surface physical ageing of the epoxy may slightly contribute to the ISE but is not the underlying cause of the ISE. Further discussions regarding the influence of physical ageing on RTM6 when tested in a composite are given in section 6.4.2.

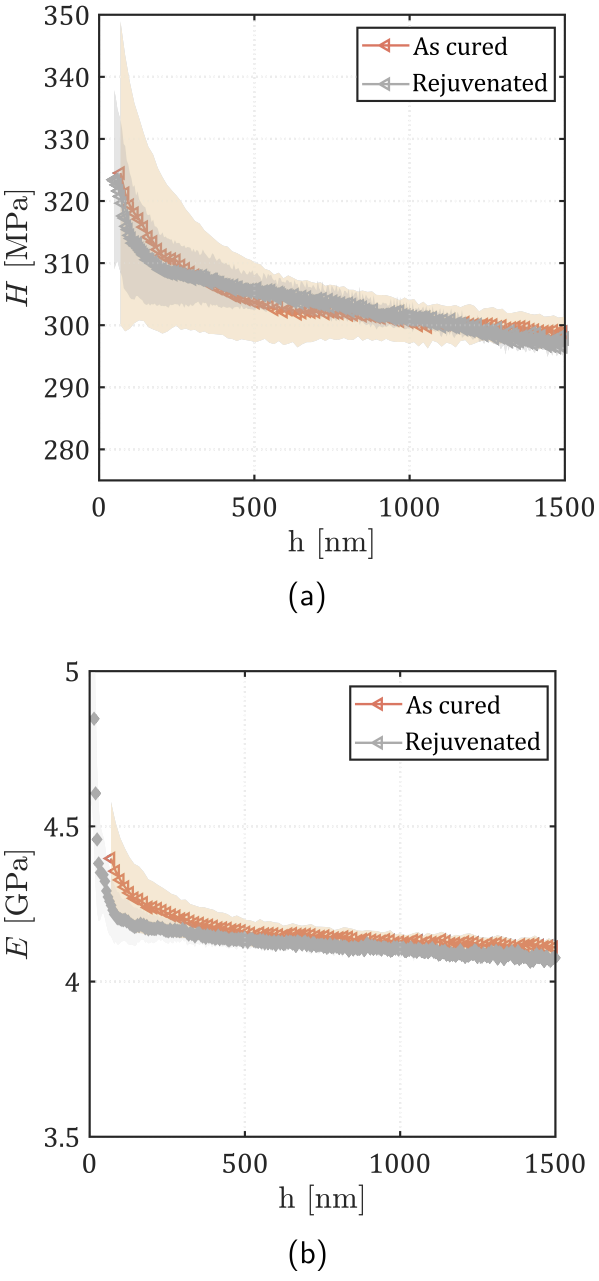


Fig. 6.2: Impact of thermal rejuvenation on the indentation (a) hardness H and (b) modulus E with respect to the indentation depth h for bulk RTM6 at a rate $\dot{\varepsilon} = \dot{F}/F = 0.05\ \mathrm{s}^{-1}$.

Influence of strain rate

During a nanoindentation test, the imposed strain rate, defined as the ratio of $\dot{F}/F$, is not directly attained and involves an exponentially decaying evolution. The range of indentation depth needed to reach the imposed strain rate depends not only on the approach parameters imposed to the machine, such as the surface stiffness detection or the surface approach rate, but also on the material itself. For instance, Baral [349] showed that, for a given choice of approach parameters, the stabilisation depth for PMMA is around 100 nm while it is 1000 nm for an elastomer. Additionally, as the imposed strain rate decreases, the stabilisation depth increases [153]. Therefore, the variation of the strain rate over the first few hundreds of nanometers raises the question about its impact on the ISE of rate sensitive materials. Voyiadjis et al. [153] assessed this influence for PC and PMMA and noted that, while the variation of the strain rate influences the amplitude of the ISE, it is not solely responsible for it.

In attempt to further investigate the ISE in RTM6, the same approach as proposed by Voyiadjis et al. [153] is used here. First, Fig. 6.3 shows the actual strain rate during indentation $\dot{F}/F$ as a function of the indentation depth for three different strain rates. The trend agrees with the aforementioned results. Note that the stabilisation depth goes from roughly 100 nm at 0.05 s^{-1} to 400 nm at 0.01 s^{-1}.

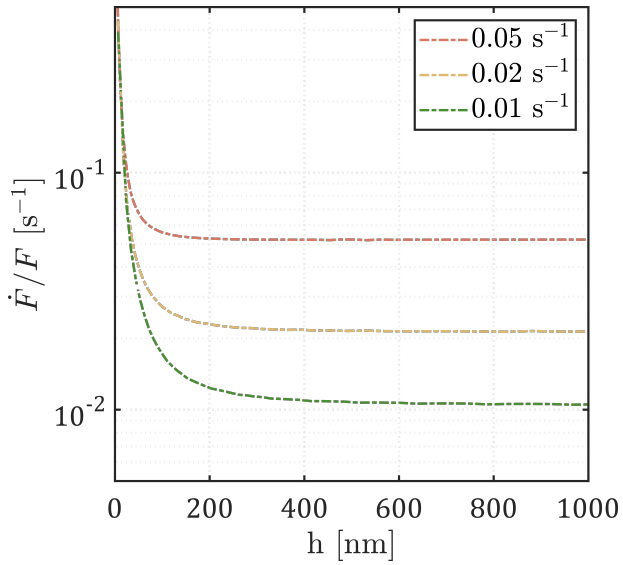
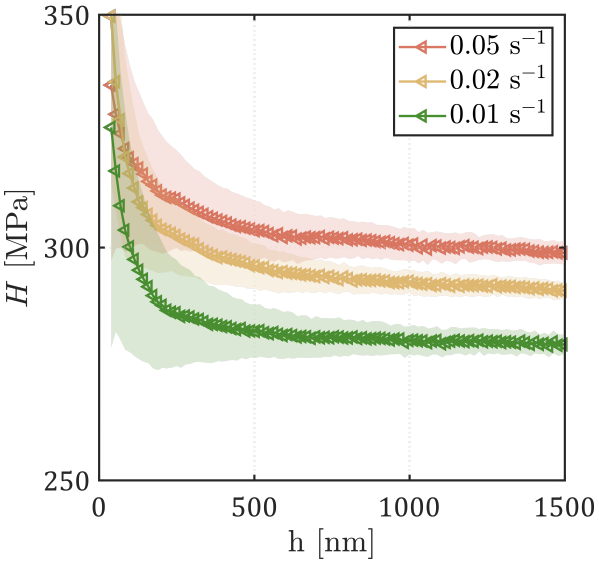


Fig. 6.3: Variation of the loading rate $\dot{F}/F$ measured experimentally with the indentation depth h. The imposed indentation loading rates are given in the figure. The lower the imposed rate, the higher the stabilisation depth.

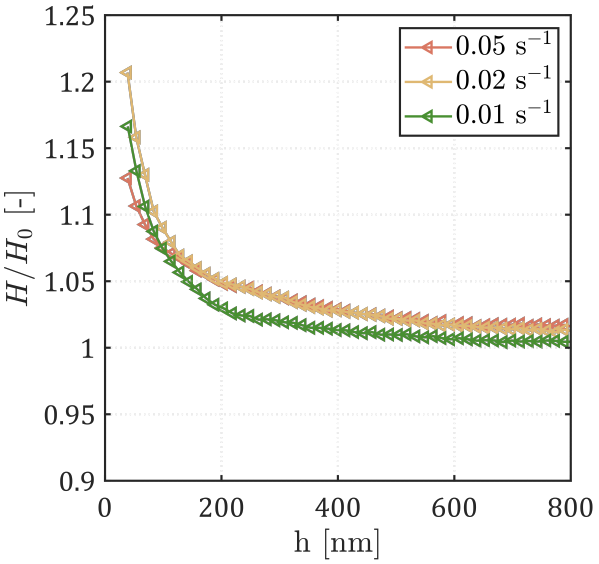
Fig. 6.4 (a) and Fig. 6.5 (a) show the H and E variations in terms of h at the rates shown in Fig 6.3. The strain rate evolution affects the hardness, but does not seem to significantly impact the modulus, in agreement with the literature for RTM6 [171]. In order to highlight the amplitude of the ISE and the effect of the strain rate, Fig. 6.4 (b) and Fig. 6.5 (b) show the same results but normalised by the plateau values H_0 and E_0. For H, the ratio H/H_0 is almost independent of the strain rate. Only the case of 0.01 s^{-1} shows a more rapid decrease of H, although the difference is only around 2%. This may be related to the evolution of $\dot{F}/F$: at 200 nm $\dot{F}/F$ still decreases for the imposed rate of 0.01 s^{-1}. The relative modulus E/E_0 shows the same trends. Overall, the measured hardness and modulus fall within 5% of the plateau value at around 200 nm.

To determine to what extent the strain rate impacts the apparent ISE, the nanoindentation rate dependency of the hardness is evaluated. To that end, the plateau hardness value is expressed as a function of the imposed strain rate $H(\dot{\varepsilon})$, which results in a linear relationship, in accordance with the macroscale results (see chapter 3). Assuming that the hardness only varies with the indentation rate $\dot{F}/F$ over the whole indentation depth, a fictitious hardness is calculated H_{calc}. This H_{calc} therefore represents the increase of hardness that results from a higher $\dot{F}/F$ at low indentation depths. Fig. 6.6 compares the experimental curves with the values of H_{calc} as a function of h. Clearly, the higher rate at low indentation depth is insufficient to cause an increase of hardness on par with the measured ISE. Still, as the imposed strain rate decreases, the rate affected part of the ISE increases, suggesting that at lower test rates, the intrinsic ISE is reduced.

Following the results of Fig. 6.6, constant contact stiffness relaxation tests, as developed by Baral et al. [341] and detailed in section 6.2, were performed to investigate the low strain rate response of RTM6. To that end, relaxation tests were carried out at 200, 300, 400 and 500 nm indentation depths. Fig. 6.7 shows the evolution of the measured hardness as a function of the strain rate under the indenter $\dot{\varepsilon_r}$ for these different depths. Two main features appear. First, as the indentation depth for the relaxation test increases, the measured H curves start to decrease and to superimpose. Most notably, at 200 nm, the values of H are roughly 15% higher than at 500 nm. This corroborates with the classical indentation tests in terms of the increase in H at lower depths. Still, the classical tests showed that, at 200 nm, the amplitude ISE was only around 5%, compared to around 20% for the relaxation tests. The difference in amplitude may be related to the test method and to the subsequent determination of the contact area and hardness. Still, both techniques suggest that an increase in H occurs at lower indentation depths. Secondly, the slopes of the H curves at 200 and 500 nm seem to change differently as the rate decreases, particularly at low rates. This can be seen by the decrease in the difference of H when comparing the hardness at $\dot{\varepsilon}_r = 10^{-6}$ s^{-1} and 10^{-4} s^{-1}.



(a)



(b)

Fig. 6.4: Variation of the (a) indentation hardness H with respect to the indentation depth h for bulk RTM6 at different strain rates and (b) of the hardness normalised by the value at the plateau H/H_0 illustrating the magnitude of the ISE as a function of the imposed rate. The amplitude of the ISE reaches less than 5% of the plateau value at $h \sim 200$nm.

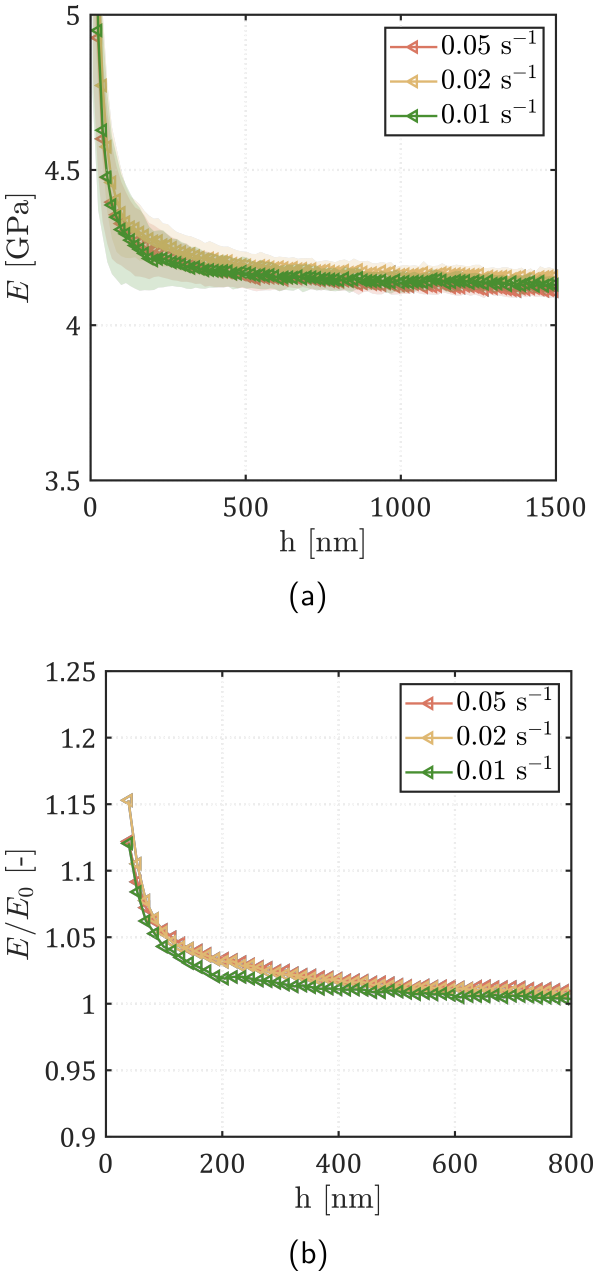


Fig. 6.5: Variation of the (a) indentation modulus E with respect to the indentation depth h for bulk RTM6 at different strain rates and (b) of the modulus normalised by the value at the plateau E/E_0 illustrating the magnitude of the ISE as a function of the imposed rate. The amplitude of the ISE reaches less than 5% of the plateau value at $h \sim 200$nm.

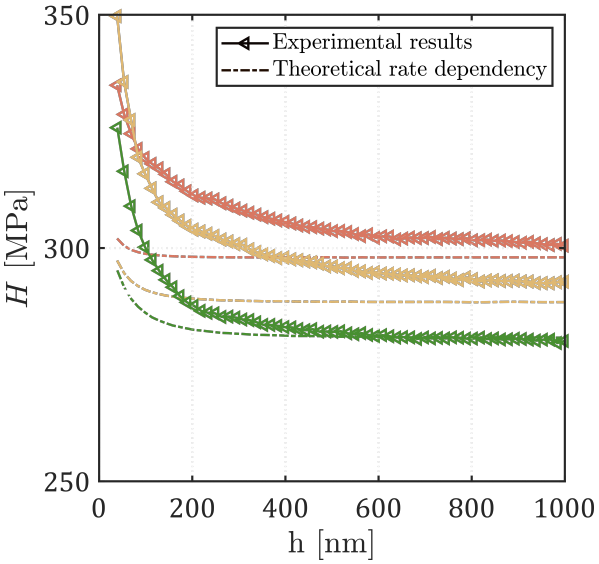


Fig. 6.6: Comparison between the experimental hardness and the calculated rate-dependent hardness (based on the plateau values) associated to the stabilisation of the strain rate during indentation The colour code is the same as in the previous figures.

To investigate this point further, Fig. 6.8 reveals the calculated activation volume for plastic flow during relaxation V and the rate sensitivity m, given by Eq. 6.9 and Eq. 6.8, as a function of $\dot{\varepsilon}_r$. V decreases as the strain rate increases, as expected [245], and is larger at lower indentation depths as it corresponds to larger H. The activation volume estimated at 200 nm indentation depth is significantly lower than for the other depths. The calculated V is in the correct order of magnitude for RTM6 (e.g. see [7] or chapter 3). The higher V at lower rates implies that intermolecular motion is facilitated, as the chains glide more easily on top of one another in the larger space, hence a lower stress level is sufficient to induce plastic flow [356]. The rate sensitivity m for each indentation depth is not strongly influenced by the strain rate, with variations of m lower than 0.005 (hence, the viscous law is adequate in that the rate sensitivity indicator is not rate sensitive). However, a slightly larger difference exist between the values at 200 and 500 nm. Particularly, the difference in m between 200-500 nm seems to decrease with decreasing strain rate. This suggests that at lower strain rates, the rate sensitivity of the material becomes less dependent on the indentation depth. This seems to align with the observed variation of H at lower rates. If verified at extremely low rates, these results would imply that the indentation size effect observed in classical indentation tests significantly decreases in amplitude as the strain rate decreases below 10^{-6} s^{-1}. Still, as mentioned before, the ISE cannot be fully captured by a rate-dependent yield at conventional strain rates. This dual dependence on

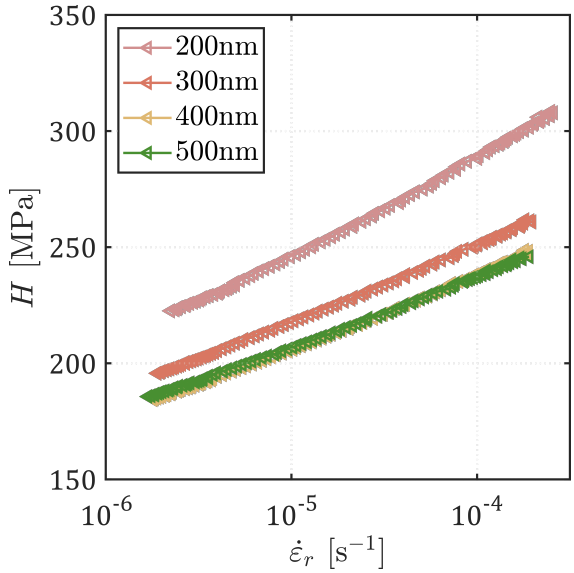


Fig. 6.7: Variation of the hardness H, as measured by constant contact stiffness relaxation, as a function of the strain rate under the indenter $\dot{\varepsilon}_r$ at different indentation depths.

the strain rate would suggest that a shift in rate-dependency of the relaxation mechanisms responsible for plastic flow occurs at low strain rates. Then, the observed ISE may simply be, to some extent, a consequence of this shift in rate-dependency.

The more fundamental question raised by these results is the relationship between the molecular mobility during viscoplastic flow and low strain rates. In particular, which mechanisms may present a shift in rate-dependency? Early results from Varnik et al. [357] using molecular dynamics simulation suggest that cooperative motions are necessary for plastic flow to occur and that a change in rate-dependency indeed exists, marked by a lower rate-dependency at low strain rates. This change was associated to the possibility of small secondary relaxation mechanisms to take place and relax some of the stress. Richeton et al. [356] also found that secondary relaxation processes need to be accounted for to describe the full rate and temperature response of glassy polymers. While the present results point towards a distinct rate-dependency at low strain rates accompanied by a lessened ISE, it remains difficult to draw any definite conclusions regarding the origin of the ISE. Additionally, the derivation of the hardness and the strain rate during the relaxation test assumes a constant modulus. This may not be entirely valid for the whole spectrum of strain rates and may induce some errors in the results. Nonetheless, the classical indentation

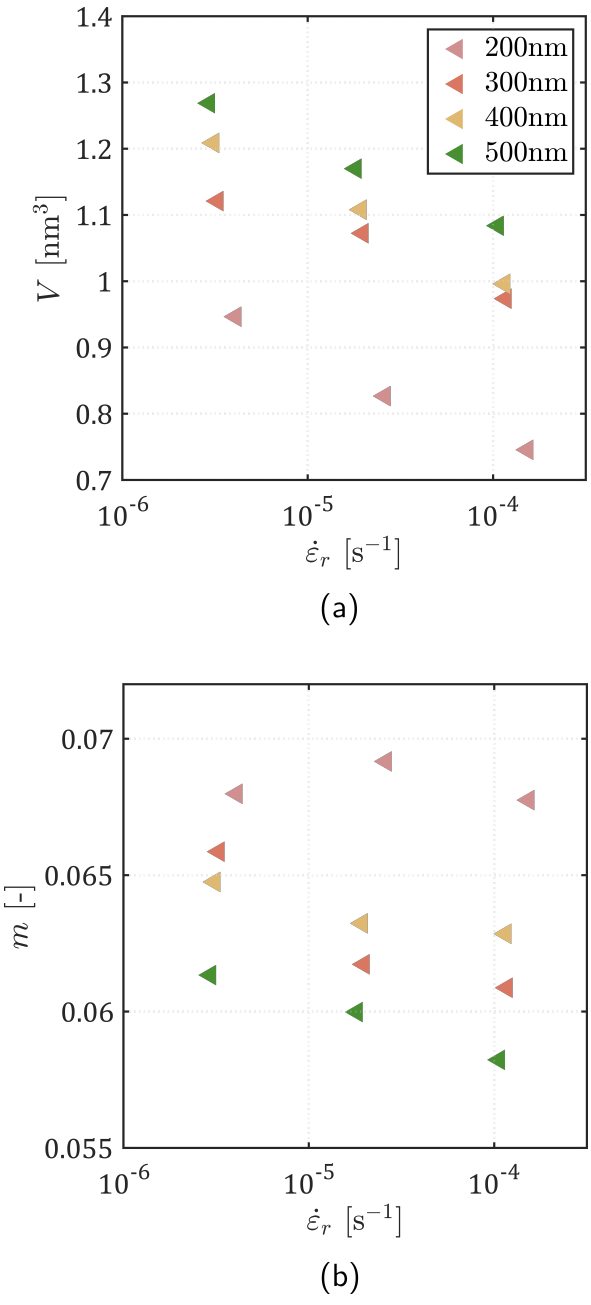


Fig. 6.8: Relaxation tests: (a) activation volume V and (b) rate sensitivity m as a function of $\dot{\varepsilon}_r$ at different indentation depths.

tests at the beginning of this section have shown that the modulus does not vary significantly with the strain rate (for a small range of rates).

Elastic or plastic origin of ISE?

As mentioned in the introduction and discussed in chapter 2, the origin of the indentation size effect in glassy polymers is often related, to some extent, to the necessity to accommodate elastic and/or plastic strain gradients. The use of strain gradient plasticity models has proven successful for metals and thus such approaches have been adapted to the case of polymers. This leads to question whether the ISE is more elastic or plastic in nature.

The idea of a significant elastic contribution is motivated by the fact that the stiffness of the backbone of the polymer chain plays an important role in the appearance of an ISE [179, 180]. Stiffer chains reduce molecular mobility (intra and inter), which may explain the ISE as the difficulty to accommodate the relatively large induced strain in the beginning of the indentation process. The backbone stiffness argument could be used to justify the amplitude of the ISE on E. However, the measure of E for polymers by nanoindentation is itself challenging and easily biased by hydrostatic pressure, for example. Thus, decorrelating the factors influencing the value of E from the ISE is not simple.

Regardless of the potential bias for the modulus, the ISE on H is certain, provided proper tip calibration was performed. Hence, a plastic origin can be associated to the ISE. The challenge is associating the right mechanisms to the ISE, e.g. kink pairs [166], STZs [61], etc. From the point of view of intermolecular mobility, the ISE on H may again be the consequence of accommodating large strain gradients with such mechanisms inside small volumes, which might not have enough of these degrees of freedom to activate. The strain rate discussion above suggested that the amplitude of the ISE decreases with decreasing strain rate. This was associated to an increased mobility of the chains at lower rates, facilitating stress relaxation.

Whether elastic or plastic in nature, it would appear that the ISE is indeed the result of constrained mobility of the chains below the indenter. The open question is to identify which relaxation mechanisms are triggered and how they are influenced by external parameters such as the strain rate or temperature.

6.4.2 In-situ indentation response inside composites

Fig. 6.9 shows the nanoindentation modulus and hardness as a function of to the indentation depth for bulk RTM6 and UD RTM6 pockets. Evidently, both the hardness and the modulus within the UD are roughly 15-20% larger than the bulk values. These results are in agreement with previous results on RTM6 [157]. As pointed out by Hardiman [193], in order to compare the properties of

the UD with bulk values, the fibre bias effect needs to be minimised. To that end, similarly to the work of Chevalier [157], a fibre constraint factor (FCF) was defined as the ratio of the distance to the closest fibre over the instantaneous indentation depth: FCF=d_{fib}/h. Fig. 6.10 shows the modulus variation with respect to the FCF. A plateau exists in the curve in the range [30-60], where the modulus is unaffected by the constraining effect of the fibres. In this work, the average distance to the closest fibre of the matrix pockets was around 17 µm. Using the appropriate range of the FCF, this gives a valid indentation depths range around 500 nm. This is also sufficiently deep as to not be within the ISE zone.

Influence of physical ageing

As mentioned at the end of chapter 2, the higher hardness and modulus within the pockets of the UD may be caused by a difference in ageing associated to the curing process. Indeed, as the curing procedure for RTM6 and the UD are identical and include a post-curing step at 180°C for 3h, the resulting ageing level may be different due to a difference in heat flow caused by the presence of the fibres. This is motivated by recent results by Gayot et al. [142], which showed that, upon thermal rejuvenation of a thermoplastic and its UD/glass fibre composite, no significant difference in properties was measured. Hence, a thermal rejuvenation of the bulk and UD specimens was performed in order to erase any difference in ageing.

The same rejuvenation treatment as mentioned above has been used, namely 15 minutes at 235°C (i.e. above T_g). The resulting nanoindentation response is given in Fig. 6.11 in terms of the hardness variation. Interestingly, the hardness in the UD remains around 15% larger than the bulk values. This suggests that the difference in properties between the bulk resin and the UD pockets must come from an intrinsic change of the local microstructure. The limited impact of ageing could have been expected under the assumption that both the bulk and UD resins are fully cured. Indeed, RTM6 has been shown to only be marginally affected by physical ageing. Morelle et al. [7] showed that the yield stress and modulus do not vary significantly under accelerated ageing at 150°C for 70h. Passilly et al. [358] performed nanoindentation tests on RTM6 aged at 130°C for 5,000h and did not find a significant change in modulus. However, they found that an oxidised surface layer was created over roughly 100 µm, leading to an increase of the modulus close to the surface. Still, considering the significant time difference between the present post-curing step and the results of Passilly et al., it is unlikely that a thick oxidised layer has formed to fully account for the higher modulus in the UD. Hence, ageing does not explain the increase in the in-situ properties for highly cross-linked epoxies such as RTM6.

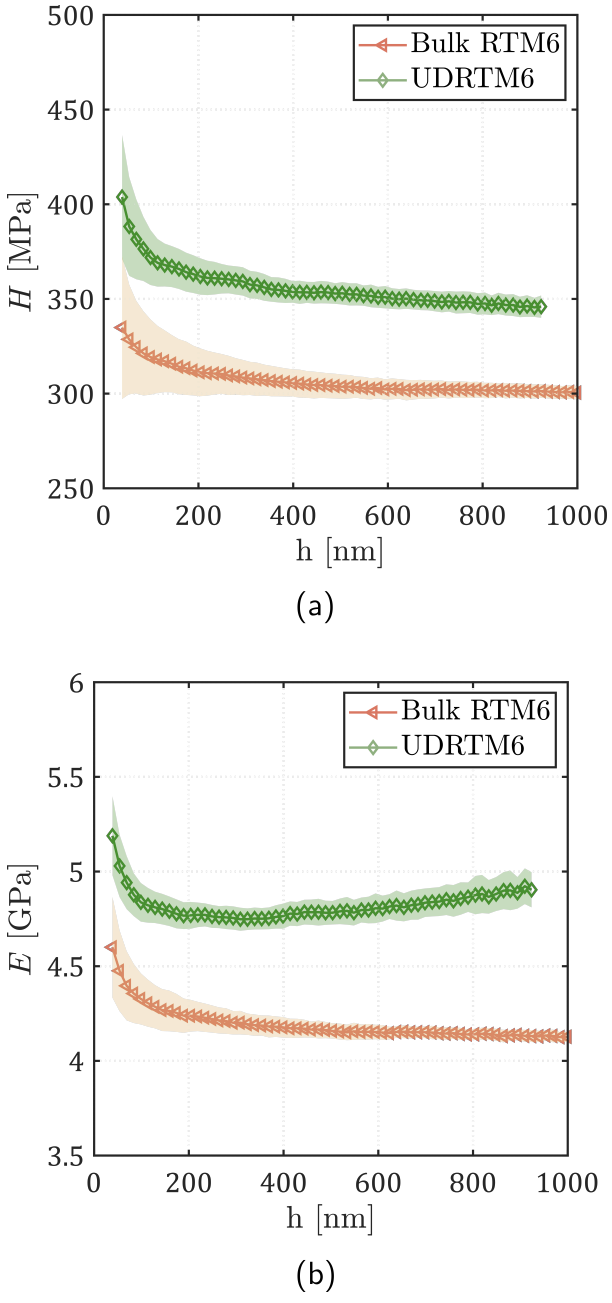


Fig. 6.9: Variation of the indentation hardness H and modulus E with respect to the indentation depth h comparing the bulk and UD pockets of RTM6 at a strain rate $\dot{\varepsilon} = \dot{F}/F = 0.05\ \mathrm{s}^{-1}$.

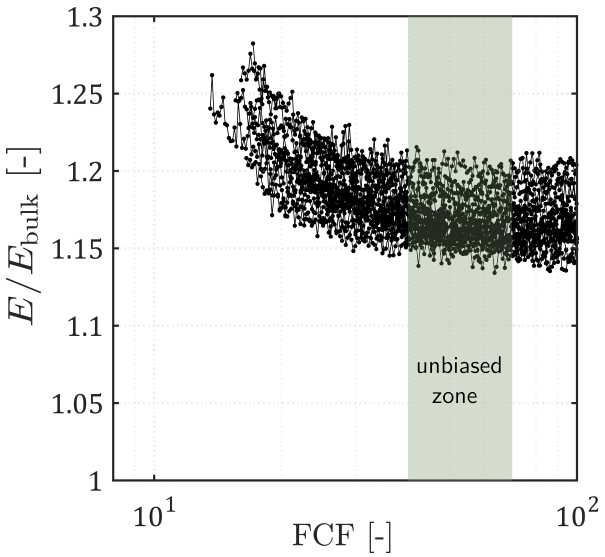


Fig. 6.10: Variation of the UDRTM6 modulus normalised by the bulk RTM6 modulus as a function of the fibre constraint factor FCF=d_{fib}/h. A stable region exists for FCF in [30-60] where the response is unbiased by the presence of the fibres.

As a difference in ageing behaviour is not the origin of the difference of the hardness and stiffness, alternative explanations need to be found for explaining why the matrix in the near fibre regions of composites does not respond as in the bulk form. Numerical investigations have shown that residual tensile stresses build up within the matrix pockets during the curing process, leading to a decrease in hardness [359]. Thus, residual stresses do not provide an answer. Hence, a possible explanation may lie within a local change of microstructure and/or an influence of the interphase region. Regarding the latter, the AFM measurements of chapter 4 indicate the presence of an interphase with a thickness of roughly 200-300 nm. Hence, the interphase may affect smaller matrix pockets (but still within appropriate FCF), but its impact on larger pockets is doubtful. Concerning the change in microstructure, physico-chemical analyses to extract a local T_g would provide crucial information about the state of the resin within the UD pockets. However, an accurate measurement of the T_g is quite challenging using typical techniques such as differential scanning calorimetry. Recalling the dependency of the yield stress to the ratio T/T_g from chapter 3 and using the method of Rodriguez et al. [213] to convert the in-situ hardness to an equivalent yield stress of around 165 MPa, the in-situ T_g would be around 250-260°C. This is an increase of 30-40°C compared to the T_g at 95% cure degree. Following the di Benedetto equation [244, 360], a T_g of 250°C can be found for 100% degree of cure, assuming this is a physically achievable state for RTM6 (which is doubtful).

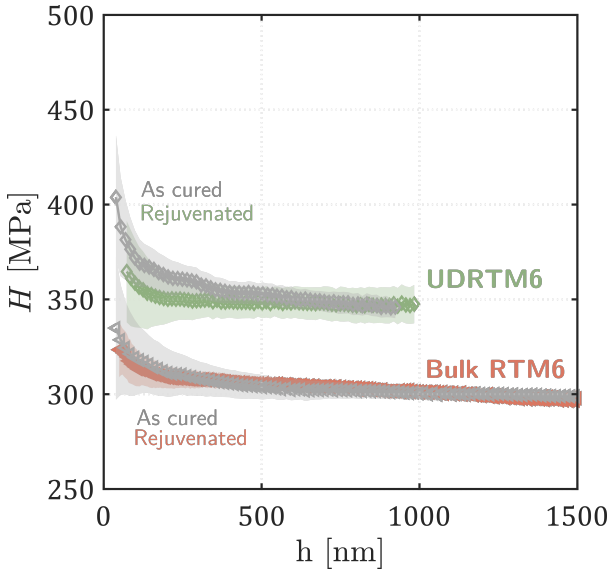


Fig. 6.11: Variation of the indentation hardness H as a function of the indentation depth h for bulk RTM6 and UDRTM6 comparing the responses after thermal rejuvenation at 235°C for 15 minutes (colour) and as-cured (grey).

As explained above, assuming that the rejuvenation process induces an equal rejuvenation of the bulk resin and the resin within the UD, a difference in ageing can be ruled out as the source of the increase in the initial in-situ properties. Nonetheless, as pointed out by Gayot et al. [142], the presence of the fibres seems to promote accelerated ageing compared to the bulk state, at least for amorphous thermoplastics. Hence, for equal time passed for physical ageing, the UD will likely reach a slightly advanced state of ageing compared to the bulk.

A last possible explanation may reside in a size effect on the yield stress (unrelated to the initial ISE) of the resin caused by the a confinement effect of the fibres. The confinement may limit the development of initial plastic deformation bands, leading to the presence of strain gradients in the matrix pocket, causing an increase in the hardness and modulus.

Rate sensitivity

In attempt to provide further insight into the deformation response of the matrix within the UD composite, nanoindentation relaxation tests are performed to characterise the rate sensitive behaviour over a wide range of strain rates. Fig. 6.12 (a) shows the variation of the hardness with the estimated plastic strain rate under the indent. Fig. 6.12 (b) shows the same but expressed in terms of the representative stress below the indent. The relaxation tests were performed

at a depth of 500 nm for both bulk and UD samples. In addition, rejuvenated and as-cured samples were tested.

First, regarding the rejuvenated condition (coloured curves), no remarkable difference can be found for the rate dependency of the UD with respect to the bulk, aside from the higher hardness (as expected). This does indeed suggest that a fundamental difference exists in the properties of the matrix pockets, which cannot be solely accounted for by physical ageing. Fig. 6.13 shows the corresponding activation volume V and the rate sensitivity m. The UD pockets show a lower activation volume, in agreement with the higher hardness, whereas m is equal to 0.64 for the UD pockets and for the bulk, confirming the apparently similar rate-dependency.

Looking at Fig. 6.12, the case of the as-cured condition appears different. For bulk RTM6, there is no significant difference in the rate-dependency with respect to the rejuvenated case. However, the response of the UD pockets differs. The variation of H or σ_r presents a lower rate sensitivity compared to the rejuvenated state, as quantified by a value of m equal to 0.05, whereas the bulk m does not vary much. This suggests a more stable and less rate-sensitive state of the UD matrix pockets, potentially hinting towards the attainment of a more pronounced physically aged state. This is particularly marked at lower strain rates, whereas at typical nanoindentation rates (e.g. 0.05 s^{-1}), the difference in H between the rejuvenated and as-cured conditions is not significant. Still, the value of V in the UD pockets is slightly higher than the rejuvenated case, which is counter-intuitive as physical ageing should reduce molecular mobility, leading to an increase in V. The difference is, however, less than 0.2 nm^3 and may therefore be caused by the experimental uncertainty. Interestingly, the difference in H seems to therefore increase with decreasing strain rate. This is in contrast to the trend observed in Fig. 6.7 for the ISE, where the gap in H is reduced at lower rates. If one considers reduced mobility of the polymer chains as a consequence of confinement (under the indenter tip or due to the fibres), one would expect a similar dependence of H on the strain rate. As this is not the case, the confinement effect in the UD pockets may cause a different impact on the development of strain gradients triggering the size effect. Alternatively, it is indeed a difference in microstructure of the epoxy that causes the increase in in-situ properties.

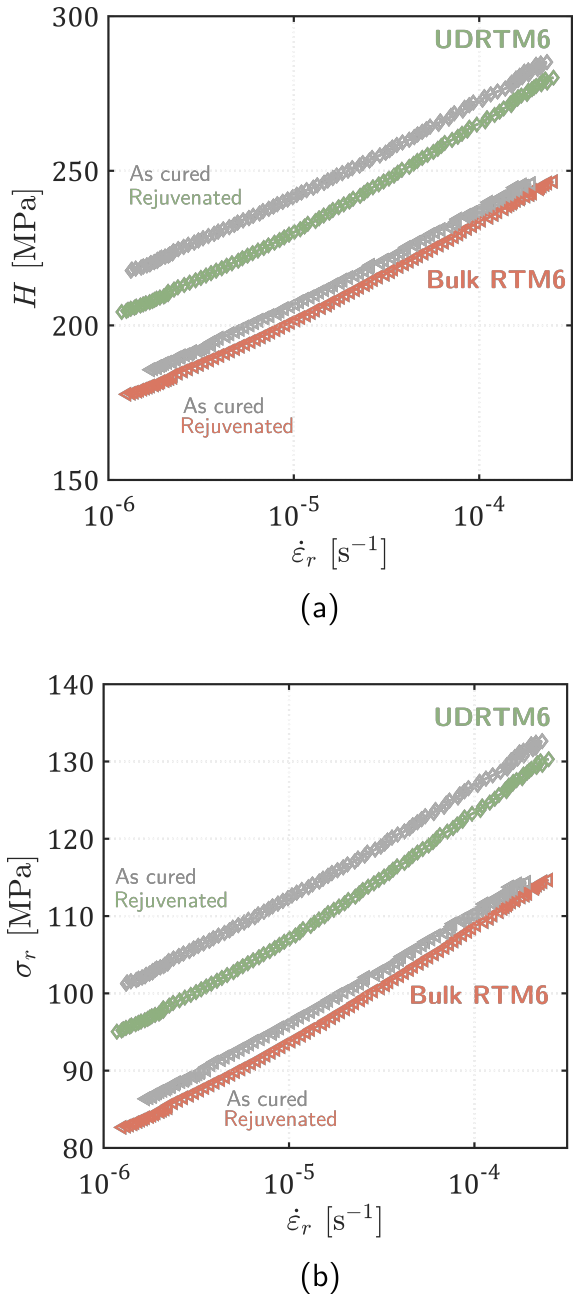


Fig. 6.12: Relaxation tests at a depth of 500 nm: variation of (a) the hardness H and (b) the representative stress σ_r as a function of $\dot{\varepsilon}_r$ for the rejuvenated (colour) and as-cured (grey) bulk and UD specimens.

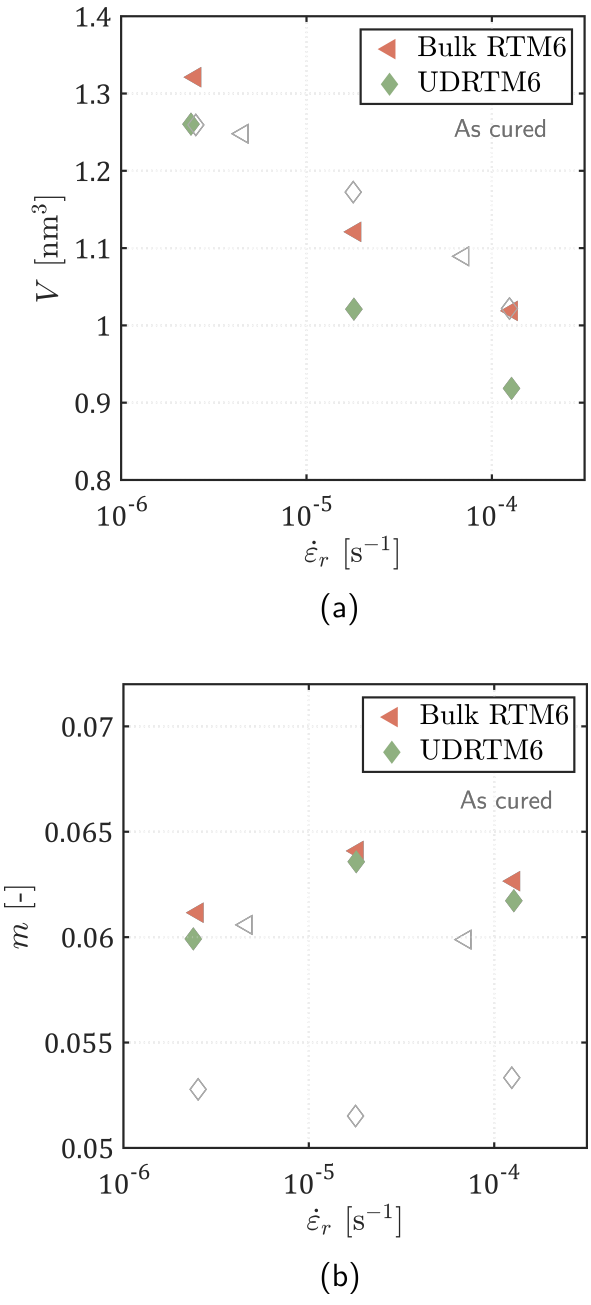


Fig. 6.13: Relaxation tests at a depth of 500 nm: (a) activation volume V and (b) rate sensitivity m as a function of $\dot{\varepsilon}_r$ for the rejuvenated (colour) and as-cured (grey) bulk and UD specimens.

In the end, the results point towards a change in rate sensitivity for the UD at lower strain rates in the as-cured condition. As this is not the case for the bulk, it may indicate a difference in physical ageing behaviour. More importantly, it shows that assessing in-situ properties of UD composites can be easily influenced by factors such as the strain rate or the state of ageing of the material. Once more, this reinforces the need to establish clear test protocols to allow a fair comparison between studies in the literature. Whatever the explanations and ways to look at it, RTM6 does intrinsically have a different mechanical response in the UD matrix pockets, for reasons that could not be elucidated in this thesis and which are open for further investigation.

6.5 Conclusion

The use of nanoindentation has provided the micromechanics community with opportunities and challenges to study the local deformation response of glassy polymers in the bulk state as well as the local in-situ properties of the matrix of fibre-reinforced composites. While the extraction of accurate material properties may be challenging, key outcomes of nanoindentation studies involve the evidence of an indentation size effect and an increase of properties when the polymer is confined (i.e. within FRPs). Still, open questions remain regarding the physical origin of these phenomena. In this work, the ISE and the in-situ properties were investigated, particularly with respect to physical ageing and the effect of extremely low strain rates. The main results are:

- The ISE has been shown to strongly depend on the force-displacement resolution of the indentation response and the accurate calibration of the area function.

- Physical ageing/rejuvenation does not show any significant impact on the amplitude of the ISE.

- Nanoindentation relaxation tests indicate that the rate sensitivity of the bulk polymer is slightly depth dependent. In particular, at lower depths, the rate sensitivity decreases with the strain rate, hinting towards a reduced ISE at very low strain rates. The physical mechanisms causing this apparent evolution of the ISE have yet to be investigated.

- For the in-situ properties, a difference in physical ageing between bulk and UD has been ruled out as being at the origin of the increased in-situ stiffness and strength of the RTM6 epoxy.

- Still, physical ageing has a different impact on the rate sensitivity extracted by relaxation tests between bulk and UD specimens. Particularly, the rate sensitivity of the UD decreases more significantly with physical ageing. This may be related to the favoured reduction of free volume in the presence of fibres, leading to more pronounced ageing.

The physical origin of both the indentation size effect and of the different in-situ properties has yet to be revealed. The strain rate has been shown to provide new insights into the local deformation response. Hence, it would be of interest to perform indentation tests at different temperatures to compare the impact of the test temperature with respect to the strain rate. The use of high temperature indentation will obviously lead to additional challenges, such as managing the thermal drift [171]. Recently, high strain rate nanoindentation tests have also been performed [354], allowing nanoindentation to provide a complete characterisation of glassy polymers. Naturally, the use of the micromorphic model of chapter 5 to study the ISE is of clear future interest. In particular, implementing rate or temperature dependencies in such a strain gradient model may help quantify the relative importance of strain gradients and rate on the low depth indentation response. Regarding the in-situ properties, the curing condition of the epoxy in confined volumes should be investigated. Particularly, does the elongated profile of the fibre bundles and the injection procedure lead to a more anisotropic cure of the matrix, promoting chain orientation? Of course, one can not set aside the potential influence of local strain gradients caused by the confinement by the fibres. Hence, numerical analyses using the micromorphic model should provide crucial information regarding this aspect in the near future.

7

Conclusion

The future of composite materials and their role in sustainable development actions rely on the fundamental understanding of the mechanics of the individual constituents in order to use these materials at their best. This was the premise of this work, set within the context of bottom-up multiscale approaches. Beyond the creation of virtual twins for structural validation, the design, manufacturing and end-of-life of composites in different sectors may also benefit from microscale-based investigations. For instance, one may design simpler composites, relying on fewer additives and making use of the intrinsic mechanisms of deformation and failure. Novel manufacturing strategies, such as automated fibre placement, can provide new opportunities to reduce the number of materials. This, in turn, will facilitate the recycling or re-use of composite materials. The integration of composite structures made of recycled constituents into applications requires an assessment of the potential loss of properties, which starts out at the microscale. Ultimately, improving the efficiency of composite materials may be slow and incremental but will require micromechanical information. This work provides a *micro* building block towards this future.

In summary, the outcomes of this PhD involve new methodologies for the characterisation and modelling at the submicron scale of FRPs in addition to some novel insights into the local response of a highly cross-linked epoxy. Chapter 3 started by demonstrating that across highly cross-linked epoxies, many macroscale properties (e.g. yield stress) are solely dependent on the microstructure of the network and, in particular, on the glass transition temperature. The apparent universality of the mechanical response further motivated the submicron quest. Chapter 4 offered a novel DIC technique leading to a nanoscale strain resolution. The submicron modelling challenges of the matrix and the difficulty to predict the macroscale composite response were tackled in Chapter 5 using a strain gradient plasticity model. This micromorphic enhancement of the constitutive response significantly improved predictions at the micro and macroscale. Lastly, Chapter 6 used nanoindentation to provide

insights into the micromechanical properties and showed that a clear difference in properties exists between bulk epoxies and matrices of composites. The effects of physical ageing and of strain rate were shown to play a significant role.

7.1 What about the main scientific questions?

This work was guided by five scientific questions, as described in the introduction of this manuscript, which followed the works of Morelle [7] and Chevalier [157]. The different chapters have provided some insights into these questions. Using the combined outcomes of all chapters, the following - still incomplete - answers can be given.

Q1 - Factors influencing the in-situ properties

Physical ageing has been thought to be responsible for the higher hardness and modulus in the matrix pockets within the UD. In fact, for PMMA-based thermoplastics, this has indeed been demonstrated [142]. RTM6 is not very susceptible to physical ageing, even in the bulk state. The comparison between rejuvenated and as-cured bulk and composite samples showed no significant difference, maintaining roughly 15% higher values of hardness and modulus for the UD. Hence, the assumption that the post-cure promoted more physical ageing in the composite due to the presence of fibres has been ruled out. The study of the low strain rate response showed that, in the as-cured condition, the matrix pockets are less rate sensitive than the bulk epoxy. This would lead to an increase in the property mismatch, suggesting that the strain rate influences the underlying deformation mechanism. Lastly, the DIC and AFM tests allowed identifying the size of the interphase to be around 200-500 nm. This size is insufficient to significantly affect the in-situ properties, considering the large fibre-unbiased region defined by the fibre constraint factor.

Q2 - Origin of in-situ properties: physical change or mechanical confinement

A first possibility for the higher local strength in the matrix pockets within the UD is an intrinsic change in network structure. Following the macroscopic empirical relationship between yield stress and glass transition temperature, the in-situ hardness could be related to a theoretically 100% cured RTM6, in contrast to the 95% cure degree of bulk RTM6. Alternatively, a mechanical size effect could explain the difference. The size effect may be intrinsic, as some studies found an increase in yield stress accompanying the increase in failure strength as the gauge volume decreases. If not, it is caused by strain gradients acting in the confined volume of matrix pockets. Here, the micromorphic

model would indeed provide crucial insights on the influence of the local strain gradients. Therefore, at this stage, it is difficult to reach a definite conclusion. Once more, the work of Gayot et al. [142] may provide an argument against the need for local strain gradients, as no difference in properties remained after thermal rejuvenation of the thermoplastic, suggesting an origin within the molecular network. Yet, this may be system dependent (i.e. fibre size, etc.).

Q3 - Heterogeneous deformation and failure at nanoscale

The nano DIC showed that the local strain fields in small matrix pockets within the UD are heterogeneous in nature. Larger matrix pockets present a more homogenous strain field. Still, in all cases, strain localisation phenomena systematically occur near the fibre/matrix interface. Such strain localisations lead to subsequent failure of the interfaces, which then promote final crack propagation through the composite. No nano DIC of pure RTM6 was performed to identify the potentially heterogeneous strain fields and to attempt to relate them to the heterogeneity determined by AFM, for instance in [361]. It is indeed not certain that variations smaller than 10-20 nm can accurately be captured by the nano DIC approach.

Q4 - Interphase response

The presence of an interphase has been demonstrated directly by AFM measurements and indirectly using the nano DIC technique. At the nanoscale, fibre/matrix decohesion was systematically preceded by strain concentrations near the fibres, over a distance covering the interphase (200-500 nm). Hence, the mechanical response of the interphase plays a crucial role in the accumulation of plastic strain leading to fibre/matrix interfacial failure. Accurately measuring the properties and the microstructure of the interphase remains challenging [362]. Nonetheless, the development of the nano DIC tool allows the identification of the presence of an interphase in composite systems, in the absence of knowledge about the fibre sizing.

Q5 - Size effects within composites

The effectiveness of even a "simple" strain gradient plasticity model based on the cumulative plastic strain to account for some effects has been demonstrated for the first time for UD composites using submicron scale validation. Regarding the DIC analysis, the SGP model provided the necessary hardening and regularisation to avoid excessive strain localisation. At the macroscale, the prediction of the stress-strain response of thick UD composites under transverse compression was significantly improved. A characteristic length of around 10 µm has been identified. No physical interpretation has yet been given to this length. Overall, considering the experimental nanoindentation results and the improved predictions of the SGP model for the UD, it seems clear that micromechanical

studies of fibre-reinforced composites in loading conditions leading to significant plasticity in the matrix require a strain gradient approach to properly account for both the local hardening and the regularisation of micro shear bands.

7.2 Prospectives and future work

While partial answers were established for the scientific questions of interest, a physical understanding of the size effect in both the bulk and matrix polymer remains open to further investigations. In that sense, some straightforward continuations of this work include: a more quantitative use of the nano DIC technique while adapting its use to study crack propagation phenomena, and incorporating pressure, strain rate and temperature dependency into the SGP model.

To pursue the nano DIC analysis and extend its use to FRPs based on more complex matrices (e.g. semi-crystalline thermoplastics), quantitative measures of critical strains, for instance related to the onset of interfacial failure, need to be determined. The goal would be to extract a microscale stress-strain relationship for the matrix pockets, which may provide further insights into the perceived higher yield stress of the matrix at this scale. A quantitative analysis of the micro shear band formation, orientation and size with respect to the local fibre arrangement may serve as important data to further understand micro shear banding phenomena. Van Vlierberghe et al. [363] has recently started such analyses, based on the outcomes of this thesis.

While the failure of epoxies has not extensively been studied here, pursuing the understanding of the fracture micromechanisms of epoxies remains of interest. As noted before, Mishra et al. [81] reported the formation of crazes in the fracture process zone. Thus, the nano DIC approach may provide an accurate measure of the strain field at the crack tip and within the fracture process zone. This information could then be related to different failure mechanisms, in attempt to unveil the physical origin of failure.

The extension of the SGP model to include the complete pressure, temperature and strain rate dependency of the model of Morelle et al. [12] is an obvious avenue of future work. To be fully representative of a glassy polymer's mechanical response, such an extension is necessary. The model could then be used to study localisation phenomena and size effects in RTM6 (for instance, using micron size epoxy fibres). Hamdoun et al. [364] very recently used a micromorphic approach to extend an isotropic viscoplastic model for polycarbonate to numerically and experimentally study localisation in uni- and biaxial tests. Regarding the composite case, an additional improvement would be the implementation of damage and failure criteria, based on the failure knowledge of RTM6. This is expected to improve the predictions of the stress-strain response

of the UD composite. Lamm et al. [365] recently published a rate-dependent micromorphic damage model for polymeric materials. Additionally, numerical studies of the nanoindentation response should be carried out with the SGP model. Indeed, it is expected that the micromorphic model will help quantify the relative contributions of the local strain gradients under the indenter at low indentation depths and the test parameters on the ISE. Furthermore, regarding the matrix pockets in the UD, a successful implementation will determine whether or not the confinement by the fibres leads to significant strain gradients causing the higher in-situ properties. This could be accopanied by indentation tests with different tip geometries (e.g. spherical), to also experimentally identify the role of strain gradients.

An alternative modelling approach for the influence of the interphase, at least for the DIC/UD simulations, would be to explicitly account for the polymer chain alignment and reduced mobility at the interface with the fibres. This chain alignment could be represented by a ring around the fibres, akin to an interphase, displaying a gradient in its properties. The key question would be to identify the right constitutive behaviour for this zone, e.g. purely elastic or viscoplastic? Regardless, the size of this zone would always not to be defined. Hence, in a way, this approach also introduces a certain length scale to the FE model.

A complete micromechanical analysis of composite materials will require an accurate representation of the interfacial behaviour. Fibre push-out tests are the current preferred way to study these interfaces, yet no systematic approach for the testing or post-treatment of the data exists. The main challenge remains the difficult sample preparation, test execution and data post-treatment. Mohtadifar [366], in her UCLouvain master thesis (2023), recently consolidated the fibre push-out test on RTM6/carbon fibre composites to extract clean experimental data.

The concept of STZs has often been used for argumentation purposes throughout this work. While no STZ modelling results are presented here, the research on the use of a mesoscale model based on the STZ formalism has been and should be pursued. In particular, the implementation of a viscoelastic matrix to more realistically capture viscoelastic effects experimentally observed in polymer glasses, such as non-linear elasticity, rate and temperature dependency, etc, would be of interest. Additionally, the potential impact of coupled viscoelastic-viscoplastic effects on the STZ activation following stress relaxations and redistributions induced by a viscoelastic matrix could be studied. The first steps have been made in this direction during this thesis, though not reported in this manuscript. The use of an STZ model within the study of composites would also be enriching, particularly to confront the nano DIC results. However, to model an STZ matrix within a composite, one would need to account for the

presence of the interphase and its impact on the STZ activation potential. If properly implemented, such an analysis could provide insights on the impact of the heterogeneous deformation of the matrix on the strain localisation phenomena observed at this scale.

Finally, this work has shown that providing novel experimental data at the microscale is beneficial for testing our understanding of the micromechanics of polymer glasses. In particular, it allows determining missing elements in our modelling approaches. Thus, a general suggestion for future studies is to increase micro or nanoscale characterisation campaigns on a variety of composite systems and to use this data to challenge current popular numerical models. In a similar line of thought, the macroscale characterisation of epoxies or glassy polymers at large should include a full physico-chemical analysis in order to determine the key factors dictating the mechanical response of such materials.

A

Nanomechanics serving polymer-based composite research

Abstract

Tremendous progress in nanomechanical testing and modelling has been made during the last two decades. This progress emerged from different areas of materials science dealing with the mechanical behaviour of thin films and coatings, polymer blends, nanomaterials or microstructure constituents as well as from the rapidly growing field of MEMS. Nanomechanical test methods include, among others, nanoindentation, in-situ testing in a scanning or transmission electron microscope coupled with digital image correlation, atomic force microscopy with new advanced dynamic modes, micropillar compression or splitting, on-chip testing, or notched microbeam bending. These methods, when combined, reveal the elastic, plastic, creep, and fracture properties at the micro- and even the nanoscale. Modelling techniques including atomistic simulations and several coarse graining methods have been enriched to a level that allows treating complex size, interface or surface effects in a realistic way. Interestingly, the transfer of this paradigm to advanced long fibre-reinforced polymer composites has not been as intense compared to other fields. Here, we show that these methods put together can offer new perspectives for an improved characterisation of the response at the elementary fibre-matrix level, involving the interfaces and interphases. Yet, there are still many open issues left to resolve. In addition, this is the length scale, typically below 10 micrometres, at which the current multiscale modelling paradigm still requires enhancements to increase its predictive potential, in particular with respect to non-linear plasticity and fracture phenomena.

Pardoen et al., Comptes Rendus Physique Tome 22 (2021) no. S3

A.1 Introduction

The field of mechanics of polymer-based composites has dramatically evolved since the turn of the millennium. This evolution was doped and structured by

the multiscale approach of the mechanical behaviour of materials. Multiscale modelling is indeed today the preferred paradigm to link materials characteristics to their end-use properties, and to combine into a single vision the materials science quest to develop better materials and the structural mechanics objective to accurately predict the integrity of composite components. The core of the multiscale approach relies on the development of micromechanics-based models, scale transition formalisms, and the necessary accompanying numerical methods that allow integrating the fibre-matrix elementary level up to the full composite level [90, 106, 367–369]. The computational modelling methods have been supplemented by rich new experimental data emerging from 3D in situ tomography [370–372] and 2D or 3D digital image/volume correlation methods (DIC/ DVC), see e.g. [294, 297, 298, 373, 374]. These experiments provide an invaluable source of information to build physical scenarios for the deformation and failure history and to validate the models, supplementing classical macro-mechanical tests. Recently, multiscale modelling approaches have been aided by machine learning methods to accelerate the simulations and/or the optimisation analysis [375–377].

Nevertheless, many fundamental questions remain regarding the material response at the lower length scale, which is the one of the fibre-matrix elementary volume – i.e. typically below 10 micrometres. Outstanding questions include:

1.a. Is the local mechanical behaviour of the matrix similar to the behaviour measured on bulk thermoset or thermoplastic samples? Contradictory data have been reported and will be discussed in the paper. When a difference is found between bulk and "in-between fibres" behaviour, the next two questions ensue:

1.b. Is the matrix material located in micrometre-sized volumes in between closely spaced fibres intrinsically different in terms of, for instance, molecular mass, cross-linking density, anisotropy, degree of crystallinity in thermoplastics or free volume as a result of the specific local curing conditions?

1.c. Or is the difference in behaviour the result of a mechanical confinement effect which modifies the development of plasticity, similar to a strain gradient plasticity effect in metals, see e.g. [378], also known to play a role in polymers [166]?

2. Are the fracture mechanisms in the matrix comparable to those occurring in bulk samples and if not, what are the fundamental failure mechanisms within the matrix? In bulk specimens, fracture is often dominated by the nucleation of microcracks on micrometre-sized defects [75] which are not observed in confined matrix regions. Recent reports show that an epoxy resin specimen of small dimensions can be very ductile compared to a larger bulk specimens [83–85, 379].

3. What is the mechanical response of the interface and interphase region between the fibre and matrix? An interphase layer, modified by the presence of fibre sizing and by the associated change of polymerization conditions, is known to develop near the fibre surface. The literature indicates such region thickness to range from a few nanometres to micrometres. The load transfer to the fibre, the possible plastic localisation and the resistance to decohesion will be considerably affected by the elastic and plastic characteristics of this interlayer with respect to the surrounding matrix.

4. What is the link between the nature of the interphase layer and the possibility of a preferential path for diffusion and/or for ageing leading to evolving mechanical strength and damage resistance?

5. What is the internal stress field existing at the scale of the confined matrix after curing, if any, and how does it relax with time?

6. The longitudinal tensile failure of composites is, to a large extent, determined by the Weibull fibre strength distribution and by the stress redistribution resulting from the failure of individual fibres. Some outstanding open questions include a possible 'in-situ' Weibull fibre strength distribution that differs from that measured in the tests conducted in dry fibres/tows, and the magnitude of stress concentration gradients across undamaged fibres located close to a broken one [380, 381].

Convincing quantitative answers to these questions could significantly enhance both the predictive capabilities of multiscale models and the capacity to pro-actively guide composite design towards novel principles for tougher materials.

The natural approach available today is to address the previous questions by borrowing from nanomechanical methods developed mainly for other material classes and, for some of them, from the solid state physics community, and apply them at the scale of interest, as schematically shown in Fig. A.1. Nanomechanical methods involve on the experimental side: nanoindentation mapping, quantitative atomic force microscopy (AFM) mapping, push-in or push-out tests, in-situ testing in a scanning electron microscope (SEM) combined to DIC, in-situ testing by x-ray microtomography coupled to DVC, micropillar compression from focused ion beam (FIB) machining; and on the modelling side: molecular dynamics (MD) studies, mesoscale shear transformation zone (STZ)-based models (developed in the context of transition state theory, borrowed from solid state physics) and advanced viscoelastic-viscoplastic models with or without length scale dependencies. Some of these methods also provide information about the chemistry and structure of the polymer matrix.

The objective of this paper is to describe how some of these nanomechanical approaches can be and have been applied at the fibre-matrix elementary level, and how they can be combined to develop a more quantitative understanding of

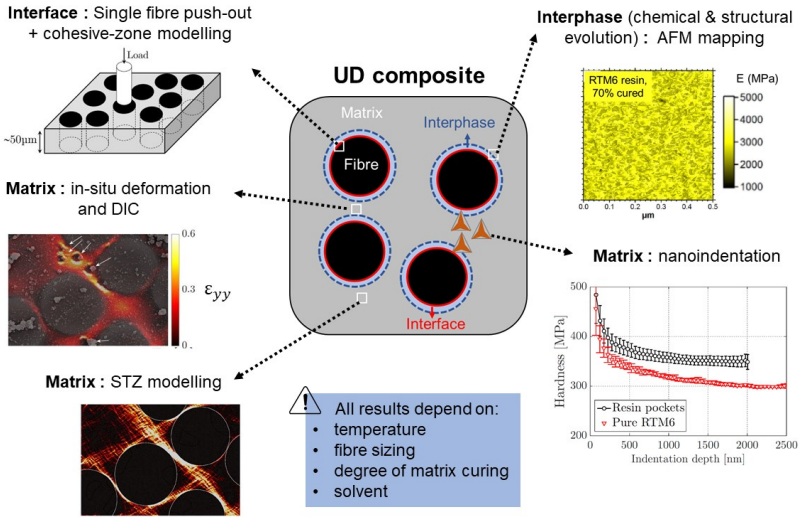


Fig. A.1: Description of some nanomechanics-based methods to quantitatively investigate the response of the matrix-fibre elementary volume, involving the confined matrix, the interphase layer, the interface with fibre and the fibre.

the local mechanical behaviour. The paper will not provide definitive responses to the questions raised above – and which will certainly remain on the roadmap for many years to come -, but will deliver some guidelines on possible answers. The presentation will illustrate the messages with results from our own studies, involving some already published data as well as some new results[1], while obviously recognising that more and more groups worldwide are working on this subject. A vast majority of these examples will focus on a standard composite material system comprising an epoxy matrix (RTM6) and carbon fibres (CF), which is a material system widely used in aeronautical applications.

A.2 Nanoindentation

Nanoindentation allows the non-destructive measurement of several mechanical properties such as hardness and elastic indentation modulus at the micro- and nanoscales, and the extraction of constitutive model characteristics through inverse modelling [105, 151]. In a nanoindentation test, a sharp pyramidal (or conical) tip with a radius of curvature typically below 100 nm penetrates into the material under load, followed by an unloading sequence, see Fig. A.2 (a). Classical nanoindentation can be defined as a depth-sensing indentation (DSI) method.

[1]The new results concern the size effect observed in nanoindentation, the analysis of the constraint effect associated to the fibres affecting the extraction of the modulus from nanoindentation data, and the fibre push out tests obtained on this system.

The continuous stiffness measurement (CSM) mode, which superimposes an oscillatory displacement on the main loading, is used to continuously measure hardness and elastic modulus and can be used to perform nano-DMA tests. This is necessary in polymers, for which indentation size effects similar to metals are usually observed [151, 158, 319]. The common theoretical approach to extract stiffness and hardness from the load-displacement curve is based on the Oliver and Pharr method [147] following the work of Sneddon [148]. This method gives the contact area based on the actual indentation depth h_c evaluated using the sink-in correction of the material around the indenter, see Fig. A.2 (a). In case of pile-up, the model by Loubet et al. is considered to be more appropriate [350].

The use of nanoindentation for the characterisation of pure polymer specimens remains a topic of controversy in the literature [150, 154] as the elastic modulus extracted with this method is often higher than the one determined with macroscale tests on the same polymer samples [154–156]. The difference is sometimes attributed to Oliver and Pharr's theoretical approach, which relies on elastic contact mechanics to describe a viscoelastic material. Additionally, the effects of pile-up under the indenter due to plasticity, viscoelasticity, hydrostatic stress and fibre constraint strongly affect the measured properties by, for instance, over- or underestimating the contact area. Hence, these factors cast doubt on the inherent accuracy of the material property measurement via nanoindentation [159]. Several models and correction factors have been proposed to address this issue: these allowed some authors to get corrected modulus values lying within $\pm$ 5% of the values obtained via macroscale tests [155, 163]. Size effects also affect the indentation response: a decrease of hardness and modulus values is detected in the first few hundreds of nanometres below the surface, until a plateau is reached at a threshold depth. This size effect can be attributed to both length scale dependent elasticity and/or plasticity effects, and to interactions with the intrinsic dimensions of the polymer structure such as the radius of gyration of the molecules [167, 168, 179, 186]. Hence, despite these unresolved challenges, nanoindentation measurements have been used to feed FE simulations [4, 163, 217], showing the potential of combining this approach with more advanced matrix continuum constitutive models.

The determination of the in-situ properties of polymer matrices within fibre-reinforced polymer composites (FRPs) adds another level of complexity to the nanoindentation data extraction. As indicated in the introduction, the presence of fibres in FRPs affects the curing process of the matrix, potentially modifying its mechanical properties within matrix pockets. A difference in

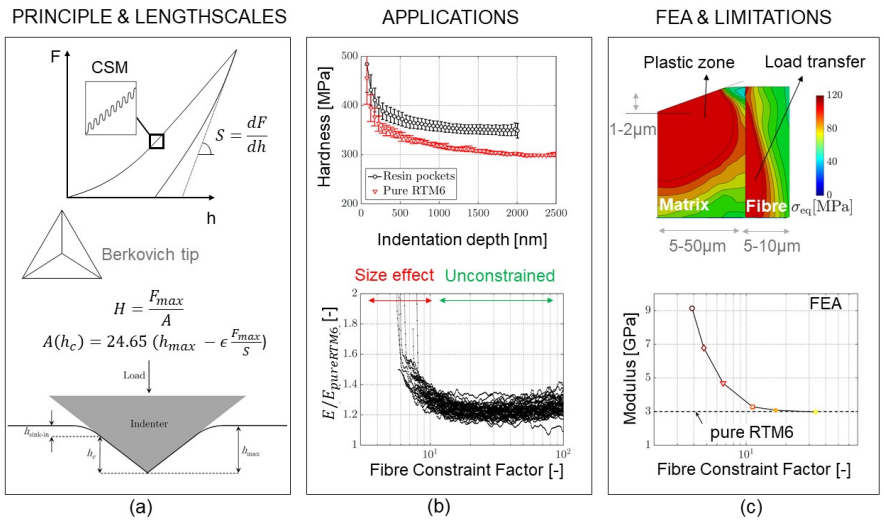


Fig. A.2: Application of nanoindentation to extract stiffness and hardness of polymer matrix in near-fibre confined volumes; (a) principle of nanoindentation; (b) example of hardness and elastic stiffness data in highly cross-linked RTM6 epoxy measured by nanoindentation, comparing bulk and confined values – the fibre constraint factor is the distance to fibre normalized by indentation depth; (c) finite element simulation of nanoindentation to account for and deconvolute the fibre constraint effect.

property measured by nanoindentation on pure polymers vs. FRPs using the exact same product has been repetitively reported, the latter exhibiting higher hardness and modulus even when the aforementioned correction factors are accounted for [164, 165]. Finite element studies demonstrated that a sub-surface stress transfer mechanism between the matrix and the fibres is present, giving rise to an extrinsic fibre constraint effect, which must be deconvoluted to determine any true changes of the material properties [191, 193], see Fig. A.2 (c). Hence, it is important to consider matrix pocket size, fibre proximity and indentation depth when measuring the in-situ properties of a composite matrix. Recently, Chevalier [157] studied the mechanical response of an epoxy matrix (RTM6) within carbon fibre unidirectional (UD) composites. The indentation results on pure RTM6 were in good agreement with other earlier studies [158, 167, 171], see Fig. A.2 (b). The bulk indentation results were compared with the ones in resin-rich composite pockets, with the latter providing 20% higher hardness and elastic modulus values. By looking at the effect of the distance to the closest fibre, the hardness was found relatively insensitive to the fibre constraint. FEA results related this observation to a decrease in the sink-in amplitude close to the fibres. Conversely, the modulus proved to be significantly impacted by fibre proximity. Finite element analyses based on an advanced classical continuum elasto-viscoplastic model [12] reproduced with fidelity both effects, see Fig. 2 (c). However, the FEA does not quantitatively capture the

higher absolute hardness values measured in the composite specimens with respect to those obtained in the pure polymer, even in large matrix pockets where the plastic zone below the indenter is not influenced by the closest fibres, see Fig. A.2 (c). Furthermore, it is obvious that the FEA - which is based on a model with no internal length scale does not capture the size effect at lower indentation depth, except if considering an unrealistically blunt indenter tip. The size effect at low indentation depths thus most presumably results from the constrained mobility of the polymer chains under the indenter, calling for more advanced constitutive model developments.

Ultimately, these studies highlight the limits of classical nanoindentation protocols to deal with the case of polymeric materials. Nonetheless, progress in instrumentation and the use of FEA allow the determination of valuable microscale properties which can be used to either elucidate the underlying deformation or feed multiscale FE models. Finally, note that the minimum penetration depth required to provide reliable results in classical DSI is rarely much below 100 nm. This leads to probed volumes with characteristic dimensions close to or just below one micrometre, making it inappropriate to determine gradients of properties in the expected interphase region between fibre and matrix and giving one reasons, among several others, to look for Atomic force microscopy (AFM)-based methods.

A.3 Atomic force microscopy

Atomic force microscopy [382] is used for the surface analysis of materials at the nanometre scale. AFM probes consist of a flexible micro-cantilever terminated by a microscopic tip with a nanometric apex which interacts with the surface. As the scanning probe encounters modifications of the surface topography and/or different materials, the tip-surface interaction forces vary, causing variations of the vertical deflection of the cantilever (contact mode) or modifying the oscillation parameters of the cantilever (tapping™ mode). Topographic imaging of the sample as well as mapping of some physical properties (e.g. elastic modulus) can be derived from these variations of the cantilever deflection or of its oscillatory behaviour. Note that hybrid DSI-AFM systems also exist, where the indenter tip also serves as a scanning probe: it is dragged over the surface before and after indentation in order to obtain topographic images. The main advantage of this technique is the possibility to locate flat regions well-suited for indentation. However, the topographic image of the indented surface is often of poor quality, due to the indenter damaging the sample surface during scanning [150]. In the same idea, interfacial force microscopy (IFM) was developed in the early 1990's [383]. The tip radius is similar to that used in the hybrid DSI-AFM systems, but smaller forces may be applied during indentation leading to less surface damage and better spatial resolution [150].

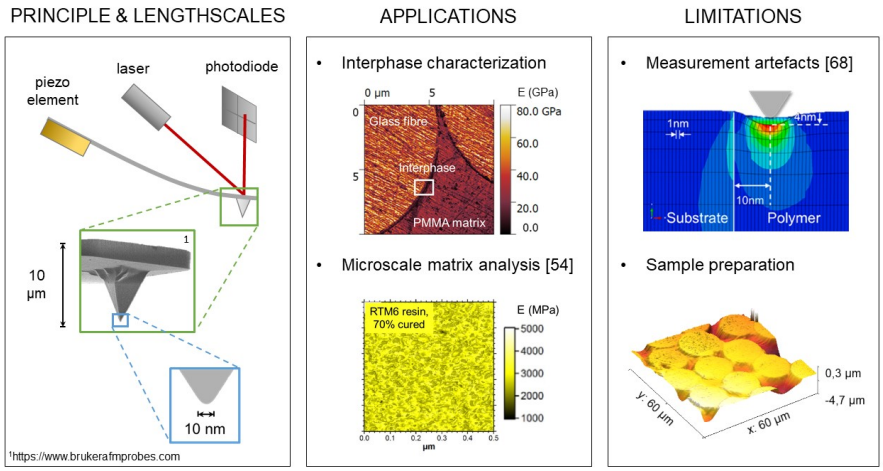


Fig. A.3: Characterisation of polymer-based composites by AFM: (a) instrumentation and length scales, (b) applications and (c) current limitations.

AFM has been used since the 1990's in the field of composite materials for the micro- and nanoscale analysis of matrix properties [361, 384] and the mechanical characterisation of interphases [160, 194, 195, 199, 314, 385–393]. As shown in Fig. A.3, subtle property variations can occur over nanometric distances in such systems (e.g. degree of matrix curing [361]), which asks for excellent spatial resolution involving both measurement sensitivity and accuracy. With a nominal tip radius generally close to or smaller than 10 nm, AFM can provide nanoscale spatial resolution [393], see Fig. A.3. Yet, until the late 2000's, mechanical mapping with AFM mostly led to qualitative results. Phase imaging in tapping™ mode could yield 'relative stiffness maps' with excellent contrast, but the phase signal could hardly be related to any intrinsic material property [199, 394] as it depends on the energy dissipation during the tip-sample contact (which itself may be due to several properties of the material). Force-modulation AFM (FM-AFM) [395] and force-volume imaging [396] were the first methods developed in the 1990's [150, 160, 199, 314] for performing mechanical mapping with AFM. However, generating images in force-volume mode was very time-consuming [394, 397] and imaging in force-modulation mode led to erroneous modulus values due to the tip and surface damage induced by the contact mode and to the variation of the contact area when the tip scanned regions of different rigidity [199].

Since then, many other modes have been developed with the objective of being able to quantitatively map mechanical properties in a reasonable amount of time. All these modes are based on a vertical modulation of the probe

position, either at one of its resonance frequencies or off-resonance. For example, the PeakForce tapping mode (PFT, off-resonance mode) [397] and the HarmoniX™ mode (resonance mode) [398] both allow, after proper calibration, a quantitative mapping of various mechanical properties (modulus, adhesion, indentation, etc.) simultaneously with a 3D topographic imaging of the surface [392, 393, 399]. Smaller indentation forces (in the pN to nN range, see e.g. [392–394, 397]) are used compared to nanoindentation techniques (μN range [199, 314]), which also improves spatial resolution and measurement sensitivity and accuracy. Two examples of nanoscale quantitative mapping performed on composite-related samples are illustrated in Fig. A.3: (1) an assessment of modulus homogeneity in a partially-cured RTM6 epoxy matrix [361] and (2) a mechanical characterisation of the interphase region in a fibre-reinforced methacrylic composite.

Yet, limitations remain when it comes to the quantitative characterisation of composite constituents with AFM. Most of them are similar to those encountered in DSI (see section 2), though the impact on measurement accuracy is much more localised in AFM. First, measurement artefacts may lead to an overestimation of the modulus close to the fibre-polymer interface [194, 195, 390, 392, 393]. As observed in DSI, the tip may either hit the fibre ('probe effect') or sense the influence from the fibre ('fibre bias') while indenting the matrix, which may mask the intrinsic interphase behaviour. FE modelling of the AFM indentation experiment has been performed for several composite systems in order to quantify the influence of these effects on modulus calculation [194, 195, 390, 392, 393]. In all cases, the impact of the fibre bias and probe effects on modulus values were limited to the first tenths of nanometres of the interphase region, see Fig. A.3 (c). The corresponding modulus values were either corrected using FEA [195, 390, 392, 393] or discarded [194]. These studies also revealed a dependency of the impacted zone size upon various factors, e.g. matrix and reinforcement moduli, peak load value and nominal radius of the AFM tip [194, 195]. Note that, in general, the size of the interaction volume in AFM (i.e. the size of the zone mechanically affected by the contact with the tip) conditions both the spatial resolution and sensitivity of the mechanical measurements [394, 400]. It should be adjusted depending on the purpose of the AFM experiment, knowing that a larger interaction volume tends to improve the property contrast and accuracy of the mechanical mapping at the expense of spatial resolution [394].

Finally, sample preparation for AFM analysis of composite surfaces is more challenging than for DSI, as surface roughness interferes even more strongly with measurement accuracy [194, 199, 401]. In particular, differential erosion between the reinforcement and matrix materials should be mitigated during the polishing step [194]. As shown in Fig. A.3 (c), differences in height up to 150 nm between the fibres and the matrix are commonly observed on composite

surfaces studied by AFM, and these are generally not accounted for when interpreting results or performing FE simulations of the experiment [388, 393]. Yet, an abrupt variation in surface slope at the fibre-matrix boundary could induce artefacts in the topographic image [401] and lead to erroneous modulus values close to the fibre surface as the tip-surface contact area does not actually correspond to the one assumed by the model used to extract the mechanical properties. Proposed solutions to limit differential erosion during preparation include ion milling [194], and the replacement of polishing pastes with diamond lapping films.

Over the past twenty years, composite interphases have been extensively characterised using semi-quantitative nanoscale techniques such as AFM. Interphase thickness and mechanical properties appear to strongly depend upon the type of fibre and fibre sizing used for composite manufacturing. Hence, interphase thickness may vary from a few nanometres for unsized fibres [196, 200], to 20-500 nm for sized carbon fibres [196, 197, 200, 402]) and even up to 0.5-10 µm for sized glass fibres [198, 199, 388, 391, 403–405]. Some interphases appear more compliant than the matrix material (possibly due to the preferential adsorption of certain resin components onto the fibre surface) [199, 200, 402, 403, 405], while others demonstrate intermediate response with respect to the fibre and matrix materials [196, 393, 404].

A.4 In situ mechanical testing in SEM coupled to DIC

Digital image correlation (DIC) is a non-contact optical method that allows tracking displacements over the deformed surface of a material. The principle relies on a correlation process using the grey level intensity of subsets of a pattern present on the material surface, each being unique, and distanced by a certain subset spacing [294, 295, 308], see Fig. A.4 (a). The pattern can either result from surface features inherent to the material (e.g. fibres in composites) or from deposition of small particles, resulting in a speckle pattern. At the macro and mesoscales, DIC is a popular technique to characterise the deformation of materials, including fibre-reinforced composites (FRPs) [297, 298, 374, 406]. Recently, DIC has also been applied at the microscale, combined with in-situ testing within a scanning electron microscope (SEM), to quantitatively investigate deformation and fracture processes. However, the use of micro DIC in the study of FRPs remains limited due to practical challenges, encompassing equipment limitations (in-situ testing in a SEM), cumbersome specimen preparation (machining, polishing, speckle pattern deposition) and limitations directly related to DIC itself and to the process of image acquisition (noise, image distortion, polymer relaxation during interrupted tests) [303, 407, 408]. In bottom-up multiscale approaches, the current micromechanical analyses

on representative volume elements (RVE) at the ply level essentially rely on matrix models, which are identified and validated at the macroscale on pure polymer specimens. Additionally, fibre-matrix interface properties used in FEA often lack experimental validation. Hence, micro DIC is particularly relevant to challenge the validity of existing models at the constituent level, and to improve the accuracy of the FE predictions at the microscale, with direct impact on the predictive capabilities of multiscale approaches regarding the macroscopic properties.

Canal et al. [224] first demonstrated the potential of micro DIC for analysing FRPs by studying the deformation mechanisms of a unidirectional (UD) E-glass/epoxy composite subjected to transverse compression inside a SEM. At high magnifications, DIC qualitatively matched with the displacement and strain fields over the region of interest (ROI) simulated by a FEA relying on an elastic material behaviour. Strain localisation within small inter-fibre matrix ligaments were also detected by DIC. Still, the average strains in each phase could not properly be quantified, as DIC strains were under- and overestimated in the matrix and fibres, respectively, due to smoothing in the correlation process at the fibre-matrix interface. The conclusion of this work was that DIC can accurately determine the average composite strain over the ROI, but not at the individual phase level.

Following the work of Canal et al. [224], Mehdikhani et al. [225] studied a UD glass fibre/epoxy composite loaded in-situ in transverse three-point bending, focusing the ROI in the zone of tensile deformation. They showed the importance of evaluating the errors related to micro DIC, such as speckle pattern quality, DIC parameters or charging effect of the fibres to ensure a quantitative data, see Fig. A.4 (c). They accurately mapped the displacement and strain fields with DIC, when compared to FEA maps considering an elastic matrix. The DIC maps also helped identify the regions subject to strain concentration, but failed to capture large strain variations in confined spaces, such as in-between two close fibres (still due to smoothing). A subsequent study by Mehdikhani et al. [226] showed that, using a high-quality speckle pattern, highly accurate displacement and strain maps could be measured in hierarchical fibre-reinforced composites (using carbon nanotubes (CNTs)), enabling the observation of debonding and CNT clusters.

Recent advances in the speckle pattern deposition allow producing consistent and controlled nanoscale patterns using simple methods, such as physical vapour deposition or multi-layer sputtering [300, 301]. Additionally, improvements of the image correlation algorithms provide more information on the initiation and evolution of fibre-matrix decohesion [409].

Ultimately, these studies illustrate the enormous potential of micro DIC

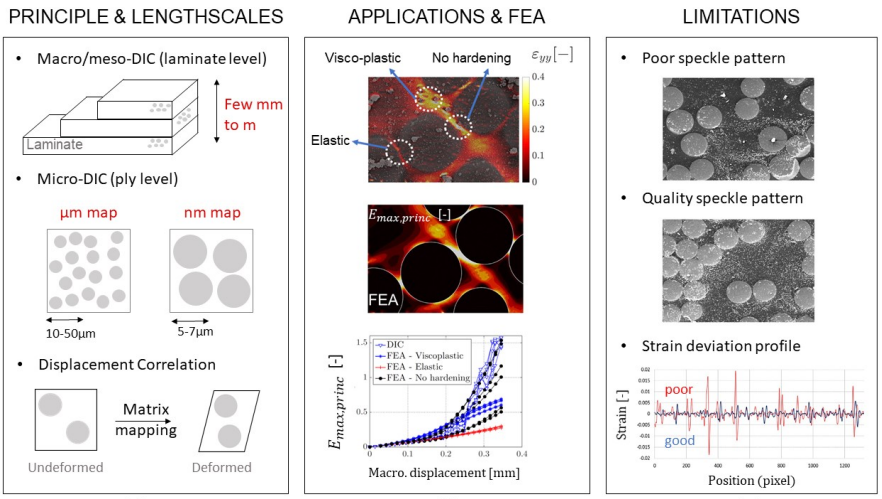


Fig. A.4: Digital image correlation applied to polymer-based composites; (a) length scales at play; (b) example of a carbon fibre-reinforced RTM6 composite [157]; (c) challenge related to speckle quality [225].

for studying the individual behaviour of FRPs constituents. Based on the aforementioned developments, and driven by the inability of micromechanical analyses using a validated model for the matrix [12] to reproduce transverse compression experimental results (i.e. matrix dominated composite response), the more complex case of matrix plasticity at the scale of the fibres was also addressed [76, 157]. In-situ transverse compression tests performed on notched UD specimens in a SEM enabled direct observation of strain localisation and cracking in the matrix at the microscale. FE models, built from the ROI microstructures (and subjected to boundary conditions determined by the DIC displacement field), were used to confront the experimental and simulated strain fields. The FE maps generated using the macroscopic model of the matrix managed to reproduce the strain field in larger matrix pockets, away from the constraint of close fibres. Reversely, in more confined areas, FEA significantly under- or overestimated the strain field measured by DIC. In the former case, the very high DIC strain amplitudes in the localisation band could be predicted by the model only when suppressing the large strain re-hardening stage in the constitutive law, see Fig. A.4 (b). In the latter case, no significant strain localisation was observed by DIC in several areas close to fibres, in disagreement with the model predictions. The key conclusion from these results is the inability of a macroscopic model - that averages the lower scale deformation and damage mechanisms in the matrix into a single continuum constitutive law - to accurately capture a microscale mechanical behaviour guided by local heterogeneities, which are either (1) inherent to the material itself, (2) related

to processing conditions or (3) related to the 'disturbing' presence of another constituent. Among other factors, this inability may be due to the absence of size effects in the constitutive model describing the matrix, or to a different material behaviour inside the interphase region.

A.5 Fibre push-out

In FRPs, the quality of the interface between the matrix and the fibres is key to ensure proper load transfer from the former to the latter, and thus to exploit the full potential of the fibres' high stiffness and high strength. Interfaces/interphases often constitute the locus of first damage in the composites [204, 205, 410]. The fibre-matrix decohesion not only reduces the ability of the fibres to carry the load, but debonded interfaces also become preferential sites for the initiation of additional damage mechanisms, i.e. transverse cracking, delamination or fibre kinking [206, 411]. Hence, the interfacial region has been the object of many studies, aiming both at understanding its mechanical behaviour and delaying the onset of decohesion. As a proof of the role played by the interfaces in the onset of damage in FRP, several authors reported an increase of the mechanical performance of FRPs at the coupon level with the improvement of the fibre-matrix interfacial adhesion (achieved by applying a chemical treatment called sizing to the surface of the fibres) [206, 411–413]. However, macroscopic tests fail at directly identifying the intrinsic properties of this fibre-matrix interface. Even when the loading conditions aim at preferentially triggering the fibre-matrix decohesion mechanism (e.g. interlaminar shear tests), the results only provide an indirect indication of the fibre-matrix bonding quality. The interface region is characterised by its own chemical and structural and properties, which are different from those of the fibres and the matrix. As a result, in micromechanical models, interfaces are usually incorporated as a third true constituent of the composite, with its own material law. Thus, direct measurement methods are heavily needed (1) to extract the necessary ingredients for micromechanical simulations (towards accurate modelling of the composite at the microscale), and (2) to develop a testing framework that would facilitate a direct quantitative comparison of interface properties as a function of, e.g., sizing type or ageing conditions.

In this respect, several experimental methods have been developed for the direct mechanical characterisation of fibre-matrix interface properties. Some of them rely on the manufacturing of a 'model composite' consisting of a single fibre embedded in the polymer matrix, in particular the single fibre fragmentation test [206, 208], the micro-droplet test [209, 210], and the single fibre pull-out test [211, 212]. While these methods require careful specimen preparation, direct interface properties can be extracted based on simplifying assumptions about the stress state at the fibre-matrix interface. However, the main drawbacks of these experimental methods lie in their inability to reproduce the real environ-

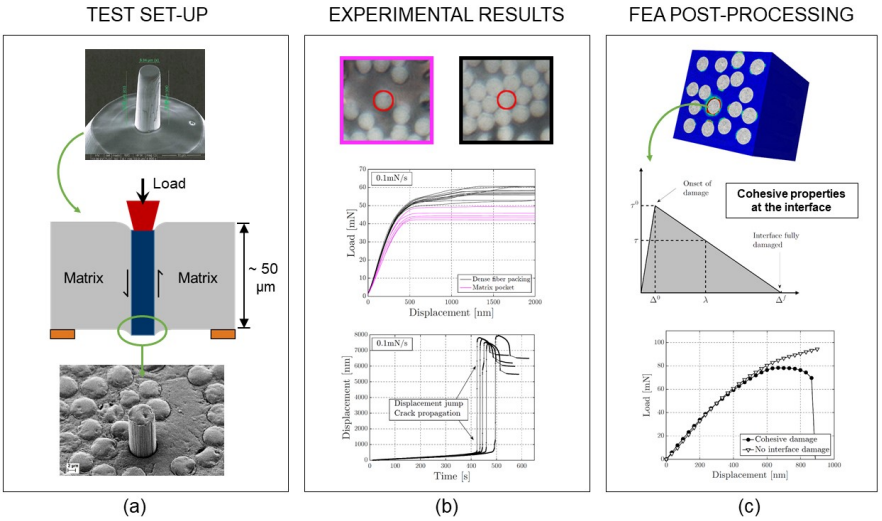


Fig. A.5: Push out test applied to polymer-based composites: (a) micrograph of a typical nanoindenter flat tip, schematic representation of the single fibre push-out test and micrograph of a debonded fibre at the end of a test; (b) micrograph showing indented fibres with different surrounding configurations, load-displacement curves resulting from fibre push-out tests and time-displacement curves showing the displacement jump characteristic of final crack propagation; (c) 3D finite element simulation of a push-out test (equivalent plastic strain in the matrix), typical bi-linear stress-displacement law for cohesive zones, load-displacement curves from FEA with and without damage at the interface.

ment of the interfaces within the composite. As a matter of fact, the interface properties depend on the processing conditions of the composite, which dictate the physical and chemical properties of the matrix (i.e. cross-linking density or crystallinity) and the build-up of thermal residual stresses [213, 214, 414–416] and are thus also dependent on the local microstructure (i.e. fibre volume fraction). Moreover, the strong dependence of the measured properties on the test set-up and test conditions are highlighted by the large scatter observed when comparing the results obtained on similar systems with different methods [417].

As a consequence, the fibre indentation/compression test methods have emerged as an attractive approach to locally extract the in-situ interface properties of the composite. A single interface is selected on the polished cross-section of a composite laminate and loaded using the tip of a nanoindenter. The fibre indentation tests are separated in two categories: the fibre push-in and the fibre push-out tests. The latter differs from the former by the requirement of carefully preparing thin slices of composite (< 100 µm in thickness) so that the fibre

is totally pushed out the specimen when the interface fails (see Fig. A.5 (a). Push-in tests do not require the same demanding specimen preparation, but the interpretation of the results does not profit from the conceptual simplicity of the push-out configuration [213]. The challenge to correctly execute and interpret push-out test results is two-fold. On the one hand, it relies on meticulous specimen preparation to produce material slices with controlled thickness and parallelism, as well as mirror-like polishing. The boundary conditions for the mechanical loading step must be chosen so as to reduce as much as possible the system compliance, ensuring the measurement of the true interface stiffness and strength. For instance, nickel or copper grids with 50x50 μm^2 wire spacing are appropriate to offer a rigid support to the specimens, while allowing the fibre to be effectively pushed out of the bottom surface. On the other hand, the analysis of the results is complex: the compliance of the set-up, the influence of the local environment (i.e. local fibre volume fraction) as well as the different energy-dissipating contributions must be understood and accounted for [214].

Fig. A.5 (b) shows examples of fibre push-out results obtained for the carbon fibre-RTM6 system. The magenta curves are representative of low fibre volume fraction areas and the black ones of densely packed regions. The load-displacement graph provides the overall response of the volume element, while the time-displacement curves highlight the displacement jump characteristic of final crack propagation at the interfaces. The curves also display a complex non-linear shape, combination of matrix plasticity, crack initiation and propagation as well as friction. Experimental procedures like the cyclic push-out test can help decipher the importance of each contribution to the test response [417]. Still, while these methods are necessary to improve the understanding of the sequence of events, FEA is always needed to extract the interface properties. The post-processing of the results using FEA requires a careful understanding of the properties that need to be implemented in the cohesive-zone models, which are the standard nowadays for modelling interfaces, see Fig. A.5 (c). Indeed, as reviewed in earlier sections, modelling the microscale behaviour of composite materials faces challenges related to the possible different behaviour of the matrix at the microscale with respect to the macroscopic one, and to the presence of an interphase region with unknown properties. Friction effects have already been successfully incorporated into interface models [76, 418], but it remains to be determined if all local effects must be included in the cohesive-zone models. To the authors' knowledge, there is still no consensus on the best practices to extract traction-separation laws from single fibre push-out tests.

A.6 Mesoscale modelling via shear transformation zone (STZ) dynamics

The local large deformation response of the polymer matrix can play a primordial role in the macroscopic deformation and failure behaviour of a FRP composite laminate. Classical methods to simulate a laminate's behaviour rely on a bottom-up multiscale modelling approach where the simulated constitutive behaviour at a certain length scale (e.g. fibre diameter) is transferred to a larger length scale of interest (e.g. ply thickness) via homogenisation techniques [419]. An ongoing challenge is to realistically model the inelastic deformation of the polymer matrix at a length scale corresponding to the distance between the fibres (i.e. 0.1 µm to 10 µm). This is, as shown in section 4, the relevant length scale at which intense localisation of the polymer via shear banding is observed [58, 105, 296] followed or cooperating with damage and interface cracking. On the one hand, one can make use of atomistic simulations such as (coarse-grained) molecular dynamic (MD) simulations. These provide insight into the fundamental deformation mechanisms dictating the polymer's (visco)plastic deformation. However, due to the high demand in computational power, constitutive MD models for polymers are typically restricted to domain sizes in the order of 10 to 100 nm [420] and very short time scales. On the other hand, there is a large amount of sophisticated (visco)elastic-(visco)plastic continuum frameworks to predict the complex large deformation response of glassy polymers [11, 287, 421–424]. These models give good agreement to measured uniaxial stress-strain curves obtained via tests on bulk specimens. However, they rely on a large number of largely phenomenological calibration parameters, and model predictions for the deformation behaviour of the matrix at the scale of the fibres have rarely been compared with micro-scale measurements, see section 4 [76].

Mesoscale computational models based on STZ dynamics offer a practical avenue to bridge typical simulation length scales of molecular dynamics and continuum models. The STZ framework was originally developed by Argon [55, 425] to predict the viscoplastic response of metallic glasses. The theory assumes that the macroscopic inelastic deformation of an amorphous material at a temperature T close to but below the glass transition temperature T_g is dictated by thermally-activated local shear deformations of small material volumes. The attempt rate for transformation of an individual STZ is calculated via transition state theory, where the activation energy barrier is calculated via Eshelby's inclusion theory. Due to elastic interaction with the surrounding matrix, the activation of an STZ may increase the probability for a neighbouring STZ to transform. The resulting avalanche of sessile STZ activations may lead to localised flow in the form of shear bands, which may ultimately lead to material failure. Extensive numerical [426–431] and some indirect experimental [60, 432, 433] evidence exists for the inelastic deformation of metallic and polymeric glasses at $T/T_g < 1$ (and at moderate strain rates) to be governed by STZ

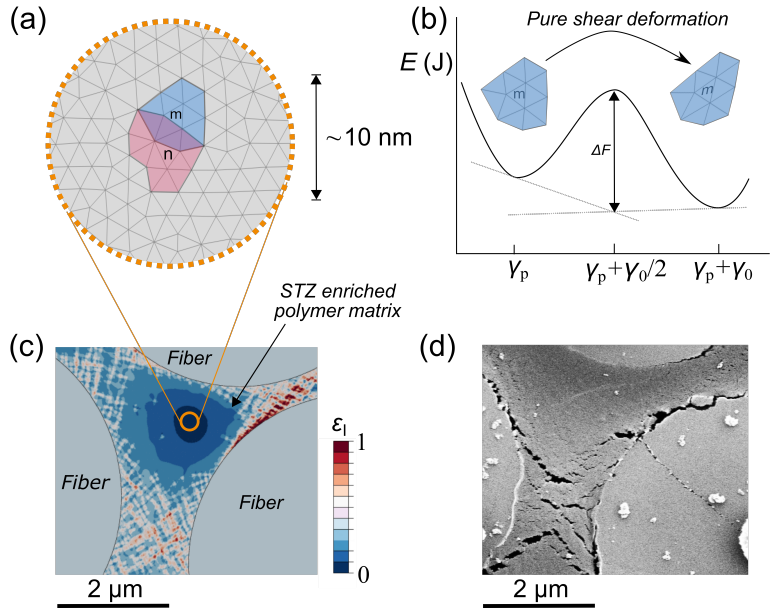


Fig. A.6: STZ approach applied to polymers. (a) Finite element mesh of the polymer matrix domain and illustration of the STZ assignment scheme: each element forms an STZ together with its node-sharing elements. (b) Illustration of the simplified energy landscape for deformation of an STZ in pure shear (via an eigenstrain of magnitude γ_0). (c) Predicted contours of constant maximum principle strain ε_I on a unidirectional fibre-matrix RVE in displacement-controlled transverse compression; the applied displacements on the RVE boundaries give an homogenised strain state equal to the homogenised strain state on a region of a SEM image (d) taken during transverse compression of a unidirectional carbon fibre-epoxy ply.

dynamics.

Recently, the UCLouvain team extended the mesoscale FE model developed by Homer and Schuh [57, 434–436] based on Argon's STZ theory [55, 437] to predict the viscoplastic deformation behaviour of polymeric glasses [58]. In brief, a linear elastic polymer matrix domain is discretised into a plane strain triangular mesh. Each element forms an STZ in combination with its neighbouring (node-sharing) elements, see Fig. A.6 (a). The average stress state of each STZ is calculated at the start of an increment by solving the boundary value problem of an STZ-enriched polymer matrix with an FE solver. The activation attempt rate of each STZ during this increment is dictated by the competition between mechanical energy provided by the homogenised stress state and the free energy barrier ΔF for the deformation of the STZ within the elastic matrix, see Fig. A.6 (b). The value of ΔF is calculated via Eshelby's inclusion theory

following Argon's approach [55, 56, 425]. We have modified this energy barrier calculation for the case of polymeric glasses; details are included in the work of Chevalier et al. [58]. A Monte Carlo method is used to select the STZs that are activated within the increment. Selected STZs are subjected to a pure shear eigenstrain γ_0 in the direction of the maximum in-plane resolved shear stress and the FE solver is used to compute the simulated domain's equilibrium stress and strain state for the next increment.

The STZ model requires the calibration of only five parameters to predict the uniaxial stress-strain response of a glassy polymer including the yield, softening, and hardening regime [58]. Due to the simulated heterogeneous nature of the inelastic deformation, the framework provides insight into typical phenomena observed in the large deformation response of polymers including the non-linear unloading behaviour, the Bauschinger effect, as well as rejuvenation/ageing. In addition, model predictions can be used to study the nucleation and growth of micro-sized shear bands in a deformed polymer matrix when confined by stiff fibres. This is shown in Fig. A.6 (c), where predicted contours of constant maximum principle strain ε_I are shown for a unidirectional fibre-matrix RVE loaded in transverse compression. The predicted distribution, orientation and width of the shear bands is in relatively good agreement with those observed on in-situ SEM micrographs of a carbon fibre-epoxy ply loaded in transverse compression, see Fig. A.6 (d), while standard continuum modelling approaches fail to predict this micro-sized shear band network as explained earlier [76]. In-situ SEM micrographs of transversally compressed UD composites also indicate that microcracks nucleate and grow along the sites of the localised shear-band type inelastic flow in the polymer matrix, see Fig. A.6 (d). Hence, the extension of the STZ model could potentially be used to study the failure of the composite material by simulating the complex interaction between matrix-fibre interfacial fracture and damage in the matrix due to intense shear localisation.

Despite the promising outlook, the use of STZ dynamics for the mesoscale modelling of the large strain, inelastic constitutive behaviour of polymer glasses (and composites made thereof) is still in its infancy. We conclude by identifying some challenges and opportunities. One avenue of future research includes the relation between the heterogeneous structural nature of the polymer on the molecular scale and the STZ activation dynamics [438]. As discussed in Section 3, AFM provides a powerful tool to probe the properties of a polymer matrix at the nanoscale. These measurements indicate that (1) the elastic field landscape of an undeformed, fully cured epoxy can be heterogeneous on the length scale corresponding to several STZs [58, 361] and (2) property gradients in the matrix close to the sizing-coated fibres exist. The effect of these phenomena on the degree of localisation (and failure) of the deformed matrix close to the fibre is an excellent case study for an STZ-enriched mesoscale model. From a more practical point of view, the sensitivity of the model response to the values of

its basic ingredients (e.g., the value of the activation eigenstrain γ_0 and of the activation volume) should be explored in more detail. This could provide a sound basis for the calibration of an STZ-based mesoscale model for a material system of interest. This calibration is typically guided by atomistic simulations (to provide, e.g., a physical range for the value of γ_0) and uniaxial deformation tests on macro-sized samples and/or (nano)indentation tests on small material volumes (to provide, e.g., a range for the activation volume). However, the final selection of the values of these fundamental parameters often remains a somewhat arbitrary stress-strain curve fitting task to date. Lastly, we note that for elevated temperatures close to T_g, the viscoelastic response of the polymer matrix may play a role in the cooperative organisation of activated STZs into shear bands. The role of viscoelastic matrix relaxation upon STZ activation should be explored in more detail too.

A.7 Conclusion and perspectives

Four different nanomechanical testing techniques – nanoindentation, AFM, SEM-DIC, fibre push in/out – and one mesoscale model based on STZ activation dynamics have been reviewed in the context of a quantitative description of the local fibre-matrix response of polymer-based composites. Experimental and modelling results on a highly cross-linked epoxy resin (RTM6) reinforced by CF have been highlighted to illustrate the methods but also to deliver the current state of understanding of the mechanisms in this reference system. These results confirm that although a qualitative description of the mechanical behaviour can be obtained with classical continuum models, yet many questions remain regarding the quantitative prediction of the viscoplastic, shear banding and damage processes as related to the unknown precise nature/structure of the material and interphase at the local fibre-matrix length scale.

Specific conclusions regarding each method have been provided inside each section. As a general conclusion, it is essential to acknowledge that a combination of several of these methods is needed to generate the full picture and shed light on the aforementioned issues, for instance:

- The interphase and confined matrix response (and thus AFM, nanoindentation and a STZ-inspired mesoscale model) are needed to simulate the push-out test data and identify, by inverse modelling, accurate interface properties;
- But, these interface failure properties are needed to simulate the in-situ SEM compression tests until fracture and make a quantitative comparison with DIC data;
- The STZ model could be used to identify the parameters of a coarse-grained cohesive law for the interface region between the fibre and the matrix. This cohesive law can be used in a continuum finite element

model of a representative volume element of the composite. To this end, an intrinsic traction-separation law for the interface should be combined with an STZ mesoscale model which explicitly takes the interphase region surrounding the fibre into account.

As indicated in the last example, challenges on scale transition methods in order to coarse grain information from the sub-micrometre length scale also exist to properly account for the impact of these lower scale effects at the macroscopic level. Another important element not addressed in the paper is related to the damage and fracture mechanisms in bulk resins, which are known to be dominated by defects in the range of micrometres to tens of micrometres. Such defects are not seen as dominating the matrix failure at fibre-confined matrix level, and care should thus be taken not to extend, again, bulk data (for instance macroscopic fracture strains) to the local level. Another important subject that could benefit from nanoscale investigation concerns the ageing mechanisms taking place at the interface/interphase levels, and that could be locally investigated by the methods above in order to develop less phenomenological ageing-induced damage models.

Finally, the extensive list of approaches described and analysed in this paper is far from being comprehensive. Atomistic simulations, x-ray synchrotron computed tomography (CT), micro fibre pull-out or micropillar compression are among the other methods available that could enrich the understanding of the local fibre-matrix response. In particular, in situ x-ray CT already mentioned in the introduction [370–372, 439] provide invaluable information on the sequence of damage events and interplay between failure mechanisms. For instance, Breite et al. [440] very recently addressed interactions effects between fiber breaks at local cluster level using ultrafast synchrotron CT scans, and Ni et al. [441], using the same technique, studied the effects of nanoscale interlaminar reinforcement on the damage progression in double-edge notched composite laminates. With the increasing resolution of synchrotron based tools one can progressively look at deformation and fracture phenomena at submicron scale with these techniques relevant for the fibre-matrix elementary length scale. The combination with digital volume correlation method made possible by the dispersion of nanoscopic markers in the matrix is nowadays offering the holy grail of extracting local 3D deformation fields together with information on the failure process [442].

List of publications

Publications in peer-reviewed journals

T. Pardoen; N. Klavzer; S. Gayot; F. Van Loock; J. Chevalier; X. Morelle; V. Destoop; F. Lani; P. Camanho; L. Brassart; B. Nysten; C. Bailly. Nanomechanics serving polymer-based composite research. Comptes Rendus. Physique, Tome 22, 2021 no. S3, pp. 331-352.

N. Klavzer, S.F. Gayot, M. Coulombier, B. Nysten, T. Pardoen, *Nanoscale digital image correlation at elementary fibre/matrix level in polymer–based composites*, Composites Part A: Applied Science and Manufacturing, Volume 168, 2023, 107455.

N. Klavzer, M. Abatour, J. Chevalier, S. Forest and T. Pardoen, *Modelling of size-dependent plasticity in polymer-based composites based on nano- and macroscale experimental results*, Composites Part A: Applied Science and Manufacturing, Volume 185, 2024, 108309.

N. Klavzer, J. Chevalier, C. Breite, X. Morelle, Y. Swolfs, T. Pardoen, *Master trends in the elasto-viscoplastic behaviour of highly cross-linked epoxy resins*, Under submission.

Publications in conferences

N. Klavzer, F. Van Loock, J. Chevalier, L. Brassart, T. Pardoen, *Visco-plastic behavior of a polymer matrix at the fibre diameter length scale: a finite element mesoscale model relying on shear transformation zone (STZ) dynamics*, 8th ECCOMAS Thematic Conference on the Mechanical Response of Composites: COMPOSITES 2021, Stockholm (Oral presentation).

N. Klavzer, J. Chevalier, T. Pardoen, *Nanomechanical characterisation of unidirectional fibre-reinforced composites at the fibre-matrix level*, 18th European Mechanics of Materials Conference (EMMC18), Oxford (Oral presentation).

N. Klavzer, F. Van Loock, J. Chevalier, L. Brassart, T. Pardoen, *A shear transformation zone mesoscale model for plasticity in polymer glasses with visco-elastic background*, 18th International Conference on Deformation, Yield and Fracture of Polymers (DYFP22), Kerkrade (Poster presentation).

N. Klavzer, J. Chevalier, C. Breite, Y. Swolfs, C. Bailly,T. Pardoen,*Major trends in the elasto-visco-plastic behaviour of highly cross-linked epoxy resins*, 11th European Solid Mechanics Conference (ESMC22), Galway (Oral presentation).

N. Klavzer, S. Gayot, J. Chevalier, F. Van Loock, P.P. Camanho, B. Nysten, T. Pardoen, *Micro- and nano-mechanical characterisation and modelling of the local matrix deformation in fibre-reinforced epoxy*, in Proceedings of 23th International Conference on Composite Materials (ICCM23), Belfast.

N. Klavzer, M. Abatour, J. Chevalier, S. Forest and T. Pardoen,*Local fibre-matrix behaviour unravelled by nano-DIC and strain gradient plasticity in a fibre-reinforced composite*, 9th International Conference on Fracture of Polymers, Composites and Adhesives, Les Diablerets (Oral presentation).

Bibliography

[1] M. F. Ashby, *Materials Selection in Mechanical Design*. Butterworth-Heinemann, 2011. DOI: 10.1016/C2009-0-25539-5.

[2] A. Arteiro, G. Catalanotti, J. Reinoso, P. Linde, and P. P. Camanho, *Simulation of the Mechanical Response of Thin-Ply Composites: From Computational Micro-Mechanics to Structural Analysis*. 2019, vol. 26, pp. 1445–1487. DOI: 10.1007/s11831-018-9291-2.

[3] J. Llorca, C. González, J. M. Molina-Aldareguía, and C. S. Lópes, "Multiscale modeling of composites: Toward virtual testing... and beyond," *JOM*, vol. 65, pp. 215–225, 2013. DOI: 10.1007/s11837-012-0509-8.

[4] C. González, J. Vilatela, J. Molina-Aldareguía, C. Lopes, and J. LLorca, "Structural composites for multifunctional applications: Current challenges and future trends," *Prog. Mater. Sci.*, vol. 89, pp. 194–251, 2017.

[5] C. Furtado *et al.*, "A methodology to generate design allowables of composite laminates using machine learning," *International Journal of Solids and Structures*, vol. 233, p. 111 095, 2021. DOI: 10.1016/j.ijsolstr.2021.111095.

[6] OECD and ITF, *ITF Transport Outlook 2023*. OECD, 2023, p. 172, ISBN: 9789282144817. DOI: 10.1787/b6cc9ad5-en.

[7] X. Morelle, "Mechanical characterization and physics-based modeling of highly-crosslinked epoxy resin," Ph.D. dissertation, Université catholique de Louvain, Louvain-la-Neuve, Belgium, 2015.

[8] A. Argon, *The Physics of Deformation and Fracture of Polymers*. Cambridge: Cambridge University Press, 2013. DOI: 10.1017/CBO9781139033046.

[9] P. B. Bowden, "The Yield Behaviour of Glassy Polymers BT - The Physics of Glassy Polymers," in R. N. Haward, Ed., Springer Netherlands, 1973, pp. 279–339. DOI: 10.1007/978-94-010-2355-9_6.

[10] C. G'Sell, "Plastic Deformation of Glassy Polymers: Constitutive Equations and Macromolecular Mechanisms," in *Strength of Metals and Alloys (ICSMA 7)*, Elsevier, 1986, pp. 1943–1982. DOI: 10.1016/B978-0-08-031640-6.50019-0.

[11] M. C. Boyce, D. M. Parks, and A. S. Argon, "Large inelastic deformation of glassy polymers. part I: rate dependent constitutive model," *Mechanics of Materials*, vol. 7, pp. 15–33, 1988.

[12] X. P. Morelle, J. Chevalier, C. Bailly, T. Pardoen, and F. Lani, "Mechanical characterization and modeling of the deformation and failure of the highly crosslinked RTM6 epoxy resin," *Mechanics of Time-Dependent Materials*, vol. 21, pp. 419–454, 2017. DOI: 10.1007/s11043-016-9336-6.

[13] X. Poulain, A. A. Benzerga, and R. K. Goldberg, "Finite-strain elasto-viscoplastic behavior of an epoxy resin: Experiments and modeling in the glassy regime," *International Journal of Plasticity*, vol. 62, pp. 138–161, 2014. DOI: 10.1016/j.ijplas.2014.07.002.

[14] G. M. Odegard and A. Bandyopadhyay, "Physical aging of epoxy polymers and their composites," *Journal of Polymer Science, Part B: Polymer Physics*, vol. 49, pp. 1695–1716, 2011. DOI: 10.1002/polb.22384.

[15] C. G.'Sell and G. B. McKenna, "Influence of physical ageing on the yield response of model DGEBA/poly(propylene oxide) epoxy glasses," *Polymer*, vol. 33, pp. 2103–2113, 1992. DOI: 10.1016/0032-3861(92)90876-X.

[16] H. G. Van Melick, L. E. Govaert, and H. E. Meijer, "Localisation phenomena in glassy polymers: Influence of thermal and mechanical history," *Polymer*, vol. 44, pp. 3579–3591, 2003. DOI: 10.1016/S0032-3861(03)00089-2.

[17] C. C. Clarijs, M. J. Kanters, M. J. van Erp, T. A. Engels, and L. E. Govaert, "Predicting plasticity-controlled failure of glassy polymers: Influence of stress-accelerated progressive physical aging," *Journal of Polymer Science, Part B: Polymer Physics*, vol. 57, pp. 1300–1314, 2019. DOI: 10.1002/polb.24870.

[18] C. Marano and M. Rink, "Shear yielding threshold and viscoelasticity in an amorphous glassy polymer: A study on a styrene-acrylonitrile copolymer," *Polymer*, vol. 42, pp. 2113–2119, 2001. DOI: 10.1016/S0032-3861(00)00570-X.

[19] O. A. Hasan and M. C. Boyce, "A constitutive model for the nonlinear viscoelastic viscoplastic behavior of glassy polymers," *Polymer Engineering and Science*, vol. 35, pp. 331–344, 1995. DOI: 10.1002/pen.760350407.

[20] E. J. Kramer, "Open questions in the physics of deformation of polymer glasses," *Journal of Polymer Science, Part B: Polymer Physics*, vol. 43, pp. 3369–3371, 2005. DOI: 10.1002/polb.20639.

[21] L. C. Van Breemen, T. A. Engels, E. T. Klompen, D. J. Senden, and L. E. Govaert, "Rate- and temperature-dependent strain softening in solid polymers," vol. 50, pp. 1757–1771, 2012. DOI: 10.1002/polb.23199.

[22] H. E. H. Meijer and L. E. Govaert, "Mechanical performance of polymer systems: The relation between structure and properties," *Progress in Polymer Science*, vol. 30, pp. 915–938, 2005. DOI: 10.1016/j.progpolymsci.2005.06.009.

[23] H. G. Van Melick, L. E. Govaert, and H. E. Meijer, "On the origin of strain hardening in glassy polymers," *Polymer*, vol. 44, pp. 2493–2502, 2003. DOI: 10.1016/S0032-3861(03)00112-5.

[24] R. S. Hoy and M. O. Robbins, "Strain hardening of polymer glasses: Effect of entanglement density, temperature, and rate," *Journal of Polymer Science Part B: Polymer Physics*, vol. 44, pp. 3487–3500, 2006. DOI: 10.1002/polb.21012.

[25] T. A. Tervoort and L. E. Govaert, "Strain-hardening behavior of polycarbonate in the glassy state," *Journal of Rheology*, vol. 44, pp. 1263–1277, 2000. DOI: 10.1122/1.1319175.

[26] D. J. Senden, S. Krop, J. A. Van Dommelen, and L. E. Govaert, "Rate- and temperature-dependent strain hardening of polycarbonate," *Journal of Polymer Science, Part B: Polymer Physics*, vol. 50, pp. 1680–1693, 2012. DOI: 10.1002/polb.23165.

[27] C. Tian, R. Xiao, and J. Guo, "An experimental study on strain hardening of amorphous thermosets: Effect of temperature, strain rate, and network density," *Journal of Applied Mechanics, Transactions ASME*, vol. 85, pp. 1–8, 2018. DOI: 10.1115/1.4040692.

[28] P. D. Wu and E. van der Giessen, "On neck propagation in amorphous glassy polymers under plane strain tension," *International Journal of Plasticity*, vol. 11, pp. 211–235, 1995. DOI: 10.1016/0749-6419(94)00043-3.

[29] H. Meijer, L. Govaert, and R. Smit, "A multi-level finite element method for modeling rubber-toughened amorphous polymers," in *Toughening of plastics : advances in modeling and experiments* (ACS symposium series), R. Pearson, H.-J. Sue, and A. Yee, Eds., ACS symposium series. American Chemical Society, 2000, pp. 50–70, ISBN: 0-8412-3657-7.

[30] L. E. Govaert, P. H. Timmermans, and W. A. Brekelmans, "The influence of intrinsic strain softening on strain localization in polycarbonate: Modeling and experimental validation," *Journal of Engineering Materials and Technology, Transactions of the ASME*, vol. 122, pp. 177–185, 2000. DOI: 10.1115/1.482784.

[31] E. M. Arruda and M. C. Boyce, "A three-dimensional constitutive model for the large stretch behavior of rubber elastic materials," *Journal of the Mechanics and Physics of Solids*, vol. 41, pp. 389–412, 1993. DOI: 10.1016/0022-5096(93)90013-6.

[32] P. Wu and E. Van Der Giessen, "On improved network models for rubber elasticity and their applications to orientation hardening in glassy polymers," *Journal of the Mechanics and Physics of Solids*, vol. 41, pp. 427–456, 1993. DOI: 10.1016/0022-5096(93)90043-F.

[33] R. Quinson, J. Perez, M. Rink, and A. Pavan, "Yield criteria for amorphous glassy polymers," *Journal of Materials Science*, vol. 32, pp. 1371–1379, 1997. DOI: https://doi.org/10.1023/A:1018525127466.

[34] T. H. Hsieh, A. J. Kinloch, K. Masania, A. C. Taylor, and S. Sprenger, "The mechanisms and mechanics of the toughening of epoxy polymers modified with silica nanoparticles," *Polymer*, vol. 51, pp. 6284–6294, 2010. DOI: 10.1016/j.polymer.2010.10.048.

[35] W. J. Cantwell and H. H. Kausch, "Fracture behaviour of epoxy resins," *Chemistry and Technology of Epoxy Resins*, pp. 144–174, 1993. DOI: 10.1007/978-94-011-2932-9_5.

[36] P. D. Wu and E. van der Giessen, "Analysis of shear band propagation in amorphous glassy polymers," *International Journal of Solids and Structures*, vol. 31, pp. 1493–1517, 1994. DOI: 10.1016/0020-7683(94)90011-6.

[37] E. van der Giessen, "Localized plastic deformations in glassy polymers," *European Journal of Mechanics A-Solids*, vol. 16, pp. 87–106, 1997.

[38] O. Hasan and M. Boyce, "Energy storage during inelastic deformation of glassy polymers," *Polymer*, vol. 34, pp. 5085–5092, 1993. DOI: 10.1016/0032-3861(93)90252-6.

[39] T. Chow, "Stress-strain behaviour of physically ageing polymers," *Polymer*, vol. 34, pp. 541–545, 1993. DOI: 10.1016/0032-3861(93)90547-N.

[40] D. J. A. Senden, J. A. W. van Dommelen, and L. E. Govaert, "Strain hardening and its relation to Bauschinger effects in oriented polymers," *Journal of Polymer Science Part B: Polymer Physics*, vol. 48, pp. 1483–1494, 2010. DOI: 10.1002/polb.22056.

[41] J. Yu, C. Breite, F. Van Loock, T. Pardoen, and Y. Swolfs, "Experimental investigation of yield and hysteresis behaviour of an epoxy resin under cyclic compression in the large deformation regime," *Express Polymer Letters*, vol. 18, pp. 133–143, 2024. DOI: 10.3144/expresspolymlett.2024.11.

[42] H. Eyring, "Viscosity, Plasticity, and Diffusion as Examples of Absolute Reaction Rates," *The Journal of Chemical Physics*, vol. 4, pp. 283–291, 1936. DOI: 10.1063/1.1749836.

[43] R. E. Robertson, "Theory for the Plasticity of Glassy Polymers," *The Journal of Chemical Physics*, vol. 44, pp. 3950–3956, 1966. DOI: 10.1063/1.1726558.

[44] A. S. Argon, "A theory for the low-temperature plastic deformation of glassy polymers," *Philosophical Magazine*, vol. 28, pp. 839–865, 1973. DOI: 10.1080/14786437308220987.

[45] P. B. Bowden and S. Raha, "A molecular model for yield and flow in amorphous glassy polymers making use of a dislocation analogue," *The Philosophical Magazine: A Journal of Theoretical Experimental and Applied Physics*, vol. 29, pp. 149–166, 1974. DOI: 10.1080/14786437408213560.

[46] C. Li and A. Strachan, "Molecular scale simulations on thermoset polymers: A review," *Journal of Polymer Science, Part B: Polymer Physics*, vol. 53, pp. 103–122, 2015. DOI: 10.1002/polb.23489.

[47] J. Konrad, R. H. Meißner, E. Bitzek, and D. Zahn, "A Molecular Simulation Approach to Bond Reorganization in Epoxy Resins: From Curing to Deformation and Fracture," *ACS Polymers Au*, vol. 1, pp. 165–174, 2021. DOI: 10.1021/acspolymersau.1c00016.

[48] S. Yang and J. Qu, "Computing thermomechanical properties of crosslinked epoxy by molecular dynamic simulations," *Polymer*, vol. 53, pp. 4806–4817, 2012. DOI: 10.1016/j.polymer.2012.08.045.

[49] A. Shokuhfar and B. Arab, "The effect of cross linking density on the mechanical properties and structure of the epoxy polymers: Molecular dynamics simulation," *Journal of Molecular Modeling*, vol. 19, pp. 3719–3731, 2013. DOI: 10.1007/s00894-013-1906-9.

[50] X. Zheng, Y. Guo, J. F. Douglas, and W. Xia, "Competing Effects of Cohesive Energy and Cross-Link Density on the Segmental Dynamics and Mechanical Properties of Cross-Linked Polymers," *Macromolecules*, vol. 55, pp. 9990–10 004, 2022. DOI: 10.1021/acs.macromol.2c01719.

[51] S. C. Chowdhury, R. M. Elder, T. W. Sirk, and J. W. Gillespie, "Epoxy resin thermo-mechanics and failure modes: Effects of cure and cross-linker length," *Composites Part B: Engineering*, vol. 186, p. 107 814, 2020. DOI: 10.1016/J.COMPOSITESB.2020.107814.

[52] K. Yashiro, T. Ito, and Y. Tomita, "Molecular dynamics simulation of deformation behavior in amorphous polymer: nucleation of chain entanglements and network structure under uniaxial tension," *International Journal of Mechanical Sciences*, vol. 45, pp. 1863–1876, 2003. DOI: 10.1016/J.IJMECSCI.2003.11.001.

[53] V. Sundararaghavan and A. Kumar, "Molecular dynamics simulations of compressive yielding in cross-linked epoxies in the context of Argon theory," *International Journal of Plasticity*, vol. 47, pp. 111–125, 2013. DOI: 10.1016/J.IJPLAS.2013.01.004.

[54] N. Vu-Bac, M. A. Bessa, T. Rabczuk, and W. K. Liu, "A Multiscale Model for the Quasi-Static Thermo-Plastic Behavior of Highly Cross-Linked Glassy Polymers," *Macromolecules*, vol. 48, pp. 6713–6723, 2015. DOI: 10.1021/acs.macromol.5b01236.

[55] A. Argon, "Plastic deformation in metallic glasses," *Acta Metall.*, vol. 27, pp. 47–58, 1979.

[56] J. D. Eshelby and R. E. Peierls, "The determination of the elastic field of an ellipsoidal inclusion, and related problems," *Proc. Math. Phys. Eng. Sci.*, vol. 241, pp. 376–396, 1957.

[57] E. R. Homer and C. A. Schuh, "Mesoscale modeling of amorphous metals by shear transformation zone dynamics," *Acta Mater.*, vol. 57, pp. 2823–2833, 2009.

[58] J. Chevalier, L. Brassart, F. Lani, C. Bailly, T. Pardoen, and X. P. Morelle, "Unveiling the nanoscale heterogeneity controlled deformation of thermosets," *J. Mech. Phys. Solids*, vol. 121, pp. 432–446, 2018.

[59] F. Van Loock, L. Brassart, and T. Pardoen, "Implementation and calibration of a mesoscale model for amorphous plasticity based on shear transformation dynamics," *International Journal of Plasticity*, vol. 145, p. 103 079, 2021. DOI: 10.1016/J.IJPLAS.2021.103079.

[60] G. Z. Voyiadjis and A. Samadi-Dooki, "Constitutive modeling of large inelastic deformation of amorphous polymers: Free volume and shear transformation zone dynamics," *Journal of Applied Physics*, vol. 119, p. 225 104, 2016.

[61] G. Z. Voyiadjis, L. Malekmotiei, and A. Samadi-Dooki, "Indentation size effect in amorphous polymers based on shear transformation mediated plasticity," *Polymer*, vol. 137, pp. 72–81, 2018. DOI: 10.1016/j.polymer.2018.01.006.

[62] C. Peng and F. Zeng, "Modeling the indentation size effects of polymers, based on couple stress elasticity and shear transformation plasticity," *Archive of Applied Mechanics*, vol. 92, pp. 3661–3681, 2022. DOI: 10.1007/s00419-022-02255-6.

[63] R. Estevez, M. G. Tijssens, and E. Van Der Giessen, "Modeling of the competition between shear yielding and crazing in glassy polymers," *Journal of the Mechanics and Physics of Solids*, vol. 48, pp. 2585–2617, 2000. DOI: 10.1016/S0022-5096(00)00016-8.

[64] D. C. Phillips, J. M. Scott, and M. Jones, "Crack propagation in an amine-cured epoxide resin," *Journal of Materials Science*, vol. 13, pp. 311–322, 1978. DOI: 10.1007/BF00647775.

[65] R. A. Gledhill and A. J. Kinloch, "Mechanics of crack growth in epoxide resins," *Polymer Engineering & Science*, vol. 19, pp. 82–88, 1979. DOI: 10.1002/pen.760190205.

[66] S. Yamini and R. J. Young, "The mechanical properties of epoxy resins - Part 2 Effect of plastic deformation upon crack propagation," *Journal of Materials Science*, vol. 15, pp. 1823–1831, 1980. DOI: 10.1007/BF00550603.

[67] S. Yamini and R. J. Young, "The mechanical properties of epoxy resins - Part 1 : Mechanisms of plastic deformation," *Journal of Materials Science*, vol. 15, pp. 1814–1822, 1980.

[68] M. D. Glad and E. J. Kramer, "Microdeformation and network structure in epoxies," *Journal of Materials Science*, vol. 26, pp. 2273–2286, 1991. DOI: 10.1007/BF01130169.

[69] I. Narisawa, T. Murayama, and H. Ogawa, "Internal fracture of notched epoxy resins," *Polymer*, vol. 23, pp. 291–294, 1982. DOI: 10.1016/0032-3861(82)90319-6.

[70] B. W. Cherry and K. W. Thompson, "The Fracture of Highly Crosslinked Polymers, Part 2 : Fractography.," *Journal of Materials Science*, vol. 16, pp. 1925–1934, 1981.

[71] W. J. Cantwell, A. C. Roulin-Moloney, and T. Kaiser, "Fractography of unfilled and particulate-filled epoxy resins," *Journal of Materials Science*, vol. 23, pp. 1615–1631, 1988. DOI: 10.1007/BF01115700.

[72] B. Fiedler, M. Hojo, S. Ochiai, K. Schulte, and M. Ando, "Failure behavior of an epoxy matrix under different kinds of static loading," *Composites Science and Technology*, vol. 61, pp. 1615–1624, 2001. DOI: 10.1016/S0266-3538(01)00057-4.

[73] E. S. Greenhalgh, *Failure Analysis and Fractography of Polymer Composites*. Woodhead Publishing, 2009.

[74] J. Chevalier, X. P. Morelle, C. Bailly, P. P. Camanho, T. Pardoen, and F. Lani, "Micro-mechanics based pressure dependent failure model for highly cross-linked epoxy resins," *Engineering Fracture Mechanics*, vol. 158, pp. 1–12, 2016. DOI: 10.1016/j.engfracmech.2016.02.039.

[75] J. Chevalier, X. Morelle, P. Camanho, F. Lani, and T. Pardoen, "On a unique fracture micromechanism for highly cross-linked epoxy resins," *Journal of the Mechanics and Physics of Solids*, vol. 122, 2019. DOI: 10.1016/J.JMPS.2018.09.028.

[76] J. Chevalier, P. P. Camanho, F. Lani, and T. Pardoen, "Multi-scale characterization and modelling of the transverse compression response of unidirectional carbon fiber reinforced epoxy," *Composite Structures*, vol. 209, pp. 160–176, 2019.

[77] S. Yamini and R. J. Young, "Stability of crack propagation in epoxy resins," *Polymer*, vol. 18, pp. 1075–1080, 1977. DOI: 10.1016/0032-3861(77)90016-7.

[78] R. A. Gledhill, A. J. Kinloch, S. Yamini, and R. J. Young, "Relationship between mechanical properties of and crack progogation in epoxy resin adhesives," *Polymer*, vol. 19, pp. 574–582, 1978. DOI: 10.1016/0032-3861(78)90285-9.

[79] K. Selby and L. E. Miller, "Fracture toughness and mechanical behaviour of an epoxy resin," *Journal of Materials Science*, vol. 10, pp. 12–24, 1975. DOI: 10.1007/BF00541027.

[80] J. Lai and E. Van Der Giessen, "A numerical study of crack-tip plasticity in glassy polymers," *Mechanics of Materials*, vol. 25, pp. 183–197, 1997. DOI: 10.1016/S0167-6636(97)00006-9.

[81] K. Mishra, L. Brassart, and A. Singh, "Rate dependent fracture behavior of highly cross-linked epoxy resin," *Engineering Failure Analysis*, vol. 140, p. 106 558, 2022. DOI: 10.1016/J.ENGFAILANAL.2022.106558.

[82] E. M. Odom and D. F. Adams, "Specimen size effect during tensile testing of an unreinforced polymer," *Journal of Materials Science*, vol. 27, pp. 1767–1771, 1992. DOI: 10.1007/BF01107202.

[83] T. Hobbiebrunken, B. Fiedler, M. Hojo, and M. Tanaka, "Experimental determination of the true epoxy resin strength using micro-scaled specimens," *Composites Part A: Applied Science and Manufacturing*, vol. 38, pp. 814–818, 2007. DOI: 10.1016/j.compositesa.2006.08.006.

[84] J. Misumi, R. Ganesh, S. Sockalingam, and J. W. Gillespie, "Experimental characterization of tensile properties of epoxy resin by using micro-fiber specimens," *Journal of Reinforced Plastics and Composites*, vol. 35, pp. 1792–1801, 2016.

[85] X. M. Sui *et al.*, "Extreme scale-dependent tensile properties of epoxy fibers," *Express Polymer Letters*, vol. 13, pp. 993–1003, 2019. DOI: 10.3144/expresspolymlett.2019.86.

[86] O. Verschatse, L. Daelemans, W. Van Paepegem, and K. De Clerck, "In-situ observations of microscale ductility in a quasi-brittle bulk scale epoxy," *Polymers*, vol. 12, p. 2581, 2020. DOI: 10.3390/polym12112581.

[87] S. Zike, B. F. Sørensen, and L. P. Mikkelsen, "Experimental determination of the micro-scale strength and stress-strain relation of an epoxy resin," *Materials and Design*, vol. 98, pp. 47–60, 2016. DOI: 10.1016/j.matdes.2016.02.102.

[88] Y. Qiao and M. Salviato, "Strength and cohesive behavior of thermoset polymers at the microscale: A size-effect study," *Engineering Fracture Mechanics*, vol. 213, pp. 100–117, 2019. DOI: 10.1016/j.engfracmech.2019.03.033.

[89] B. Zhang, J. Ge, F. Cheng, J. Huang, S. Liu, and J. Liang, "Failure prediction for fiber reinforced polymer composites based on virtual experimental tests," *Journal of Materials Research and Technology*, vol. 24, pp. 8924–8939, 2023. DOI: 10.1016/J.JMRT.2023.05.123.

[90] A. R. Melro, P. P. Camanho, F. M. Andrade Pires, and S. T. Pinho, "Micromechanical analysis of polymer composites reinforced by unidirectional fibres: Part II – Micromechanical analyses," *International Journal of Solids and Structures*, vol. 50, pp. 1906–1915, 2013. DOI: 10.1016/J.IJSOLSTR.2013.02.007.

[91] Y. Swolfs, I. Verpoest, and L. Gorbatikh, "A review of input data and modelling assumptions in longitudinal strength models for unidirectional fibre-reinforced composites," *Composite Structures*, vol. 150, pp. 153–172, 2016. DOI: 10.1016/J.COMPSTRUCT.2016.05.002.

[92] S. C. Garcea, I. Sinclair, and S. M. Spearing, "Fibre failure assessment in carbon fibre reinforced polymers under fatigue loading by synchrotron X-ray computed tomography," *Composites Science and Technology*, vol. 133, pp. 157–164, 2016. DOI: 10.1016/J.COMPSCITECH.2016.07.030.

[93] C. Breite, "Aligning Fibre Break Models for Composites with the Observable Micro-Scale Material Behaviour," Ph.D. dissertation, Katholieke Universiteit Leuven, 2021.

[94] J. Srisuriyachot *et al.*, "Synchrotron micro-CT in kink-band formation of UD-CFRP laminates with microdefects," *Composites Part B: Engineering*, vol. 266, p. 111 038, 2023. DOI: 10.1016/J.COMPOSITESB.2023.111038.

[95] Q. Sun *et al.*, "Experimental and computational analysis of failure mechanisms in unidirectional carbon fiber reinforced polymer laminates under longitudinal compression loading," *Composite Structures*, vol. 203, pp. 335–348, 2018. DOI: 10.1016/J.COMPSTRUCT.2018.06.028.

[96] L. Wan, Y. Ismail, Y. Sheng, J. Ye, and D. Yang, "A review on micromechanical modelling of progressive failure in unidirectional fibre-reinforced composites," *Composites Part C: Open Access*, vol. 10, p. 100 348, 2023. DOI: 10.1016/J.JCOMC.2023.100348.

[97] E. K. Gamstedt and B. A. Sjögren, "Micromechanisms in tension-compression fatigue of composite laminates containing transverse plies," *Composites Science and Technology*, vol. 59, pp. 167–178, 1999. DOI: 10.1016/S0266-3538(98)00061-X.

[98] F. París, E. Correa, and V. Mantič, "Kinking of transversal interface cracks between fiber and matrix," *Journal of Applied Mechanics, Transactions ASME*, vol. 74, pp. 703–716, 2007. DOI: 10.1115/1.2711220.

[99] E. Correa, M. I. Valverde, M. L. Velasco, and F. París, "Microscopical observations of inter-fibre failure under tension," *Composites Science and Technology*, vol. 155, pp. 213–220, 2018. DOI: 10.1016/J.COMPSCITECH.2017.12.009.

[100] T. Hobbiebrunken, M. Hojo, T. Adachi, C. De Jong, and B. Fiedler, "Evaluation of interfacial strength in CF/epoxies using FEM and in-situ experiments," *Composites Part A: Applied Science and Manufacturing*, vol. 37, pp. 2248–2256, 2006. DOI: 10.1016/J.COMPOSITESA.2005.12.021.

[101] N. Baral, H. Guezenoc, P. Davies, and C. Baley, "High modulus carbon fibre composites: Correlation between transverse tensile and mode I interlaminar fracture properties," *Materials Letters*, vol. 62, pp. 1096–1099, 2008. DOI: 10.1016/J.MATLET.2007.07.071.

[102] E. Correa, V. Mantič, and F. París, "A micromechanical view of inter-fibre failure of composite materials under compression transverse to the fibres," *Composites Science and Technology*, vol. 68, pp. 2010–2021, 2008. DOI: 10.1016/J.COMPSCITECH.2008.02.022.

[103] P. L. Zumaquero, E. Correa, J. Justo, and F. París, "Microscopical observations of interface cracks from inter-fibre failure under compression in composite laminates," *Composites Part A: Applied Science and Manufacturing*, vol. 110, pp. 76–83, 2018. DOI: 10.1016/J.COMPOSITESA.2018.04.004.

[104] R. M. Christensen and S. J. DeTeresa, "Failure plane orientations for transverse loading of a unidirectional fiber composite," *International Journal of Solids and Structures*, vol. 40, pp. 7055–7062, 2003. DOI: 10.1016/S0020-7683(03)00354-8.

[105] C. González and J. LLorca, "Mechanical behavior of unidirectional fiber-reinforced polymers under transverse compression: Microscopic mechanisms and modeling," *Composites Science and Technology*, vol. 67, pp. 2795–2806, 2007. DOI: 10.1016/J.COMPSCITECH.2007.02.001.

[106] A. R. Melro, P. P. Camanho, F. M. Andrade Pires, and S. T. Pinho, "Micromechanical analysis of polymer composites reinforced by unidirectional fibres: Part I – Constitutive modelling," *International Journal of Solids and Structures*, vol. 50, pp. 1897–1905, 2013. DOI: 10.1016/j.ijsolstr.2013.02.009.

[107] T. A. Collings, "Transverse compressive behaviour of unidirectional carbon fibre reinforced plastics," *Composites*, vol. 5, pp. 108–116, 1974. DOI: 10.1016/0010-4361(74)90548-5.

[108] T. J. Vogler and S. Kyriakides, "Inelastic behavior of an AS4/PEEK composite under combined transverse compression and shear. Part I: experiments," *International Journal of Plasticity*, vol. 15, pp. 783–806, 1999. DOI: 10.1016/S0749-6419(99)00011-X.

[109] L. Yang, Y. Yan, Y. Liu, and Z. Ran, "Microscopic failure mechanisms of fiber-reinforced polymer composites under transverse tension and compression," *Composites Science and Technology*, vol. 72, pp. 1818–1825, 2012. DOI: 10.1016/J.COMPSCITECH.2012.08.001.

[110] Y. Hu, N. Kar, and S. Nutt, "Transverse compression failure of unidirectional composites," *Polymer Composites*, vol. 36, pp. 756–766, 2015. DOI: 10.1002/pc.22996.

[111] F. Naya, C. Gonzalez, C. S. Lopes, S. Van der Veen, and J. Llorca, "Combined Mutli-scale Simulations in Fiber-reinforced Composites," ECCM16 - 16TH European Conference on Composite Materials, 2014, pp. 22–26.

[112] F. Naya, C. González, C. S. Lopes, S. Van der Veen, and F. Pons, "Computational micromechanics of the transverse and shear behavior of unidirectional fiber reinforced polymers including environmental effects," *Composites Part A: Applied Science and Manufacturing*, vol. 92, pp. 146–157, 2017. DOI: 10.1016/J.COMPOSITESA.2016.06.018.

[113] E. Totry, C. González, and J. LLorca, "Failure locus of fiber-reinforced composites under transverse compression and out-of-plane shear," *Composites Science and Technology*, vol. 68, pp. 829–839, 2008. DOI: 10.1016/J.COMPSCITECH.2007.08.023.

[114] E. Totry, C. González, and J. LLorca, "Influence of the loading path on the strength of fiber-reinforced composites subjected to transverse compression and shear," *International Journal of Solids and Structures*, vol. 45, pp. 1663–1675, 2008. DOI: 10.1016/J.IJSOLSTR.2007.10.014.

[115] L. Wan *et al.*, "Computational micromechanics-based prediction of the failure of unidirectional composite lamina subjected to transverse and in-plane shear stress states," *Journal of Composite Materials*, vol. 54, pp. 3637–3654, 2020. DOI: 10.1177/0021998320918015.

[116] R. Guo, L. Mao, Z. Xin, and L. Ding, "Experimental characterization and micro-modeling of transverse tension behavior for unidirectional glass fibre-reinforced composite," *Composites Science and Technology*, vol. 222, p. 109 359, 2022. DOI: 10.1016/J.COMPSCITECH.2022.109359.

[117] M. Rueda-Ruiz, M. Herráez, F. Sket, F. Gálvez, C. González, and J. M. Molina-Aldareguia, "Study of the effect of strain rate on the in-plane shear and transverse compression response of a composite ply using computational micromechanics," *Composites Part A: Applied Science and Manufacturing*, vol. 168, p. 107 482, 2023. DOI: 10.1016/J.COMPOSITESA.2023.107482.

[118] M. May, N. Ledford, M. Isakov, P. Hahn, H. Paul, and S. Nagasawa, "The effect of strain rate on the orientation of the fracture plane in a unidirectional polymer matrix composite under transverse compression loading," *Composites Part A: Applied Science and Manufacturing*, vol. 138, p. 106 057, 2020. DOI: 10.1016/J.COMPOSITESA.2020.106057.

[119] M. Herráez, and F. Naya an C. González and M. Monclús, J. Molina, C. Lopes, and J. LLorca, "Microscale Characterization Techniques of Fibre-Reinforced Polymers," in *The Structural Integrity of Carbon Fiber Composites: Fifty Years of Progress and Achievement of the Science, Development, and Applications*, 2016, ch. Microscale, pp. 283–299, ISBN: 9783319461205. DOI: 10.1007/978-3-319-46120-5.

[120] A. Sharma, S. Daggumati, A. Gupta, and W. Van Paepegem, "On the prediction of the bi-axial failure envelope of a UD CFRP composite lamina using computational micromechanics: Effect of microscale parameters on macroscale stress–strain behavior," *Composite Structures*, vol. 251, p. 112 605, 2020. DOI: 10.1016/J.COMPSTRUCT.2020.112605.

[121] Q. Sun *et al.*, "Multi-scale computational analysis of unidirectional carbon fiber reinforced polymer composites under various loading conditions," *Composite Structures*, vol. 196, pp. 30–43, 2018. DOI: 10.1016/J.COMPSTRUCT.2018.05.025.

[122] Q. Sun *et al.*, "Failure criteria of unidirectional carbon fiber reinforced polymer composites informed by a computational micromechanics model," *Composites Science and Technology*, vol. 172, pp. 81–95, 2019. DOI: 10.1016/J.COMPSCITECH.2019.01.012.

[123] L. Riaño, J. F. Chailan, and Y. Joliff, "Evolution of effective mechanical and interphase properties during natural ageing of glass-fibre/epoxy composites using micromechanical approach," *Composite Structures*, vol. 258, p. 113 399, 2021. DOI: 10.1016/J.COMPSTRUCT.2020.113399.

[124] S. C. Chowdhury and J. W. Gillespie, "Strain-rate dependent mixed-mode traction laws for glass fiber-epoxy interphase using molecular dynamics simulations," *Composites Part B: Engineering*, p. 111 351, 2024. DOI: 10.1016/J.COMPOSITESB.2024.111351.

[125] T. Q. Bui and X. Hu, "A review of phase-field models, fundamentals and their applications to composite laminates," *Engineering Fracture Mechanics*, vol. 248, p. 107 705, 2021. DOI: 10.1016/J.ENGFRACMECH.2021.107705.

[126] J. Macías, A. Arteiro, F. Otero, P. P. Camanho, and J. Reinoso, "Micromechanical analysis of composite materials using Phase-Field models of brittle fracture," *European Journal of Mechanics - A/Solids*, vol. 102, p. 105 069, 2023. DOI: 10.1016/J.EUROMECHSOL.2023.105069.

[127] W. Tan and E. Martínez-Pañeda, "Phase field predictions of microscopic fracture and R-curve behaviour of fibre-reinforced composites," *Composites Science and Technology*, vol. 202, p. 108 539, 2021. DOI: 10.1016/J.COMPSCITECH.2020.108539.

[128] Y. Lee and R. S. Porter, "Crystallization of PEEK in Carbon Fiber Composites," *Polymer Engineering and Science*, vol. 26, pp. 633–639, 1986.

[129] S.-L. Gao and J.-K. Kim, "Cooling rate influences in carbon fibre/PEEK composites.PartII:interlaminarfracture toughness," *Composites Part A: Applied Science and Manufacturing*, vol. 31, pp. 517–530, 2000.

[130] L. E. Asp, L. A. Berglund, and R. Talreja, "Prediction of matrix-initiated transverse failure in polymer composites," *Composites Science and Technology*, vol. 56, pp. 1089–1097, 1996. DOI: 10.1016/0266-3538(96)00074-7.

[131] B. Fiedler, M. Hojo, S. Ochiai, K. Schulte, and M. Ochi, "Finite-element modeling of initial matrix failure in CFRP under static transverse tensile load," *Composites Science and Technology*, vol. 61, pp. 95–105, 2001. DOI: 10.1016/S0266-3538(00)00198-6.

[132] T. J. Vaughan and C. T. McCarthy, "Micromechanical modelling of the transverse damage behaviour in fibre reinforced composites," *Composites Science and Technology*, vol. 71, pp. 388–396, 2011. DOI: 10.1016/j.compscitech.2010.12.006.

[133] E. Correa, F. París, and V. Mantič, "Effect of thermal residual stresses on the matrix failure under transverse compression at micromechanical level – A numerical and experimental study," *Composites Part A: Applied Science and Manufacturing*, vol. 43, pp. 87–94, 2012. DOI: 10.1016/J.COMPOSITESA.2011.09.016.

[134] F. Danzi, D. Fanteria, E. Panettieri, and M. C. Mancino, "A numerical micro-mechanical study on damage induced by the curing process in carbon/epoxy unidirectional material," *Composite Structures*, vol. 210, pp. 755–766, 2019. DOI: 10.1016/J.COMPSTRUCT.2018.11.059.

[135] P. T. Gonçalves, A. Arteiro, N. Rocha, and L. Pina, "Numerical Analysis of Micro-Residual Stresses in a Carbon/Epoxy Polymer Matrix Composite during Curing Process," *Polymers*, vol. 14, p. 2653, 2022. DOI: 10.3390/polym14132653.

[136] H. Ghayoor, C. C. Marsden, S. V. Hoa, and A. R. Melro, "Numerical analysis of resin-rich areas and their effects on failure initiation of composites," *Composites Part A: Applied Science and Manufacturing*, vol. 117, pp. 125–133, 2019. DOI: 10.1016/J.COMPOSITESA.2018.11.016.

[137] H. Ahmadian, M. Yang, and S. Soghrati, "Effect of resin-rich zones on the failure response of carbon fiber reinforced polymers," *International Journal of Solids and Structures*, vol. 188-189, pp. 74–87, 2020. DOI: 10.1016/J.IJSOLSTR.2019.10.004.

[138] X. Pang *et al.*, "Effect of resin-rich areas on failure behavior of unidirectional CFRP under transverse pure shear," *Computational Materials Science*, vol. 219, p. 112 023, 2023. DOI: 10.1016/J.COMMATSCI.2023.112023.

[139] F. Huang, X. Pang, F. Zhu, S. Zhang, Z. Fan, and X. Chen, "Transverse mechanical properties of unidirectional FRP including resin-rich areas," *Computational Materials Science*, vol. 198, p. 110 701, 2021. DOI: 10.1016/J.COMMATSCI.2021.110701.

[140] S. F. M. de Almeida and Z. d. S. N. Neto, "Effect of void content on the strength of composite laminates," *Composite Structures*, vol. 28, pp. 139–148, 1994. DOI: 10.1016/0263-8223(94)90044-2.

[141] H. Zhu, B. Wu, D. Li, D. Zhang, and Y. Chen, "Influence of Voids on the Tensile Performance of Carbon/epoxy Fabric Laminates," *Journal of Materials Science & Technology*, vol. 27, pp. 69–73, 2011. DOI: 10.1016/S1005-0302(11)60028-5.

[142] S. F. Gayot *et al.*, "Influence of physical ageing and fibre proximity on the local mechanical response of the Elium® thermoplastic composite matrix," *Composites Part A: Applied Science and Manufacturing*, p. 108 141, 2024. DOI: 10.1016/J.COMPOSITESA.2024.108141.

[143] O. Vallmajó, A. Arteiro, J. M. Guerrero, A. R. Melro, A. Pupurs, and A. Turon, "Micromechanical analysis of composite materials considering material variability and microvoids," *International Journal of Mechanical Sciences*, vol. 263, p. 108 781, 2024. DOI: 10.1016/J.IJMECSCI.2023.108781.

[144] D. Ashouri Vajari, C. González, J. Llorca, and B. N. Legarth, "A numerical study of the influence of microvoids in the transverse mechanical response of unidirectional composites," *Composites Science and Technology*, vol. 97, pp. 46–54, 2014. DOI: 10.1016/J.COMPSCITECH.2014.04.004.

[145] Y. Chu, L. Sun, X. Yang, J. Wang, and W. Huang, "Multiscale simulation and theoretical prediction for the elastic properties of unidirectional fiber-reinforced polymer containing random void defects," *Polymer Composites*, vol. 42, pp. 2958–2972, 2021. DOI: 10.1002/pc.26028.

[146] T. Pardoen *et al.*, "Nanomechanics serving polymer-based composite research," *Comptes Rendus Physique*, vol. 22, pp. 1–22, 2021. DOI: 10.5802/crphys.56.

[147] W. Oliver and G. Pharr, "An improved technique for determining hardness and elastic modulus using load and displacement sensing indentation experiments," *J. Mater. Res.*, vol. 7, pp. 1564–1583, 1992.

[148] I. N. Sneddon, "The relation between load and penetration in the axisymmetric boussinesq problem for punch of arbitrary profile," *Int. J. Eng. Sci.*, vol. 3, pp. 47–57, 1965.

[149] J. M. Kranenburg, C. A. Tweedie, K. J. Van Vliet, and U. S. Schubert, "Challenges and progress in high-throughput screening of polymer mechanical properties by indentation," *Advanced Materials*, vol. 21, pp. 3551–3561, 2009. DOI: 10.1002/adma.200803538.

[150] M. R. VanLandingham, J. S. Villarrubia, W. F. Guthrie, and G. F. Meyers, "Nanoindentation of polymers: an overview," *Macromolecular Symposia*, vol. 167, pp. 15–44, 2001. DOI: 10.1002/1521-3900(200103)167:13.0.CO;2-T.

[151] M. Hardiman, T. J. Vaughan, and C. T. McCarthy, "A review of key developments and pertinent issues in nanoindentation testing of fibre reinforced plastic microstructures," *Composite Structures*, vol. 180, pp. 782–798, 2017. DOI: 10.1016/j.compstruct.2017.08.004.

[152] R. Seltzer, J. K. Kim, and Y. W. Mai, "Elevated temperature nanoindentation behaviour of polyamide 6," *Polymer International*, vol. 60, pp. 1753–1761, 2011. DOI: 10.1002/pi.3146.

[153] G. Z. Voyiadjis and L. Malekmotiei, "Variation of the Strain Rate During CSM Nanoindentation of Glassy Polymers and Its Implication on Indentation Size Effect," *J. Polym. Sci., Part B: Polym. Phys*, vol. 54, pp. 2179–2187, 2016. DOI: 10.1002/polb.24127.

[154] D. Tranchida, S. Piccarolo, J. Loos, and A. Alexeev, "Accurately evaluating young's modulus of polymers through nanoindentations: A phenomenological correction factor to the oliver and pharr procedure," *Appl. Phys. Lett.*, vol. 89, p. 171 905, 2006.

[155] R. Martinez and L. R. Xu, "Comparison of the young's moduli of polymers measured from nanoindentation and bending experiments," *MRS Commun*, vol. 4, pp. 89–93, 2014.

[156] M. Hardiman, T. Vaughan, and C. McCarthy, "The effects of pile-up, viscoelasticity and hydrostatic stress on polymer matrix nanoindentation," *Polym. Test.*, vol. 52, pp. 157–166, 2016.

[157] J. Chevalier, "Micromechanics of an epoxy matrix for fiber reinforced composites: Experiments and physics-based modelling," Ph.D. dissertation, Université Catholique de Louvain, 2018.

[158] F. Alisafaei, C.-S. Han, and N. Lakhera, "Characterization of indentation size effects in epoxy," *Polymer Testing*, vol. 40, pp. 70–78, 2014. DOI: 10.1016/j.polymertesting.2014.08.012.

[159] D. Tranchida, S. Piccarolo, J. Loos, and A. Alexeev, "Mechanical characterization of polymers on a nanometer scale through nanoindentation. A study on pile-up and viscoelasticity," *Macromolecules*, vol. 40, pp. 1259–1267, 2007. DOI: 10.1021/ma062140k.

[160] M. VanLandingham, R. Dagastine, R. Eduljee, R. McCullough, and J. Gillespie, "Characterization of nanoscale property variations in polymer composite systems: 1. experimental results," *Compos. Part A Appl. Sci. Manuf.*, vol. 30, pp. 75–83, 1999.

[161] B. J. Briscoe and K. Savio Sebastian, "The elastoplastic response of poly(methyl methacrylate) to indentation," *Proceedings of the Royal Society A: Mathematical, Physical and Engineering Sciences*, vol. 452, pp. 439–457, 1996. DOI: 10.1098/rspa.1996.0023.

[162] A. G. Atkins and D. Tabor, "Plastic indentation in metals with cones," *Journal of the Mechanics and Physics of Solids*, vol. 13, pp. 149–164, 1965. DOI: 10.1016/0022-5096(65)90018-9.

[163] M. Rodríguez, J. M. Molina-Aldareguía, C. González, and J. Llorca, "Determination of the mechanical properties of amorphous materials through instrumented nanoindentation," *Acta Materialia*, vol. 60, pp. 3953–3964, 2012. DOI: 10.1016/J.ACTAMAT.2012.03.027.

[164] J. Gregory and S. Spearing, "Nanoindentation of neat and polymers in polymer-matrix composites," *Compos. Sci. Technol.*, vol. 65, pp. 595–607, 2005.

[165] M. Hardiman, T. J. Vaughan, and C. T. McCarthy, "Fibrous composite matrix characterisation using nanoindentation: The effect of fibre constraint and the evolution from bulk to in-situ matrix properties," *Composites Part A: Applied Science and Manufacturing*, vol. 68, pp. 296–303, 2015. DOI: 10.1016/j.compositesa.2014.09.022.

[166] D. C. C. Lam and A. C. M. Chong, "Indentation model and strain gradient plasticity law for glassy polymers," *Journal of Materials Research*, vol. 14, pp. 3784–3788, 1999. DOI: 10.1557/JMR.1999.0512.

[167] A. C. M. Chong and D. C. C. Lam, "Strain gradient plasticity effect in indentation hardness of polymers," *Journal of Materials Research*, vol. 14, pp. 4103–4110, 1999. DOI: 10.1557/JMR.1999.0554.

[168] F. Alisafaei and C.-S. Han, "Indentation Depth Dependent Mechanical Behavior in Polymers," *Advances in Condensed Matter Physics*, pp. 1–20, 2015. DOI: 10.1155/2015/391579.

[169] A. N. Bucsek, F. Alisafaei, C. S. Han, and N. Lakhera, "On thresholds in the indentation size effect of polymers," *Polymer Bulletin*, vol. 73, pp. 763–772, 2016. DOI: 10.1007/s00289-015-1517-y.

[170] R. V. Tatiraju, C. S. Han, and S. Nikolov, "Size dependent hardness of polyamide/imide," *Open Mechanics Journal*, vol. 2, pp. 89–92, 2008. DOI: 10.2174/1874158400802010089.

[171] P. Frontini, S. Lotfian, M. A. Monclús, and J. M. Molina- Aldareguia, "High temperature nanoindentation response of rtm6 epoxy resin at different strain rates," *Exp. Mech.*, vol. 55, pp. 851–862, 2015.

[172] C. A. Tweedie, G. Constantinides, K. E. Lehman, D. J. Brill, G. S. Blackman, and K. J. Van Vliet, "Enhanced stiffness of amorphous polymer surfaces under confinement of localized contact loads," *Advanced Materials*, vol. 19, pp. 2540–2546, 2007. DOI: 10.1002/adma.200602846.

[173] X. Li *et al.*, "Indentation size effect: an improved mechanistic model incorporating surface undulation and indenter tip irregularity," *Journal of Materials Research and Technology*, vol. 23, pp. 143–153, 2023. DOI: 10.1016/j.jmrt.2023.01.001.

[174] S. Fulco, S. Wolf, J. E. Jakes, Z. Fakhraai, and K. T. Turner, "Effect of surface detection error due to elastic–plastic deformation on nanoindentation measurements of elastic modulus and hardness," *Journal of Materials Research*, vol. 36, pp. 2176–2188, 2021. DOI: 10.1557/s43578-021-00223-4.

[175] Z. Qian and G. B. McKenna, "On the extreme depth dependence of the hardness of PDMS rubber: A problem of false surface detection," *Journal of Polymer Science, Part B: Polymer Physics*, vol. 55, pp. 30–38, 2017. DOI: 10.1002/polb.24147.

[176] D. C. Lam, F. Yang, A. C. Chong, J. Wang, and P. Tong, "Experiments and theory in strain gradient elasticity," *Journal of the Mechanics and Physics of Solids*, vol. 51, pp. 1477–1508, 2003. DOI: 10.1016/S0022-5096(03)00053-X.

[177] Y. J. Deng, L. F. Peng, X. M. Lai, M. W. Fu, and Z. Q. Lin, "Constitutive modeling of size effect on deformation behaviors of amorphous polymers in micro-scaled deformation," *International Journal of Plasticity*, vol. 89, pp. 197–222, 2017. DOI: 10.1016/j.ijplas.2016.11.011.

[178] Y. Deng, J. Wang, P. Yi, L. Peng, X. Lai, and Z. Lin, "Numerical Studies on Size Effect Behaviors of Glassy Polymers Based on Strain Gradient Elastoviscoplastic Model," *Journal of Applied Mechanics, Transactions ASME*, vol. 86, pp. 1–11, 2019. DOI: 10.1115/1.4041765.

[179] C.-S. Han, "Influence of the molecular structure on indentation size effect in polymers," *Materials Science and Engineering: A*, vol. 527, pp. 619–624, 2010. DOI: 10.1016/j.msea.2009.08.033.

[180] J. A. Tjernlund, E. K. Gamstedt, and Z. H. Xu, "Influence of molecular weight on strain-gradient yielding in polystyrene," *Polymer Engineering and Science*, vol. 44, pp. 1987–1997, 2004. DOI: 10.1002/pen.20202.

[181] D. C. Lam and A. C. Chong, "Effect of cross-link density on strain gradient plasticity in epoxy," *Materials Science and Engineering: A*, vol. 281, pp. 156–161, 2000. DOI: 10.1016/s0921-5093(99)00724-8.

[182] W. D. Nix and H. Gao, "Indentation size effects in crystalline materials: A law for strain gradient plasticity," *Journal of the Mechanics and Physics of Solids*, vol. 46, pp. 411–425, 1998. DOI: 10.1016/S0022-5096(97)00086-0.

[183] N. A. Fleck, G. M. Muller, M. F. Ashby, and J. W. Hutchinson, "Strain gradient plasticity: Theory and experiment," *Acta Metallurgica Et Materialia*, vol. 42, pp. 475–487, 1994. DOI: 10.1016/0956-7151(94)90502-9.

[184] H. Gao, Y. Huang, W. D. Nix, and J. W. Hutchinson, "Mechanism-based strain gradient plasticity - I. Theory," *Journal of the Mechanics and Physics of Solids*, vol. 47, pp. 1239–1263, 1999. DOI: 10.1016/S0022-5096(98)00103-3.

[185] C. S. Han and S. Nikolov, "Indentation size effects in polymers and related rotation gradients," *Journal of Materials Research*, vol. 22, pp. 1662–1672, 2007. DOI: 10.1557/jmr.2007.0197.

[186] G. Chandrashekar and C.-S. Han, "Length scale effects in epoxy: The dependence of elastic moduli measurements on spherical indenter tip radius," *Polymer Testing*, vol. 53, pp. 227–233, 2016. DOI: 10.1016/j.polymertesting.2016.06.002.

[187] H. Lin, T. Jin, L. Lv, and Q. Ai, "Indentation size effect in pressure-sensitive polymer based on a criterion for description of yield differential effects and shear transformation-mediated plasticity," *Polymers*, vol. 11, 2019. DOI: 10.3390/polym11030412.

[188] S. Swaddiwudhipong, L. H. Poh, J. Hua, Z. S. Liu, and K. K. Tho, "Modeling nano-indentation tests of glassy polymers using finite elements with strain gradient plasticity," *Materials Science and Engineering: A*, vol. 404, pp. 179–187, 2005. DOI: 10.1016/j.msea.2005.05.063.

[189] N. Garg and C. S. Han, "Axisymmetric couple stress elasticity and its finite element formulation with penalty terms," *Archive of Applied Mechanics*, vol. 85, pp. 587–600, 2015. DOI: 10.1007/s00419-014-0932-0.

[190] N. Garg, C. S. Han, and F. Alisafaei, "Length scale dependence in elastomers - Comparison of indentation experiments with numerical simulations," *Polymer*, vol. 98, pp. 201–209, 2016. DOI: 10.1016/j.polymer.2016.06.020.

[191] Z. Hu, M. Farahikia, and F. Delfanian, "Fiber bias effect on characterization of carbon fiber-reinforced polymer composites by nanoindentation testing and modeling," *Journal of Composite Materials*, vol. 49, pp. 3359–3372, 2015. DOI: 10.1177/0021998314562221.

[192] M. Pecora, O. Smerdova, and M. Gigliotti, "In-situ characterization of the local mechanical behaviour of polymer matrix in 3D carbon fiber composites by cyclic indentation test," *Composite Structures*, vol. 244, p. 112 268, 2020. DOI: 10.1016/j.compstruct.2020.112268.

[193] M. Hardiman, T. Vaughan, and C. McCarthy, "The effect of fibre constraint in the nanoindentation of fibrous composite microstructures: A finite element investigation," *Comput. Mater. Sci.*, vol. 64, pp. 162–167, 2012.

[194] X. Cheng, K. W. Putz, C. D. Wood, and L. C. Brinson, "Characterization of local elastic modulus in confined polymer films via afm indentation," *Macromol. Rapid Commun.*, vol. 36, pp. 391–397, 2015.

[195] M. Zhang, Y. Li, P. V. Kolluru, and L. C. Brinson, "Determination of mechanical properties of polymer interphase using combined atomic force microscope (AFM) experiments and finite element simulations," *Macromolecules*, vol. 51, pp. 8229–8240, 2018.

[196] L. Liu *et al.*, "Interfacial characterization, control and modification of carbon fiber reinforced polymer composites," *Compos. Sci. Technol.*, vol. 121, pp. 56–72, 2015.

[197] M. Munz, H. Sturm, E. Schulz, and G. Hinrichsen, "The scanning force microscope as a tool for the detection of local mechanical properties within the interphase of fibre reinforced polymers," *Composites Part A: Applied Science and Manufacturing*, vol. 29, pp. 1251–1259, 1998. DOI: 10.1016/S1359-835X(98)00077-3.

[198] R. M. Winter and J. E. Houston, "Interphase mechanical properties in an epoxy-glass fiber composite as measured by interfacial microscopy," in *Proceedings of the SEM Spring Conference on Experimental and Applied Mechanics and Experimental/Numerical Mechanics in Electronic Packaging III*, Houston, Texas (USA), 1998, pp. 355–358.

[199] T. D. Downing, R. Kumar, W. M. Cross, L. Kjerengtroen, and J. J. Kellar, "Determining the interphase thickness and properties in polymer matrix composites using phase imaging atomic force microscopy and nanoindentation," *Journal of Adhesion Science and Technology*, vol. 14, pp. 1801–1812, 2000. DOI: 10.1163/156856100743248.

[200] T. A. Bogetti, T. Wang, M. R. Vanlandingham, and J. W. Gillespie, "Characterization of nanoscale property variations in polymer composite systems: 2. Numerical modeling," *Composites Part A: Applied Science and Manufacturing*, vol. 30, pp. 85–94, 1999. DOI: 10.1016/S1359-835X(98)00097-9.

[201] S. Wang, Y. Yang, L. M. Zhou, and Y. W. Mai, "Size effect in microcompression of epoxy micropillars," *Journal of Materials Science*, vol. 47, pp. 6047–6055, 2012. DOI: 10.1007/s10853-012-6513-0.

[202] M. Rueda-Ruiz, M. A. Monclús, B. D. Beake, F. Gálvez, and J. M. Molina-Aldareguia, "High strain rate compression of epoxy micropillars," *Extreme Mechanics Letters*, vol. 40, p. 100 905, 2020. DOI: 10.1016/j.eml.2020.100905.

[203] M. Flores, A. Sharits, R. Wheeler, N. Sesar, and D. Mollenhauer, "Experimental analysis of polymer matrix composite microstructures under transverse compression loading," *Composites Part A: Applied Science and Manufacturing*, vol. 156, p. 106 859, 2022. DOI: 10.1016/J.COMPOSITESA.2022.106859.

[204] E. Gamstedt and B. Sjögren, "Micromechanisms in tensioncompression fatigue of composite laminates containing transverse plies," *Compos. Sci. Technol.*, vol. 59, pp. 167–178, 1999.

[205] T. Hobbiebrunken, M. Hojo, T. Adachi, C. De Jong, and B. Fiedler, "Evaluation of interfacial strength in cf/epoxies using fem and in-situ experiments," *Compos. Part A Appl. Sci. Manuf.*, vol. 37, pp. 2248–2256, 2006.

[206] M. S. Madhukar and L. T. Drzal, "Fiber-matrix adhesion and its effect on composite mechanical properties: I. inplane and interlaminar shear behavior of graphite/epoxy composites," *J.Compos. Mater.*, vol. 25, pp. 932–957, 1991.

[207] S. AhmadvashAghbash, I. Verpoest, Y. Swolfs, and M. Mehdikhani, "Methods and models for fibre–matrix interface characterisation in fibre-reinforced polymers: a review," *International Materials Reviews*, vol. 68, pp. 1245–1319, 2023. DOI: 10.1080/09506608.2023.2265701.

[208] J. Varna, R. Joffe, and L. Berglund, "Interfacial toughness evaluation from the single-fiber fragmentation test," *Compos. Sci. Technol.*, vol. 56, pp. 1105–1109, 1996.

[209] B. Miller, P. Muri, and L. Rebenfeld, "A microbond method for determination of the shear strength of a fiber/resin interface," *Compos. Sci. Technol.*, vol. 28, pp. 17–32, 1987.

[210] F. Hoecker and J. Karger-Kocsis, "Effects of the interface on the mechanical response of cf/ep microcomposites and macrocomposites," *Composites*, vol. 25, pp. 729–738, 1994.

[211] M. R. Piggott and S. R. Dai, "Fiber pull out experiments with thermoplastics," *Polym. Eng. Sci.*, vol. 31, pp. 1246–1249, 1991.

[212] K. Tanaka, K. Minoshima, W. Grela, and K. Komai, "Characterization of the aramid/epoxy interfacial properties by means of pull-out test and influence of water absorption," *Compos. Sci. Technol.*, vol. 62, pp. 2169–2177, 2002.

[213] M. Rodríguez, J. Molina-Aldareguía, C. González, and J. LLorca, "A methodology to measure the interface shear strength by means of the fiber push-in test," *Compos. Sci. Technol.*, vol. 72, pp. 1924–1932, 2012.

[214] J. Jäger, M. Sause, F. Burkert, J. Moosburger-Will, M. Greisel, and S. Horn, "Influence of plastic deformation on single-fiber push-out tests of carbon fiber reinforced epoxy resin," *Compos. Part A Appl. Sci. Manuf.*, vol. 71, pp. 157–167, 2015.

[215] J. J. Sha, J. X. Dai, J. Li, Z. Q. Wei, J.-M. Hausherr, and W. Krenkel, "Measurement and analysis of fiber-matrix interface strength of carbon fiber-reinforced phenolic resin matrix composites," *Journal of Composite Materials*, vol. 48, pp. 1303–1311, 2014.

[216] C. Medinam, J. M. Molina-Aldareguía, C. González, M. F. Melendrez, P. Flores, and J. Llorca, "Comparison of push-in and push-out tests for measuring interfacial shear strength in nano-reinforced composite materials," *Journal of Composite Materials*, vol. 50, pp. 1651–1659, 2016. DOI: 10.1177/0021998315595115.

[217] W. Tan *et al.*, "The role of interfacial properties on the intralaminar and interlaminar damage behaviour of unidirectional composite laminates: Experimental characterization and multiscale modelling," *Composites Part B: Engineering*, vol. 138, pp. 206–221, 2018. DOI: 10.1016/J.COMPOSITESB.2017.11.043.

[218] S. Ghaffari, G. Seon, and A. Makeev, "In-situ SEM based method for assessing fiber-matrix interface shear strength in CFRPs," *Materials and Design*, vol. 197, p. 109 242, 2021. DOI: 10.1016/j.matdes.2020.109242.

[219] B. Rohrmüller, P. Gumbsch, and J. Hohe, "Calibrating a fiber matrix interface failure model to single fiber push-out tests and numerical simulations," *Composites Part A: Applied Science and Manufacturing*, vol. 150, p. 106 607, 2021. DOI: 10.1016/j.compositesa.2021.106607.

[220] Q. T. L. Vu *et al.*, "Evaluating Residual Stress in Carbon Fiber-Reinforced Polymer (CFRP) at Microscale Using Fiber Push-Out Experiment and Finite Element Modeling," *Polymers*, vol. 15, 2023. DOI: 10.3390/polym15122596.

[221] J. Blaber, B. Adair, and A. Antoniou, "Ncorr: Open-Source 2D Digital Image Correlation Matlab Software," *Experimental Mechanics*, vol. 55, pp. 1105–1122, 2015. DOI: 10.1007/s11340-015-0009-1.

[222] R. Harilal and M. Ramji, "Adaptation of Open Source 2D DIC Software Ncorr for Solid Mechanics Applications," *9th International Symposium on Advanced Science and Technology in Experimental Mechanics*, pp. 1–6, 2014.

[223] J. Holmes, S. Sommacal, R. Das, Z. Stachurski, and P. Compston, "Digital image and volume correlation for deformation and damage characterisation of fibre-reinforced composites: A review," *Composite Structures*, vol. 315, p. 116 994, 2023. DOI: 10.1016/J.COMPSTRUCT.2023.116994.

[224] L. P. Canal, C. González, J. M. Molina-Aldareguía, J. Segurado, and J. LLorca, "Application of digital image correlation at the microscale in fiber-reinforced composites," *Composites Part A: Applied Science and Manufacturing*, vol. 43, pp. 1630–1638, 2012.

[225] M. Mehdikhani, M. Aravand, B. Sabuncuoglu, M. G. Callens, S. V. Lomov, and L. Gorbatikh, "Full-field strain measurements at the microscale in fiber-reinforced composites using digital image correlation," *Composite Structures*, vol. 140, pp. 192–201, 2016.

[226] M. Mehdikhani, A. Matveeva, M. A. Aravand, B. L. Wardle, S. V. Lomov, and L. Gorbatikh, "Strain mapping at the micro-scale in hierarchical polymer composites with aligned carbon nanotube grafted fibers," *Composites Science and Technology*, vol. 137, pp. 24–34, 2016. DOI: 10.1016/j.compscitech.2016.10.021.

[227] I. Tabiai, D. Texier, P. Bocher, D. Therriault, and M. Levesque, "In-situ Full Field Out of Plane Displacement and Strain Measurements at the Micro-Scale in Single Reinforcement Composites under Transverse Load," *Experimental Mechanics*, vol. 60, pp. 359–377, 2020. DOI: 10.1007/s11340-019-00541-z.

[228] O. Verschatse, W. Van Paepegem, K. De Clerck, and L. Daelemans, "Development of a versatile speckle pattern of nano-sized polymer particles for high-resolution SEM-DIC," *Polymer Testing*, vol. 125, p. 108 134, 2023. DOI: 10.1016/j.polymertesting.2023.108134.

[229] E. C. Aifantis, "On the Microstructural Origin of Certain Inelastic Models," *Journal of Engineering Materials and Technology*, vol. 106, pp. 326–330, 1984. DOI: 10.1115/1.3225725.

[230] N. A. Fleck and J. W. Hutchinson, "A phenomenological theory for strain gradient effects in plasticity," *Journal of the Mechanics and Physics of Solids*, vol. 41, pp. 1825–1857, 1993. DOI: 10.1016/0022-5096(93)90072-N.

[231] G. Z. Voyiadjis and Y. Song, *Gradient-Enhanced Continuum Plasticity*. Elsevier, 2020, ISBN: 9780128177662. DOI: 10.1016/C2018-0-02162-3.

[232] S. Forest, "Micromorphic Approach for Gradient Elasticity, Viscoplasticity, and Damage," *Journal of Engineering Mechanics*, vol. 135, pp. 117–131, 2009. DOI: 10.1061/(asce)0733-9399(2009)135:3(117).

[233] S. Forest, "Nonlinear regularization operators as derived from the micromorphic approach to gradient elasticity, viscoplasticity and damage," *Proceedings of the Royal Society A: Mathematical, Physical and Engineering Sciences*, vol. 472, 2016. DOI: 10.1098/rspa.2015.0755.

[234] S. M. Lee, "Plastic Deformation in Epoxy Resins.," in *Polymeric Materials Science and Engineering, Proceedings of the ACS Division of Polymeric Material*, vol. 56, ACS, 1987, pp. 253–256. DOI: 10.1021/bk-1988-0367.ch011.

[235] E. Oleynik, "Plastic deformation and mobility in glassy polymers," *Relaxation in Polymers*, pp. 140–150, 1989. DOI: 10.1007/bfb0115425.

[236] C. G'Sell and A. Souahi, "Influence of crosslinking on the plastic behavior of amorphous polymers at large strains," *Journal of Engineering Materials and Technology, Transactions of the ASME*, vol. 119, pp. 223–227, 1997. DOI: 10.1115/1.2812248.

[237] A. E. Mayr, W. D. Cook, and G. H. Edward, "Yielding behaviour in model epoxy thermosets - I. Effect of strain rate and composition," *Polymer*, vol. 39, pp. 3719–3724, 1998. DOI: 10.1016/S0032-3861(97)10334-2.

[238] A. S. Argon and M. I. Bessonov, "Plastic flow in glassy polymers," *Polymer Engineering and Science*, vol. 17, pp. 174–182, 1977. DOI: 10.1002/pen.760170306.

[239] S. Yamini and R. J. Young, "Crack propagation in and fractography of epoxy resins," *Journal of Materials Science*, vol. 14, pp. 1609–1618, 1979. DOI: 10.1007/BF00569280.

[240] L. E. Asp, L. A. Berglund, and R. Talreja, "A criterion for crack initiation in glassy polymers subjected to a composite-like stress state," *Composites Science and Technology*, vol. 56, pp. 1291–1301, 1996. DOI: 10.1016/S0266-3538(96)00090-5.

[241] A. J. Kinloch, "Relationships between the microstructure and fracture behavior of rubber-toughened thermosetting polymers," in *Rubber-Toughened Plastics*, ch. 3, pp. 67–91. DOI: 10.1021/ba-1989-0222.ch003.

[242] J. Gu, Y. Bai, Z. Zhao, and C. Zhang, "Temperature and strain rate sensitivity of modulus and yield strength of epoxy resin under compressive loads," *Polymer*, vol. 295, p. 126 744, 2024. DOI: 10.1016/J.POLYMER.2024.126744.

[243] S. Tamrakar, R. Ganesh, S. Sockalingam, B. Z. Haque, and J. W. Gillespie, "Experimental Investigation of Strain Rate and Temperature Dependent Response of an Epoxy Resin Undergoing Large Deformation," *Journal of Dynamic Behavior of Materials*, vol. 4, pp. 114–128, 2018. DOI: 10.1007/s40870-018-0144-8.

[244] J. Moosburger-Will, M. Greisel, M. G. Sause, R. Horny, and S. Horn, "Influence of partial cross-linking degree on basic physical properties of RTM6 epoxy resin," *Journal of Applied Polymer Science*, vol. 130, pp. 4338–4346, 2013. DOI: 10.1002/app.39722.

[245] W. D. Cook, A. E. Mayr, and G. H. Edward, "Yielding behaviour in model epoxy thermosets - II. Temperature dependence," *Polymer*, vol. 39, pp. 3725–3733, 1998. DOI: 10.1016/S0032-3861(97)10335-4.

[246] O. Sindt, J. Perez, and J. F. Gerard, "Molecular architecture-mechanical behaviour relationships in epoxy networks," *Polymer*, vol. 37, pp. 2989–2997, 1996. DOI: 10.1016/0032-3861(96)89396-7.

[247] K. J. Calzia and A. J. Lesser, "Correlating yield response with molecular architecture in polymer glasses," *Journal of Materials Science*, vol. 42, pp. 5229–5238, 2007. DOI: 10.1007/s10853-006-1268-0.

[248] A. J. Lesser and K. J. Calzia, "Molecular parameters governing the yield response of epoxy-based glassy networks," *Journal of Polymer Science, Part B: Polymer Physics*, vol. 42, pp. 2050–2056, 2004. DOI: 10.1002/polb.20090.

[249] B. Fiedler, T. Hobbiebrunken, M. Hojo, and K. Schulte, "Influence of stress state and temperature on the strength of epoxy resins," *11th International Conference on Fracture 2005, ICF11*, vol. 3, pp. 2271–2275, 2005.

[250] J. Lemay, B. Swetlin, and F. Kelley, "Characterization of Highly Crosslinked Polymers," *Chemical & Engineering News Archive*, vol. 62, p. 22, 1984. DOI: 10.1021/cen-v062n027.p022.

[251] S. Behzadi and F. R. Jones, "Yielding behavior of model epoxy matrices for fiber reinforced composites: Effect of strain rate and temperature," *Journal of Macromolecular Science - Physics*, vol. 44 B, pp. 993–1005, 2005. DOI: 10.1080/00222340500393881.

[252] N. M. Ames, V. Srivastava, S. A. Chester, and L. Anand, "A thermo-mechanically coupled theory for large deformations of amorphous polymers. Part II: Applications," *International Journal of Plasticity*, vol. 25, pp. 1495–1539, 2009. DOI: 10.1016/J.IJPLAS.2008.11.005.

[253] L. Anand, N. M. Ames, V. Srivastava, and S. A. Chester, "A thermo-mechanically coupled theory for large deformations of amorphous polymers. Part I: Formulation," *International Journal of Plasticity*, vol. 25, pp. 1474–1494, 2009. DOI: 10.1016/j.ijplas.2008.11.004.

[254] M. Uchida, K. Kamimura, T. Yoshida, and Y. Kaneko, "Viscoelastic-viscoplastic modeling of epoxy based on transient network theory," *International Journal of Plasticity*, vol. 153, p. 103 262, 2022. DOI: 10.1016/J.IJPLAS.2022.103262.

[255] C. Park, J. Jung, and G. J. Yun, "Multiscale micromorphic theory compatible with MD simulations in both timescale and length-scale," *International Journal of Plasticity*, vol. 129, p. 102 680, 2020. DOI: 10.1016/J.IJPLAS.2020.102680.

[256] T. Barriere, X. Gabrion, and S. Holopainen, "A compact constitutive model to describe the viscoelastic-plastic behaviour of glassy polymers: Comparison with monotonic and cyclic experiments and state-of-the-art models," *International Journal of Plasticity*, vol. 122, pp. 31–48, 2019. DOI: 10.1016/J.IJPLAS.2019.05.010.

[257] R. Xiao, C. Tian, Y. Xu, and P. Steinmann, "Thermomechanical coupling in glassy polymers: An effective temperature theory," *International Journal of Plasticity*, vol. 156, p. 103 361, 2022. DOI: 10.1016/J.IJPLAS.2022.103361.

[258] T. Lan, Y. Jiang, and P. Wu, "A thermodynamically-based constitutive theory for amorphous glassy polymers at finite deformations," *International Journal of Plasticity*, vol. 158, p. 103 415, 2022. DOI: 10.1016/J.IJPLAS.2022.103415.

[259] J. Wang, L. F. Peng, Y. J. Deng, X. M. Lai, M. W. Fu, and J. Ni, "A finite strain thermodynamically-based constitutive modeling and analysis of viscoelastic-viscoplastic deformation behavior of glassy polymers," *International Journal of Plasticity*, vol. 122, pp. 135–163, 2019. DOI: 10.1016/J.IJPLAS.2019.06.013.

[260] S. M. Mirkhalaf, F. M. Andrade Pires, and R. Simoes, "Modelling of the post yield response of amorphous polymers under different stress states," *International Journal of Plasticity*, vol. 88, pp. 159–187, 2017. DOI: 10.1016/J.IJPLAS.2016.10.008.

[261] K. S. Khare and F. R. Phelan, "Integration of Atomistic Simulation with Experiment Using TimeTemperature Superposition for a Cross-Linked Epoxy Network," *Macromolecular Theory and Simulations*, vol. 29, pp. 1–16, 2020. DOI: 10.1002/mats.201900032.

[262] J. LLorca, C. González, J. M. Molina-Aldareguía, and C. S. Lópes, "Multiscale Modeling of Composites: Toward Virtual Testing ... and Beyond," *JOM*, vol. 65, pp. 215–225, 2013.

[263] Hexcel, *HexPly 8552 - Product Data Sheet*, 2023.

[264] WestlakeEpoxy, *Technical Data Sheet - EPON Resin 827 Product*, 2021.

[265] A. Bahrami, "Contributions of atomic force microscopy to the mechanical property mapping of polymer blends and nanocomposites," PhD thesis, UCLouvain, 2018.

[266] Sicomin, "Technical Datasheet SiPreg SR 8500 / KTA 31x," vol. 33, pp. 29–34, 2014.

[267] Hexcel, "HexFlow RTM6/RTM6-2 Product Data Sheet," *Hexcel Corporation*, pp. 1–14, 2022.

[268] Huntsman, "Technical Datasheet of Araldite MY 721 Resin," p. 5, 2016.

[269] S. Gabriel, *Effet de synergie entre du phénoxy et des CSRs sur la ténacité d'une résine époxy hautement réticulée*, 2017.

[270] P. Van Velthem, S. Gabriel, T. Pardoen, C. Bailly, and W. Ballout, "Synergy between phenoxy and csr tougheners on the fracture toughness of highly cross-linked epoxy-based composites," *Polymers*, vol. 13, pp. 1–16, 2021. DOI: 10.3390/polym13152477.

[271] H. Chen, P. Song, T. Commins, A. Graham, A. R. Trivedi, and C. R. Siviour, "Characterization and modelling of bisphenol a type epoxy polymer over a wide range of rates and temperatures," *Polymer*, vol. 249, p. 124 860, 2022. DOI: 10.1016/J.POLYMER.2022.124860.

[272] J. Diani, P. Gilormini, and J. S. Arrieta, "Direct experimental evidence of timetemperature superposition at finite strain for an amorphous polymer network," *Polymer*, vol. 58, pp. 107–112, 2015. DOI: 10.1016/J.POLYMER.2014.12.045.

[273] C. E. Federico, J. L. Bouvard, C. Combeaud, and N. Billon, "Large strain/time dependent mechanical behaviour of PMMAs of different chain architectures. Application of time-temperature superposition principle," *Polymer*, vol. 139, pp. 177–187, 2018. DOI: 10.1016/J.POLYMER.2018.02.021.

[274] W. Zhao, R. Xiao, P. Steinmann, and S. Pfaller, "Timetemperature correlations of amorphous thermoplastics at large strains based on molecular dynamics simulations," *Mechanics of Materials*, vol. 190, p. 104 926, 2024. DOI: 10.1016/J.MECHMAT.2024.104926.

[275] C. Bauwens-Crowet, J. .-C. Bauwens, and G. Homes, "The temperature dependence of yield of polycarbonate in uniaxial compression and tensile tests," *Journal of Materials Science*, vol. 7, pp. 176–183, 1972. DOI: 10.1007/bf00554178.

[276] J. Richeton, S. Ahzi, K. S. Vecchio, F. C. Jiang, and R. R. Adharapurapu, "Influence of temperature and strain rate on the mechanical behavior of three amorphous polymers: Characterization and modeling of the compressive yield stress," *International Journal of Solids and Structures*, vol. 43, pp. 2318–2335, 2006. DOI: 10.1016/J.IJSOLSTR.2005.06.040.

[277] J. D. Littell, C. R. Ruggeri, R. K. Goldberg, G. D. Roberts, W. A. Arnold, and W. K. Binienda, "Measurement of Epoxy Resin Tension, Compression, and Shear Stress–Strain Curves over a Wide Range of Strain Rates Using Small Test Specimens," *Journal of Aerospace Engineering*, vol. 21, pp. 162–173, 2008. DOI: 10.1061/(asce)0893-1321(2008)21:3(162).

[278] A. Gilat, R. K. Goldberg, and G. D. Roberts, "Strain Rate Sensitivity of Epoxy Resin in Tensile and Shear Loading," *Journal of Aerospace Engineering*, vol. 20, pp. 75–89, 2007. DOI: 10.1061/(asce)0893-1321(2007)20:2(75).

[279] R. N. Haward and R. J. Young, *Physics of Glassy Polymers.* Springer Netherlands, 2012.

[280] J. P. Foreman, S. Behzadi, D. Porter, and F. R. Jones, "Multi-scale modelling of the effect of a viscoelastic matrix on the strength of a carbon fibre composite," *Philosophical Magazine*, vol. 90, pp. 4227–4244, 2010. DOI: 10.1080/14786435.2010.495361.

[281] E. Farotti, E. Mancini, A. Lattanzi, M. Utzeri, and M. Sasso, "Effect of temperature and strain rate on the formation of shear bands in polymers under quasi-static and dynamic compressive loadings: Proposed constitutive model and numerical validation," *Polymer*, vol. 245, p. 124 690, 2022. DOI: 10.1016/J.POLYMER.2022.124690.

[282] S. Ito *et al.*, "Effects of resin hydrophilicity on water sorption and changes in modulus of elasticity," *Biomaterials*, vol. 26, pp. 6449–6459, 2005. DOI: 10.1016/J.BIOMATERIALS.2005.04.052.

[283] D. Melot, B. Escaig, J. M. Lefebvre, R. P. Eustache, and F. Lauprêtre, "Mechanical properties of unsaturated polyester resins in relation to their chemical structure: 2. Plastic deformation behavior," *Journal of Polymer Science Part B: Polymer Physics*, vol. 32, pp. 1805–1811, 1994. DOI: 10.1002/polb.1994.090321102.

[284] J. Ho, L. Govaert, and M. Utz, "Plastic Deformation of Glassy Polymers: Correlation between Shear Activation Volume and Entanglement Density," *Macromolecules*, vol. 36, pp. 7398–7404, 2003. DOI: 10.1021/ma025733d.

[285] L. David, R. Quinson, C. Gauthier, and J. Perez, "The role of anelasticity in high stress mechanical response and physical properties of glassy polymers," *Polymer Engineering and Science*, vol. 37, pp. 1633–1640, 1997. DOI: 10.1002/pen.11811.

[286] H. S. Jung, Y. Park, C. W. Nah, J. C. Lee, K. Y. Kim, and C. S. Lee, "Evaluation of the Mechanical Properties of Polyether Sulfone-Toughened Epoxy Resin for Carbon Fiber Composites," *Fibers and Polymers*, vol. 22, pp. 184–195, 2021. DOI: 10.1007/s12221-021-9261-4.

[287] R. N. Haward and G. Thackray, "The use of a mathematical model to describe isothermal stress-strain curves in glassy thermoplastics," *Proceedings of the Royal Society of London. Series A. Mathematical and Physical Sciences*, vol. 302, pp. 453–472, 1968.

[288] J. Rojek, C. Breite, Y. Swolfs, and L. Laiarinandrasana, "Void growth measurement and modelling in a thermosetting epoxy resin using SEM and tomography techniques," *Continuum Mechanics and Thermodynamics*, vol. 32, pp. 471–488, 2020. DOI: 10.1007/s00161-020-00865-5.

[289] C. van Innis and T. Pardoen, "Thickness-dependent selection of adhesive joints," *Journal of Adhesion*, vol. 00, pp. 1–54, 2023. DOI: 10.1080/00218464.2023.2294131.

[290] P. Nikaeen, A. Samadi-Dooki, G. Z. Voyiadjis, P. Zhang, W. M. Chirdon, and A. Khattab, "Effect of plastic deformation on the nanomechanical properties of glassy polymers: An experimental study," *Mechanics of Materials*, vol. 159, p. 103 900, 2021. DOI: 10.1016/J.MECHMAT.2021.103900.

[291] N. Klavzer, S. F. Gayot, M. Coulombier, B. Nysten, and T. Pardoen, "Nanoscale digital image correlation at elementary fibre/matrix level in polymer–based composites," *Composites Part A: Applied Science and Manufacturing*, vol. 168, p. 107 455, 2023. DOI: 10.1016/j.compositesa.2023.107455.

[292] C.-S. Han, "Indentation Size Effect in Polymers," *Advances in Materials Science Research*, vol. 10, pp. 393–413, 2011.

[293] R. M. Winter and J. E. Houston, "Interphase mechanical properties in epoxy-glass fiber composites as measured by interfacial force microscopy," *Sandia National Laboratories*, 1998.

[294] M. Bornert *et al.*, "Assessment of Digital Image Correlation Measurement Errors: Methodology and Results," *Experimental Mechanics*, vol. 49, pp. 353–370, 2009. DOI: 10.1007/s11340-008-9204-7.

[295] F. Lagattu, F. Bridier, P. Villechaise, and J. Brillaud, "In-plane strain measurements on a microscopic scale by coupling digital image correlation and an in situ SEM technique," *Materials Characterization*, vol. 56, pp. 10–18, 2006.

[296] E. Totry, C. González, J. LLorca, and J. M. Molina-Aldareguía, "Mechanisms of shear deformation in fiber-reinforced polymers: experiments and simulations," *International Journal of Fracture*, vol. 158, pp. 197–209, 2009.

[297] G. Catalanotti, P. P. Camanho, J. Xavier, C. G. Dávila, and A. T. Marques, "Measurement of resistance curves in the longitudinal failure of composites using digital image correlation," *Composites Science and Technology*, vol. 70, pp. 1986–1993, 2010.

[298] S. V. Lomov *et al.*, "Full-field strain measurements for validation of meso-FE analysis of textile composites," *Composites Part A: Applied Science and Manufacturing*, vol. 39, pp. 1218–1231, 2008.

[299] J. L. W. Carter, M. D. Uchic, and M. J. Mills, "Impact of speckle pattern parameters on dic strain resolution calculated from in-situ sem experiments," 2015.

[300] C. B. Montgomery, B. Koohbor, and N. R. Sottos, "A robust patterning technique for electron microscopy-based digital image correlation at submicron resolutions," *Experimental Mechanics*, vol. 59, pp. 1063–1073, 2019.

[301] J. P. M. Hoefnagels, M. van Maris, and T. Vermeij, "One-step deposition of nano-to-micron-scalable, high-quality digital image correlation patterns for high-strain in-situ multi-microscopy testing," *Strain*, vol. 55, p. 12 330, 2019.

[302] Y. S. Jung, D. W. Lee, and D. Y. Jeon, "Influence of dc magnetron sputtering parameters on surface morphology of indium tin oxide thin films," *Applied Surface Science*, vol. 221, pp. 136–142, 2004. DOI: 10.1016/S0169-4332(03)00862-6.

[303] M. A. Sutton, N. Li, D. C. Joy, A. P. Reynolds, and X. Li, "Scanning electron microscopy for quantitative small and large deformation measurements part i: Sem imaging at magnifications from 200 to 10,000," *Experimental Mechanics*, vol. 47, pp. 775–787, 2007.

[304] M. A. Sutton *et al.*, "Scanning electron microscopy for quantitative small and large deformation measurements - part II: Experimental validation for magnifications from 200 to 10,000," *Experimental Mechanics*, vol. 47, p.789–804, 2007. DOI: 10.1007/s11340-007-9041-0.

[305] S. S. Maraghechi, J. P. M. Hoefnagels, R. H. J. Peerlings, O. Rokos, and M. Geers, "Correction of scanning electron microscope imaging artifacts in a novel digital image correlation framework," *Experimental Mechanics*, vol. 59, pp. 489–516, 2019.

[306] S. Maraghechi, J. P. Hoefnagels, R. H. Peerlings, and M. G. Geers, "Correction of scan line shift artifacts in scanning electron microscopy: An extended digital image correlation framework," *Ultramicroscopy*, vol. 187, pp. 144–163, 2018. DOI: https://doi.org/10.1016/j.ultramic.2018.01.002.

[307] A. W. Mello, T. A. Book, A. Nicolas, S. E. Otto, C. J. Gilpin, and M. D. Sangid, "Distortion Correction Protocol for Digital Image Correlation after Scanning Electron Microscopy: Emphasis on Long Duration and Ex-Situ Experiments," *Experimental Mechanics*, vol. 57, pp. 1395–1409, 2017. DOI: 10.1007/s11340-017-0303-1.

[308] A. D. Kammers and S. H. Daly, "Digital image correlation under scanning electron microscopy: Methodology and validation," *Experimental Mechanics*, vol. 53, pp. 1743–1761, 2013.

[309] V. E.
bibinitperiod Materials, *Vem thin film evaporation guide 2017.*

[310] H. M. I. n.d., *High purity evaporation materials.*

[311] CDC, *Niosh pocket guide to chemical hazards - indium n.d.*

[312] D. System, *Abaqus 6.11 Glossary.*

[313] M. Maes, "Mechanical properties of high performance recyclable thermoplastic based composites," Master thesis, UCLouvain, 2020.

[314] M. R. Vanlandingham, S. H. McKnight, G. R. Palmese, T. A. Bogetti, R. F. Eduljee, and J. W. Gillespie, "Characterization of interphase regions using atomic force microscopy," *MRS Proceedings*, vol. 458, p. 313, 1996. DOI: 10.1557/PROC-458-313.

[315] M. Jebahi and S. Forest, "Scalar-based strain gradient plasticity theory to model size-dependent kinematic hardening effects," *Continuum Mechanics and Thermodynamics*, vol. 33, pp. 1223–1245, 2021. DOI: 10.1007/s00161-020-00967-0.

[316] C. S. Lopes, C. González, O. Falcó, F. Naya, J. LLorca, and B. Tijs, "Multiscale virtual testing: the roadmap to efficient design of composites for damage resistance and tolerance," *CEAS Aeronautical Journal*, vol. 7, pp. 607–619, 2016. DOI: 10.1007/s13272-016-0210-7.

[317] Q. D. Yang, B. N. Cox, X. J. Fang, and Z. Q. Zhou, "Virtual testing for advanced aerospace composites: Advances and future needs," *Journal of Engineering Materials and Technology*, vol. 133, pp. 1–6, 2011. DOI: 10.1115/1.4002637.

[318] X. Bai, M. A. Bessa, A. R. Melro, P. P. Camanho, L. Guo, and W. K. Liu, "High-fidelity micro-scale modeling of the thermo-visco-plastic behavior of carbon fiber polymer matrix composites," *Composite Structures*, vol. 134, pp. 132–141, 2015. DOI: 10.1016/J.COMPSTRUCT.2015.08.047.

[319] C.-S. Han, S. H. R. Sanei, and F. Alisafaei, "On the origin of indentation size effects and depth dependent mechanical properties of elastic polymers," *Journal of Polymer Engineering*, vol. 36, pp. 103–111, 2016. DOI: 10.1515/polyeng-2015-0030.

[320] A. Samadi-Dooki, L. Malekmotiei, and G. Z. Voyiadjis, "Characterizing shear transformation zones in polycarbonate using nanoindentation," *Polymer*, vol. 82, pp. 238–245, 2016. DOI: 10.1016/j.polymer.2015.11.049.

[321] D. C. Lam, L. H. Keung, and P. Tong, "Size-dependent behavior of macromolecular solids II: Higher-order viscoelastic theory and experiments," *CMES - Computer Modeling in Engineering and Sciences*, vol. 66, pp. 73–99, 2010.

[322] C. Liebold and W. H. Müller, "Comparison of gradient elasticity models for the bending of micromaterials," *Computational Materials Science*, vol. 116, pp. 52–61, 2016. DOI: 10.1016/j.commatsci.2015.10.031.

[323] V. Marcadon, D. Brown, E. Hervé, P. Mélé, N. D. Albérola, and A. Zaoui, "Confrontation between Molecular Dynamics and micromechanical approaches to investigate particle size effects on the mechanical behaviour of polymer nanocomposites," *Computational Materials Science*, vol. 79, pp. 495–505, 2013. DOI: 10.1016/j.commatsci.2013.07.002.

[324] V. Marcadon, E. Herve, and A. Zaoui, "Micromechanical modeling of packing and size effects in particulate composites," *International Journal of Solids and Structures*, vol. 44, pp. 8213–8228, 2007. DOI: 10.1016/j.ijsolstr.2007.06.008.

[325] D. Davydov *et al.*, "Size Effects in a Silica-Polystyrene Nanocomposite: Molecular Dynamics and Surface-enhanced Continuum Approaches," *Soft Materials*, vol. 12, S142–S151, 2014. DOI: 10.1080/1539445X.2014.959597.

[326] H. T. Zhu, H. M. Zbib, and E. C. Aifantis, "Strain gradients and continuum modeling of size effect in metal matrix composites," *Acta Mechanica*, vol. 121, pp. 165–176, 1997. DOI: 10.1007/BF01262530.

[327] G. Z. Voyiadjis, A. Shojaei, and N. Mozaffari, "Strain gradient plasticity for amorphous and crystalline polymers with application to micro- and nano-scale deformation analysis," *Polymer*, vol. 55, pp. 4182–4198, 2014. DOI: 10.1016/j.polymer.2014.06.015.

[328] V. D. Nguyen, F. Lani, T. Pardoen, X. P. Morelle, and L. Noels, "A large strain hyperelastic viscoelastic-viscoplastic-damage constitutive model based on a multi-mechanism non-local damage continuum for amorphous glassy polymers," *International Journal of Solids and Structures*, vol. 96, pp. 192–216, 2016. DOI: 10.1016/j.ijsolstr.2016.06.008.

[329] V. D. Nguyen, L. Wu, and L. Noels, "A micro-mechanical model of reinforced polymer failure with length scale effects and predictive capabilities. Validation on carbon fiber reinforced high-crosslinked RTM6 epoxy resin," *Mechanics of Materials*, vol. 133, pp. 193–213, 2019. DOI: 10.1016/j.mechmat.2019.02.017.

[330] M. Mazière and S. Forest, "Strain gradient plasticity modeling and finite element simulation of Lüders band formation and propagation," *Continuum Mechanics and Thermodynamics*, vol. 27, pp. 83–104, 2015. DOI: 10.1007/s00161-013-0331-8.

[331] M. Rezaee Hajidehi and S. Stupkiewicz, "Gradient-enhanced model and its micromorphic regularization for simulation of Lüders-like bands in shape memory alloys," *International Journal of Solids and Structures*, vol. 135, pp. 208–218, 2018. DOI: 10.1016/j.ijsolstr.2017.11.021.

[332] M. Abatour, S. Forest, K. Ammar, C. Ovalle, N. Osipov, and S. Quilici, "Toward robust scalar-based gradient plasticity modeling and simulation at finite deformations," *Acta Mechanica*, vol. 234, pp. 911–958, 2023. DOI: 10.1007/s00707-022-03411-3.

[333] V. D. Nguyen, T. Pardoen, and L. Noels, "A nonlocal approach of ductile failure incorporating void growth, internal necking, and shear dominated coalescence mechanisms," *Journal of the Mechanics and Physics of Solids*, vol. 137, p. 103 891, 2020. DOI: 10.1016/j.jmps.2020.103891.

[334] H. Holthusen, T. Brepols, S. Reese, and J. W. Simon, "An anisotropic constitutive model for fiber-reinforced materials including gradient-extended damage and plasticity at finite strains," *Theoretical and Applied Fracture Mechanics*, vol. 108, p. 102 642, 2020. DOI: 10.1016/j.tafmec.2020.102642.

[335] J. Friedlein, J. Mergheim, and P. Steinmann, "Observations on additive plasticity in the logarithmic strain space at excessive strains," *International Journal of Solids and Structures*, vol. 239-240, p. 111 416, 2022. DOI: 10.1016/j.ijsolstr.2021.111416.

[336] *Zset Software,Non-linear material & structure analysis suite. www.zset-software.com*, 2022. [Online]. Available: http://www.zset-software.com/.

[337] J. Besson, G. Cailletaud, J. Chaboche, S. Forest, and B. M, "Non-linear mechanics of materials," in *Solid mechanics and its applications 167*, Springer-Verlag Berlin Heidelberg, 2009, ch. Solid Mech. DOI: doi:10.1007/978-90-481-3356-7.

[338] M. Geers G.D., R. de Borst, W. Brekelmans A.M., and R. Peerlings H.J., "On the use of local strain fields for the determination of the intrinsic length scale," *J. Phys. IV France*, vol. 08, Pr8–167–Pr8–174, 1998.

[339] M. G. Geers, R. D. Borst, W. A. Brekelmans, and R. H. Peerlings, "Validation and internal length scale determination for a gradient damage model: application to short glass-fibre-reinforced polypropylene," *International Journal of Solids and Structures*, vol. 36, pp. 2557–2583, 1999. DOI: 10.1016/S0020-7683(98)00123-1.

[340] N. M. Cordero, S. Forest, and E. P. Busso, *Generalised continuum modelling of grain size effects in polycrystals*, 2012. DOI: 10.1016/j.crme.2012.02.009.

[341] P. Baral, G. Guillonneau, G. Kermouche, J. M. Bergheau, and J. L. Loubet, "A new long-term indentation relaxation method to measure creep properties at the micro-scale with application to fused silica and PMMA," *Mechanics of Materials*, vol. 137, p. 103 095, 2019. DOI: 10.1016/j.mechmat.2019.103095.

[342] "Indentation stress relaxation of sol–gel-derived organic/inorganic hybrid coating," *Acta Materialia*, vol. 53, pp. 4455–4462, 2005. DOI: 10.1016/J.ACTAMAT.2005.06.005.

[343] D. E. Stegall, M. A. Mamun, B. Crawford, and A. A. Elmustafa, "Repeated load relaxation testing of pure polycrystalline nickel at room temperature using nanoindentation," *Applied Physics Letters*, vol. 104, pp. 1–4, 2014. DOI: 10.1063/1.4862799.

[344] K. L. Johnson, "The correlation of indentation experiments," *Journal of the Mechanics and Physics of Solids*, vol. 18, pp. 115–126, 1970. DOI: 10.1016/0022-5096(70)90029-3.

[345] A. Technologies, *Keysight Nano Indenter G200*. 2017.

[346] G. M. Pharr, E. G. Herbert, and Y. Gao, "The Indentation Size Effect: A Critical Examination of Experimental Observations and Mechanistic Interpretations," *Annual Review of Materials Research*, vol. 40, pp. 271–292, 2010. DOI: 10.1146/annurev-matsci-070909-104456.

[347] G. Guillonneau, G. Kermouche, S. Bec, and J. L. Loubet, "Extraction of Mechanical Properties with Second Harmonic Detection for Dynamic Nanoindentation Testing," *Experimental Mechanics*, vol. 52, pp. 933–944, 2012. DOI: 10.1007/s11340-011-9561-5.

[348] G. Guillonneau, G. Kermouche, J. M. Bergheau, and J. L. Loubet, "A new method to determine the true projected contact area using nanoindentation testing," *Comptes Rendus - Mecanique*, vol. 343, pp. 410–418, 2015. DOI: 10.1016/j.crme.2015.06.004.

[349] P. Baral, "Caractérisation mécanique des phénomènes dépendants du temps par nanoindentation instrumentée en température," Ph.D. dissertation, Ecole Centrale de Lyon, 2019.

[350] J. L. Loubet, M. Bauer, A. Tonck, S. Bec, and B. Gauthier-Manuel, "Nanoindentation with a surface force apparatus," in *Mechanical properties and deformation behavior of materials having ultra-fine microstructures*, M. Nastasi, D. M. Parkin, and H. Gleiter, Eds., Dordrecht: Springer Netherlands, 1993, pp. 429–447.

[351] B. J. Briscoe, L. Fiori, and E. Pelillo, "Nano-indentation of polymeric surfaces," *Journal of Physics D: Applied Physics*, vol. 31, pp. 2395–2405, 1998. DOI: 10.1088/0022-3727/31/19/006.

[352] F. J. Calleja, A. Flores, and G. H. Michler, "Microindentation studies at the near surface of glassy polymers: Influence of molecular weight," *Journal of Applied Polymer Science*, vol. 93, pp. 1951–1956, 2004. DOI: 10.1002/app.20665.

[353] H. Lin, L. Lv, T. Jin, and Q. Yin, "Investigation on the influences of hygrothermal aging on the indentation size effects and micro-indentation measurements of PMMA. Part II: Analysis and modeling," *Polymer Testing*, vol. 93, p. 106 938, 2021. DOI: 10.1016/j.polymertesting.2020.106938.

[354] M. Rueda-Ruiz, B. D. Beake, and J. M. Molina-Aldareguia, "Determination of Rate-Dependent Properties in Cohesive Frictional Materials by Instrumented Indentation," *JOM*, vol. 74, pp. 2206–2219, 2022. DOI: 10.1007/s11837-022-05268-2.

[355] F. Alisafaei, C. S. Han, and N. Garg, "On couple-stress elasto-plastic constitutive frameworks for glassy polymers," *International Journal of Plasticity*, vol. 77, pp. 30–53, 2016. DOI: 10.1016/j.ijplas.2015.09.011.

[356] J. Richeton, S. Ahzi, and L. Daridon, "Thermodynamic investigation of yield-stress models for amorphous polymers," *Philosophical Magazine*, vol. 87, pp. 3629–3643, 2007. DOI: 10.1080/14786430701381162.

[357] F. Varnik, L. Bocquet, and J. L. Barrat, "A study of the static yield stress in a binary Lennard-Jones glass," *Journal of Chemical Physics*, vol. 120, pp. 2788–2801, 2004. DOI: 10.1063/1.1636451.

[358] B. Passilly and R. Delannoy, "Characterization of the ageing of an epoxy resin using high temperature nanoindentation," *Matériaux & Techniques*, vol. 107, p. 206, 2019. DOI: 10.1051/mattech/2019004.

[359] M. Hardiman, T. Vaughan, and C. McCarthy, "The effect of microscale residual stress from thermal cooldown on the nanoindentation properties of fibre-reinforced composites," *Journal of Composite Materials*, vol. 50, pp. 4147–4158, 2016. DOI: 10.1177/0021998316632603.

[360] A. T. DiBenedetto, "Prediction of the glass transition temperature of polymers: A model based on the principle of corresponding states," *Journal of Polymer Science Part B: Polymer Physics*, vol. 25, pp. 1949–1969, 1987. DOI: 10.1002/polb.1987.090250914.

[361] A. Bahrami, X. Morelle, L. D. Hông Minh, T. Pardoen, C. Bailly, and B. Nysten, "Curing dependent spatial heterogeneity of mechanical response in epoxy resins revealed by atomic force microscopy," *Polymer*, vol. 68, pp. 1–10, 2015.

[362] L. Liu *et al.*, "Interfacial characterization, control and modification of carbon fiber reinforced polymer composites," *Composites Science and Technology*, vol. 121, pp. 56–72, 2015. DOI: 10.1016/j.compscitech.2015.08.002.

[363] E. Van Vlierberghe, S. Gayot, N. Klavzer, C. Breite, Y. Swolfs, and T. Pardoen, "Microstructural strain localisation phenomena in fibre-reinforced polymer composites: Insights from nanoscale digital image correlation and finite element modelling," *Composites Science and Technology*, vol. Under. Sub. 2024.

[364] A. Hamdoun and R. Mahnken, "A large deformation gradient theory for glassy polymers by means of micromorphic regularization," *Archive of Applied Mechanics*, 2024. DOI: 10.1007/s00419-024-02570-0.

[365] L. Lamm *et al.*, "Gradient-extended damage modelling for polymeric materials at finite strains: Rate-dependent damage evolution combined with viscoelasticity," *European Journal of Mechanics, A/Solids*, vol. 103, p. 105 121, 2024. DOI: 10.1016/j.euromechsol.2023.105121.

[366] N. Mohtadifar, "Nano-mechanical characterization of the fiber-matrix interface of polymer composites," Master thesis, Université Catholique de Louvain, 2023.

[367] Y. Liu, F. V. der Meer, L. Sluys, and J. Fan, "A numerical homogenization scheme used for derivation of a homogenized viscoelastic-viscoplastic model for the transverse response of fiber-reinforced polymer composites," *Compos. Struct.*, vol. 252, 2020.

[368] Z. Liu, M. Bessa, and W. K. Liu, "Self-consistent clustering analysis: An efficient multi-scale scheme for inelastic heterogeneous materials," *Comput. Methods Appl. Mech. Eng.*, vol. 306, pp. 319–341, 2016.

[369] R. Bedzra, S. Reese, and J.-W. Simon, "Hierarchical multi-scale modelling of flax fibre/epoxy composite by means of general anisotropic viscoelastic-viscoplastic constitutive models: Part i – micromechanical model," *Int. J. Solids Struct.*, vol. 202, pp. 58–74, 2020.

[370] R. Kopp *et al.*, "Damage micro-mechanisms in notched hierarchical nano-engineered thin-ply composite laminates studied by in-situ synchrotron X-ray microtomography," in *AIAA Scitech 2019 Forum*, San Diego, California: American Institute of Aeronautics and Astronautics, 2019, ISBN: 978-1-62410-578-4.

[371] S. Garcea, I. Sinclair, S. Spearing, and P. Withers, "Mapping fibre failure in situ in carbon fibre reinforced polymers by fast synchrotron X-ray computed tomography," *Compos. Sci. Technol.*, vol. 149, pp. 81–89, 2017.

[372] E. Schöberl *et al.*, "Fibre-direction strain measurement in a composite ply under quasi-static tensile loading using digital volume correlation and in situ synchrotron radiation computed tomography," *Compos. Part A Appl. Sci. Manuf.*, vol. 137, 2020.

[373] A. Buljac *et al.*, "Digital volume correlation: Review of progress and challenges," *Exp. Mech.*, vol. 58, pp. 661–708, 2018.

[374] M. Zhu *et al.*, "Digital image correlation assisted characterization of mode i fatigue delamination in composites," *Compos. Struct.*, vol. 253, p. 112 746, 2020.

[375] I. Rocha, P. Kerfriden, and F. van der Meer, "Micromechanics-based surrogate models for the response of composites: A critical comparison between a classical mesoscale constitutive model, hyper-reduction and neural networks," *Eur. J. Mech. - A Solids*, vol. 82, 2020.

[376] M. Bessa *et al.*, "A framework for data-driven analysis of materials under uncertainty: Countering the curse of dimensionality," *Comput. Methods Appl. Mech. Eng.*, vol. 320, pp. 633–667, 2017.

[377] S. Tang *et al.*, "Map123-ep: A mechanistic-based data-driven approach for numerical elastoplastic analysis," *Comput. Methods Appl. Mech. Eng.*, vol. 364, 2020.

[378] N. Fleck and J. Hutchinson, "A reformulation of strain gradient plasticity," *J. Mech. Phys. Solids*, vol. 49, pp. 2245–2271, 2001.

[379] O. Verschatse, L. Daelemans, W. Van Paepegem, and K. De Clerck, "In-situ observations of microscale ductility in a quasi-brittle bulk scale epoxy," *Polymers*, vol. 12, p. 2581, 2020.

[380] C. Breite *et al.*, "Blind benchmarking of seven longitudinal tensile failure models for two virtual unidirectional composites," *Compos. Sci. Technol.*, 2020.

[381] C. Breite *et al.*, "Detailed experimental validation and benchmarking of six models for longitudinal tensile failure of unidirectional composites," *submitted to Compos. Part A Appl. Sci. Manuf.*, 2020.

[382] G. Binnig, C. F. Quate, and C. Gerber, "Atomic force microscope," *Physi. Rev. Lett.*, vol. 56, pp. 930–933, 1986.

[383] S. A. Joyce and J. E. Houston, "A new force sensor incorporating force feedback control for interfacial force microscopy," *Rev. Sci. Instrum.*, vol. 62, pp. 710–715, 1991.

[384] A. Bahrami *et al.*, "Synergistic local toughening of high performance epoxy-matrix composites using blended block copolymer-thermoplastic thin films," *Compos. Part A Appl. Sci. Manuf.*, vol. 91, pp. 398–405, 2016.

[385] S. A. Syed Asif, K. J. Wahl, R. J. Colton, and O. L. Warren, "Quantitative imaging of nanoscale mechanical properties using hybrid nanoindentation and force modulation," *J. Appl. Phys.*, vol. 90, pp. 1192–1200, 2001.

[386] S.-L. Gao and E. Mader, "Characterisation of interphase nanoscale property variations in glass fibre reinforced polypropylene and epoxy resin composites," *Compos. Part A Appl. Sci. Manuf.*, vol. 33, pp. 559–576, 2002.

[387] J. He and Y. Huang, "Afm characterization of interphase properties of silver-coated carbon fibre reinforced epoxy composites," *Polym. Polym. Compos.*, vol. 14, pp. 123–134, 2006.

[388] Y. Wang and T. H. Hahn, "Afm characterization of the interfacial properties of carbon fiber reinforced polymer composites subjected to hygrothermal treatments," *Compos. Sci. Technol.*, vol. 67, pp. 92–101, 2007.

[389] S. Q. Wang, S. D. Nair, D. Hurley, and S. H. Lee, "Characterizing interphase properties in fiber reinforced polymer composite with advanced afm based tools," *Adv. Mater. Res.*, vol. 123-125, pp. 403–406, 2010.

[390] M. Qu, F. Deng, S. M. Kalkhoran, A. Gouldstone, A. Robisson, and K. J. Van Vliet, "Nanoscale visualization and multiscale mechanical implications of bound rubber interphases in rubber–carbon black nanocomposites," *Soft Matter*, vol. 7, pp. 1066–1077, 2011.

[391] V. Cech, E. Palesch, and J. Lukes, "The glass fiber–polymer matrix interface/interphase characterized by nanoscale imaging techniques," *Compos. Sci. Technol.*, vol. 83, pp. 22–26, 2013.

[392] P. F. Brune *et al.*, "Direct measurement of rubber interphase stiffness," *Macromolecules*, vol. 49, pp. 4909–4922, 2016.

[393] L. K. Babu, "The use of afm indentation to quantify mechanical properties of the interphase region in fiber-reinforced composites," Ph.D. dissertation, Oklahoma State University, Oklahoma City, OK, USA, 2019.

[394] A. Bahrami, C. Bailly, and B. Nysten, "Spatial resolution and property contrast in local mechanical mapping of polymer blends using afm dynamic force spectroscopy," *Polymer*, vol. 165, pp. 180–190, 2019.

[395] P. Maivald *et al.*, "Using force modulation to image surface elasticities with the atomic force microscope," *Nanotechnology*, vol. 2, pp. 103–106, 1991.

[396] M. Heuberger, G. Dietler, and L. Schlapbach, "Mapping the local young's modulus by analysis of the elastic deformations occurring in atomic force microscopy," *Nanotechnology*, vol. 6, pp. 12–23, 1995.

[397] S. C. Minne, Y. Hu, S. Hu, B. Pittenger, and C. Su, "Nanoscale quantitative mechanical property mapping using peak force tapping atomic force microscopy," *Microsc. Microanal.*, vol. 16, pp. 464–465, 2010.

[398] O. Sahin, S. Magonov, C. Su, C. F. Quate, and O. Solgaard, "An atomic force microscope tip designed to measure time-varying nanomechanical forces," *Nat. Nanotechnol.*, vol. 2, pp. 507–514, 2007.

[399] J. A. Ramos, M. Blanco, I. Zalakain, and I. Mondragon, "Nanoindentation study of interphases in epoxy/amine thermosetting systems modified with thermoplastics," *J. Colloid Interface Sci.*, vol. 336, pp. 431–437, 2009.

[400] L. Belec and Y. Joliff, "Mechanically affected zone in afm force measurements — focus on actual probe tip geometry," *Mater. Des.*, vol. 104, pp. 217–226, 2016.

[401] P. Eaton and P. West, *Atomic Force Microscopy*. Oxford, England: Oxford University Press, 2010, ISBN: 978-0-19-957045-4.

[402] J. Williams, M. Donnellan, M. James, and W. Morris, "Properties of the interphase in organic matrix composites," *Mater. Sci. Eng. A*, vol. 126, 1990.

[403] K. Mai, E. Mäder, and M. Mühle, "Interphase characterization in composites with new non-destructive methods," *Compos. Part A Appl. Sci. Manuf.*, vol. 29, pp. 1111–1119, 1998.

[404] Z. Boufaida, "Analyse des propriétés mécaniques de composites taffetas verre/matrice acrylique en relation avec les propriétés d'adhésion des fibres sur la matrice," Ph.D. dissertation, Université de Lorraine, Oklahoma City, OK, USA, 2015.

[405] I. Rocha, S. Raijmaekers, F. van der Meer, R. Nijssen, H. Fischer, and L. Sluys, "Combined experimental/numerical investigation of directional moisture diffusion in glass/epoxy composites," *Compos. Sci. Technol.*, vol. 151, pp. 16–24, 2017.

[406] I. Miskdjian, M. Hajikazemi, and W. Van Paepegem, "Automatic edge detection of ply cracks in glass fiber composite laminates under quasi-static and fatigue loading using multi-scale digital image correlation," *Compos. Sci. Technol.*, vol. 200, 2020.

[407] H. W. Schreier, "Systematic errors in digital image correlation caused by intensity interpolation," *Opt. Eng.*, vol. 39, p. 2915, 2000.

[408] J. L. W. Carter, M. D. Uchic, and M. J. Mills, "Impact of Speckle Pattern Parameters on DIC Strain Resolution Calculated from In-situ SEM Experiments," in *Fracture, Fatigue, Failure, and Damage Evolution, Volume 5*, J. Carroll and S. Daly, Eds., Cham, Switzerland: Springer International Publishing, 2015, pp. 119–126.

[409] R. Naylor, C. Fagiano, M. Hirsekorn, B. Tranquart, and E. Baranger, "Mesures de champs de déformations par corrélations d'images pour l'identification de modèles mécaniques microscopiques de composites à matrice polymère," in *Compte Rendus des JNC 20*, École des Ponts ParisTech, Paris, France, 2017, pp. 1–9.

[410] B. Harris, *Fatigue in composites: science and technology of the fatigue response of fibre-reinforced plastics*. Cambridge, England: Woodhead Publishing, 2003, ISBN: 1-85573-608-X.

[411] M. S. Madhukar and L. T. Drzal, "Fiber-matrix adhesion and its effect on composite mechanical properties: Iii. longitudinal (0 degree) compressive properties of graphite/epoxy composites," *J. Compos. Mater.*, vol. 25, pp. 932–957, 1991.

[412] B. Larson and L. Drzal, "Glass fibre sizing/matrix interphase formation in liquid composite moulding: Effects on fibre/matrix adhesion and mechanical properties," *Composites*, vol. 25, pp. 711–721, 1994.

[413] S. Subramanian, J. Lesko, K. Reifsnider, and W. Stinchcomb, "Characterization of the fibre-matrix interphase and its influence on mechanical properties of unidirectional composites," *J. Compos. Mater.*, vol. 30, pp. 309–332, 1996.

[414] M. Desaeger and I. Verpoest, "On the use of the micro-indentation test technique to measure the interfacial shear strength of fibre-reinforced polymer composites," *Compo.s Sci. Technol.*, vol. 48, pp. 215–226, 1993.

[415] J. Sha, J. Dai, J. Li, Z. Wei, J.-M. Hausherr, and W. Krenkel, "Measurement and analysis of fiber-matrix interface strength of carbon fiber-reinforced phenolic resin matrix composites," *J. Compos. Mater.*, vol. 48, pp. 1303–1311, 2014.

[416] M. Greisel, J. Jäger, J. Moosburger-Will, M. Sause, W. Mueller, and S. Horn, "Influence of residual thermal stress in carbon fiber-reinforced thermoplastic composites on interfacial fracture toughness evaluated by cyclic single-fiber push-out tests," *Compos. Part A Appl. Sci. Manuf.*, vol. 66, pp. 117–127, 2014.

[417] M. Piggott, "Why interface testing by single-fibre methods can be misleading," *Compos. Sci. Technol.*, vol. 57, pp. 965–974, 1997.

[418] G. Alfano and E. Sacco, "Combining interface damage and friction in a cohesive-zone model: Combining interface damage and friction in a cohesive-zone model," *Int. J. Numer. Meth. Eng.*, vol. 68, pp. 542–582, 2006.

[419] J. LLorca *et al.*, "Multiscale Modeling of Composite Materials: a Roadmap Towards Virtual Testing," *Advanced Materials*, vol. 23, pp. 5130–5147, 2011.

[420] T. E. Gartner and A. Jayaraman, "Modeling and simulations of polymers: A roadmap," *Macromolecules*, vol. 52, pp. 755–786, 2019.

[421] C. Buckley, "Glass-rubber constitutive model for amorphous polymers near the glass transition," *Polymer*, vol. 36, pp. 3301–3312, 1995.

[422] E. T. J. Klompen, T. A. P. Engels, L. E. Govaert, and H. E. H. Meijer, "Modeling of the postyield response of glassy polymers: Influence of thermomechanical history," *Macromolecules*, vol. 38, pp. 6997–7008, 2005.

[423] J. Johnsen, A. H. Clausen, F. Grytten, A. Benallal, and O. S. Hopperstad, "A thermo-elasto-viscoplastic constitutive model for polymers," *J. Mech. Phys. Solids*, vol. 124, pp. 681–701, 2019.

[424] V. Srivastava, S. A. Chester, N. M. Ames, and L. Anand, "A thermo-mechanically-coupled large-deformation theory for amorphous polymers in a temperature range which spans their glass transition," *Int. J. Plast.*, vol. 26, pp. 1138–1182, 2010.

[425] A. Argon and L. Shi, "Development of visco-plastic deformation in metallic glasses," *Acta Metall.*, vol. 31, pp. 499–507, 1983.

[426] M. L. Falk and J. S. Langer, "Dynamics of viscoplastic deformation in amorphous solids," *Phys. Rev. E*, vol. 57, pp. 7192–7205, 1998.

[427] M. Zink, K. Samwer, W. L. Johnson, and S. G. Mayr, "Plastic deformation of metallic glasses: Size of shear transformation zones from molecular dynamics simulations," *Phys. Rev. B*, vol. 73, pp. 2–4, 2006.

[428] Y. C. Hu *et al.*, "Unveiling atomic-scale features of inherent heterogeneity in metallic glass by molecular dynamics simulations," *Phys. Rev. B*, vol. 93, p. 214 202, 2016.

[429] K. E. Avila, S. Küchemann, I. A. Alhafez, and H. M. Urbassek, "Shear-transformation zone activation during loading and unloading in nanoindentation of metallic glasses," *Materials*, vol. 12, 2019.

[430] P. H. Mott, A. S. Argon, and U. W. Suter, "Atomistic modelling of plastic deformation of glassy polymers," *Philos. Mag. A*, vol. 67, pp. 931–978, 1993.

[431] E. F. Oleinik, S. N. Rudnev, and O. B. Salamatina, "Evolution in concepts concerning the mechanism of plasticity in solid polymers after the 1950s," *Polym. Sci. Ser. A*, vol. 49, pp. 1302–1327, 2007.

[432] A. Argon and H. Kuo, "Plastic flow in a disordered bubble raft (an analog of a metallic glass)," *Mater. Sci. Eng.*, vol. 39, pp. 101–109, 1979.

[433] D. Pan, A. Inoue, T. Sakurai, and M. W. Chen, "Experimental characterization of shear transformation zones for plastic flow of bulk metallic glasses," *Proc. Natl. Acad. Sci.*, vol. 105, pp. 14 769–14 772, 2008.

[434] E. R. Homer, D. Rodney, and C. A. Schuh, "Kinetic monte carlo study of activated states and correlated shear-transformation-zone activity during the deformation of an amorphous metal," *Phys.l Rev. B*, vol. 81, 2010.

[435] E. R. Homer and C. A. Schuh, "Three-dimensional shear transformation zone dynamics model for amorphous metals," *Model. Simul. Mater. Sci. Eng.*, vol. 18, p. 065 009, 2010.

[436] L. Li, E. Homer, and C. Schuh, "Shear transformation zone dynamics model for metallic glasses incorporating free volume as a state variable," *Acta Mater.*, vol. 61, pp. 3347–3359, 2013.

[437] V. V. Bulatov and A. S. Argon, "A stochastic model for continuum elasto-plastic behavior. i. numerical approach and strain localization," *Model. Simul. Mater. Sci. Eng.*, vol. 2, pp. 167–184, 1994.

[438] S. Im *et al.*, "Direct determination of structural heterogeneity in metallic glasses using four-dimensional scanning transmission electron microscopy," *Ultramicroscopy*, vol. 195, pp. 189–193, 2018.

[439] M. Mehdikhani, I. Straumit, L. Gorbatikh, and S. V. Lomov, "Detailed characterization of voids in multidirectional carbon fiber/epoxy composite laminates using x-ray micro-computed tomography," *Compos. Part A Appl. Sci. Manuf.*, vol. 125, 2019.

[440] C. Breite, E. Schöberl, M. Mavrogordato, L. Gorbatikh, S. Lomov, and Y. Swolfs, "Automated image analysis of ultrafast synchrotron ct scans to experimentally characterise the fibre break development during in-situ tensile tests," presented at the 22nd International Conference on Composite Materials, Melbourne, Australia, Aug. 2019.

[441] X. Ni *et al.*, "In situ synchrotron computed tomography study of nanoscale interlaminar reinforcement and thin-ply effects on damage progression in composite laminates," *Compos. Part B Eng.*, p. 108 623, 2021.

[442] C. Schöberl Erich andBreite, S. Rosini, Y. Swolfs, M. N. Mavrogordato, I. Sinclair, and S. M. Spearing, "A novel particle-filled carbon-fibre reinforced polymer model composite tailored for the application of digital volume correlation and computed tomography," *J. Compos. Mater.*, 2021.